

**DEVELOPMENT OF NOVEL ANALYTICAL TECHNIQUES
FOR USE IN SEARCHES FOR ULTRA HIGH ENERGY
GAMMA RAY SOURCES**

by

David William Idenden B.Sc.

Submitted in accordance with the requirements
for the degree of Doctor of Philosophy

The candidate confirms that the work submitted is his own and that appropriate credit
has been given where reference has been made to the work of others

The University of Leeds

Department of Physics

September 1991

Abstract

The work of the thesis aims at providing improved analysis techniques to be used in searches made for ultra high energy ($>1\text{PeV}$) gamma ray sources, using data obtained at the Haverah Park gamma ray telescope (GREX). After a brief introductory review of the field (Chapter 1), which sets ultra high energy gamma ray astronomy in the context of cosmic ray origin, and a short description of the GREX instrument (Chapter 2), innovative analysis techniques developed by the author are described (Chapters 3-5); two of these techniques are used in a study of the candidate X-ray binary sources, Her X-1 and 1E2259+589 in Chapter 6. A rapid method of shower core location has been developed and implemented in the data analysis and a new method of estimating the background contribution in source searches has been introduced. However the possibility of using the shower age as a discriminator against the large hadronic background did not prove practical because of the relatively small number of detectors in the GREX telescope. Hence the source searches had to be made without such discrimination. They were based on over 3.3×10^7 events recorded during 4-5 years. Neither of the two candidate objects displayed any evidence of emission above the level of sensitivity of the instrument on time scales of days to years. The limits are competitive with those from similar experiments which lack large area muon detectors.

CONTENTS

Chapter 1 Introduction

1.0	Introduction	1
1.1	Discovery of Cosmic Radiation	1
1.2	Identifying the Primary Radiation	2
1.3	Extensive Air Showers	3
1.4	Development of Extensive Air Showers	7
1.4.1	Photon Initiated EAS	7
1.4.2	Proton Induced Showers	9
1.4.3	Differences between Proton and γ -ray Induced Showers	10
1.5	Recent PeV observations	11

Chapter 2 The GREX γ -ray telescope at Haverah Park

2.0	Introduction	15
2.1	The Geometry of the Array	15
2.2	The Detectors	17
2.2.1	Lead shielding	18
2.2.2	Testing of Lead Shielded Detectors	19
2.2.2.1	Side-by-Side Detector Comparisons	19
2.2.2.2	Sub-array Comparisons	20
2.3	Data Acquisition and Recording Electronics	21
2.4	The History of the GREX array	22
2.5	The Performance of the GREX Array	23
2.5.1	Measurement of the Barometric Coefficient	23
2.5.1.1	Pressure Measurement	23

2.5.1.2	Shower Rate as a Function of Pressure	25
2.5.1.3	D1 and D2 Rates as a Function of Pressure	26
2.5.2	Diurnal Trigger Rate Variation	29
2.6	Derivation of Attenuation Length from Barometric Coefficient	35
2.7	Conclusions	37

Chapter 3 Data Analysis and Reduction

3.0	Introduction	38
3.1	Data Reduction- a brief overview	39
3.2	Data Conversion	39
3.3	Data Analysis	41
3.3.1	Core Search	41
3.3.1.1	Fitting of Observed Densities to Expected.	41
3.3.1.2	Saturated and below Threshold Densities	45
3.3.1.3	χ^2 Minimisation Algorithm	46
3.3.1.4	Choice of the Direction Vector, \mathbf{n}	51
3.3.1.5	Line Minimisation	52
3.3.1.6	Minimisation Applied to Core Search	55
3.3.1.7	Accuracy of Core Position	55
3.3.1.8	Statistical Uncertainty in χ^2 minimum	56
3.3.1.9	Error in Locating the χ^2 minimum	61
3.3.1.10	Total Error in Core Location	63
3.3.2	Finding an Accurate Arrival Direction	63
3.3.2.1	Shower Front Curvature	65
3.3.2.2	Determination of Time Weights	67
3.3.2.3	Angular Resolution of GREX Array	71
3.3.2.4	The Effect of Core Location Errors on the Measured Shower Arrival Directions	71
3.3.3	Data Compression	78

3.4	Conclusions	79
Chapter 4 The Measurement of the Age Parameter		
4.0	Introduction	82
4.1	Measurement of the Age Parameter	83
4.2	Usefulness of the Determined Age Parameter	84
4.3	Array Response as a Function of Age	85
4.4	Assessment of Simultaneous χ^2 Minimisation Applied to Simulated Showers	87
4.5	Correlation Between Simulated Age and Analysis-Determined Age	88
4.6	Deriving a Better estimate of the True Age of Showers	91
4.7	Random Uncertainties in Shower Age	93
4.8	Measurement of Ages of Real Showers	95
4.9	Transition Effects in Lead shielding	103
4.10	Zenith angle Dependence of Age	103
4.11	Use of the Age Parameter to Distinguish Between Nucleon and γ -ray Initiated EAS	105
4.12	Conclusions	109
Chapter 5 Methods of Searching for Sources of γ-rays		
5.0	Introduction	110
5.1	The 'dec strip' Method of Source Searching	112
5.1.1	Signal to Noise Ratio Dependence on Bin Size	112
5.1.2	Choice of Bin Size for use with Haverah Park Data	116
5.1.3	Methods of Guaranteeing Equal Exposure in On- and Off- Source Bins	118
5.1.4	Equal On-Time Method	119
5.1.5	Equal Exposure Method	121

5.2	Azimuthal Method	123
5.2.1	The Azimuthal Asymmetry of the GREX Array	125
5.2.2	Correcting for the Azimuthal Asymmetry	138
5.2.3	Testing the Accuracy of the Azimuthal Corrections	139
5.2.4	Sources that Transit Close to the Zenith	139
5.3	Comparison of the Azimuthal and Equal Exposure Methods.	141
5.3.1	Check for Systematic Errors in Signal and Background Rates.	141
5.3.2	Comparison of Useful on-times and off-source Solid Angle Obtained by the Two Methods	143
5.4	Conclusions	145

Chapter 6 A Search for γ -ray emission from Hercules X-1 and 1E2259+586

6.0	Introduction	147
6.1	A search for γ -ray emission from Hercules X-1	147
6.1.1	Observations at X-ray energies	147
6.1.2	Her X-1 at Optical and Infra-Red Wavelengths	149
6.1.3	TeV and PeV Observations	149
6.1.4	Observations of Hercules X-1 Using the GREX array	154
6.1.4.1	Search for DC Emission from Her X-1	155
6.1.4.2	Test for Modulation at 1.7d and 35d periods of Her X-1	156
6.1.4.3	Search for Sporadic emission from Her X-1	158
6.2	Search for γ -ray emission from 1E2259+586	161
6.2.1	Radio and X-ray Observations	162
6.2.2	Infra-Red and Optical Observations	163
6.2.3	VHE and Underground Muon Observations	165
6.2.4	Observations of 1E2259+586 with the GREX array	166
6.2.4.1	Search for DC Emission	167
6.2.4.2	Search for Long Term Burst Emission	167

6.2.4.3	Search for Emission on a Day-to-Day Basis	171
6.3	Conclusions	174
	Appendix Angular Resolutions of the GREX array	176
	References	180
	Acknowledgements	184

LIST OF FIGURES

- Figure 2.1 16
The layout of the 36 detector array. New detectors are numbered 33 to 36. Detectors in the two 50m subarrays used for assessing angular resolutions are marked by hatched and open symbols.
- Figure 2.2 27
The natural logarithm of the daily event rate is shown plotted as a function of atmospheric pressure measured on the Barograph for January 1990. The straight line is a least squares fit to the data and has a gradient (the barometric coefficient) of 0.0090 ± 0.0001 .
- Figure 2.3 28
(i) (ii) and (iii). The barometric coefficients, mean daily event rates corrected to a pressure of 1000mb, and the standard deviations of those rates respectively are shown plotted for the months June 1989 to May 1990 which are numbered sequentially 1 to 12...
- Figure 2.4 30
(i) and (ii). The barometric coefficients for the D1 and D2 trigger rates respectively are shown plotted for each detector and for two periods of the array: 1st to 15th October 1989 and 4th to 24th November 1989. These periods are denoted by the filled and open symbols respectively.
- Figure 2.5 31
The mean pressure corrected shower rate is shown plotted as a function of hour of the solar day for October 1989.
- Figure 2.6 33
(i) and (ii) show the mean pressure corrected D1 and D2 trigger rates averaged over all detectors plotted as a function of hour of the solar day for the period 2nd to 16th October 1989. (iii) shows the D1 rates for detectors 15,16,25 and 32 which are inside huts
- Figure 2.7 34
A schematic representation of the particle density as a function of core distance for two showers with different Molière units. The ordinate is in units Density \times Core distance so that the area below the graph represents the total number of particles in the shower.
- Figure 3.1 43
(i) and (ii) The integral distributions of core shifts and arrival direction shifts.
- Figure 3.2 47
A contour plot of normalised χ^2 as a function of trial core position. The minimum in χ^2 is marked by the 'x'. The value of the contours increases from red through black to blue. The peaks at the detectors are caused by the singularity in the NKG function at $R=0$.
- Figure 3.3 50
Flow diagram of χ^2 minimisation algorithm used in the determination of core positions.
- Figure 3.4 54
Steepest descent method of traversing a long narrow valley. Each step is constrained to be perpendicular to the last.
- Figure 3.5 54
Inverse parabolic interpolation used to find the minimum of a function of a single variable. A parabola is fitted to three points, a, b, and c on the function $f(x)$. The position of the minimum of that parabola is a good approximation to the position of the minimum of the function.

Figure 3.6

Integral frequency distribution of statistical errors in the position of the χ^2 minimum obtained from the radius of the $\chi^2_{\min} + 3.5$ contour in the χ^2 surface.

Figure 3.7

Statistical errors in the position of the χ^2 minimum are shown plotted against size ($S(50)$) for showers from each era. The broken lines are to guide the eye and do not represent the data between points

Figure 3.8

Statistical errors in the position of the χ^2 minimum are shown plotted against zenith angle for showers from each era.

Figure 3.9

(i) and (ii) The integral and differential frequency distributions respectively of the distances between the position of the χ^2 minimum and the core location assigned by routine analysis. Showers are from the period during which the array consists of 36 lead covered detectors.

Figure 3.10

The mean distance between the analysis assigned core position and the minimum in χ^2 plotted as a function of the uncertainty in the position of the minimum.

Figure 3.11

Plot of time delays from the plane against core distance for observed densities of approximately 1.5m^{-2} (open circles) and 5.5m^{-2} (filled circles) for showers from the unleaded array, graph(i) and lead covered array, graph (ii). The solid ($S=1.5\text{m}^{-2}$) and broken ($S=5.5\text{m}^{-2}$) lines are parametrisations of these delays.

Figure 3.12

Plot of the observed (open symbols) and predicted (filled symbols) time delays from the plane against core distance for showers of approximate $S(50)$'s 5.5m^{-2} (circles) and 23m^{-2} (diamonds) for showers from the unleaded array, graph(i) and lead covered array, graph (ii).

Figure 3.13

Frequency distribution of time differences between detector 15 and 16 corrected for their spatial separation and time of flight differences for density $\approx 1.5\text{m}^{-2}$ and core distance 35m. The solid line shows a gaussian of width $\sigma_{t15-t16}$. The broken line is a gaussian of width given by the range of $t_{15} - t_{16}$.

Figure 3.14

Observed timing uncertainties plotted against core distance for densities $\approx 1.5\text{m}^{-2}$, open circles and 5.5m^{-2} , closed circles for showers from (i) Un-leaded array and (ii) Leaded array. The solid and broken lines in each plot show the parametrisations of those uncertainties for $S=1.5\text{m}^{-2}$ and $S=5.5\text{m}^{-2}$ respectively

Figure 3.15

The parametrisations of the timing uncertainties as a function of core distance for $S=1.5$, solid lines and $S=5.5$. The thick and thin lines are for showers from the un-leaded and leaded array respectively.

Figure 3.16

The change in assigned arrival direction due to shifts in the core position derived by the analysis is shown plotted against those shifts for showers from different eras (i) and $S(50)$ bands (ii).

Figure 3.17	77
(i) and (ii) The integral and differential frequency distributions respectively of space angle shifts due to core uncertainties.	
Figure 4.1	86
Triggering probabilities of the GREX array are shown as a function of age for showers of various sizes as determined by simulations. The figures on each plot show shower size in terms of the density at 50m (m^{-2}). (i) and (ii) show the probabilities for vertical showers triggering the 32 and 36 detector arrays respectively and (iii) and (iv) are for showers inclined at 40° to the vertical for the two arrays.	
Figure 4.2	89
Scatter plots of measured age against simulated age for vertical showers with cores distributed uniformly across the 36 detector array and $S(50)$'s (i) $1.4 m^{-2}$, (ii) $2.0 m^{-2}$, (iii) $2.8 m^{-2}$, (iv) $4.0 m^{-2}$.	
Figure 4.3	90
Histogram of simulated ages of showers with $S(50) = 2.8 m^{-2}$ for which the measured age lies between 1.1 and 1.3	
Figure 4.4	90
(i) and (ii) Scatter plots of measured age against simulated age for showers with cores lying within 30m of the array centre and with $S(50)$'s $1 m^{-2}$ and $1.4 m^{-2}$ respectively.	
Figure 4.5	92
Straight line fits of simulated age to measured age for vertical showers of various sizes are shown for comparison. The inset gives the shower size in density at 50m for each fit	
Figure 4.6	92
The RMS error in the 'corrected' age parameter, s_c , is shown plotted against zenith angle for showers of various sizes with cores distributed uniformly across the whole of the 36 detector array.	
Figure 4.7	94
The RMS errors in the corrected age parameter of vertical showers are shown plotted against shower size and are compared for the 36 detector (triangle symbols) and 32 detector (diamonds) arrays and for cores lying within 30m of the centre (un-filled symbols) and those uniformly distributed across the whole of the array (filled symbols)	
Figure 4.8	94
Comparison is made of the errors in the corrected age parameter of vertical showers for the array consisting of 32 detectors with saturation at 20 particles and 45 particles - triangular and diamond symbols respectively. Open and filled symbols represent showers with cores falling within 30m of the array centre and uniformly distributed across the whole array respectively.	
Figure 4.9	96
The mean (corrected) ages of showers falling within 30m of the array centre (32 detectors, un-leaded) are shown plotted against shower size for 4 zenith angle ranges (refer to labels). The shower size is in particles for the equivalent shower inclined at 20° to the horizontal, which corresponds to an atmospheric depth of $1083 gcm^{-2}$.	
Figure 4.10	97
The mean (corrected) ages of showers falling within 30m of the array centre (32 detectors, un-leaded) are shown plotted against $S(50)$ for 4 zenith angle ranges (refer to labels).	
Figure 4.11	99
The mean measured age parameters un-corrected for the limited dynamic range of detectors are shown plotted against $S(50)$ for 4 zenith angle ranges (refer to labels). All showers have cores lying within	

30m of the array centre, and the array consists of 32 un-leaded detectors.

Figure 4.12 100

The mean age of showers is shown plotted against $S(50)$ for cores lying within 30m of the array centre (square symbols), and for those with cores spread over the whole of the array (triangular symbols)

Figure 4.13 104

Comparison of the age parameter measured with lead covered and un-covered detectors. The mean ages of vertical showers with cores lying within 30m of the array centre are shown plotted against $S(50)$.

Figure 5.1 113

Binning events in the 'dec strip' method of source searching. Bins are of dimensions $\Delta\delta \times \Delta RA$. On-source events are accumulated in the central bin while off-source events are accumulated in the remaining bins. All bins pass through the same range of zenith and azimuthal angle as they each transit in turn.

Figure 5.2 115

The signal to noise ratio (in arbitrary units) is shown plotted as a function of bin diameter for circular bins and width for square bins. Bin dimensions are in units of standard deviations of the assumed source point spread function.

Figure 5.3 117

Comparison of the largest ($\Delta\delta = 4.66^\circ$) and smallest ($\Delta\delta = 1.37^\circ$) square bins used for source searches after Bloomer (1990). The width of the bins in RA is given by $\Delta\delta / \cos\delta$.

Figure 5.4 117

The 'shortened sidereal day'. Events are only accepted with zenith angle less than θ_{\max} and hence in the time interval between the rise of the leading edge of the search strip rising above the θ_{\max} horizon (T_{rise}) and the trailing edge of the strip setting below this horizon (T_{set}).

Figure 5.5 120

A typical day in which the demand for equal on-time in all bins does not lead to equal exposure across the whole strip. The array is on for the whole sidereal day except for a short period between T_2 (fig. (ii)) and T_3 (fig. (iii)) during which all bins are above the θ_{\max} horizon.

Figure 5.6 120

Equal exposure in all bins is guaranteed by only accepting events with hour angles in the range HA_{\min} to HA_{\max} , the hour angles of the leading edge of the search strip at array turn on and that of the trailing edge at turn off respectively.

Figure 5.7 122

The count rate for a number of search bins is shown as a function of time. The bins are numbered leading edge first (refer to fig. 4.6). The array is turned on some time after bin 1 has risen (T_{on}) and off before bin 7 has set. Selecting minimum and maximum hour angle between which to accept events is equivalent to switching each bin, i , on and off at different times (T_{on}^i and T_{off}^i) to maintain the same exposure (area under graphs) in each.

Figure 5.8 124

The azimuthal strip technique for calculating the background. On-source events are collected within the circular bin centred on the source at coordinates (θ_s, ϕ_s) while the background is calculated in the annulus between zenith angles θ_1 and θ_2 , and corrected for the difference in solid angle of the azimuthal strip and on-source bin (see text).

Figure 5.9	126
(i) and (ii) The height of detectors above a horizontal plane through 15 and 16 is shown plotted against the x and y coordinates of the detectors	
Figure 5.10	128
The azimuthal distribution of events selected for source searching.	
Figure 5.11	130
(i) and (ii) The amplitudes and phases respectively of the first harmonics in the azimuthal distribution are shown as a function of shower size for events at all zenith angles. Harmonics with peaks in the north are represented by positive amplitudes, while those with peaks in the south have negative amplitudes.	
Figure 5.12	132
(i) and (ii) The amplitudes and phases respectively of the first harmonics in the azimuthal distribution are shown plotted as a function of zenith angle for showers with $S(50) \geq 5m^{-2}$.	
Figure 5.13	133
A schematic view looking along the plane of the array and illustrating the difference in projected area of the array for showers at the same zenith angles, but different azimuths. ϕ_n and θ_n are the azimuthal and zenith angles respectively of the vector normal to the plane of the array. The two showers have directions (θ, ϕ_n) and $(\theta, \phi_n + 180^\circ)$	
Figure 5.14	135
(i) and (ii) The amplitudes and phases respectively of the first harmonics in the azimuthal distribution are shown plotted as a function of zenith angle for showers with $S(50) \leq 0.5m^{-2}$.	
Figure 5.15	136
(i) and (ii) The amplitudes and phases respectively of the second harmonics in the azimuthal distribution are shown plotted as a function of $S(50)$ for showers at all zenith angles.	
Figure 5.16	137
(i) and (ii) The amplitudes and phases respectively of the second harmonics in the azimuthal distribution are shown plotted as a function of zenith angle for showers at all zenith angles.	
Figure 5.17	140
The azimuthal distribution after correction for the 1st and 2nd harmonics as described in the text.	
Figure 5.18	142
(i) and (ii) The percentage difference in on-source and off-source counts respectively obtained using the azimuthal and equal exposure methods for calculating backgrounds are shown plotted as a function of source declination...	
Figure 5.19	144
The percentage increase in useful on-time of the azimuthal technique over the equal exposure technique is shown plotted as a function of source declination.	
Figure 5.20	144
The effective number of off-source bins (the ratio of off-source to on-source solid angle) for the azimuthal technique is shown plotted against source declination.	

- Figure 6.1 153
 Claimed fluxes for transient emissions and upper-limits for long term observations of Hercules X-1.
 The legend gives references and epochs of observations for transient emissions
- Figure 6.2 155
 The cumulative excess of on-source counts over background counts for Hercules X-1 is shown as a function of the number of sidereal days since 1/1/86. Also shown are the 'excesses' that would correspond to signals/deficits with significances of 1σ , 2σ , 3σ , -1σ , -2σ , and -3σ .
- Figure 6.3 157
 (i) and (ii) The excess of on-source events over background for Her X-1 is shown plotted in standard deviations against phase in the 1.7d and 35d periods respectively.
- Figure 6.4 160
 The value of the Protheroe statistic, Ψ , ($\times 1000$) is shown plotted as a function of trial period for observations of Her X-1 on 20th May 1989. The expected X-ray period is shown along with the period measured by the Los Alamos group ...
- Figure 6.5 164
 The 1E2259+586 pulsar periods measured by satellite observations are plotted as a function of epoch. The period measured by the Durham group is also shown for comparison. The straight line is a fit to the satellite measured periods only and has a gradient of $\dot{P} = (5.83 \pm 0.30) \times 10^{-13} \text{ss}^{-1}$.
- Figure 6.6 164
 The Rayleigh scan performed on 1E data collected in observations made by the Durham group between the 4th and 11th October 1988.
- Figure 6.7 168
 The cumulative excess of on-source counts over background counts for 1E2259+586 is shown as a function of the number of sidereal days since 1/1/86.
- Figure 6.8 168
 Histogram of the number of counts in annuli centred on 1E plotted against the square of the angular radius. Each bin has approximately the same solid angle. The points represent the expected background, B_i , in each bin. The thick and thin error bars show the uncertainty in the background and \sqrt{B} respectively.

LIST OF TABLES

Table 2.1	24
The History of the GREX Array, showing changes to the array and the 'operational eras'	
Table 3.1	49
Comparison of centre of gravity cores. n is the power of the measured density used to weight the triggered detectors' coordinates and ΔR is the mean distance between the trial core and the position of the true minimum in χ^2 .	
Table 3.2	58
Mean statistical uncertainties, ΔR , in the position of the χ^2 minimum for events from each operational era.	
Table 3.3	60
The RMS statistical errors for showers of each pattern type and era are shown.	
Table 3.4	62
The mean and RMS errors in assigned core positions are given for showers from each era.	
Table 3.5	73
(i) Shows the definition of S(50) and θ bins, and (ii) resolution groups used to parametrise directional uncertainties of showers.	
Table 3.6	76
The coefficients for the quadratic fit of the space angle shift in arrival direction, $\Delta\psi$, for a shift in core position, DR: $\Delta\psi = a\Delta R + b\Delta R^2$. These coefficients are a function of shower size and are affected by the addition of lead to the detectors.	
Table 3.7	77
The rms space angle shifts due to uncertainties in the core position are shown for showers from each era	
Table 3.8	80
The information stored in each compressed record used for source searching is shown along with the number of bytes used to store each shower parameter.	
Table 5.1	115
The round and square bin widths that maximise signal to noise ratios in source searches in units of angular resolution.	
Table 5.2	128
The amplitude and phases of the first and second harmonics in the azimuthal distribution of events selected for source searching.	
Table 6.1	159
The Hercules X-1 days having less than 1% Poisson probability. N_{on} is the number of on-source events, B the background and ϕ_{35} and $\phi_{1.7}$ are the phase in the 35 day and 1.7 day periods respectively when the source is at transit.	
Table 6.2	172
The 1E2259+586 days having less than 1% Poisson probability. N_{on} and B are the on-source and background counts respectively and P_{Pois} is the Poisson probability of the counting excess. Also given are the results of the 7s period search...	

CHAPTER ONE

INTRODUCTION

1.0 Introduction

Cosmic rays, with energies ranging from $\sim 10^9$ eV to over 10^{20} eV, fill space in the neighbourhood of our solar system with an energy density of ~ 1 eV cm^{-3} which is approximately that of galactic starlight and the 3K primeval radiation combined. If the space between galaxies is also filled with cosmic rays at this density, then they must emanate from a very important energy source indeed. The nature and origin of this radiation have been the subject of many investigations over the past century. The mechanism of a cosmic accelerator producing particles at energies greater than 100 million times those achieved by the best manmade accelerators is naturally of great interest, not only to astrophysicists but also to particle and high energy physicists.

1.1 Discovery of Cosmic radiation

The discovery of cosmic rays came at around the beginning of this century, though it was some time before their extra-terrestrial origin was confirmed. It had been noticed that isolated electroscopes lost charge slowly and this was attributed to the presence of ionising radiation. Initially, it was thought that the radiation emanated from radio active impurities presumably local in nature. That the radiation was highly penetrating was evidenced by the continued discharge of electroscopes, even when shielded by a 5 ton mass of lead (Rutherford and Cooke, 1903). The ionisation rate fell considerably over lakes and glaciers thought to be relatively free of radioactive material, but nevertheless a residual amount remained. Although measurements in the Eiffel tower by Wulf in 1910 did show a fall in ionisation levels with increasing altitude, as might be expected for a ground based source for the radiation, the drop was much less than

predicted. The ionisation fell by only ~50% at the top of the tower (330m) compared to the expected 95% had the ionisation been due to γ -rays which have an absorption length of ~80m.

Measurements by Hess (1913) in balloon flights showed that, after an initial decrease in the intensity of the radiation, it began to increase rapidly with altitude. These observations caused great excitement as they gave clear indications that the radiation came from outside our atmosphere. Millikan, initially suspicious of these findings, was later to put the extra-terrestrial origin of at least a significant fraction of the ionising radiation observed at sea level (the remaining 75%, being due to radioactive impurities as initially expected) beyond doubt. Measurements were made by lowering electroscopes into snow fed lakes at different altitudes (Millikan and Cameron, 1926). A drop in radiation was observed with increasing depth in the lakes. This drop was similar to that observed in reducing altitude

1.2 Identifying the primary radiation

The precise nature of the radiation, nevertheless, was still largely unknown. Very high energy γ -rays were still favoured due to their (relatively) long absorption lengths. Long straight tracks observed in cloud chambers were soon identified as high energy electrons and it was realised that these particles must be secondary in nature, losing energy too rapidly by ionisation to have penetrated the whole of the atmosphere. Originally it was thought that these electrons were produced by Compton scattering of γ -rays on atomic electrons.

Measurement by Clay (1932) indicated that the intensity of radiation was lower near the equator than at higher latitudes. Later it was found that there was no increase in intensity above a latitude of 53° . These measurements, though somewhat affected by the variation in atmospheric conditions at the different latitudes, pointed towards charged particles for the primary radiation. The horizontal component of the earth's magnetic field is maximum at the equator, so that a vertically moving charged particle will

experience the maximum deflection here, and require a larger energy to reach the ground. On going to higher latitudes, lower energy particles are allowed into the geomagnetic field, so that the total flux of particles is increased. The energies of the primary particles were estimated to be from below 4×10^9 eV (this being the minimum energy required to penetrate the atmosphere) to above 3×10^{10} eV, the minimum energy required to reach earth at the equator. The earth's magnetic field was, later, to enable still better identification of the primary radiation. Experiments by Johnson (1933) and Alvarez and Compton (1933) showed more particles to come from West of the zenith than from the East. It was realised that the particles must be positively charged, the most likely candidates being protons. More recent measurements by satellite and high altitude balloons have shown that the vast majority are indeed protons but in addition, at energies greater than ~ 4 GeV, there are $\sim 0.01\%$ γ -rays, $\sim 2\%$ electrons and positrons and perhaps 10% heavier nuclei (though this fraction is energy dependent).

1.3 Extensive air showers

Although these early measurements had given some indication of the high energies of the primary radiation, it was not until 1938 that the extent of the spectrum was appreciated. Measurements were made of the rate at which two Geiger-Muller tubes discharged simultaneously when placed 1m apart (Auger *et al.* 1939). The rate was found to be very much larger than expected from simple probability arguments for accidental coincidences. It seemed that the particles were related, having a common origin, indeed that they were part of a shower of particles produced by a single primary. In further experiments, Auger separated the tubes by up to 300m. Even at these distances, coincidences were still observed (though at a much reduced rate), with densities measured by the tubes of $\sim 10\text{m}^{-2}$ (their collecting area was 0.1m^2). If this density were uniform across the space between the detectors, then the total number of particles in the shower would be $\sim 10^5$. Auger reasoned that if these particles each had energies of $\sim 100\text{MeV}$ (below which they would be rapidly absorbed in air by ionisation

losses), the energy of the initiating particle would be in the region of 10^{14} eV. In fact, the loss of energy by particles in air by ionisation on traversing the atmosphere amounts to more than the total energy of particles at sea level. Auger's estimate of the primary energy, therefore, was on the conservative side (a better estimate would have been 10^{15} eV!). The showers observed by Auger are now known as Extensive Air Showers (EAS). The principle of using widely spaced ground based counters for the indirect detection of cosmic rays at energies $>10^{14}$ eV is still used today. The very low flux of particles, with only ~ 6 per m^2 per steradian per month at these energies make their direct detection by satellite or balloon borne experiments impractical. Sophisticated timing electronics enable the relative arrival times of the shower front at different detectors to be measured and an arrival direction to be determined. At lower energies, in the range 0.1 to 10 TeV, EAS are absorbed before reaching ground level even at mountain altitudes. Nevertheless, detection is still possible via the Cerenkov light produced by electrons and positrons travelling at speeds greater than the velocity of light in air. The Cerenkov photons are produced some 10-12km above sea level and travel to earth in a narrow cone which forms a pool of light some 400m in diameter at ground level. The photons are easy to detect with optical reflectors and photomultiplier tubes and have an arrival direction within $\sim 1^\circ$ of the initiating primary particle. The effective area of the Cerenkov detector is the area covered by the pool of Cerenkov light and is thus $\sim 10^5 \text{m}^2$.

Cosmic rays, then, with energies in excess of 100GeV fall into two main categories: those detected via Cerenkov radiation with energies in the TeV range (0.1 to 10×10^{12} eV) and those detected by arrays of particle detectors, an extension of the Auger discovery technique, with energies greater than 100TeV (these energies are often referred to as 'PeV' energies, as $1\text{PeV} \equiv 10^{15}\text{eV}$). The terms Very High Energy (VHE) and Ultra High Energy (UHE) have been coined to describe these two regions of the spectrum. It is primarily the latter regime with which this thesis is concerned.

The existence of such high energy particles naturally raises the question of their origin. Unfortunately, simply measuring their arrival direction does not immediately

answer this question. They arrive very nearly isotropically, the reason for this becoming apparent when one considers the effects on the motion of charged particles of the tangled magnetic fields that pervade our galaxy with a strength of a few micro Gauss. The gyroradius (measured in pc) of a proton of energy E (measured in eV) in a field of strength $3\mu\text{G}$ is given by:

$$R(\text{pc}) = \frac{E(\text{eV})}{3 \times 10^{15}} \quad \dots \text{Eqn 1.1}$$

Thus a proton of energy 10^{15} eV will have a gyroradius of $\sim 0.3\text{pc}$ which is considerably less than the thickness of the Galactic disc ($\sim 600\text{pc}$). A heavy nucleus of the same energy has an even smaller gyroradius due to its larger charge. At energies of 2×10^{18} eV, the gyroradius for protons increases to the thickness of the galactic disc. Early EAS experiments set out to measure anisotropies at such energies and greater, in the hope that the arrival directions of such cosmic rays might reveal their true origins. Unfortunately, the flux of events at this energy is extremely small, amounting to only $1 \text{ km}^{-2} \text{ year}^{-1} \text{ sr}^{-1}$ at $E \geq 5 \times 10^{18}$ eV. Consequently, no significant anisotropies were observed.

Hope was at hand in experiments at lower energies. In 1972, a group in the Crimea reported an excess of TeV cosmic rays from a direction consistent with that of a binary X-ray source known as Cygnus X-3 which lies in the galactic plane some 10kpc ($\sim 30,000$ light years) from our own sun (Vladimirsky *et al.* 1973). This report came shortly after a spectacular radio outburst from the source which gave weight to the claim. This excess could not have been due to protons or nuclei as, for reasons given above, charged particles of these energies would not retain any directional information. Rather, the signal was attributed to neutral particles - presumably γ -rays. The flux of such γ -rays is very low. They constitute only $\sim 0.01\%$ of the total cosmic ray flux, the remainder of which constitute the background against which they must be detected. In 1983, the Kiel group (Samorski and Stamm, 1983) reported a signal of PeV γ -rays from the direction of Cygnus X-3. This signal appeared modulated at the 4.8hr X-ray period and was strongest in showers with relatively flat lateral distribution functions (see

chapter 4) Confirmation from the Haverah Park group followed shortly (Lloyd Evans *et al.* 1983). No significant dc effect was observed at Haverah Park, though a very significant peak (with a chance probability of 2.8×10^{-5}) was found in phase range of 0.225-0.25 of the X-ray period which was consistent with but much narrower than the preferred phase range in the Kiel result.

Mechanisms had been proposed that could accelerate charged particles such as electrons to energies in excess of 10^{12} eV in rapidly changing magnetic fields such as those found close to a fast spinning neutron star. These electrons could produce γ -rays via synchrotron radiation in the same magnetic fields responsible for their acceleration. At higher energies, however, a fatal problem exists with this scenario: PeV γ -rays produced by this mechanism would be absorbed in the intense magnetic fields producing electron/positron pairs. In addition, electrons would be difficult to accelerate to such high energies due to this continuous loss of energy by synchrotron radiation. Protons, however, due to their greater mass lose energy much less rapidly by synchrotron radiation. It is possible that protons could be accelerated to energies approaching 10^{15} eV in the environment of a neutron star, in a manner similar to that proposed for electrons. These protons striking a gas target within the system, but remote from the intense magnetic fields close to the surface of the neutron star, would produce pions. Subsequent decay of neutral pions could account for γ -ray production. Thus observation of a γ -ray flux from a point source also implies a proton flux. Charged particles with energies below $\sim 10^{15}$ eV may be trapped by the galactic fields for very long periods of time. Thus a source emitting steadily at the flux originally claimed for Cygnus X-3 could account for the majority of UHE cosmic rays observed in our galaxy (Hillas 1984). It now seemed that experiments at PeV energies offered the most promising method of determining the origin of cosmic rays.

The processes involved in the development of EAS are now believed to be well understood, and the properties of the showers comprising the signal observed by Kiel - muon content consistent with background (proton induced showers) and flatter lateral distributions than background - need to be compared to what might be expected for

γ -ray induced showers. At this point, therefore, it is useful to describe the development of extensive air showers.

1.4 Development of Extensive air showers

1.4.1 PHOTON INITIATED EAS

A photon of energy 10^{15} eV entering the atmosphere will produce an electron/positron pair in passing close to an air molecule (required to conserve momentum) with a mean free path of 48 gcm^{-2} . Each electron/positron pair, decelerated in the field of a nucleus, will emit bremsstrahlung photons. Each of these photons will go on to pair produce, and an electromagnetic cascade will develop rapidly in the upper atmosphere. Electrons lose $(1-1/e)$ of their energy in bremsstrahlung radiation, on average, on traversing 1 radiation length, X_0 , the value of which is 37.6 gcm^{-2} in air. The mean free path, λ_{pp} , for pair production in air is very nearly equal to the radiation length,

$$\lambda_{pp} \approx \frac{9}{7} X_0 \quad \dots \text{Eqn 1.2}$$

so that the total number of particles in the cascade is approximately doubled, and their mean energy halved in passing through a thickness $X_0 \ln 2$ ($=26 \text{ gcm}^{-2}$) of air. Electrons begin to lose energy more rapidly by ionisation as their energy drops. These losses become more important than radiation losses for energies below the critical energy, E_c , of 84.2 MeV in air. For photons, energy losses by Compton scattering dominate at energies below 20 MeV . Thus after the initial growth of the cascade, it begins to decay as the particle energies fall below E_c . The shower maximum occurs when the mean particle energy is equal to the critical energy and is at a depth, X_{\max} , given by

$$X_{\max} \approx X_0 \ln \left(\frac{E_\gamma}{E_c} \right) \quad \dots \text{Eqn 1.3}$$

where E_γ is the energy of the initiating γ -ray. After reaching a maximum, the number of particles decreases approximately exponentially with a characteristic length known as the

attenuation length whose exact value is a function of energy and is $\sim 185 \text{gcm}^{-2}$ at 10^{15} eV .

Thus a PeV photon entering the atmosphere is expected to produce an essentially electromagnetic cascade. The lateral spread of particles within an air shower arises mainly from Coulomb scattering of electrons. The RMS scattering angle is dependent on electron energy and is given by

$$\theta_{\text{rms}} = \frac{21}{E(\text{MeV})} \sqrt{\frac{x}{X_0}} \quad \dots \text{Eqn 1.4}$$

for an electron traversing through an atmospheric thickness, x . Thus after traversing 1 radiation length, an electron with critical energy will be scattered 0.25 radians. The effect of these deflections can be compared to the opening angle of electron/positron pair production, θ_{pp} and the emission angle for bremsstrahlung, θ_{Brem} , which are both $\sim 6 \times 10^{-3}$ radians at this energy. They also vary as $1/E$ so that the lateral spread caused by these two processes is considerably less important than that due to Coulomb scattering at all energies. The RMS lateral distance through which electrons are scattered is known as the Molière unit and is the characteristic length of the lateral distribution of electrons in EAS. The value of the Molière unit is dependent on the altitude of observation and the atmospheric conditions (the height difference - measured in metres - corresponding to 1 radiation length depends directly on the density of air). The value adopted for use at Haverah Park, which is close to sea level, is 79m.

The lateral distribution of electrons in an electromagnetic shower is approximated by a formula determined by Nishimura and Kamata (1952) and modified by Greisen(1956) known as the NKG function. The density at a distance, r , is given by:

$$S(r) = \frac{N}{R_0^2} C(s) \left(\frac{r}{R_0} \right)^{s-2} \left(\frac{r}{R_0} + 1 \right)^{s-4.5} \quad \dots \text{Eqn 1.5}$$

for a shower of N particles. s is the age of the shower, describing the state of its development and varies between 0 and 2 (chapter 4). $C(s)$ is a normalisation constant weakly dependent on s .

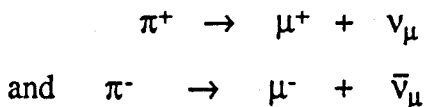
1.4.2 PROTON INDUCED SHOWERS

A PeV proton entering the atmosphere will interact with a nucleus - most likely nitrogen or oxygen with a mean free path of $\sim 80 \text{ gcm}^{-2}$ of air. In this first interaction, occurring approximately 20km above sea level, the proton will produce many pions in approximately equal numbers of each charge (π^0 , π^- , π^+) and a small number ($\sim 10\%$) of kaons, hyperons and other exotic particles. The proton loses approximately half of its energy in this interaction and may be changed to a neutron by charge exchange. It continues its progress through the atmosphere, feeding the cascade with pions and halving its energy at each interaction. Because the proton is not lost in the first interaction, the exponential fall of the flux of protons of given energy has a characteristic length of 120 gcm^{-2} which is larger than the mean free path for pion production ($\sim 80 \text{ gcm}^{-2}$).

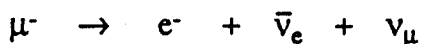
The number of pions produced at each interaction (multiplicity) decreases as the proton energy decreases and is given by:

$$n_{\pi} \sim 2.7 E_p^{0.25} \quad \dots \text{Eqn 1.6}$$

where E_p is the radiated energy (approximately half the proton energy) measured in GeV. Thus a 10^{15} eV primary will produce ~ 50 pions. Charged pions have a rest lifetime of only $\sim 2.6 \times 10^{-8} \text{ s}$, but at highly relativistic energies ($\geq 5 \times 10^{10} \text{ eV}$) they tend to interact with an air nucleus producing pions and losing half their energies, in a similar way to protons. As the pion energies fall, they become more likely to decay into muons than interact:



Muons have very small interaction cross sections and consequently long mean free paths ($> 10^5 \text{ gcm}^{-2}$). In addition, muons are relatively stable, having a rest lifetime of $\sim 2.2 \times 10^{-6} \text{ s}$ which means that, with the help of relativistic time dilation, the majority (75%) reach sea level. The remainder decay to either positrons or electrons:



$$\text{and } \mu^+ \rightarrow e^+ + \nu_e + \bar{\nu}_\mu$$

Neutral pions are extremely short lived ($\tau \approx 10^{-16}\text{s}$), decaying almost instantaneously to two γ -rays. These photons are the beginning of the electromagnetic component of the proton induced cascade. Each photon pair produces in the field of a nucleus. These particles go on to emit bremsstrahlung radiation and so on. Each subcascade produced by γ 's from π^0 decay goes on to develop in the same way as γ -ray initiated air showers described in the previous section. Additional lateral spread in proton showers comes from the transverse momentum, $\sim 0.4 \text{ GeV}/c$, acquired by the pions at production. The angle of emission increases as the pion energy decreases. The emission angles of the neutral pions contribute to the spread of the electromagnetic component, while those of charged pions are responsible for the spread of the muon component. The pions decaying to muons, with energies of $\sim 10^{10} \text{ eV}$ to 10^{11} eV are produced some 6-7 km above sea level at opening angles of $\sim 2.5^\circ$. Thus, the pions' transverse momenta lead to muons reaching a distance of $\sim 300\text{m}$ from the core at sea level.

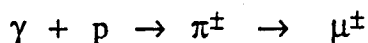
1.4.3 DIFFERENCES BETWEEN PROTON AND γ -RAY SHOWERS

The main constituents of both proton and γ -ray showers at sea level are electromagnetic in nature, and it turns out that showers produced by the two primaries appear very similar at observation level. They are however expected to differ in two aspects:

(i) Muon content

It was thought that processes producing muons in γ -ray showers were relatively unimportant compared to those in proton induced showers of the same size. The initial detection of Cygnus X-3, however, and other claimed detections since have shown γ -ray showers, if indeed γ -rays are responsible for the signals, to have anomalously high muon content and led to a re-examination of the possible muon production processes in γ -ray showers.

The most likely process for muon production is by nucleonic interaction of γ -rays and subsequent decay of pions produced:



After production, the pions follow a similar interaction chain to those described in the previous section. The pion production cross section varies between 1.5 mb and 2.4 mb at 10^{10} eV and 10^{15} eV respectively. These low cross sections make pion production ~ 500 times less likely than the usual electron/positron pair production with cross section ~ 0.7 b. Still less likely is the more direct process of muon pair production with a cross section of only $2\mu\text{b}$ for photons of 10^{15} eV. Monte Carlo simulations by a number of researchers, eg Stanev *et al.* 1985, have shown the expected number of muons in γ -ray showers to be only 10% of those in proton showers. However, it is worth mentioning that the quoted interaction cross sections can only be calculated by extrapolation from particle accelerator data, as direct measurement at these energies is currently impossible. It is possible, but unlikely that the pion production cross sections increase unexpectedly at energies close to 10^{15} eV.

(ii) Lateral distribution of shower particles

Despite the differences in shower development, it is thought that the lateral spread of particles is similar in both showers. In fact the NKG function, developed to describe γ -ray induced showers only, is found to be a good fit to experimental data consisting mainly of proton showers. Simulations by, for example Fenyves (1985) and Cheung and MacKeown (1987), do however show that γ -ray induced showers should appear slightly younger than proton induced showers. The Kiel result, therefore, is at odds with this prediction. This is discussed more fully in Chapter 4.

1.5 Recent PeV observations

The idea that compact objects could be responsible for the production of UHE cosmic rays was tremendously exciting and led to the building of many new EAS

telescopes designed with the identification of point sources of PeV γ -rays in mind. Important design criteria were a large collecting area and good angular resolution, both of which are needed to provide good signal to noise ratios to detect the relatively low fluxes expected. One such telescope was the Gamma Ray EXperiment (GREX) array built at Haverah Park which began operation in March 1986 and is described in greater detail in subsequent chapters. Unfortunately, the results of these experiments have been somewhat disappointing, and the field has not lived up to its early promise with a wealth of detections. Indeed, Cygnus X-3, originally the most promising UHE source has apparently turned off. If it had continued to emit at the rate reported by Kiel, detection by modern arrays, with improved angular resolutions and increased collecting areas and observation times would surely have been guaranteed at undisputable levels of significance. Such detections, however, have not been forthcoming. Only the Tata group (Tonwar *et al.* 1988) have reported a dc signal from Cygnus X-3 without invoking a 4.8hr periodicity analysis. A 3.4σ excess was seen in data collected between June 1984 and November 1987. Again this excess was seen in flatter showers, though the precise age at which the data was cut appears somewhat difficult to justify. Showers were also cut at what appears to be a rather arbitrary choice of shower size. Such cuts and apparent inconsistencies in data handling have received much criticism in the past (eg Chardin and Gerbier, 1989) and have led to much scepticism in what were, in the first place, marginal detections. Similar criticisms could also be levelled at the recent claims for emission from Cygnus X-3 modulated at the 4.8hr X-ray period from the Ohya group (Muraki *et al.* 1991). A 4.7σ excess was seen in the phase bin 0.25 to 3.0 in showers with numbers of muons less than expected for background events. However, the significance of this observation is greatly reduced by the fact that the muon cut was not made *a-priori* but was rather the cut that appeared to maximise the signal. The selection of shower size also seems to be somewhat arbitrary as no explanation is given for the cut ($N > 1 \times 10^5$), and it is evident that other cuts have been applied to the data. The initial shower selection criteria allow showers with $N \geq 2 \times 10^4$ to be examined, and the search for DC emission was performed on showers with

$N \geq 2 \times 10^5$.

Naturally other X-ray binary systems gained considerable attention after the detection of Cygnus X-3. Hercules X-1 is of particular interest. At TeV energies, Her X-1 is one of the most studied of sources, claims for its detection being mainly reliant on signal modulation at the 1.24s period of its X-ray pulsar. It was this modulation that led to the first claim for its detection by the Durham group (Dowthwaite *et al.* 1984) and subsequent confirmation by the Whipple observatory (Gorham *et al.* 1986a,b). It appears particularly transitory in nature, with reports of bursts lasting anywhere between 3 and 100 minutes (Baltrusaitis *et al.* 1985). At PeV energies, the Fly's Eye group reported a burst of γ -rays lasting ~ 40 minutes. This result is surprising for two reasons: (i) X-ray emission is further modulated on a 35 day cycle and TeV bursts occur nearly always during the X-ray on-state of this cycle, whereas this burst occurred during the off-state. (ii) Observations made simultaneously at the same site by the Durham Group at TeV energies indicate no excess (Chadwick *et al.* 1985). Hercules X-1 is discussed in greater depth in Chapter 6.

Vela X-1, another X-ray binary system, was examined by the Adelaide group for emission at PeV energies for the period 1979 to 1981. Evidence was found for the emission at a phase of ~ 0.63 in the 8.9 day orbital period at the 0.01% level (Protheroe *et al.* 1984). The Potchefstroom Group (Van der Walt *et al.* 1987) also find evidence for emission during the same period, but at an orbital phase of ~ 0.13 . However, this detection was marginal, with an estimated chance probability of 1.8%. Confirmation of emission also came from the Chacaltaya Group (Suga *et al.* 1985) after examination of data recorded during the 1960's. Poor angular resolution meant using a very large source bin, ($10^\circ \times 10^\circ$). Events were selected with low muon content. 19 events were seen when only 10.8 were expected. However, continued observations by the Adelaide experiment showed no evidence for continued emission from Vela X-1 (Clay *et al.* 1987).

The Adelaide Group have also found evidence for emission from LMC X-4

(Protheroe *et al.* 1985) though at a marginal level of significance (99.1%). This X-ray binary source lies some 50kpc from earth, so that electron/positron pair production by interaction of PeV γ -rays in the microwave primeval radiation must result in significant attenuation of the signal. The pair production cross section has a resonance at $\sim 2.5 \times 10^{15}$ eV so that any γ -rays reaching earth from this distance must have energies in excess of 10×10^{15} eV. If the signal from LMC X-4 is real, its magnitude would imply (taking account of absorption) a luminosity 10 times that originally claimed for Cygnus X-3.

Summarising, then, only a handful of PeV γ -ray sources have been detected. None of these detections have been at an unassailable level of significance, and lack of corroborating evidence has led to much skepticism over claims for emission. The plethora of marginal detections only serve to emphasise the need to maximise signal to noise ratios. The optimisations of analysis procedures and source searching strategies described in this thesis are aimed at achieving this all important goal.

CHAPTER TWO

THE GREX γ -RAY TELESCOPE AT HAVERAH PARK

2.0 Introduction

The GREX γ -ray telescope which became operational in March 1986 was built to observe Pev γ -ray emission from point sources such as Cygnus X-3 following reports of emission from that source by the Kiel group (Samorski and Stamm, 1983) and subsequent confirmation of γ -ray emission at the 4.8 hr period by Lloyd Evans et al. (1983). Important design criteria for such a telescope are a large exposure and good angular resolution due to the small flux expected at these energies. The first of these has been achieved with the large area covered by the array ($\sim 3.5 \times 10^4 \text{ m}^2$) and by increasing the useful on-time of the array by reducing the dead time with a fast transfer data handling system. An angular resolution of $\sim 1^\circ$ has been obtained by using fast timing and by shielding the detectors with lead. The trigger rate of the array and its sensitivity to small showers have recently been increased by the addition of 4 new detectors.

This chapter describes briefly the GREX experiment, the analysis of data from which is the subject of the remainder of this thesis. A more detailed description can be found elsewhere (Bloomer 1990).

2.1 The Geometry of the array

The layout of the GREX array is shown in figure 2.1. A number of features are of interest:

- (i) The four additional and identical detectors (33 to 36) which became operational at the beginning of June 1989.

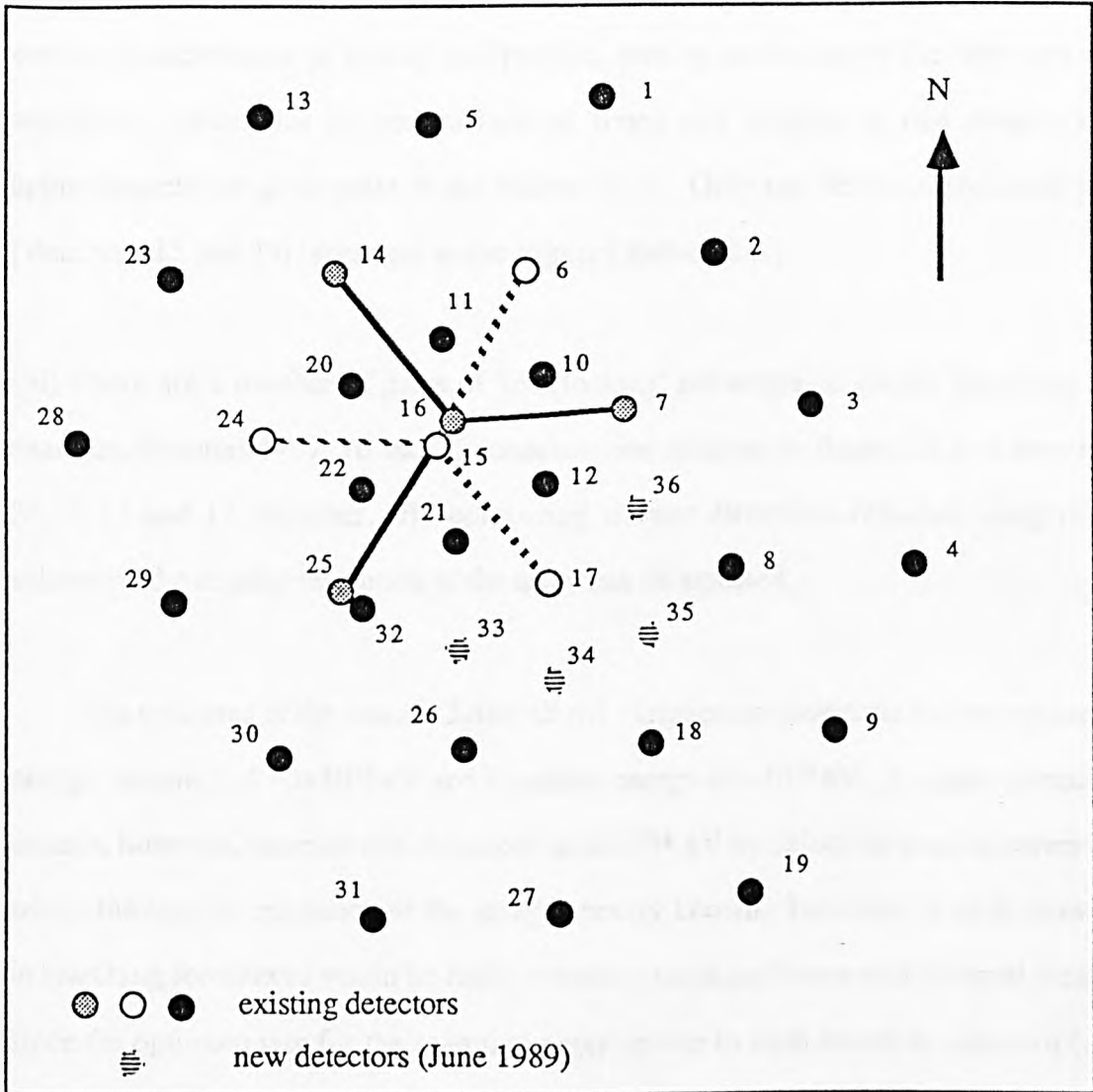


Figure 2.1 The layout of the 36 detector array. New detectors are numbered 33 to 36. Detectors in the two 50m subarrays used for assessing angular resolutions are marked by hatched and open symbols.

(ii) There are two pairs of side by side detectors, 15 and 16, and 25 and 32. These enable measurements of timing and particle density resolutions of the detectors and associated electronics by comparison of times and heights of two detectors at approximately the same point in the shower front. Only one detector from each pair (detectors 15 and 25) takes part in the trigger (section 2.3)

(iii) There are a number of pairs of 'interlocking' subarrays of similar geometry, for example, detectors 14, 7, 16 and 25 constitute one subarray in figure 2.1, and detectors 24, 6, 15 and 17 the other. By comparing shower directions obtained using these subarrays, the angular resolution of the array can be assessed.

The total area of the array is $3.46 \times 10^4 \text{ m}^2$. Triggering conditions lead to a primary energy threshold of $\sim 3 \times 10^{14} \text{ eV}$ and a median energy of $\sim 10^{15} \text{ eV}$. Analysis selection criteria, however, increase this threshold to $5 \times 10^{14} \text{ eV}$ by rejecting small showers for which the angular resolution of the array is poorly known. Inclusion of such showers in searching for sources would be likely to reduce the significance of any signal present since the optimum size for the search bin appropriate to such events is unknown (see Chapter 5)

2.2 The Detectors

Each GREX detector consists of two slabs of 10 cm thickness NE102A scintillator placed side by side and covering a total area of 0.8 m^2 , held 60 cm above a 70mm photomultiplier. Originally Phillips XP 2312B tubes were used. EMI 9821B tubes have been used in the four additional detectors as well as for replacement tubes as Phillips no longer supply the original XP 2312B tube. Both tubes have similar characteristics with rise times of 2.5 ns and 2.1 ns and are run at E.H.T. potentials of approximately -1.9kV and -2.1kV respectively. The E.H.T.s are all finely adjusted so that the measured response of each detector is the same for the passage of a single vertical muon through the

scintillator.

Aluminium foil is placed on top of the scintillator to reflect upwards going light back into the tube. The whole arrangement is contained in a light tight box painted matt black to prevent late pulses due to internal reflection. Each detector is shielded with an 8mm thickness of lead to improve angular resolution. This is dealt with in the following section. Detectors 15 and 16 are situated in the central hut along with the data acquisition and recording electronics. Detectors 25 and 32 are housed within one of the huts of the old 50m experiment while the remaining detectors are each enclosed in their own weather proof housing which is not temperature controlled.

A charged particle passing through the scintillator will give up some of its energy to the scintillator which will re-emit the energy $\sim 1\text{ns}$ later in the form of photons of wavelength $\sim 420\text{nm}$. The photons entering the photomultiplier tube will produce an electrical signal. The distribution of signal heights is characterised by: (i) The single particle peak, whose shape is due to the range of directions of travel and points of impact on the scintillator of the charged particles, and (ii) Low level photomultiplier tube noise.

The signal from each detector is transmitted to the recording electronics via 75 Ω Aerialite 363 coaxial cable.

2.2.1 LEAD SHIELDING

A thickness of 8mm of lead was placed on top of all detectors on the 29th June 1987 following suggestions by Linsley (1986,1987) that this would result in improved angular resolution for the GREX array. This concept was tested prior to the end of June '87 by comparison of signals in side-by-side detectors and of directions obtained by independent sub arrays (see the following section and Bloomer *et al.* 1988).

The high nuclear charge of the lead shielding means that the critical energy of electrons and positrons is lower in the lead ($\epsilon_c \approx 7.8\text{ MeV}$) than in air ($\epsilon_c \approx 84\text{ MeV}$).

The rate of energy absorption by the lead (radiation length $\approx 5.8 \text{ gcm}^{-2}$) is also greater per gcm^{-2} penetrated than in air (radiation length $\approx 36.1 \text{ gcm}^{-2}$). Thus the energy lost in 8mm of lead is approximately that lost in 400m of air at sea level. The results of these transition characteristics are as follows:

(i) Electrons with energies greater than the critical energy will multiply via bremsstrahlung and pair production processes and hence give rise to larger scintillator signals

(ii) High energy photons will pair produce and hence give rise to a larger scintillator signal

(iii) Low energy electrons and photons will be rapidly absorbed and not produce any signal in the scintillator.

Adding lead to the detectors would, therefore, cause them to trigger earlier as they would be more sensitive to the high energy electrons and photons travelling at the leading edge of the shower front. The number of spurious late times caused by low energy particles that trail the shower front would be reduced. The distribution of arrival times was therefore expected to be made narrower by the addition of lead and this was, indeed found to be the case.

2.2.2 TESTING OF LEAD SHIELDED DETECTORS

2.2.2.1 Side-by-side detector comparisons

The triggering times and particle densities measured by two side by side detectors one of which was shielded with various thicknesses of lead were compared. Triggering times were corrected for the expected difference in arrival times of the particle front in

inclined showers at each detector. The maximum difference in triggering times between shielded and unshielded detectors was obtained with 9mm of lead when the shielded detector was found to trigger, on average, 0.82ns earlier. A detector with this amount of shielding was also found to give a signal approximately 30% larger than an unshielded detector.

2.2.2.2 Sub Array Comparisons

To test the effect of the addition of lead on the angular resolution, arrival directions obtained using times from the ring of detectors 30m from the centre of the array were compared with those obtained using each of the two 50m subarrays highlighted in figure 2.1, one of which had all detectors shielded with 9mm of lead (Bloomer *et al.* 1988). Showers triggering all detectors in the 30m array and the two 50m subarrays and with cores falling within 10 m of the array centre were selected for this analysis. For each shower, the difference in the direction cosines, l and m , of the directions determined using 30m ring of detectors and (i) the 50 metre lead covered array (Δl_{pb} and Δm_{pb}) and (ii) the 50 metre unshielded array, (Δl_{Un} and Δm_{Un}) were calculated. It was found that the spread in Δl_{pb} and Δm_{pb} were each less than Δl_{Un} and Δm_{Un} respectively. This work appeared to demonstrate that the addition of lead to the detectors did indeed improve the angular resolution of the array, and 8mm of lead was subsequently placed on top of the detectors. After this work was completed, it was discovered that statistical errors had been underestimated, and the results were inconclusive. Subsequent work, however, in comparing sub-array directions for the completely covered array (Bloomer 1990) has confirmed that the addition of lead to the detectors does indeed improve the resolution of the array with a reduction of $\sim 37\%$ in the solid angle uncertainty in assigned arrival directions. It has also been shown that the apparent shower front curvature is reduced by the lead (Chapter 3) and this leads to a reduction in the arrival direction uncertainties due to core location errors.

2.3 Data Acquisition and Recording electronics

For each detector the data acquisition electronics consist of a discriminator board, a time to digital converter (TDC), (a single channel of a Le Croy 4208) operating on a nanosecond clock and an analogue to digital converter (ADC) (a single channel of a Le Croy 4300 FERA). In addition a coincidence unit detects the simultaneous triggering of detectors which constitutes an air shower and causes the timing electronics to measure the detector triggering times as well as prompting the recording electronics to record the 'event'.

The signals from the detectors are each fed into the discriminator board which uses a Le Croy MVL407 voltage comparator. Each signal is fed into two discriminators, one of which gives an output 'high' when the input exceeds the voltage corresponding to a single particle traversing the detector- the D2 level. The other D1 level is set just above the tube noise level of $\sim 1/3$ of a particle.

The D2 pulse is of $1\mu\text{s}$ duration and is fed to the coincidence unit which performs an analogue addition of all the D2 levels and gives a 'common pulse' when the sum is equal to or exceeds that of 5 D2 pulses. This pulse indicates that the array has been triggered and that 5 or more detectors have seen at least 1 particle each. The common pulse prompts those TDCs that have already started counting to stop and the remainder to start counting. The D1 pulse initiates counting in the TDC where no common pulse has yet been received and stops counting when it arrives after the common pulse. Hence, when an event is observed, the TDCs hold times of triggering of detectors relative to the common pulse which are recorded as negative if the detector was triggered before the coincidence and positive after. The common pulse also prompts the event timer, which is synchronised every hour to a 60kHz radio pulse from Rugby, to record the time of the trigger to 1ms accuracy.

Each detector output is fed via a 20ns delay cable into a D1 gated input of an ADC which gives particle density information. The gate ensures that only densities greater than $\sim 1/3$ of a particle are recorded. If no event occurs within $1\mu\text{s}$ of a D1 trigger, a

fast pulse is issued to clear all TDCs and ADCs. $1\mu\text{s}$ after a common pulse has been issued, the coincidence unit produces an EOW (end of window pulse). This inhibits the input of the ADCs and TDCs. The 'look at me' flag, LAM, is set which informs the computer that the CAMAC module needs to be read. Recently the time taken to read the CAMAC module has been greatly reduced from 350ms to 2ms by incorporating a GPIB fast transfer system. This system was designed at Haverah Park (Perrett and Patel 1987) and replaces the Le Croy 8901 GPIB Crate Controller used previously. Once the data have been read, the system is reset and is ready to accept another event.

Originally, GREX was under the control of a North Star *Horizon*. On the 23rd November 1987 this was replaced by Uman computer which was itself superseded by an expandable system of VME modules based around a Motorola 68020 microprocessor which became operational on the 5th February 1989. Data are written to hard disk as they are acquired. When the hard disk is full its data are transferred to tape. The VME system's 'multitasking' capabilities enable this transfer to take place without interrupting the acquisition of data. Some on-line processing of each event, such as the computation of an approximate core position and arrival direction and the compilation of certain diagnostic statistics such as D1, D2 and coincidence rates, is also possible using this system.

For each background D1 pulse, from any of the 36 detectors, $2\mu\text{s}$ deadtime is incurred. This includes the $1\mu\text{s}$ window during which a coincidence may occur and the time taken to clear the TDCs and ADCs. In addition it takes $\sim 2\text{ms}$ to process each event and reset the system.

2.4 The history of the GREX array

A number of important changes to the GREX array during its first 4.5 years of operation have already been described. These include the increase in the dynamic range of detectors from 20 particles to 45 particles in September 1986, the addition of lead to the detectors at the end of June 1987 and the addition of 4 new detectors to the array in May 1989. These 3 changes have each had effects on density and timing measurements,

the range over which these take place and the triggering sensitivities of the array. They therefore divide the 4.5 years into 4 operational eras: (1) Pre-ADC change (2) Post-ADC change, pre-lead (3) Lead shielded 32 detector array and (4) Lead shielded 36 detector array. These dates of these changes along with other minor alterations to the array are shown in table 2.1

2.5 Performance Assessment of the GREX array

At the time of installation of the four new additional detectors in May 1989 it was realised that the substantially higher trigger rate (0.4 Hz compared to 0.3Hz) gave an enhanced possibility of detecting transient emission from candidate objects on a daily basis. To achieve this it is necessary to understand the background rate of events in detail (see Chapter 5) and it was realised that measurements of this important quantity could be improved if background assessments from days adjacent to the day of interest were available. The use of these adjacent days requires a detailed knowledge of the variation of trigger rate with atmospheric pressure and so careful determination of the barometric coefficient was made. This has had the additional advantages that the shower rate (after pressure correction) can be used as a monitor of the stability of operation of the array. It has also been possible to use the barometric coefficient to give an estimation of the attenuation length of showers.

2.5.1 MEASUREMENT OF THE BAROMETRIC COEFFICIENT

2.5.1.1 Pressure Measurement

A total of three independent measurements of pressure are made at Haverah Park. One of these is made by the Nottingham University group who run the muon detector situated in the central hut and is written to tape along with event information. This pressure measurement has, however, been found to be unreliable on occasions and has

	Date	Change
Era 1	18/02/86	32 detector system becomes operational under control of North Star Horizon
	5/03/86	First data successfully analysed
Era 2	15/09/86	Increase in dynamic range of ADC's from 20 particles to 45 particle
	29/06/87	Lead placed on all detectors
Era 3	23/11/87	U-man takes over control of GREX, dead-time reduced from ~1s to ~500ms
	5/02/89	VME system becomes operational
	15/03/89	Fast transfer introduced. Dead-time to ~2ms
Era 4	31/05/89	36 detector system becomes fully operational
	30/09/90	Last date covered by analysis in this thesis

Table 1.1 The History of the GREX Array, showing changes to the array and the 'operational eras'

not been used in the present analysis. In addition to this measurement, measurements are also made on a Fortin barometer and a barograph. The Fortin barometer must be read manually while the barograph plots a continuous graphical record and therefore represents the most convenient method for routine pressure measurements. Checks have shown that the Fortin pressure, F , (an absolute measure) is related to the barograph pressure, B by:

$$F = 1.1038 B - 122.3 \quad \dots \text{Eqn 2.1}$$

where F and B are in units of mb. For what follows, only barograph pressures have been used.

2.5.1.2 Shower rate as a function of pressure

The number of particles in an air shower induced by a primary particle of given energy is a function of observation height or, more precisely, the 'thickness' of air traversed (in gcm^{-2}). The threshold energy of the primary particles for showers to trigger the GREX array is $\sim 3 \times 10^{14}$ eV, and these showers, being observed at sea level, are past their maximum and have hence begun to decay (see Chapter 1) The number of particles in such showers decreases with increasing atmospheric depth, and the probability of their detection, therefore decreases with increasing pressure. A negative correlation is therefore expected between the observed event rate and atmospheric pressure. This relationship is indeed observed, and it is found that the event rate (R) varies as an exponential function of pressure (P) and is parametrised by equation 2.2:

$$\ln(R) = \beta P + R_0 \quad \dots \text{Eqn 2.2}$$

where β is the pressure coefficient, and R_0 is a constant

The event rate of the GREX array has been monitored on a daily basis for 12 months of operation of the 36 detector array from June 1989 to May 1990 inclusive. This period began shortly after the upgrade of the array to 36 detectors when it was realised that daily pressure corrections could be used to improve background estimates for short term burst observations: the count rates on days close to the period of interest

could be corrected to the equivalent rate at the pressure of that period. Additionally, this 12 month period was expected to be a particularly stable one in terms of the uninterrupted operation of the array. At this time, data was written straight to a hard disk and transferred to tape later with no interruption to data acquisition.

For each of the twelve monthly periods, the natural logs of the daily event rates (in counts per minute) were plotted as a function of barograph pressure and the barometric coefficients obtained by straight line fits to these plots. For reasons that will be explained shortly, only complete days were used for this analysis. Figure 2.2 shows one of these plots for the month of January 1990. The barometric coefficients are shown plotted for each month in Figure 2.3(i). The mean barometric coefficient for the whole period was found to be 0.0094 ± 0.0001 (0.0085 ± 0.0001 for the Fortin scale)

By correcting event rates measured at different pressures to a standard pressure, meaningful comparisons can be made between them. 1000mb is arbitrarily chosen as a standard pressure, and the corrected rate, R_{1000} for a measured rate, R , at pressure P is given by:

$$\ln R_{1000} = \ln (R) - \beta(P-1000) \quad \dots \text{Eqn 2.3}$$

The mean pressure corrected rates and their standard deviations are shown plotted in Figure 2.3(ii) and (iii) respectively. There is evidence to suggest that it is insufficient to parametrise the event rate solely in terms of pressure: the pressure corrected event rates are not constant on a month by month basis. In addition, the spread in daily pressure corrected rates is consistently larger than the $\sim 0.12 \text{ min}^{-1}$ one would expect from Poisson statistics. It was suspected that these additional fluctuations were caused by temperature effects. This is dealt with in more detail in section 2.5.2. However, comparison of pressure corrected rates shows that any residual effects cause fluctuations in the rate of order $\sim 1\%$ compared to fluctuations of $\sim 10\%$ before correction.

2.5.1.3 D1 and D2 rates as a function of pressure

The D1 and D2 trigger rates also show a negative correlation with atmospheric

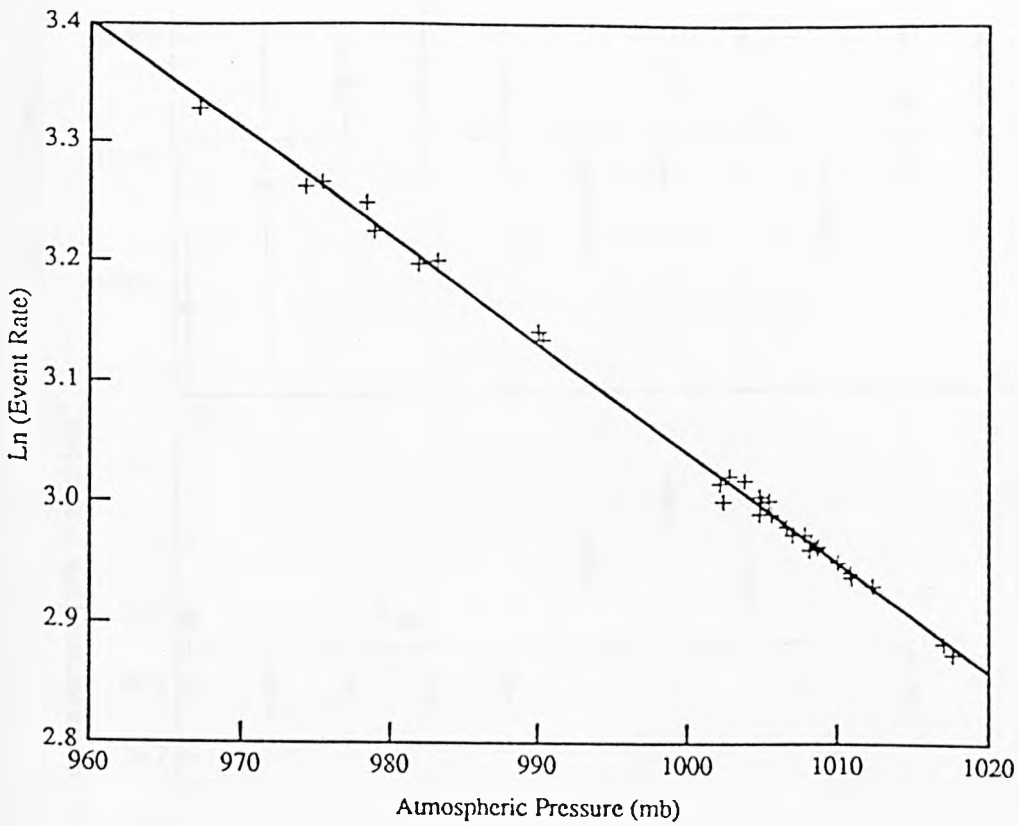


Figure 2.2 The natural logarithm of the daily event rate is shown plotted as a function of atmospheric pressure measured on the Barograph for January 1990. The straight line is a least squares fit to the data and has a gradient (the barometric coefficient) of 0.0090 ± 0.0001 .

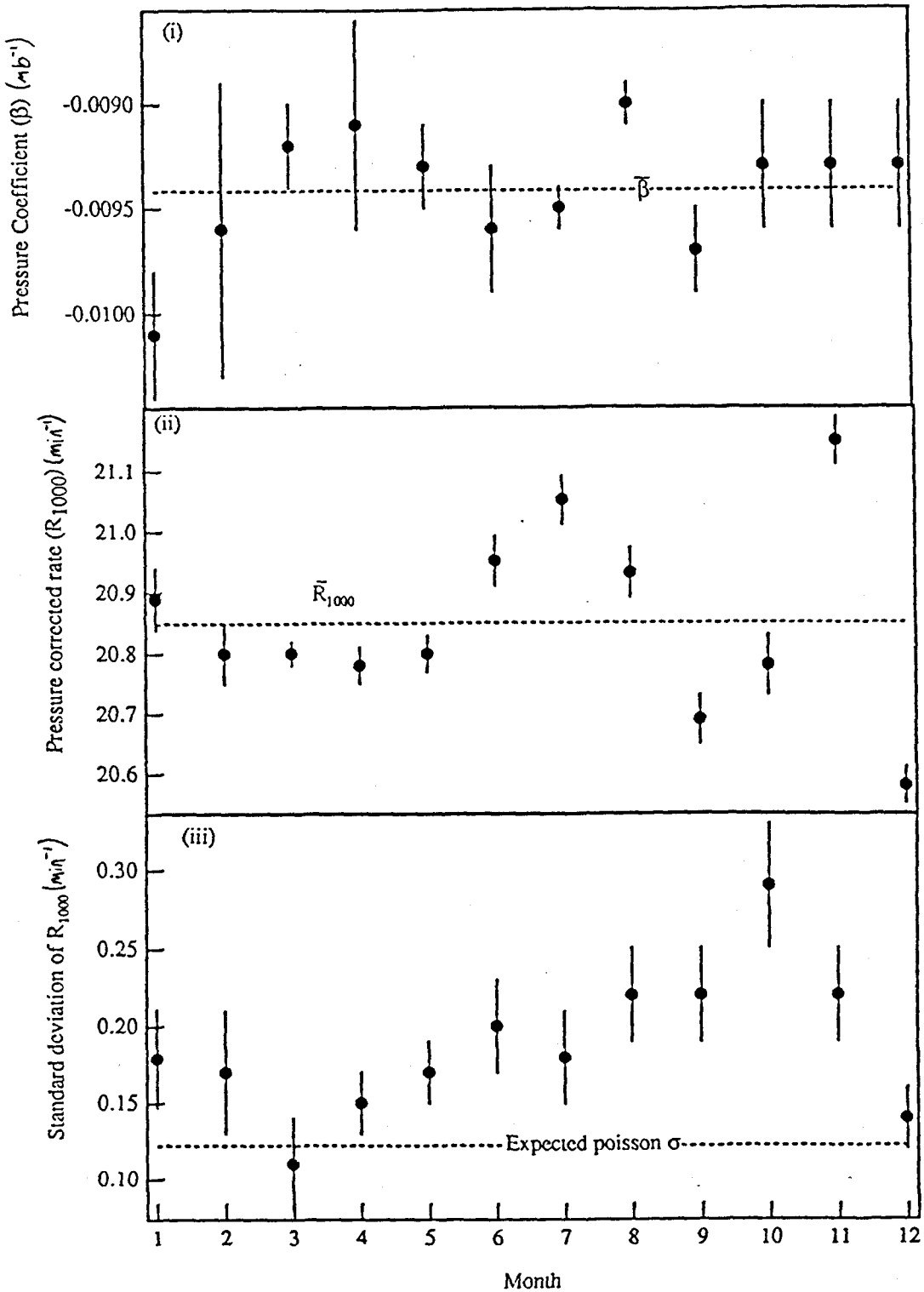


Figure 2.3 (i) (ii) and (iii). The barometric coefficients, mean daily event rates corrected to a pressure of 1000mb, and the standard deviations of those rates respectively are shown plotted for the months June 1989 to May 1990 which are numbered sequentially 1 to 12. The lines plotted on figures (i) to (iii) show the mean barometric coefficient, event rate and expected Poisson standard deviation respectively for the whole period.

pressure with a similar relationship to event rates. The barometric coefficients for the D1 and D2 rates of all detectors were calculated for two periods: the first two weeks in October 1989 and for the period 4th November '89 to 24th November '89. The D1 and D2 coefficients are shown plotted for comparison in Figures 2.4(i) and (ii) respectively. It can be seen that the magnitudes of the coefficients are consistently lower for the second period. Again variation in temperature was suspected as the cause of this difference.

These plots also illustrate the use of D1 and D2 rates as diagnostic tools. Detector 13 in October, and detectors 17 and 19 in November were seen to have unusual D1 and D2 barometric coefficients. The D1 and D2 rates were also seen to be rather erratic on a day-to-day basis during this period. These problems were solved by reseating the photomultiplier tubes in their sockets.

2.5.2 DIURNAL TRIGGER RATE VARIATION

During June and July 1989, comparisons were made of event rates during partial days on which the array was turned off for hardware and software maintenance from 10am till 4pm. These showed that the pressure corrected rate was slightly, but significantly higher in the morning period (midnight to 10am) than in the afternoon (4pm to midnight). A diurnal rate variation was implied by these results and this effect was further investigated during October '89. The mean pressure corrected shower rate for this month is shown plotted as a function of the hour of the solar day in Figure 2.5. Only days in which the array had 100% on-time were used in determining the event rates. The plot shows a significant diurnal variation with amplitude of $\sim 1\%$ which is thought to be due to variation in temperature which is in general lower in the morning than afternoon. That this effect is due changing characteristics in shower development rather than in instrumental sensitivities is evidenced by the fact that the D2 rates show no significant diurnal variation. The individual detector D1 pressure corrected trigger rates do however show a diurnal variation, but one that is 180° out of phase with the event rate, the D1 rates being lower in the morning than afternoon. The histograms in figure

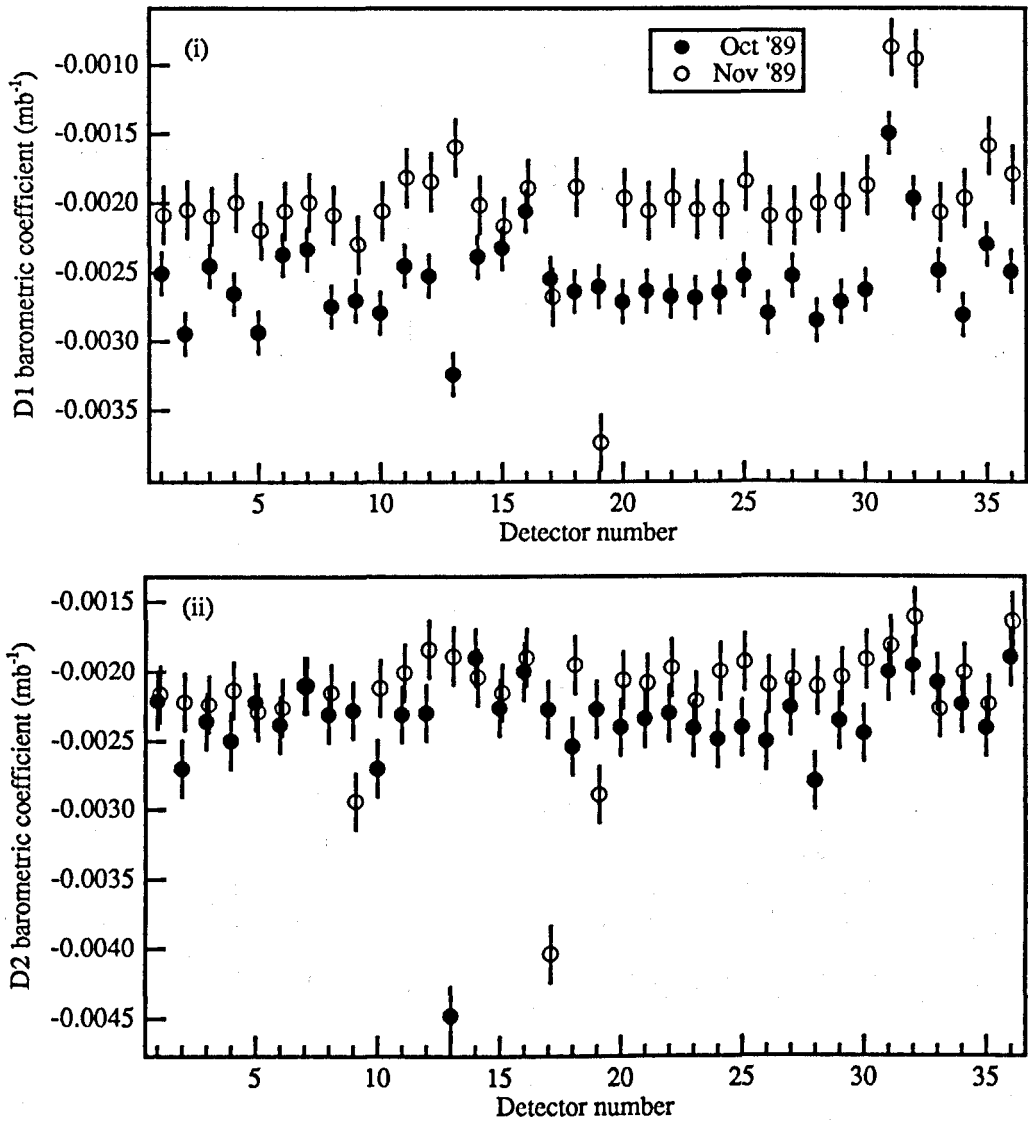


Figure 2.4 (i) and (ii). The barometric coefficients for the D1 and D2 trigger rates respectively are shown plotted for each detector and for two periods of the array: 1st to 15th October 1989 and 4th to 24th November 1989. These periods are denoted by the filled and open symbols respectively.

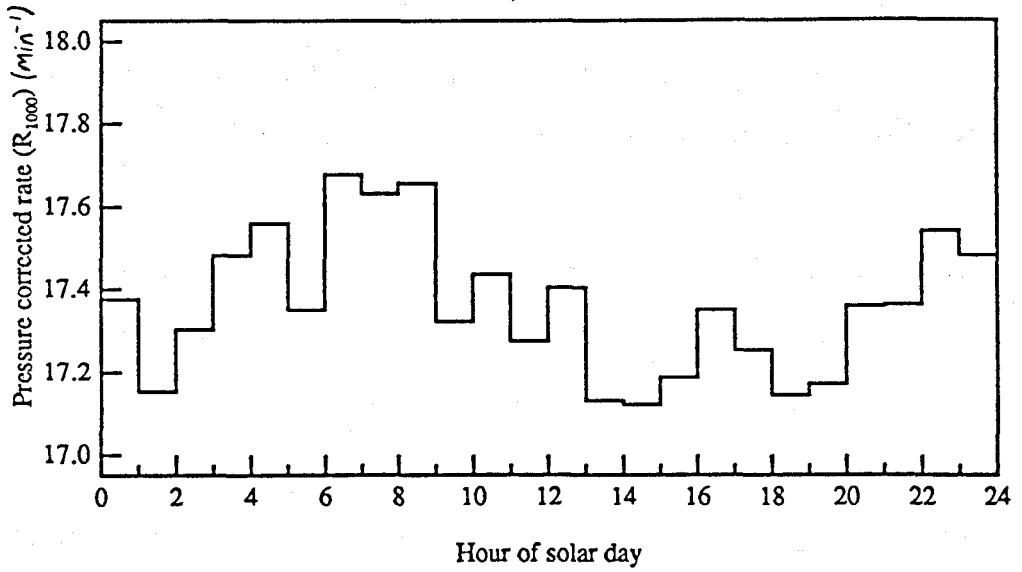


Figure 2.5 The mean pressure corrected shower rate is shown plotted as a function of hour of the solar day for October 1989.

2.6(i) and (ii) show the pressure corrected D1 and D2 rates respectively averaged over all detectors plotted as a function of solar time for the period 2nd to 16th October 1989 inclusive. It was suspected that the observed diurnal variation in D1 rates was instrumental in origin. Increased sensitivity of the photomultipliers with temperature may cause this effect, or perhaps increased amplitude of noise pulses, as the D1 rate is set only slightly above the noise level. It is unlikely that the recording electronics would be affected by changes in temperature as they are situated within the main hut and experience little temperature variation. The same could be said of detectors 15 and 16 and also detectors 25 and 32 which are inside huts. The plot in figure 2.6(iii) shows the mean pressure corrected D1 rates for these detectors as a function of time. It is seen that the diurnal variation is just as strong for these detectors as for the remaining detectors, and it is unlikely, therefore that this effect is instrumental in origin

The negative correlation of shower rate with temperature may be explained by considering the temperature effect on the mean lateral distance through which electrons are scattered in one radiation length through Compton interactions. This distance is known as the Molière unit and parametrises the lateral spread of particles at sea level (section 1.4.1).

As the air temperature rises, the density of air must decrease for the pressure to remain constant. Hence, the distance travelled by a particle in traversing one radiation length in air increases and so too must the lateral distance through which it is scattered. The Molière unit, therefore, increases as temperature increases at a given atmospheric pressure and the shower particles become more 'spread out'.

The graph in figure 2.7 shows a schematic representation of the distribution of particles as a function of core distance for two showers observed at the same atmospheric depth and produced by primary particles of the same energy but for which the Molière units are different. The density of particles is plotted in units (density x core distance) such that the total area under the graph represents the total number of particles in the shower. The total number of particles in showers of the same initiating energy but different Molière units are the same. In the case where the value of the

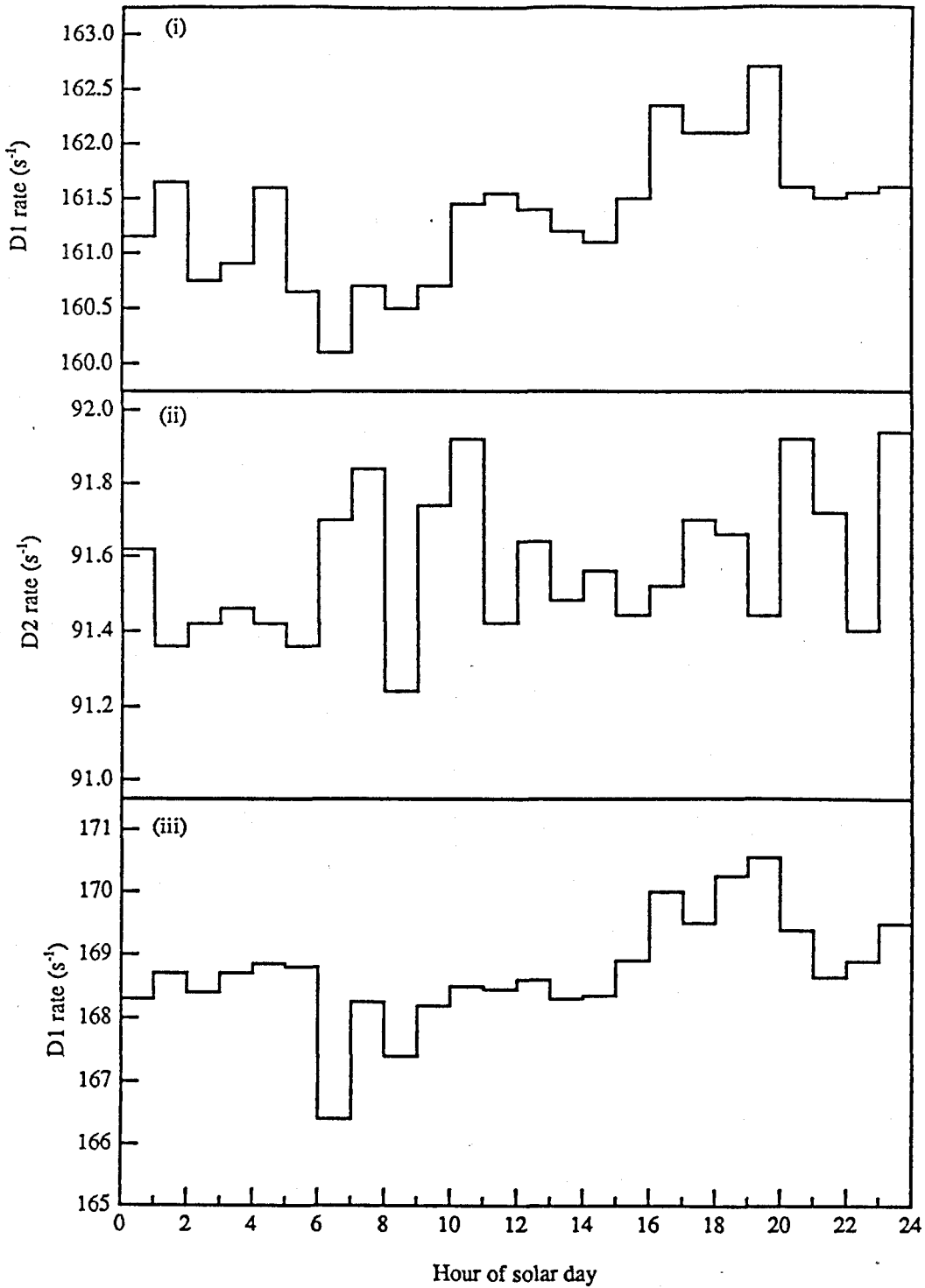


Figure 2.6 (i) and (ii) show the mean pressure corrected D1 and D2 trigger rates averaged over all detectors plotted as a function of hour of the solar day for the period 2nd to 16th October 1989. (iii) shows the D1 rates for detectors 15,16,25 and 32 which are inside huts

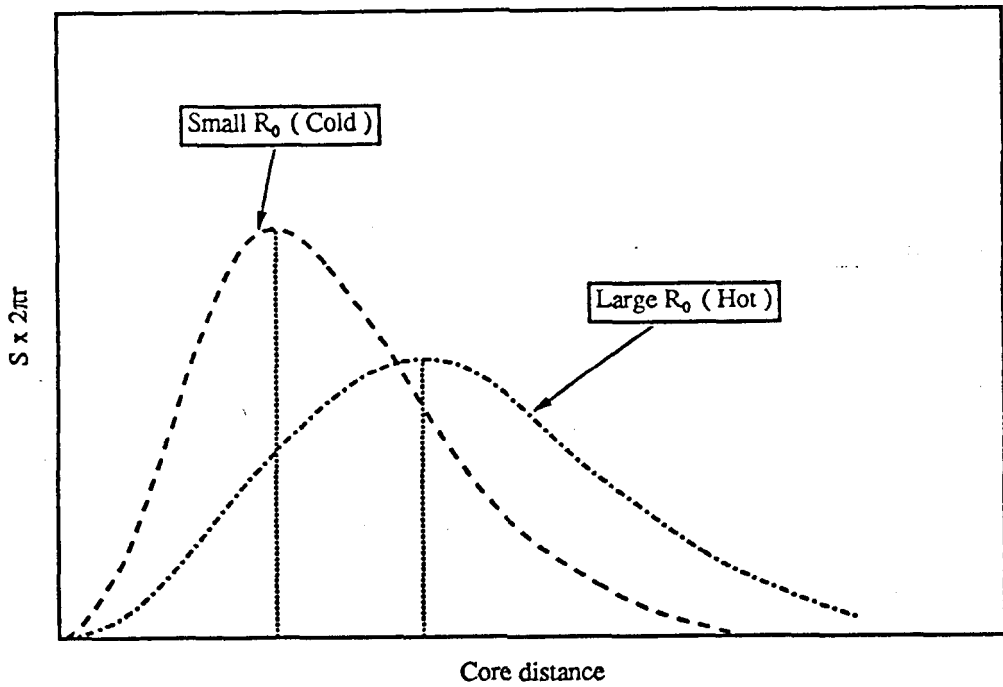


Figure 2.7 A schematic representation of the particle density as a function of core distance for two showers with different Molière units. The ordinate is in units Density \times Core distance so that the area below the graph represents the total number of particles in the shower.

Molière unit is higher, however, the particles are spread over a greater area. This leads to smaller densities at distances less than the Molière unit and increased densities at larger distances. The effect of increasing the Molière unit on the triggering sensitivity of the array is, therefore dependent on the detector spacing. In the case of the GREX array, the triggered detectors are expected to be at distances less than the Molière unit from the core for showers close to the array threshold. The triggering probability would, therefore, be reduced if the value of the Molière unit were to increase, as it does, with increase in temperature.

2.6 Derivation of Attenuation Length from the Barometric Coefficient

The size of an air shower, S , past maximum development decays approximately exponentially as it propagates deeper in the atmosphere with a characteristic decay length known as the attenuation length, λ :

$$S = S_0 \exp\left(-\frac{x}{\lambda}\right) \quad \dots \text{Eqn 2.4}$$

where x is the atmospheric depth past maximum and S_0 is the size at maximum. The precise value of λ is different for different size parameters and is a weak function of the primary energy. Direct measurement of the attenuation length is possible by comparing fluxes of showers inclined at different zenith angles as these have passed through different atmospheric thicknesses. At each of a number of zenith angles, θ_i , the values of S_i are determined that satisfy the condition that the rate of showers with $S > S_i$ is a constant, R . If we assume that the flux of particles incident at the top of the atmosphere is isotropic, then showers of size S_1 at θ_1 will be produced by primary particles of the same energy as those of size S_2 at θ_2 and S_n at θ_n providing all the showers used in the analysis are significantly *larger* than the array threshold. The effective atmospheric observation depth of a shower inclined at an angle θ to the vertical is $X \sec\theta$ where X is the vertical depth. Taking the natural logarithm of Equation 2.4 yields:

$$\ln S = \ln S_0 - \frac{X}{\lambda} \sec \theta \quad \dots \text{Eqn 2.5}$$

so that the attenuation length can be obtained from a plot of $\ln S$ vs $\text{Sec } \theta$. A

preliminary measurement by Watson (1987) using this method yielded an estimate of $\lambda \sim 150 \text{gcm}^{-2}$.

A more indirect but simpler method of calculating λ which does not require knowledge of showers' zenith angles was used by Galbraith (1958). Measurements of the rate of showers R above a fixed size at different atmospheric depths *can* be used to calculate the absorption length, Λ , where

$$\frac{1}{\Lambda} = -\frac{d \ln R}{dx} \quad \dots \text{Eqn 2.6}$$

The value of λ is related to Λ by the relationship:

$$\lambda = \gamma \Lambda \quad \dots \text{Eqn 2.7}$$

where γ is the slope of the integral size spectrum and Λ is related to the barometric coefficient by the relationship:

$$\Lambda = \frac{13.6}{\beta - 4\alpha} \quad \dots \text{Eqn 2.8}$$

where β and α are the fractional change in event rate with pressure (measured in cm of Hg) and temperature ($^{\circ}\text{C}$). The diurnal rate variations have shown α to be small- the fluctuations in event rate due to temperature changes during a whole day being no more than 2%. With a conservative estimate of a minimum 5°C temperature variation throughout the day, this would imply a value of $\alpha < -0.4\% \text{ } ^{\circ}\text{C}^{-1}$ (the value used by Galbraith was -0.38 for Geiger counter measurements). The barometric coefficient derived by this work is $-0.0085 \pm 0.0001 \text{ mb}^{-1}$ for the 36 lead covered array. This is equivalent to $-(11.2 \pm 0.1)\% \text{ cm}_{\text{Hg}}^{-1}$ which compares well with the value of $-11.2\% \text{ cm}_{\text{Hg}}^{-1}$ derived by Lawrence (Watson, 1988) from the zenith angle distribution. Ignoring the term 4α , which is seen to be very much smaller than β , and assuming that the value of γ is approximately the index of the primary energy spectrum, $\gamma \approx 2$, equations 2.7 and 2.8 yield a value for the attenuation length of $\lambda = 243^{+3}_{-24} \text{gcm}^{-2}$ for the 36 lead covered detector array. The error takes into account the upper limit derived for α . This value can be compared to $\lambda \sim 260 \text{gcm}^{-2}$ derived by Watson using the same technique (1988) for the unshielded detector array.

2.7 Conclusions

Extensive measurements of the barometric coefficients, pressure corrected event rates and individual detector D1 and D2 rates have shown the operational stability of the GREX array to be extremely good. Accurate knowledge of these quantities can be used to improve the accuracy of background measurements in the search for transient bursts - considered an important strategy in looking for sources of UHE γ -rays. Measurements of these quantities will continue in the future and provide useful diagnostics with which to monitor the performance of the array.

CHAPTER THREE

DATA ANALYSIS AND REDUCTION

3.0 Introduction

The data processing and storage problems associated with the GREX experiment are considerable. Improvements to the array and associated electronics since data were first collected in March 1986 (Section 2.4) have led to an increase in the trigger rate from $\sim 6 \text{ min}^{-1}$ to 20 min^{-1} . 16 Mbytes of raw data per day are obtained by the data acquisition electronics and recorded onto hard disk (Section 2.3). These raw data undergo considerable analysis and reformatting to enable anisotropies and the physics of air showers to be investigated.

Copies of the data are stored at each major step in the analysis, so that for the 4.5 years of operation of the GREX array the total amount of data stored is estimated to be 250 Gbytes. The data are analysed on the Amdahl mainframe computer at Leeds University and the complete data set is stored on magnetic tapes. Storage space in which data can be immediately accessed is limited to a total of 920 Mbytes in the form of hard disks. At present, this space is only just sufficient to store a compressed version of every event record to enable source searches over the whole of the data set to take place. In addition to the data storage problems, the limited CPU time allocated to the Haverah Park group on the Amdahl puts constraints on the accuracy to which shower parameters i.e. the core position and shower direction, can be obtained for each shower. The increased event rate over the past few years has meant that a corresponding increase in the speed of the analysis programs, in particular the core finding procedure, has been necessary to enable data to be processed at the same rate as it is produced.

This chapter is concerned with the data processing that has taken place at Leeds University up to the end of September 1990. The core location algorithm and analysis procedures, being the work of the author, are described in greatest depth.

3.1 Data reduction - A brief overview

Each shower striking and triggering the GREX array is recorded as a string of 582 characters on hard disk in the central hut at Haverah Park. When this disk is full, its contents are copied to a tape which is transferred to Leeds University for analysis on the Amdahl mainframe. The string of characters contains the following information : event trigger time to the nearest ms (MR), the event type, pressure, day time, date, and temperature in addition to the heights and relative triggering times recorded by each of the 36 detectors. Digits in each of these data are recorded as their EBCDIC character code. For instance a 5 digit integer number such as '15962' will be represented by 5 bytes, each byte being the EBCDIC code for one digit. A '6', for instance, is encoded as the hexadecimal number 'F6', or in binary '1110110'. The beginning and end of each event are each flagged by single characters to allow data subsequent to a corrupted event, which may have too many or too few characters, to be read without confusion. Corrupted events are relatively rare, occurring in less than 1 in 10,000 events or approximately 3 per day. In addition, D1 and D2 trigger rates are calculated every 200 half minutes and written to the hard disk as a string of 280 EBCDIC characters. This information is flagged to distinguish it from event information.

The tapes from Haverah Park are read at Leeds University on the Amdahl mainframe by a program that converts the EBCDIC character codes into their equivalent ASCII codes and writes these to a human readable text file known as a DQ file. The length of a DQ file is machine limited to 1.8 Mbytes, so that approximately 9 DQ files, equivalent to 16Mbytes, are produced per day and these are stored permanently in the Amdahl file store.

3.2 Data Conversion

The next stage in the data reduction is the conversion of the character codes into their numerical representation so that the event information is more readily accessible to

Pascal programs. In addition the signal heights are scaled to give the particle numbers recorded by the detectors, and the times corrected to give relative arrival times of the particles at the detectors.

A raw signal height, encoded as 4 ASCII characters, each representing a hexadecimal digit, is converted to a numerical 8 byte real representation. This height is then multiplied by 0.022 to convert it to the equivalent number of particles passing through the detector. This factor is found by assuming that the peak in the integrated signal height distribution occurs at the ADC count corresponding to the passage of a single particle through the detector and that the pulse height and ADC count is proportional to the number of particles passing through the detector. In a similar way, raw times, represented by 6 ASCII characters, are converted to 8 byte reals. These raw times are those at which the signals from the detectors were recorded at the electronics housed in the central hut and must be corrected to the arrival time of the particles at the detectors by subtracting the delays associated with photomultipliers, cables, TDCs and discriminators which are each different for different detectors.

The MR, day time, date and pressure, also encoded as strings of ASCII characters, are converted to numerical representation, with MR and temperature as 8 byte real numbers and the remainder as 4 byte integers. 5 characters in the string are reserved for recording air temperature, though these have yet to be used. It seems likely that there exists a correlation between event rate and air temperature (Section 2.5.2) and it is certain that the value of the Molière unit is a function of temperature. It would, therefore, be useful to record the temperature in the event record. For each event, this information along with the final trigger times and particle densities are written to a Pascal record of 1192 bytes. The rate information is also extracted from the DQ file and tabulated in a human readable form.

Some additional diagnostic information is also written to the Pascal record of each event. The reliability of the MR is determined by comparing it to the day time which is obtained from an independent clock. In addition, the event rate is monitored at this stage, and gaps in the data or apparent 'backward' going MRs are flagged. Changes to

the array and problems with the array, such as a detector being disconnected or ADC's or TDC's being unreliable, are signalled at this stage with Boolean flags in the event record, and the heights and/or times replaced by default values accordingly.

3.3 Data Analysis

The data analysis takes place in 2 stages. The first is to find an approximate arrival direction and core position and the second is to refine the arrival direction and produce a compressed summary of each event that is readily accessible for source searches.

3.3.1 CORE SEARCH

The core of an air shower is the region in which the density of particles is greatest. It lies on the axis of the shower disk and is the centre of symmetry of the disk in the plane perpendicular to the axis (the 'shower plane'). The shower front curvature is known as a function of the distance from this core, and only by allowing for this curvature, can an accurate shower arrival direction be found. It is therefore necessary to obtain an accurate core position to calculate the expected arrival times of the particles at the detectors for a given direction.

3.3.1.1 Fitting of observed densities to expected

The core position of an air shower is found by fitting the observed densities to the expected lateral distribution function (l.d.f.) of particles. The predicted density at a distance of R metres from the core is given by:

$$S_e = kf(R) \qquad \dots \text{Eqn 3.1}$$

where k is a size parameter of the shower and f(R) is given by:

$$f(R) = \left(\frac{R}{R_0}\right)^{s-2} \left(1 + \frac{R}{R_0}\right)^{s-4.5} \quad \dots \text{Eqn 3.2}$$

where s is the 'age' or steepness of the l.d.f.. A young shower with small s has a steep lateral distribution compared to older showers. The determination of shower age and its possible use in distinguishing between nucleonic cosmic ray and γ -ray induced air showers is discussed in greater depth in chapter 4. R_0 is the rms lateral distance through which electrons are Coulomb scattered in traversing 1 radiation length (the 'Molière' unit). R_0 is dependent on the air density and hence on temperature and pressure and was discussed in Section 1.4.

The l.d.f. gives the expected density of charged particles as a function of radial distance from the shower core in the *shower* plane. It is therefore necessary to transform the coordinates of the detectors into a plane parallel to the shower plane. To achieve this, an approximate arrival direction is found by fitting a plane shower front to the detectors with the 4 largest densities and the transformation made into a plane perpendicular to this direction. No knowledge of the core position is required for this type of fit. This approximate arrival direction used to find the shower plane naturally leads to an error in the core position (coordinates (x_1, y_1)) found in this way. Repeated iterations using the refined direction to obtain the shower plane and hence core position would obviously minimise this error, but would be rather time consuming. The rms shift in direction between the 'first try' direction, (θ_1, ϕ_1) , and refined direction, (θ_2, ϕ_2) , is $\sim 4.8^\circ$. When the refined direction is used to obtain the shower plane and hence an improved core with coordinates (x_2, y_2) , the rms distance between this core and the one found using the approximate shower plane is 6m. However, in 90% of showers the shift is less than 3m, the rather large rms shift being due to the long tail in the distribution which is shown in Figure 3.1(i). The effect on the final direction of using the approximated plane fit to find the core position can be seen by calculating the space angle between (θ_2, ϕ_2) and (θ_3, ϕ_3) , the refined arrival direction obtained using the improved core, (x_2, y_2) . The integral frequency distribution of these space angle shifts is shown in Figure 3.1(ii). 90% of events have their arrival direction shifted by less

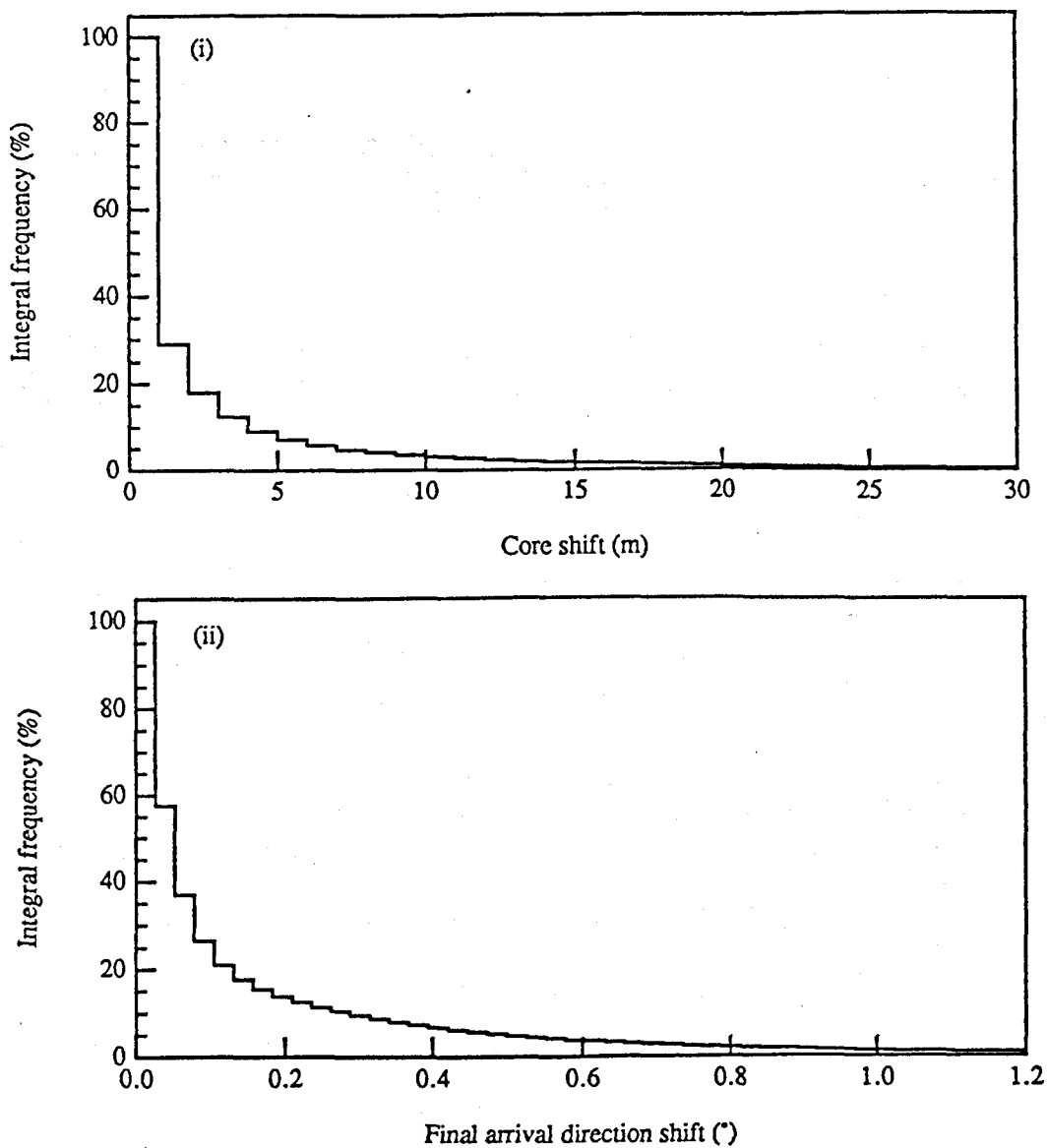


Figure 3.1 (i) and (ii) The integral distributions of, respectively, the core shifts and final arrival direction shifts due to using the first try plane fit arrival direction to find the shower plane used in the core finding algorithm.

than 0.3° which is seen to be insignificant when added in quadrature with the total angular resolution ($\sim 1^\circ$).

The fit of the l.d.f. to the observed densities is achieved by minimising χ^2 , the goodness of fit parameter, given by:

$$\chi^2 = \sum_i \frac{(S_e(R_i) - S_i)^2}{\sigma_i^2} \quad \dots \text{Eqn 3.3}$$

where S_i is the observed density at the i th detector, $S_e(R_i)$ is the expected density for a detector R_i meters from the core and σ_i is the uncertainty in the predicted density at detector i .

The uncertainty, σ , in the densities was determined empirically by J. Perrett (1986) who compared densities measured in each of two side by side detectors and is given by:

$$\sigma = 0.77 S^{0.615} \quad \dots \text{Eqn 3.4}$$

which corresponds to fluctuations less than Poissonian ($\sigma = S^{0.5}$) for densities less than ~ 10 particles/m². Low energy photons lose energy rapidly within scintillators by producing electron /positron pairs which are subsequently absorbed or by Compton scattering. They may, therefore, produce a signal in the scintillator which is considerably lower than that produced by a single high energy charged particle passing straight through the detector. Low energy electrons that are completely absorbed within the scintillator will also produce a similar response, so that a total signal corresponding to a density of only a few particles may be the result of contributions from a very much larger number of low energy photons and charged particles. The fluctuations in such signals, then, are expected to be less than those due to Poisson fluctuations in the equivalent density for particles passing through the detector. For the purpose of minimising χ^2 , the predicted densities are used to calculate the density weights, since for a detector at a fixed distance from the core in a shower of given size, the spread in observed densities is equal to the uncertainty in the predicted density.

3.3.1.2 Saturated and below Threshold densities

Since the density at a detector is not well known when the tube is saturated (≥ 45 particles) or when the density is below the D1 threshold (≤ 0.3 particles), equation 3.3 is of little use in determining how well these densities fit the predicted densities. It is, however, possible to evaluate the probability, P of observing such a density for a given expected density, S_e . If the distribution of densities around the expected density is assumed to be Gaussian, the width of which, σ_{S_e} , is given in equation 3.4. the approximate probability of observing a density above saturated density, S_{sat} , is then given by

$$P(>S_{sat}) = \frac{1}{\sqrt{2\pi} \sigma_{S_e}} \int_{S_{sat}}^{\infty} \exp\left(\frac{-(S-S_e)^2}{2\sigma_{S_e}^2}\right) dS \quad \dots\text{Eqn 3.5}$$

similarly, for densities below threshold, ρ_{thresh} ,

$$P(<S_{thresh}) = \frac{1}{\sqrt{2\pi} \sigma_{S_e}} \int_{-\infty}^{S_{thresh}} \exp\left(\frac{-(S-S_e)^2}{2\sigma_{S_e}^2}\right) dS \quad \dots\text{Eqn 3.6}$$

These probabilities can be converted into χ^2 contributions, $\Delta\chi^2$:

$$\Delta\chi^2 = -2\ln P \quad \dots\text{Eqn 3.7}$$

For large expected densities, the spread in observed densities is caused mainly by Poissonian fluctuations in the number of particles passing through the detector. This distribution is well approximated by the assumed Gaussian distribution. For small expected densities, below a few particles, the instrumental contribution to the spread in observed density, due to the large range of impacts on, and paths through the scintillator of individual particles, becomes more important. In addition, as explained in the previous section, small signals are comprised of contributions from many low energy photons and charged particles. For these reasons a Poisson distribution of densities is not assumed for small expected densities but rather a Gaussian distribution

3.3.1.3 χ^2 minimisation algorithm

The core position and size of an air shower are obtained by minimising χ^2 as a function of these parameters. The shower size parameter, k , for a given core position, (x_c, y_c) , is given by:

$$k = \frac{\sum_i \frac{S_i f(R_i)}{\sigma_i^2}}{2 \sum_i \frac{f^2(R_i)}{\sigma_i^2}} \quad \dots \text{Eqn 3.8}$$

and is the analytic solution for the equation

$$\frac{\partial \chi^2}{\partial k} = 0 \quad \dots \text{Eqn 3.9}$$

The shower size parameter in terms of the number of particles at sea level, N , is given by

$$k = \frac{N}{R_0^2} C(s) \quad \dots \text{Eqn 3.10}$$

where $C(s)$ is given by

$$C(s) = \frac{\Gamma(4.5-s)}{2\pi \Gamma(s) \Gamma(4.5-2s)} \quad \dots \text{Eqn 3.11}$$

The more usual parameter used to describe shower size at Haverah Park is the density at 50m from the shower core, $S(50)$, given by

$$S(50) = kf(R) \quad \dots \text{Eqn 3.12}$$

with $R = 50\text{m}$. $S(50)$ is chosen as a suitable shower parameter, as showers of the same size, but different ages, will have approximately the same density at 50m from the core.

The problem of finding the shower core is reduced to the minimisation of χ^2 in two dimensions. The χ^2 surface for a particular shower is shown in Figure 3.2. It can be seen that the surface is extremely complicated. There is a peak in the surface at each detector which reflects the singularity in the N.K.G. function at $R=0$, where the expected density is infinite. A trial core placed close to a detector will cause a very large density to be predicted in that detector and give a large contribution to χ^2 . These peaks cause long, narrow valleys between detectors and local minima.

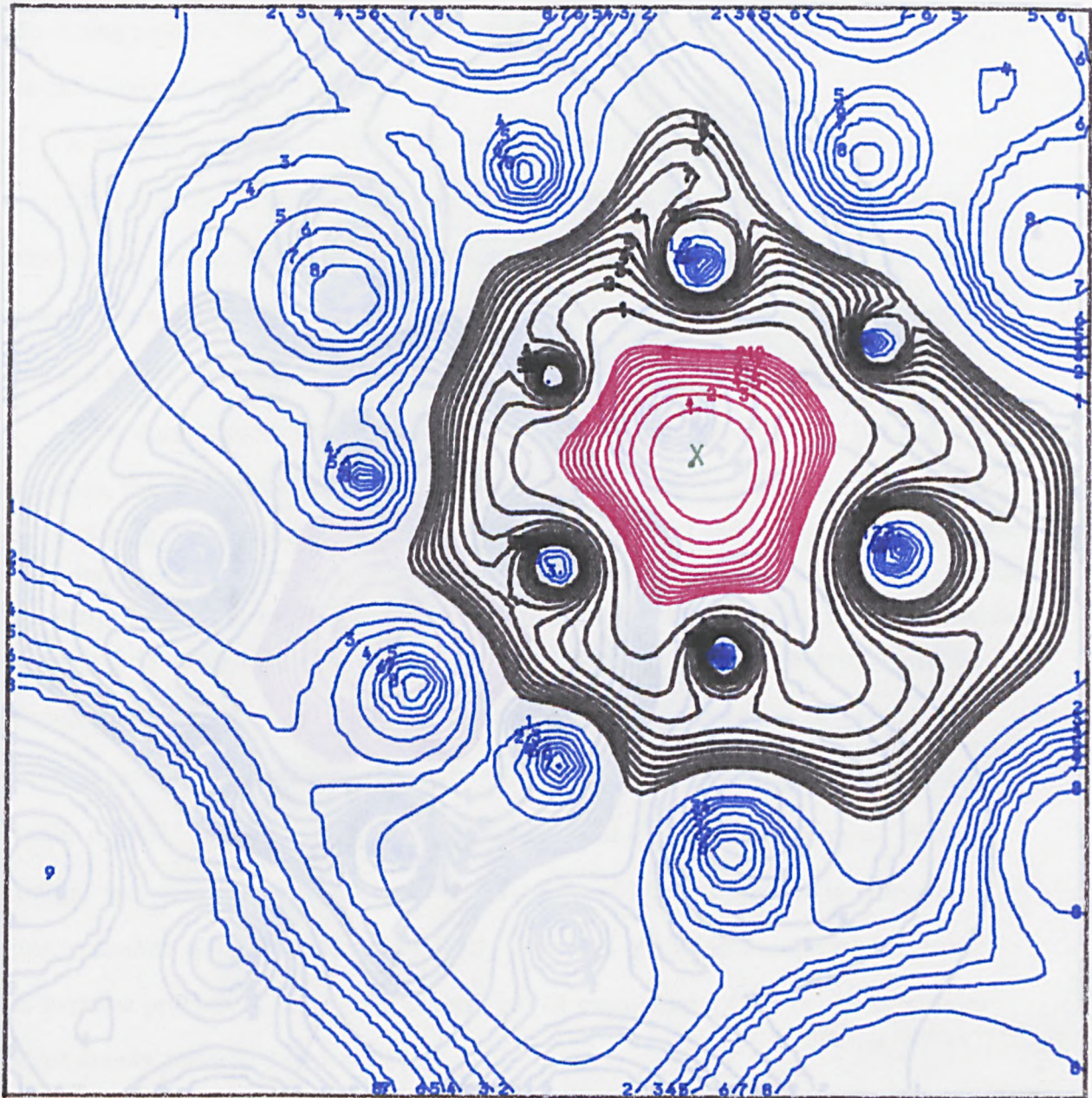


Figure 3.2 A contour plot of normalised χ^2 as a function of trial core position. The minimum in χ^2 is marked by the 'x'. The value of the contours increases from red through black to blue. The peaks at the detectors are caused by the singularity in the NKG function at $R=0$.

The simplest method of finding the χ^2 minimum is a grid search method, where χ^2 is evaluated at every node on a large, close spaced grid and selecting the point at which χ^2 is minimum as the true core. This method enables the minimum to be found to any degree of accuracy. However, many evaluations of χ^2 are required and this is a very time consuming process. For the purpose of routine analysis of GREX events such a grid search is impractical due to time constraints.

A more efficient method of minimisation is to evaluate χ^2 at a small number of points and find the minimum by extrapolation. A search is started at some point and continues in a direction such that χ^2 decreases (the 'downhill' direction) until the minimum is reached. The method can be optimised by choosing a good starting trial core and an efficient algorithm for moving in a downhill direction.

As a core is most likely to have landed near the detectors with the highest densities, the initial trial core is chosen to be the centre of gravity of the triggered detectors weighted with the square of their densities. Table 3.1 shows a comparison of centre of gravity cores where the triggered detectors' coordinates for each core have been weighted with different powers of the measured densities. For each weighting, the mean distance between the starting core and the minimum in χ^2 , ΔR is found on a sample of ~ 16500 showers. The weightings S^2 and $S^{2.5}$ get closest to the minimum in χ^2 of all the weightings. The use of S^2 weighting, however, while not giving significantly better results than $S^{2.5}$, may be justified by the fact that it is faster to compute. While a straight forward S^1 weighted centre of gravity would be even faster to compute, a greater amount of time would subsequently be lost in χ^2 minimisation which, being an iterative process, is more CPU intensive than calculation of the centre of gravity which is only performed once per event.

Having found the starting core, the subsequent minimisation consists of an iteration in 2 parts. Each step consists of (a) calculating the local gradient and choosing a direction vector, \mathbf{n} , in which χ^2 tends to decrease and (b) finding the point which has the minimum value of all the points on the vector \mathbf{n} , this point being known as the line minimum. The steps in the algorithm are best illustrated by a flow diagram, Figure 3.3.

n	ΔR	$\sigma_{\Delta R}$
0.5	23.3 ± 0.1	15.7
1.0	15.6 ± 0.1	11.5
1.5	10.9 ± 0.1	9.3
2.0	9.4 ± 0.1	8.2
2.5	9.4 ± 0.1	7.7
3.0	9.9 ± 0.1	7.7
3.5	10.5 ± 0.1	7.9
4.0	11.1 ± 0.1	8.1
4.5	11.5 ± 0.1	8.3
5.0	11.9 ± 0.1	8.6

Table 3.1 Comparison of centre of gravity cores. n is the power of the measured density used to weight the triggered detectors' coordinates and ΔR is the mean distance between the trial core and the position of the true minimum in χ^2 .

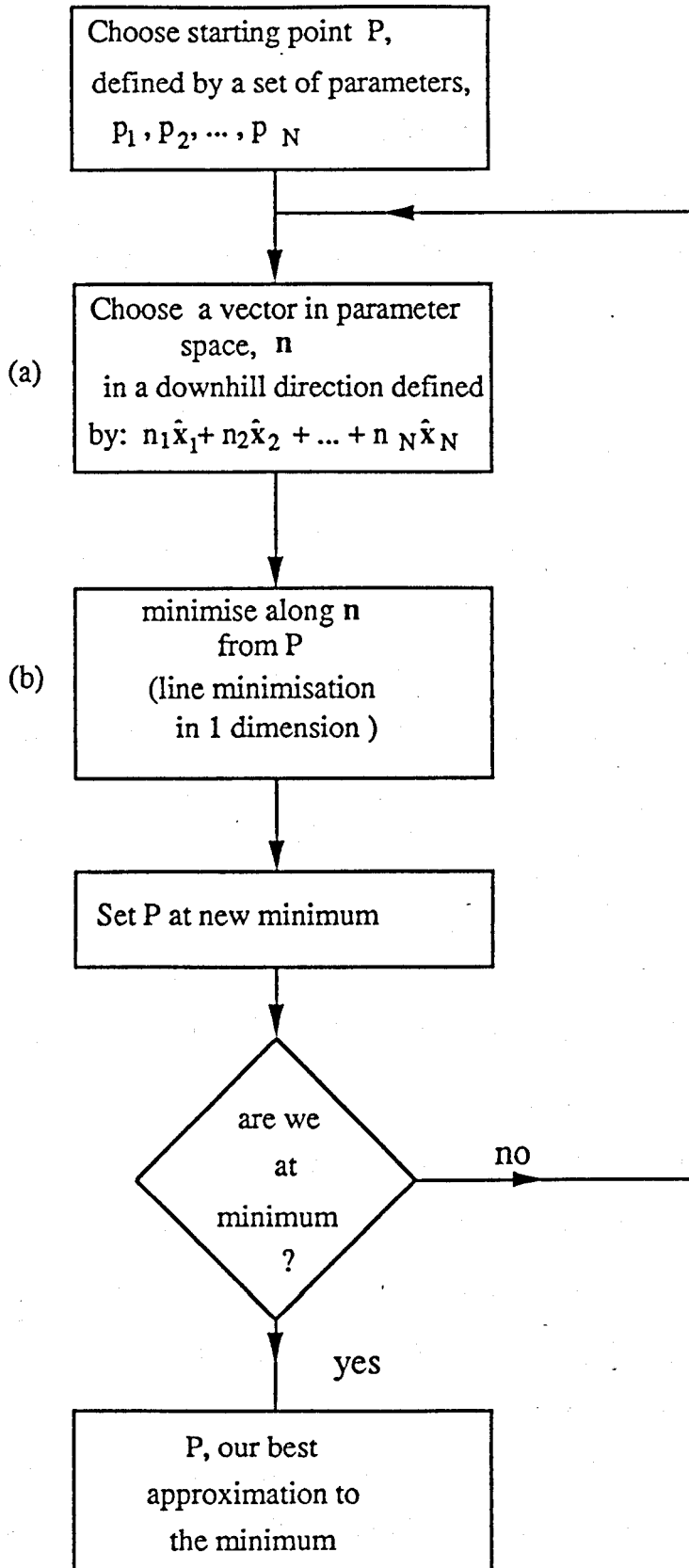


Figure 3.3 Flow diagram of χ^2 minimisation algorithm used in the determination of core positions.

3.3.1.4 Choice of the direction vector, n

The most obvious direction along which to move from any given point to minimise a function in two dimensions is the direction of steepest descent, ie the one in which the rate of decrease in the function is maximum. At some point, (x_i, y_i) , in an arbitrary function, f , this is given by:

$$g_i = -\nabla f(x, y) \Big|_{x_i, y_i} = -\hat{x} \frac{\partial f}{\partial x} \Big|_{x_i, y_i} - \hat{y} \frac{\partial f}{\partial y} \Big|_{x_i, y_i} \quad \dots \text{Eqn 3.13}$$

where \hat{x} and \hat{y} are unit vectors in the x and y directions.

Having begun a minimisation at a point, (x_1, y_1) , and moved to the line minimum in the direction of steepest descent, g_1 , (x_2, y_2) , the new direction of steepest descent, g_2 must now be perpendicular to g_1 . There can be no component of gradient along g_1 , since the gradient of the projection of f along g_1 at (x_2, y_2) is zero by definition of the line minimum.

Hence, a steepest gradient search will consist of a large number of steps, each of which will be constrained to be perpendicular to the last. In traversing a long narrow valley, Figure 3.4, this method *may be found to be* extremely inefficient. The problem arises from the fact that the line minimum of the first step, n_1 , will not (unless n_1 is perpendicular to the length of the valley) be at the base of the valley, but slightly off it. The next step being at a right angle to the first will cross the base of the valley and begin to ascend the slope just descended. The motion along this vector, however, will always be in a downhill direction as the rate of *descent* due to the component of the vector *along* the valley will be greater than the rate of *ascent* due to the component *perpendicular* to the length of the valley until the line minimum is reached. A steepest descent algorithm may, therefore, take many steps in traversing a long narrow valley and is thus wasteful of machine time.

The conjugate gradient method (Press *et al.* 1986) introduced in the GREX analysis is, in general, a more efficient minimisation algorithm. Each step is constructed

from the last, and the present gradient so as not to 'spoil' the previous minimisation. This requirement is satisfied by the constraint that the change in gradient, $\delta\nabla f$, along the direction moved is perpendicular to the last direction moved. ie

$$\mathbf{n}_{i-1} \cdot \delta\nabla f_{\mathbf{n}_i} = 0 \quad \dots\text{Eqn 3.14}$$

If two vectors, \mathbf{n}_{i-1} and \mathbf{n}_i along which the change in gradient $\delta\nabla f_{\mathbf{n}_i}$ occurs, satisfy this condition, they are known as mutually conjugate vectors. For any arbitrary function, it is not possible to predict the way in which the gradient will change on moving along any given direction when all that is known are the gradients from the present and previous iterations. However, by approximating the function to a quadratic, the change in gradient along any particular direction can be calculated from this information, and a vector, \mathbf{n}_i , found which satisfies equation 3.14. In this way a series of vectors, \mathbf{h}_i , can be constructed, each of which is conjugate to the last:

$$\mathbf{h}_i = \mathbf{g}_i + \gamma_{i-1} \mathbf{h}_{i-1}, \quad \dots\text{Eqn 3.15}$$

where \mathbf{g}_i is the direction of steepest descent and γ_{i-1} is constructed from the present gradient and that of the last iteration as:

$$\gamma_{i-1} = \frac{(\mathbf{g}_i - \mathbf{g}_{i-1}) \cdot \mathbf{g}_i}{\mathbf{g}_{i-1} \cdot \mathbf{g}_{i-1}} \quad \dots\text{Eqn 3.16}$$

For the first iteration, the direction chosen along which to minimise is that of the steepest descent. Subsequent directions are then each, in turn, calculated from the previous according to equation 3.15. An algorithm selecting vectors in this way will find the minimum of a perfectly quadratic function of N parameters in just N steps. For less simple functions, the algorithm will converge quadratically on the minimum.

3.3.1.5 Line minimisation

Line minimisation is the second stage in each iteration leading to the minimum of the function. Having chosen some vector, \mathbf{n}_i , along which to move, the point on that vector at which the function is least is found. By assuming that the starting point on \mathbf{n}_i

is close to the real line minimum, and not some local minimum, the projection of the function along the vector, n_i , is approximated to a parabola. The position of the minimum of this parabola is found by interpolation, and is a good approximation to the true line minimum (Figure 3.5). The function is evaluated at three points along the vector, a , the starting point, b , and c .

By solving the 3 simultaneous equations that arise from substituting the three values of x and the corresponding values of the function into the general form of a quadratic equation, the coefficients can be calculated. The line minimum is obtained by imposing the condition

$$\partial f/\partial x = 0 \quad \dots\text{Eqn 3.17}$$

and is given by:

$$z = b - \frac{(b-a)^2[f(b)-f(c)] - (b-c)^2[f(b)-f(a)]}{2\{(b-a)[f(b)-f(c)] - (b-c)[f(b)-f(a)]\}} \quad \dots\text{Eqn 3.18}$$

This is a general solution for the point on the line at which the gradient is zero, which is also the case at a maximum. When the surface is convex, therefore, it is necessary to ensure that the algorithm does not step in an uphill, rather than a downhill, direction to the top of a peak.

In the general case, where the function to be minimised is not perfectly parabolic, this interpolation will converge, with repeated iterations on the line minimum.

As has already been stated, it is necessary to assume that the starting point on the vector, n_i , is sufficiently close to the line minimum and not separated from it by a local minimum. In the case of χ^2 minimisation applied to core searching, this is normally true for a good choice of starting core. In addition the intervening peaks may be caused by local anomalies such as the singularity in the N.K.G. function at $R=0$. In this situation, evaluating the function at positions close to a trial core may predict the shape of the function along the vector in the absence of these peaks and, indeed, still give a good estimate of the position of the true line minimum.

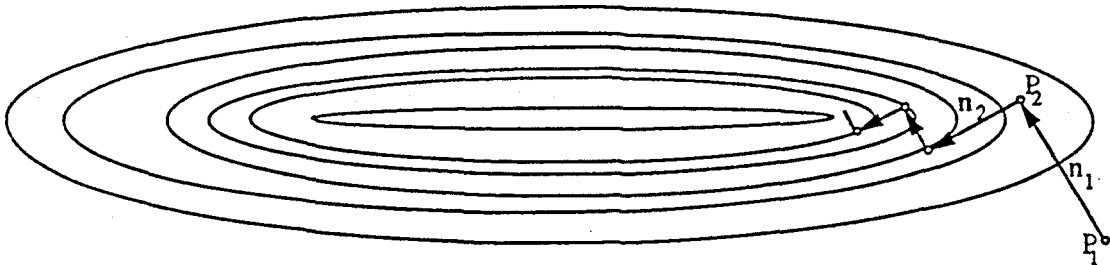


Figure 3.4 Steepest descent method of traversing a long narrow valley. Each step is constrained to be perpendicular to the last.

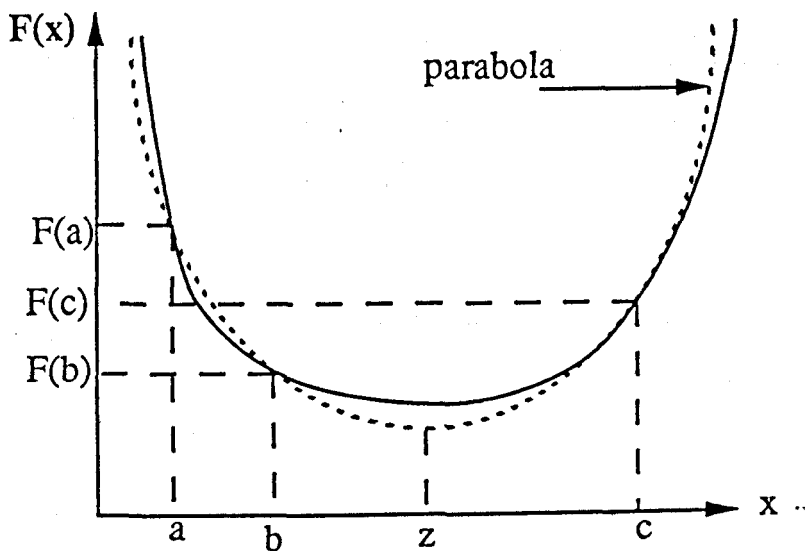


Figure 3.5 Inverse parabolic interpolation used to find the minimum of a function of a single variable. A parabola is fitted to three points, a , b , and c on the function $f(x)$. The position of the minimum of that parabola is a good approximation to the position of the minimum of the function.

3.3.1.6 Minimisation applied to core search

The core finding procedure of the GREX analysis consists of a conjugate gradient search with a one step parabolic interpolation as described in the previous sections. A number of other features are also included to make it more robust.

The value of χ^2 at each intermediate core is checked to ensure that it is less than the previous minimum. Should this not be the case, the previous minimum is returned to, the direction of steepest descent chosen along which to minimise, and the distances between points used to find the line minimum by interpolation are reduced. As explained in the previous section, it is necessary to check that the surface is not convex and that the line maximum is not found, rather than the minimum. In this case, the core would be placed in the uphill, $-n$, direction, of the starting core. This possibility is tested for, and, if found to be true, the new core placed at c , (Refer to Figure 3.5 for notation) as this would be the point at which the lowest value of χ^2 had been found so far. It is necessary to limit the amount of time spent looking for the core of each event to enable all events to be analysed within the CPU time available on the Amdahl. This is achieved by demanding that the change in χ^2 for 2 iterations of the algorithm is greater than 67% for subsequent iterations to take place. In this way minimisation of χ^2 will only continue to take place if the χ^2 surface is steep, and the algorithm is making rapid progress towards the minimum. In general, this leads to the program making only 2 steps towards the minimum. Naturally, this leads to inaccuracies in the core position. These inaccuracies, along with those inherent in the χ^2 minimisation technique itself are described in the following sections.

3.3.1.7 Accuracy of core position

The errors in the core position have contributions from two essentially independent sources. Limitations on the amount of CPU time spent in finding the minimum in χ^2 means that the core position assigned to each shower is frequently

several metres from the true minimum (Section 3.3.1.9). In addition to this error, there is an un-avoidable statistical uncertainty in the position of the minimum and how close that minimum is to the true shower core (Section 3.3.1.8). This last uncertainty puts limitations of the technique of χ^2 minimisation itself, whatever the chosen method of finding the minimum. The two errors may be added in quadrature to determine the total uncertainty in the core position found using the method described.

Errors in finding the core position are important in that they lead to uncertainties in the final arrival direction assigned to the shower. This will be discussed in Section 3.3.2.4 after the arrival direction determination has been described. The errors described in each section were determined for a set of ~ 17000 showers for each of the four 'operational eras' of the GREX array which are described in detail in chapter 2 and summarised in Table 2.1. The selection criteria used for these showers were the same as those used in source searches: (i) $S(50) > 0.2 \text{ m}^{-2}$, (ii) Shower cores lying inside array boundaries only, (iii) There must be at least 5 detectors within 80m of the core having density $\geq 1.25 \text{ m}^{-2}$. These criteria select $\sim 60\%$ of all showers striking the array. In addition to these criteria, all shower parameters are checked to ensure that they are within sensible physical limits.

3.3.1.8 Statistical uncertainty in χ^2 minimum

When obtaining physical parameters by fitting a function to observed data, fluctuations in that data naturally lead to errors in the determined parameters. According to Lampton et al. (1976), the standard errors in the parameters derived by minimising χ^2 are given at the $(\chi^2_{\min} + S_p)$ level in the *un-normalised* χ^2 surface, where χ^2_{\min} is the minimum value of χ^2 and S_p is a number whose value is dependent only on the number of dimensions, P , in which minimisation takes place, or the number of parameters determined by the minimisation. Hence, for a given minimisation, an appropriate value of S_p is chosen according to the number of parameters involved and, in 68% of all experiments, the true values of the parameters will lie within the $(\chi^2_{\min} + S_p)$ contour.

In the case of the core search algorithm, χ^2 is minimised to determine 3 parameters, the x and y coordinates of the core position and k, the size parameter. Hence $P=3$ and according to Lampton et al., $S_3=3.5$. Thus, the uncertainty in core position for any particular shower is given by the radius of the $(\chi^2_{\min} + 3.5)$ contour in the x,y plane.

The statistical uncertainties, ΔR_{STAT} , were determined on the four sets of showers described in the previous section. The position of the minimum in χ^2 , (x_{\min}, y_{\min}) , for each shower was determined by repeated iterations of the algorithm described above, and checked by a grid search. The distance to the $(\chi^2_{\min} + 3.5)$ contour was determined in four directions, the positive and negative x and y directions. The statistical error in (x_{\min}, y_{\min}) was the set to the mean of these 4 distances. The integral frequency distribution of these errors for the 36 detector period is shown in Figure 3.6. The shape of this distribution is typical of showers of all eras. The rms statistical errors in core positions are shown for each era in Table 3.2. It is somewhat surprising that the increase in the dynamic range of the ADC's which accounts for the difference between the first and second operational eras actually leads to an increase in the statistical uncertainty in the χ^2 minimum. The reduction in the core position uncertainties with the addition of lead implies a reduction in density fluctuations. These fluctuations have yet to be measured for the lead covered detectors. Such measurements would optimise still further the core location analysis, though the improvement would be expected to be marginal. The extra 4 detectors in the array reduce ΔR_{STAT} still further as the mean separation of the detectors is reduced (see below).

It is to be expected that the shape of the χ^2 surface and hence the statistical error in (x_{\min}, y_{\min}) is dependent on the number and configuration of triggered detectors as well as on the size and orientation of the shower. A convenient method for describing the configuration of triggered detectors was developed by Bloomer (1990), who classified showers into 'patterned' and 'un-patterned'. 'Patterned' showers are those in which at least 5 of the triggered detectors lie on the same sub-array of 30m or 50m detector spacing. Such a shower would be expected to give accurate shower arrival directions due to the good geometrical arrangement of the timing detectors. 'Un-patterned'

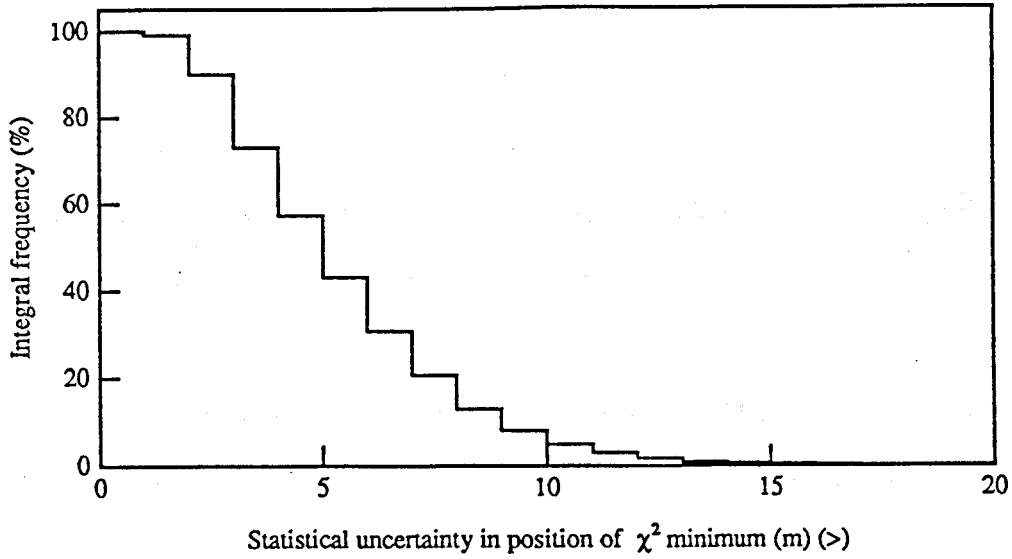


Figure 3.6 Integral frequency distribution of statistical errors in the position of the χ^2 minimum obtained from the radius of the $\chi^2_{\min} + 3.5$ contour in the χ^2 surface.

era	mean ΔR	RMS ΔR	$\sigma_{\Delta R}$
1	6.08 ± 0.02	6.73	2.88
2	6.40 ± 0.02	7.20	3.31
3	5.33 ± 0.02	6.07	2.92
4	4.92 ± 0.02	5.62	2.71

Table 3.2 Mean statistical uncertainties, ΔR , in the position of the χ^2 minimum for events from each operational era.

showers are ones in which the triggered detectors tend to be strung out in a line so that measurement of the arrival direction is difficult. 'Patterned' showers are subdivided into 7 types according to the number of triggered detectors and the spacing of the sub-array on which those detectors lie. The definitions of the pattern types are given in Table 3.3, along with the rms statistical errors for showers of each pattern type for the 4 eras. The errors are seen to decrease with the increase in the number of triggered detectors. This is a direct result of the increase in the amount of information from which the position of the minimum may be calculated. It is also evident that when triggered detectors lie on a 30m grid (30m triggers), the core may be located more accurately than when the detectors lie on a 50m grid (50m triggers). Hence having detectors close to the core is advantageous in locating that core. Thus, there is a trade off between the potential decrease in the arrival direction error due to timing uncertainties and the *reduced* accuracy of the the core location in increasing the spacing of detectors (Section 3.3.2.4). Un-patterned showers show the greatest uncertainty in (x_{\min}, y_{\min}) of all as the core is unlikely to be surrounded by detectors and will, therefore, be difficult to locate.

The shower size dependence of the statistical error in (x_{\min}, y_{\min}) was investigated by binning showers in equal increments of $\ln[S(50)]$. The mean statistical errors are shown plotted against $S(50)$ (calculated from the mean $\ln[S(50)]$ for each bin) for each era in Figure 3.7. In all but showers from the first operational era of the array, ΔR_{stat} decreases with shower size for showers with $S(50) > 1\text{m}^{-2}$. This is due to both the increase in the number of triggered detectors and the reduction in the fractional uncertainty of the larger densities measured in those detectors. Although these effects also tend to reduce the uncertainty in core locations for showers from era 1, they are compensated for by the effect of saturated densities. During this period, the dynamic range of the ADC's only allowed densities of up to 20m^{-2} to be measured accurately compared to subsequent eras when the saturated density was 45m^{-2} . The number of detectors measuring densities above saturated increases with shower size and reduces the accuracy of the core location. Naturally, this effect is greatest for the 1st era. Hence

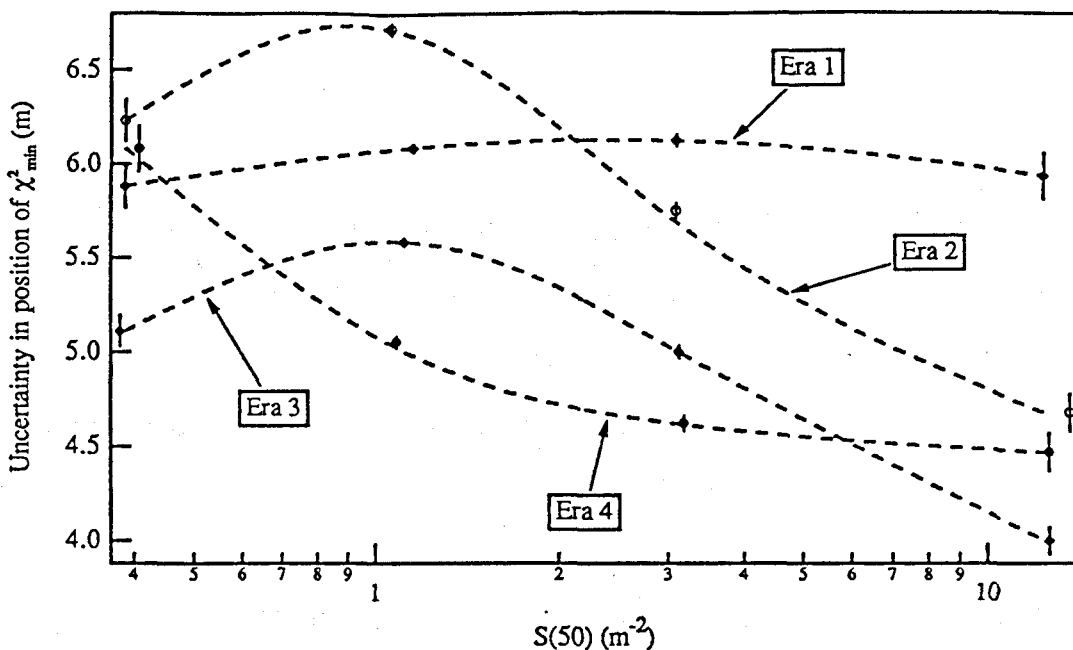


Figure 3.7 Statistical errors in the position of the χ^2 minimum are shown plotted against size ($S(50)$) for showers from each era. The broken lines are to guide the eye and do not represent the data between points

Pat. types	sub-array spacing(m)	N triggered detectors	RMS statistical error on core position			
			era 1	era 2	era 3	era 4
0	Un-patterned		8.86 ± 0.05	9.06 ± 0.04	7.52 ± 0.03	6.92 ± 0.04
1	50	7	4.78 ± 0.03	4.28 ± 0.03	3.37 ± 0.03	3.05 ± 0.04
2	50	6	5.27 ± 0.03	5.14 ± 0.04	4.14 ± 0.03	3.66 ± 0.05
3	50	5	6.32 ± 0.03	6.15 ± 0.04	5.56 ± 0.03	5.24 ± 0.04
4	30	7	3.63 ± 0.07	3.41 ± 0.08	2.60 ± 0.08	2.69 ± 0.07
5	30	6	4.66 ± 0.04	4.62 ± 0.05	3.76 ± 0.04	3.57 ± 0.05
6	30	5	5.59 ± 0.03	5.76 ± 0.04	4.91 ± 0.04	4.76 ± 0.04
7	Any other 7 fold		7.50 ± 0.05	7.61 ± 0.06	5.93 ± 0.06	5.29 ± 0.06

Table 3.3 The RMS statistical errors for showers of each pattern type and era are shown.

χ^2 minimum uncertainties for showers from this era show little dependence on shower size.

The slight increase in ΔR_{STAT} for showers of $S(50) \approx 1\text{m}^{-2}$ detected by the 32 detector array after the ADC change may be explained by the increase in the number of 50m triggers with increasing shower size. As previously shown, these showers have their core located less accurately than 30m showers. The effect is greatly reduced by the addition of the 4 detectors which reduce the mean separation of the detectors and reduce the fraction of events where triggered detectors are 50m apart.

The zenith angle dependence of the statistical uncertainties in core location was determined by binning the showers from each era in equal increments of $\sec \theta$ which represent equal increments in atmospheric depth that the showers have traversed. The general trends in the zenith angle dependence are illustrated by the graph in Figure 3.8 which shows the mean statistical uncertainties of the showers within each bin plotted against θ (calculated from the mean value of $\sec \theta$ within each bin) for the four operational eras. It can be seen that the statistical uncertainties in $(x_{\text{min}}, y_{\text{min}})$ for showers of all operational eras show a weak zenith angle dependence, being larger for showers of greater inclination. This theta effect is probably caused by the decrease in area of the detectors presented to the shower at larger zenith angles, and hence the decrease in observed densities for a shower of any given size and the increase in the fractional error in those densities.

3.3.1.9 Error in locating the χ^2 minimum

As previously explained, limitations imposed on the CPU time spent locating the position of the χ^2 minimum put additional restrictions on the accuracy to which the core positions of air showers may be determined in the routine analysis of GREX events. It is trivial, however to assess this additional error which will henceforth be referred to as the 'location error'. For a small sample of showers, it is possible to locate the precise χ^2 minimum, $(x_{\text{min}}, y_{\text{min}})$, as described in the previous section., The location error is

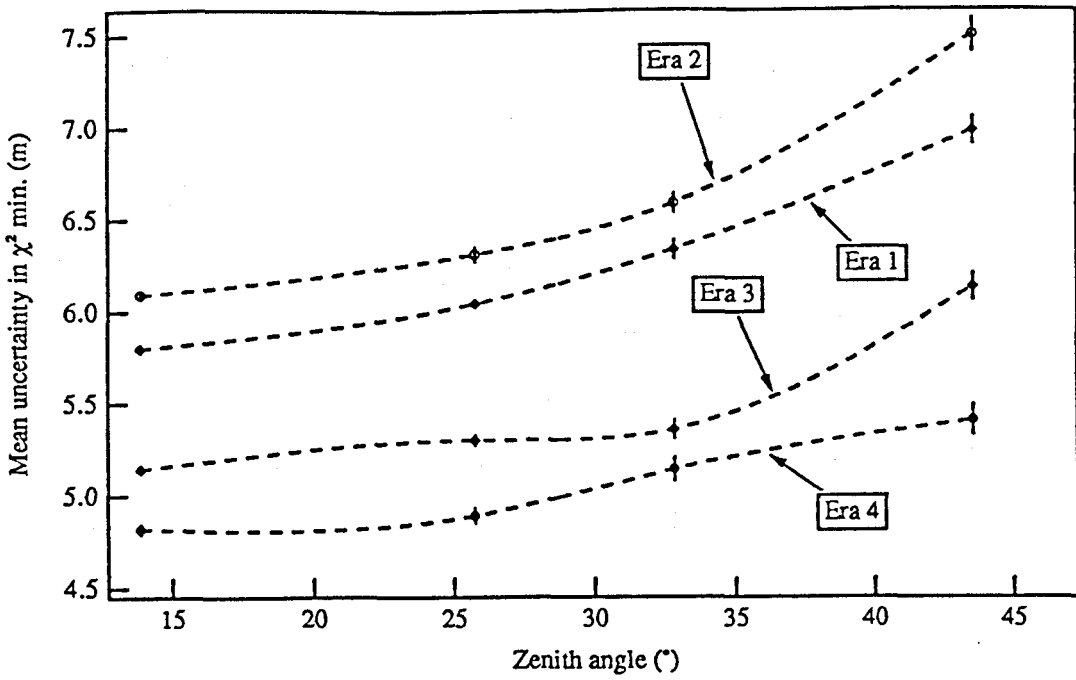


Figure 3.8 Statistical errors in the position of the χ^2 minimum are shown plotted against zenith angle for showers from each era.

Era	$\overline{(\Delta R)}$ (m)	ΔR_{RMS} (m)
1	8.15 ± 0.06	12.18
2	8.53 ± 0.06	12.36
3	7.73 ± 0.04	9.94
4	7.32 ± 0.04	9.23

Table 3.4 The mean and RMS errors in assigned core positions are given for showers from each era.

then the distance in the ground plane between the core position assigned to the shower in the analysis (x_a, y_a) and (x_{\min}, y_{\min}) . The histograms in Figure 3.9 shows the integral (i) and differential (ii) frequency distributions of location errors for the sample of ~ 16600 showers from the present era of the array.

It may be expected that the location error in a particular shower is correlated to the statistical uncertainty in the minimum. A large statistical error in the position of the minimum would indicate a rather flat χ^2 surface resulting in the minimum being difficult to locate. To test this hypothesis, showers were binned according to the statistical error in χ^2 minimum. Figure 3.10 shows the mean location error of showers within each bin plotted against the mean statistical uncertainty of those showers. It is seen that the location error does indeed increase with statistical error.

3.3.1.10 Total error in core location

The direction of the true core position from the χ^2 minimum is independent of that of the assigned core from the minimum. It is, therefore, possible to add the statistical error and the location error in quadrature for an individual shower to find the total expected error in the assigned core position, (x_a, y_a) . The total errors were found for the samples of showers for all eras. The mean and RMS errors in the assigned core positions for showers of different eras are shown in the Table 3.4. As demonstrated in the previous section, the magnitudes of the statistical uncertainties and location errors are positively correlated so that the shower type, size and theta correlations observed for statistical errors also exist for the total errors. More details of the expected errors in core location and how they result in directional uncertainties are given in Section 3.3.2.4.

3.3.2 FINDING AN ACCURATE ARRIVAL DIRECTION

The method for deriving an accurate shower arrival direction was developed by Bloomer (1990) and consists of an iterative process in essentially two stages: (a) for a

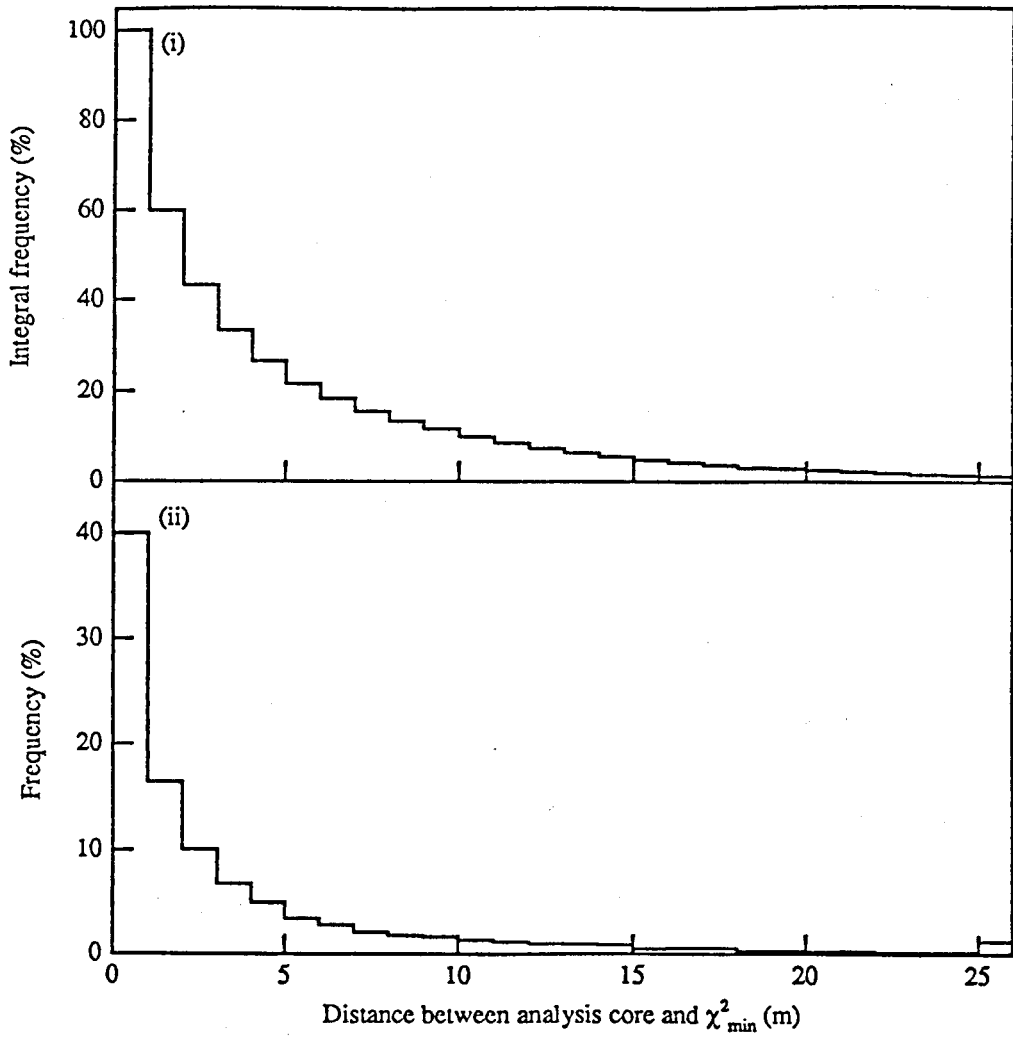


Figure 3.9 (i) and (ii) The integral and differential frequency distributions respectively of the distances between the position of the χ^2 minimum and the core location assigned by routine analysis. Showers are from the period during which the array consists of 36 lead covered detectors.

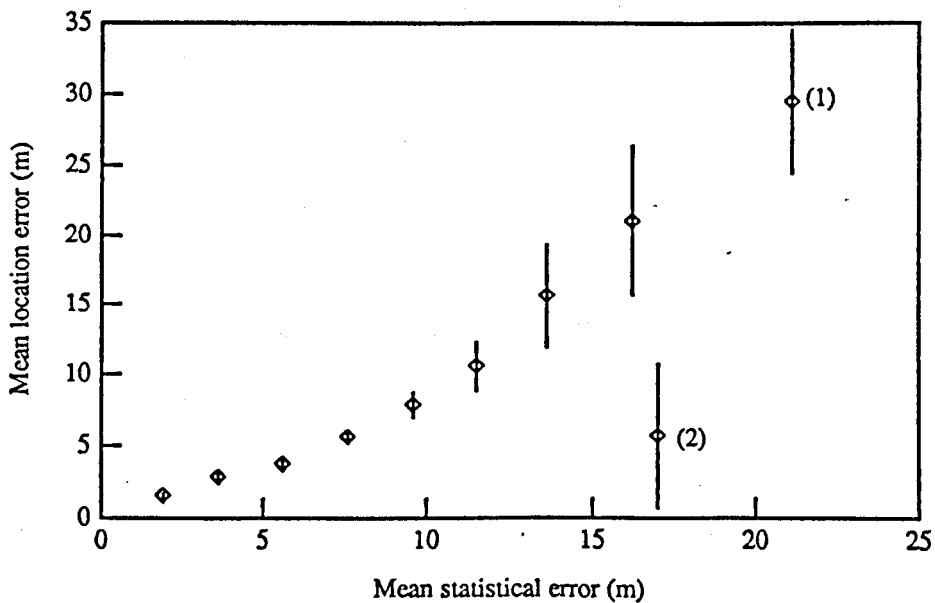


Figure 3.10 The mean distance between the analysis assigned core position and the minimum in χ^2 plotted as a function of the uncertainty in the position of the minimum.

given arrival direction, the shower front curvature is used to calculate the delays in the arrival times of the particles at each detector from the plane shower front. These delays are deducted from the observed arrival times, so that for a good choice of direction, the residual times are those at which particles travelling in a plane shower front would be expected to arrive at the detectors and (b) A new direction is now deduced by a weighted analytic fit of the residual times to a plane shower front. This process is repeated until the change in arrival direction between consecutive iterations is less than 0.004° in space angle. Both the shower front curvature and the weights used in the analytic plane fit were determined empirically by the author and S.Bloomer (1990).

3.3.2.1 Shower front curvature

The shower front curvature was found for the two eras of the array ;(i) 'Pre-lead' ie before lead was placed on the top of the detectors and (ii) 'lead' ie after the addition of lead. It was derived by fitting a plane shower front to the observed arrival times of 3 detectors all of which were approximately equidistant from the shower core. By symmetry, this arrival direction would be expected to be a good approximation to the true arrival direction, and would certainly not differ systematically from it. The difference in observed times of the remaining detectors and those expected for a plane shower front were then found. These time delays, Δt are parametrised by straight line fits to core distance, r , for a given observed density. Fits for densities of 1.5 and 5.5 are compared to observed time differences in Figures 3.11 (i) and (ii) for the un-covered and lead shielded detectors respectively. The time delay from the plane front varies between 7ns at 50m from the core for large densities of $\sim 10\text{m}^{-2}$ and 16ns at 50m for densities close to threshold (0.3m^{-2}). The gradients of these lines for the two periods decrease with density and are parametrised by assuming a linear relationship between $\ln(d\Delta t/dr)$ and $\ln(\text{density})$. For the unleaded era, this relationship is given by:

$$\ln(d\Delta t/dr) = -0.25\ln(S) - 1.45 \quad \dots\text{Eqn 3.19}$$

where S is the observed density and r the core distance.

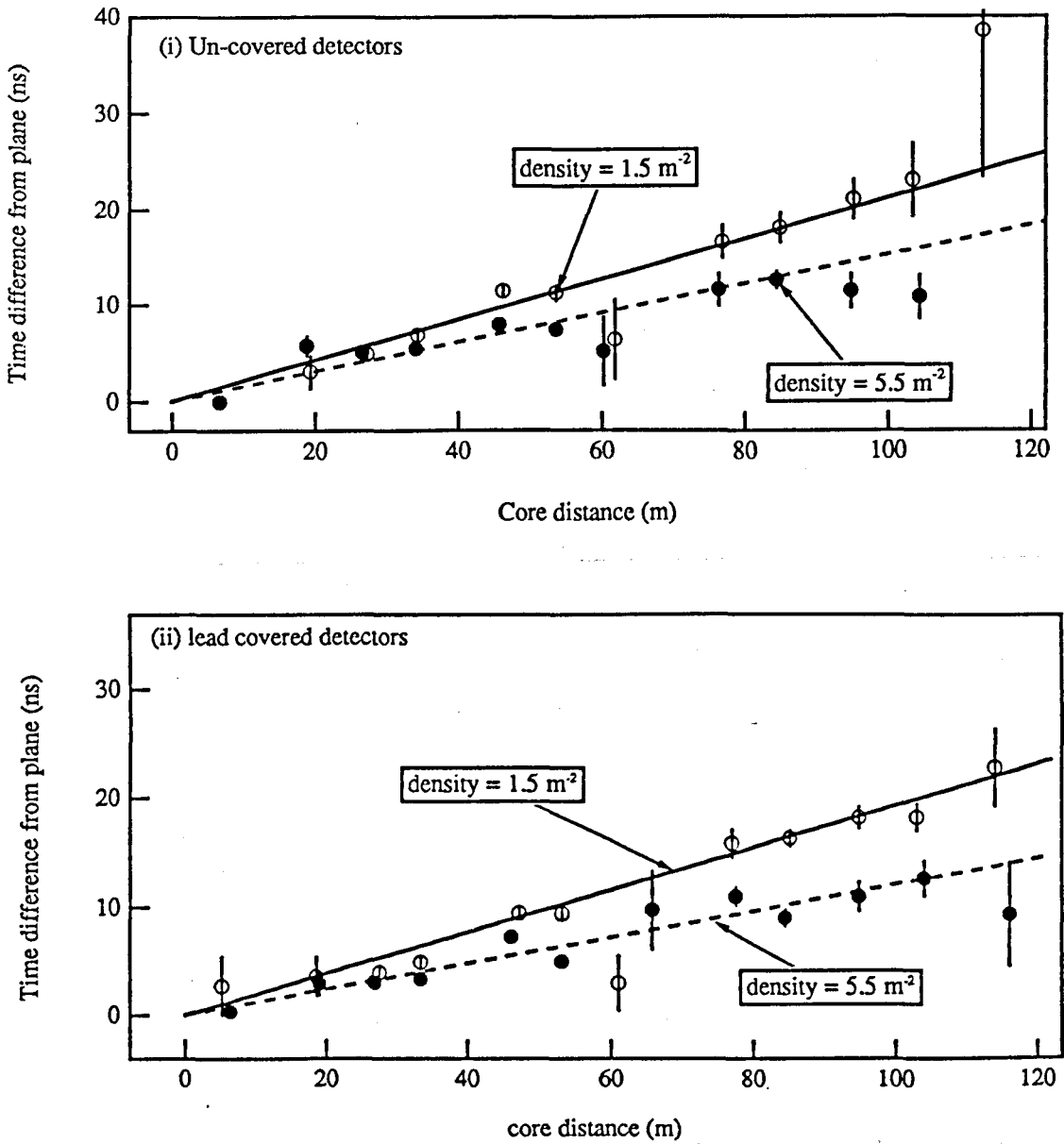


Figure 3.11 Plot of time delays from the plane against core distance for observed densities of approximately 1.5 m^{-2} (open circles) and 5.5 m^{-2} (filled circles) for showers from the unleaded array, graph(i) and lead covered array, graph (ii). The solid ($S=1.5 \text{ m}^{-2}$) and broken ($S=5.5 \text{ m}^{-2}$) lines are parametrisations of these delays.

This gives

$$\Delta t = r e^{-(0.25 \ln(S)+1.45)} \quad \dots \text{Eqn 3.20}$$

Similarly for the leaded period, the time delay is given by:

$$\Delta t = r e^{-(0.29 \ln(S)+1.51)} \quad \dots \text{Eqn 3.21}$$

As expected the lead covered detectors trigger on earlier particles (Section 2.2.1) than uncovered detectors so that the shower front appears less curved.

When these parametrisations are folded with the observed lateral distribution function for showers of a given size, the resultant predicted front is spherical at core distances ≤ 60 m becoming conical at larger distances. The observed time delays for showers of different sizes are compared to the predicted delays in the graphs in Figure 3.12 (i) and (ii) for the un-covered and lead-covered arrays respectively.

3.3.2.2 Determination of time weights

The timing uncertainties used in fitting the plane wave front to the curvature corrected arrival times of particles at detectors were determined empirically by the comparison of relative triggering times of the pair of side by side detectors, 15 and 16. The condition that only times for which both detectors recorded densities within 20% of each other were accepted for the compilation of statistics. The trigger time differences between 15 and 16 were binned as a function of the mean density in the two detectors and the distance of the detectors from the core in the shower plane. The shower plane was that obtained by the 'first try' plane fit to the times of the 4 detectors recording the largest densities. Each time difference was corrected for the expected time of flight difference of the shower particles at each detector due to the small spatial separation of the detectors and the inclination of the shower. For detectors 15 and 16 separated as they are by ~ 1 m this correction is up to 1.5ns for a shower inclined at 30° . The distribution of time delays at a distance of between 30m and 40m and density $\sim 1.5 \text{m}^{-2}$ is shown in Figure 3.13. The shape of this distribution is typical of all distance and density bins. A Gaussian of width equal to the standard deviation of the distribution is

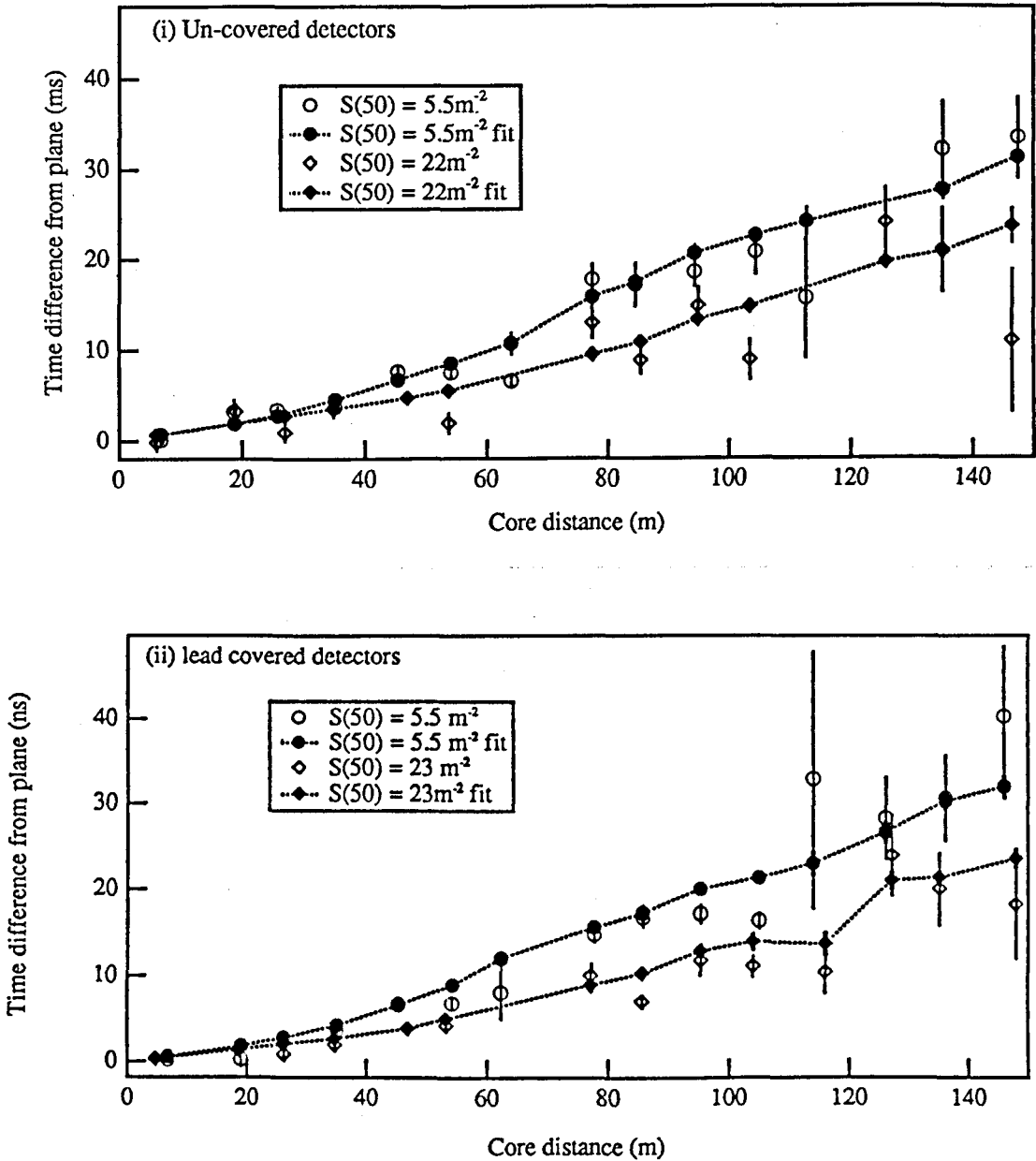


Figure 3.12 Plot of the observed (open symbols) and predicted (filled symbols) time delays from the plane against core distance for showers of approximate $S(50)$'s 5.5 m^{-2} (circles) and 23 m^{-2} (diamonds) for showers from the unleaded array, graph (i) and lead covered array, graph (ii).

shown by the solid line for comparison. The Gaussian is seen to be a poor fit to the bulk of the distribution. A better fit is obtained by using the standard deviation obtained using the 'range'. The standard deviation of the parent distribution of a variable can be obtained from the mean absolute difference of pairs of variables (the range of the distribution) drawn from this distribution. If we assume that the distribution of times at a fixed density and radial core distance is Gaussian, we obtain (Pugh-Winslow):

$$\sigma_t = \frac{\sqrt{\pi}}{2} \overline{|\Delta t|} \quad \dots \text{Eqn 2.22}$$

The uncertainty in the time difference is therefore

$$\sigma_{\Delta t} = \sqrt{2} \sigma_t \quad \dots \text{Eqn 3.23}$$

A Gaussian of this width is shown by the dashed line superimposed of the distribution shown in Figure 3.13 and is seen to be a better fit to the bulk of the data. The reason for this is that in the case where the parent distribution is not truly Gaussian, the uncertainty using the range technique is less sensitive to long tails in the distribution than finding the standard deviation directly. It is this standard deviation, σ_t , found by the 'range' technique that is used to determine the time weights. σ_t is parametrised in density and core distance in a similar way to the time delays for the leaded and unleaded eras as follows:

(a) un-leaded array:

$$\sigma_i(R,S) = \frac{\sqrt{\pi}}{2} [(R-30)P(S) - Q(S)] \quad \dots \text{Eqn 3.24}$$

where $P(S) = e^{-[0.51 \ln(S) + 2.04]}$

and $Q(S) = e^{-[0.76 \ln(S) + 1.79]}$

for $R < 30\text{m}$, $P(S)$ is set to $P(S)/2$

(b) lead covered array:

$$\sigma_t = R \exp^{-[0.642 \ln(S) + 2.347]} \quad \dots \text{Eqn 3.25}$$

for distances less than 30m, R is set equal to 30m.

The observed and predicted uncertainties are compared for a number of observed

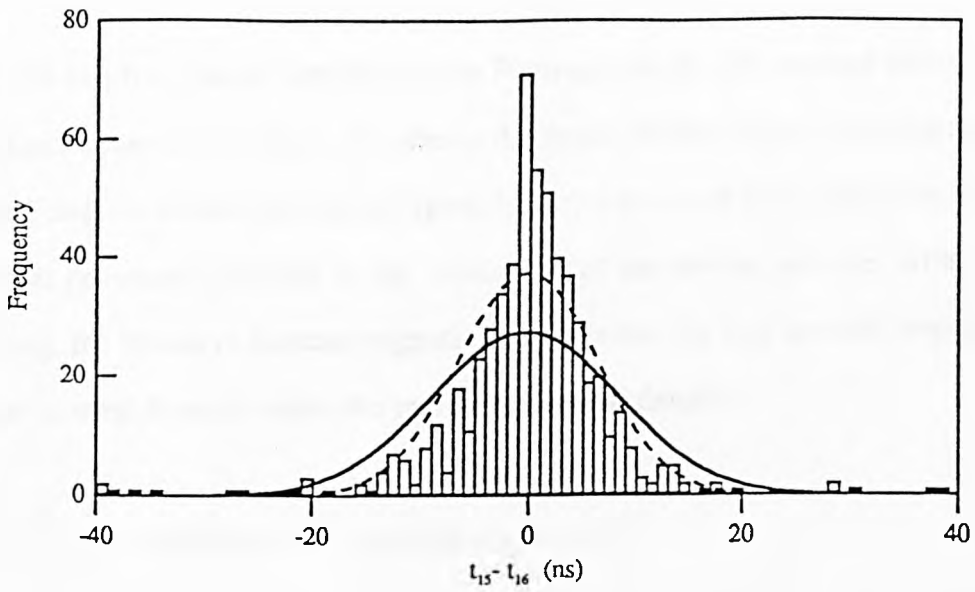


Figure 3.13 Frequency distribution of time differences between detector 15 and 16 corrected for their spatial separation and time of flight differences for density $\approx 1.5\text{m}^{-2}$ and core distance 35m. The solid line shows a gaussian of width $\sigma_{t_{15}-t_{16}}$. The broken line is a gaussian of width given by the range of $t_{15} - t_{16}$.

densities as a function of core distance in Figures 3.14 (i) (Un-covered detectors) and (ii) (Lead covered detectors). The fits to the timing uncertainties are compared for the 'leaded' and 'un-leaded' periods in Figure 3.15. As expected from consideration of the physical processes involved in the interaction of the shower particles with the lead sheeting, the spread in detector triggering times is less for lead covered detectors than for un-covered detectors when the two record similar densities.

3.3.2.3 Angular resolution of the GREX array

Bloomer determined the angular resolution of the GREX array by comparing directions obtained from detectors on two independent sub-arrays. He showed that the angular resolution for patterned showers is dependent on shower size, zenith angle and pattern type. The additional contribution of errors in arrival direction due to the core position, $\Delta\psi_{\text{core}}$, have also been shown to be functions of these parameters. Bloomer divided showers according to their pattern types into four 'resolution' groups. Showers of the same size and zenith angle within each group have approximately the same associated angular resolutions. In addition, showers within each group were subdivided according to size (4bins) and zenith angle (4bins). The details of the bins are shown in Table 3.5. The angular resolution of unpatterned showers was impossible to determine due to the lack of suitable sub-arrays from which independent measurements of shower arrival directions could be made. The angular resolutions of showers determined independent of core location errors are given for each bin in the Appendix. Also given in the Appendix are the rms space angle shifts caused by core uncertainties. The determination of these errors is discussed in the following section.

3.3.2.4 The effect of core location errors on measured shower arrival directions

Expected time delays from the shower plane which describe the shower front curvature, and are detailed in Section 3.3.2.1 are determined as a function of the

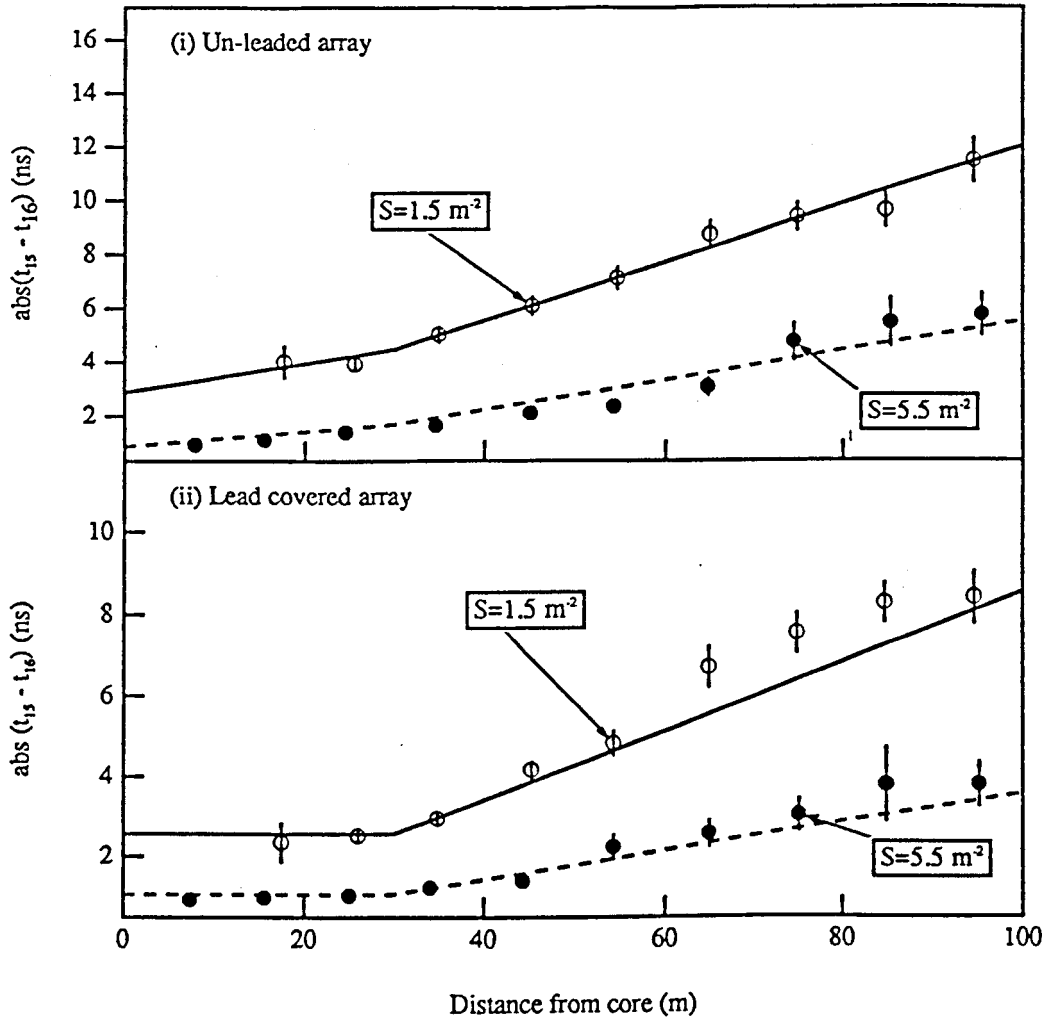


Figure 3.14 Observed timing uncertainties plotted against core distance for densities $\approx 1.5 \text{ m}^{-2}$, open circles and 5.5 m^{-2} , closed circles for showers from (i) Un-leaded array and (ii) Leaded array. The solid and broken lines in each plot show the parametrisations of those uncertainties for $S \approx 1.5 \text{ m}^{-2}$ and $S \approx 5.5 \text{ m}^{-2}$ respectively

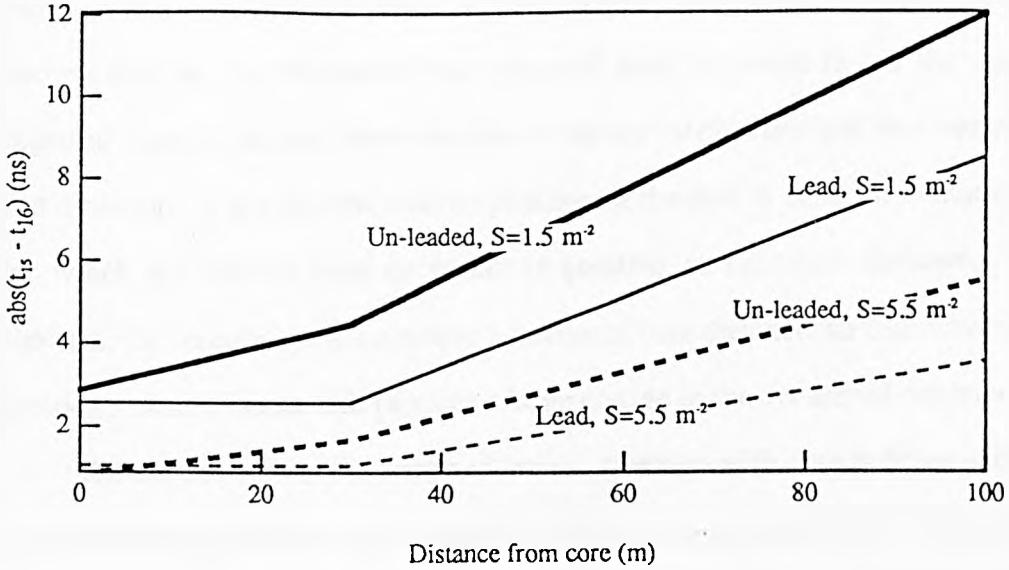


Figure 3.15 The parametrisations of the timing uncertainties as a function of core distance for $S=1.5$, solid lines and $S=5.5$. The thick and thin lines are for showers from the un-leaded and lead array respectively.

Bin	$\ln[S(50)]$	$S(50)$	$\sec \theta$	θ	(ii)	R grp	Pattern
1	-2.07 to -0.69	0.125 to 0.5	1 to 1.076	0° to 21.66°		0	0
2	-0.69 to -0.69	0.5 to 2.0	1.076 to 1.153	21.66° to 29.85°		1	1
3	-0.69 to 2.08	2.0 to 8.0	1.153 to 1.229	29.85° to 35.54°		2	2,3,7
4	>2.08	>8.0	1.229 to 1.305	35.54° to 40.00°		3	4
						4	5,6

Table 3.5 (i) Shows the definition of $S(50)$ and θ bins, and (ii) resolution groups used to parametrise directional uncertainties of showers.

distance from the shower core in the shower plane, It therefore follows that uncertainties in the position of the core will lead to poorer fits of the observed to expected times in the final determination of the arrival direction and thus uncertainties in that direction. It is expected that the position of the core is most important in showers for which the shower front curvature is greatest, ie for small showers. For these showers, the time delays are a strong function of core distance, so that moving the core position a short distance will produce a large change in shower arrival direction.

The dependence of the assigned arrival direction with core position can be found by determining the arrival direction (θ_1, ϕ_1) for the core at the χ^2 minimum, shifting the core by some distance ΔR , and re-determining the arrival direction (θ_2, ϕ_2) . The space angle shift $\Delta\psi$ is the calculated using:

$$\cos \Delta\psi = \cos \theta_1 \cos \theta_2 + \sin \theta_1 \sin \theta_2 \cos(\phi_1 - \phi_2) \quad \dots \text{Eqn 3.26}$$

The mean space angle shifts for selected showers are shown plotted against core shifts for the four eras in Figure 3.16(i). This graph illustrates that the space angle shifts are generally larger at a given core shift for showers from the period when the detectors were un-covered than when they were shielded with lead, and hence accurate determination of core position was more important during this period. This is as expected qualitatively from the reduction in the observed shower front curvature produced by the addition of lead to the detectors. A similar effect is seen when comparing the change in arrival directions for showers of different S(50)'s. Figure 3.16(ii) shows mean $\Delta\psi$ plotted against ΔR for different bands of S(50). The showers were from the period when the array consisted of 36 lead covered detectors. However, the trends observed are typical of all other operational eras of the array. $\Delta\psi$ decreases with increase in shower size for a given core shift. As has already been explained, this is due to the reduction in shower front curvature in larger showers. The space angle shifts in showers of S(50)~13 m⁻² are approximately half of those in showers of S(50)~0.3 m⁻².

Quadratic fits were made of $\Delta\psi$ to ΔR for each S(50) band. So that the expected arrival direction uncertainty due to uncertainties in core location for a particular shower

is approximated by the expression:

$$\Delta\psi = a\Delta R + b\Delta R^2 \quad \dots\text{Eqn 3.27}$$

where the coefficients, a and b , are given for each era and S(50) band in Table 3.6. These fits are good for $\Delta R \leq 60\text{m}$ and are shown superimposed on the observed data in Figure 3.16(ii). The total core shifts and the consequent space angle shifts were determined for the sample of selected showers from each era. The rms space angle shifts due to uncertainties in core position are given for each era in Table 3.7. The integral and differential frequency distributions of space angle shifts for the present era of the GREX array are shown in Figure 3.17 (i) and (ii) respectively and are typical in shape of the distributions of the other eras.

The contribution to the uncertainty in one orthogonal component of the direction vector, for instance declination is given by:

$$\sigma_{\Delta\delta} = \Delta\psi_{\text{RMS}} / \sqrt{2} \quad \dots\text{Eqn 3.28}$$

Prosser (private com.) compared directions found by two subarrays of 4 detectors each using independent cores derived using density information from triggered detectors within each of the subarrays. He compared space angle shifts found in this way to those obtained by Bloomer who determined the angular resolution of the array in the absence of core uncertainties. Prosser found that the additional directional uncertainty due to core shifts could be accounted for by multiplying Bloomer's resolutions by 1.25. For the present era, the 'core' contribution to the uncertainty in declination is $\sigma_{\Delta\delta} = 0.45^\circ$. When added in quadrature to the mean angular resolution obtained by Bloomer for this period of $\sim 1.1^\circ$, it can be seen that the increase in angular resolution is only by a factor of ~ 1.1 . However, Prosser's analysis does not take account of the fact that the core finding algorithm procedure uses untriggered detectors to set an upper limit on the density at the detectors location and hence locate the core more accurately. Hence, density information is obtained from all 36 locations of the GREX array rather than from the relatively small number of triggered detectors in the average shower. It may be expected, therefore, that the true core uncertainty is very much less than that estimated by sub-array comparison. The rms space angle shifts due to core location errors were

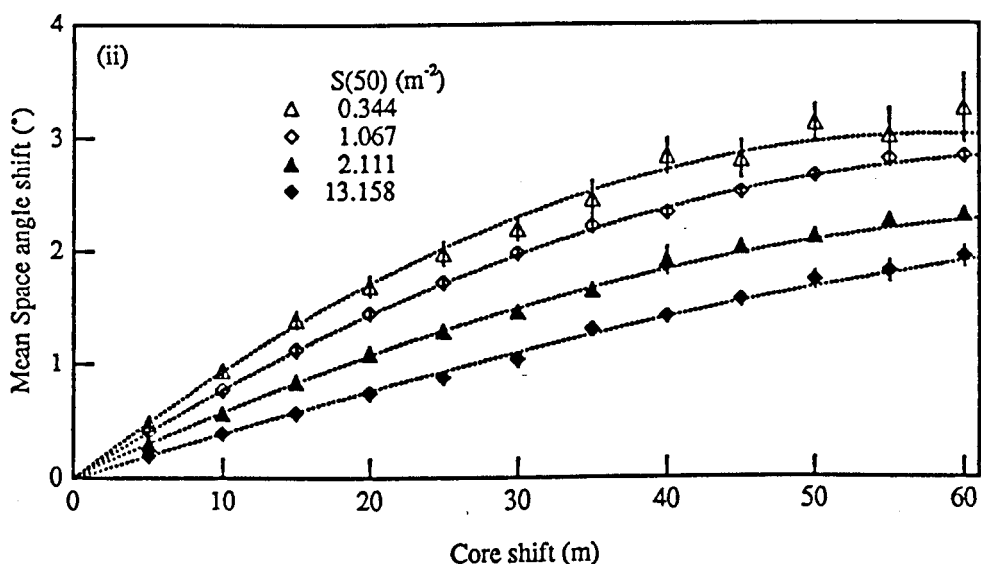
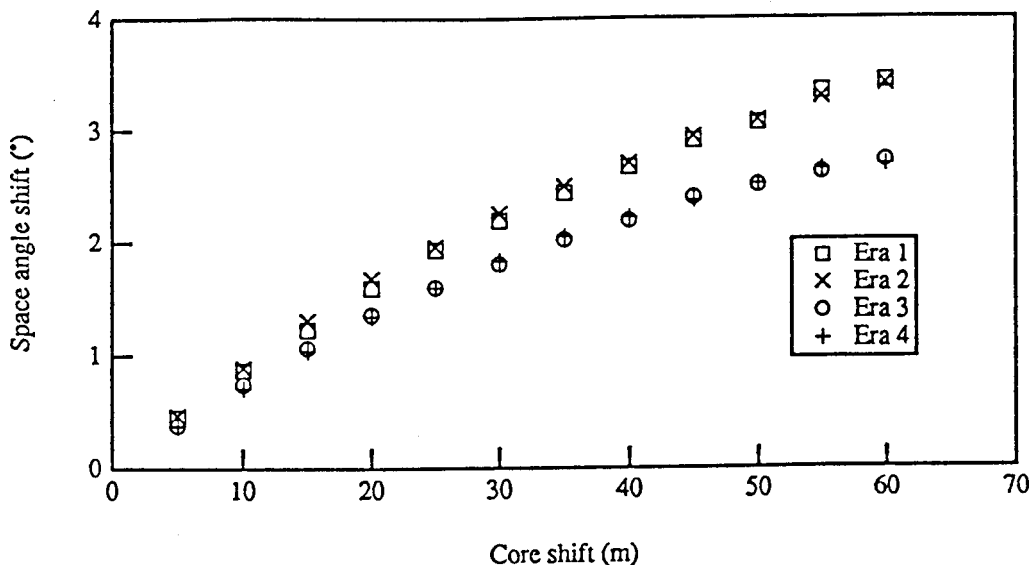


Figure 3.16 The change in assigned arrival direction due to shifts in the core position derived by the analysis is shown plotted against those shifts for showers from different eras (i) and S(50) bands (ii).

S(50) bin	range S(50)	un-leaded array		leaded array	
		a	b	a	b
1	0.125 to 0.5	0.120	-0.00099	0.094	-0.00070
2	0.5 to 2.0	0.094	-0.00060	0.084	-0.00061
3	2.0 to 8.0	0.067	-0.00031	0.061	-0.00036
4	>8.0	0.040	-0.000057	0.040	-0.00012

Table 3.6 The coefficients for the quadratic fit of the space angle shift in arrival direction, $\Delta\psi$, for a shift in core position, DR: $\Delta\psi = a\Delta R + b\Delta R^2$. These coefficients are a function of shower size and are affected by the addition of lead to the detectors.

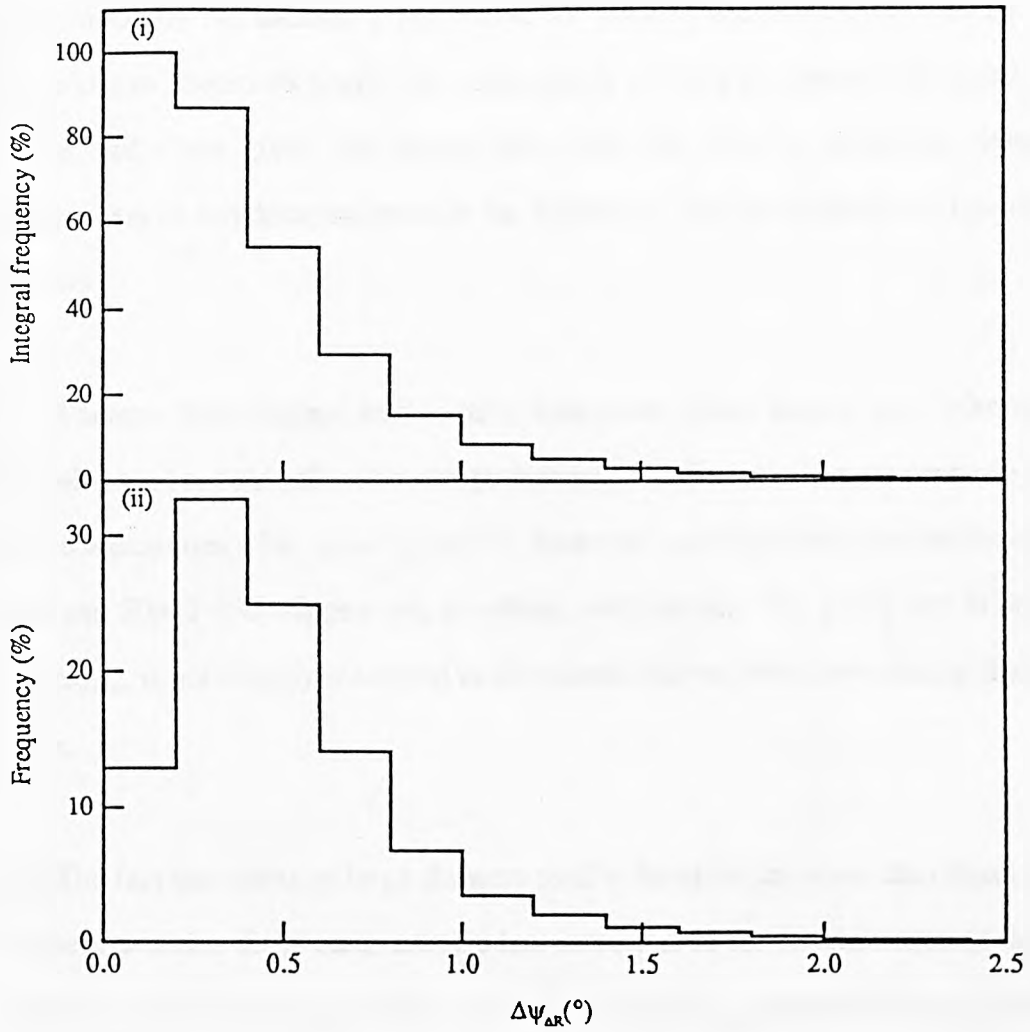


Figure 3.17 (i) and (ii) The integral and differential frequency distributions respectively of space angle shifts due to core uncertainties.

Era	$\Delta\Psi_{\Delta R}$ (RMS)
1	0.813 ± 0.003
2	0.720 ± 0.003
3	0.628 ± 0.003
4	0.627 ± 0.003

Table 3.7 The rms space angle shifts due to uncertainties in the core position are shown for showers from each era

determined by the method given above for each of the subsets of showers binned according to Bloomer's resolution, zenith angle and size groupings (Section 3.3.1.8). These shifts are given for comparison with the angular resolution determined independent of core location errors in the Appendix. The main features of interest are as follows:

(i) Whereas '30m triggers' tend to have their cores better located than '50m triggers', they also tend to be smaller showers so that the final direction is more sensitive to small core uncertainties. The errors in arrival direction associated with core uncertainties in 30m and 50m 7 fold triggers are, therefore, very similar. It is partly due to this effect that $\Delta\psi_{\text{core}}$ is not directly correlated to directional uncertainties due to timing fluctuations alone.

(ii) The fact that cores of large showers tend to be easier to locate than those of small showers *and* that those cores are also less important in the determination of the arrival direction leads to a strong negative correlation of $\Delta\psi_{\text{core}}$ with shower size. Hence the rms $\Delta\psi_{\text{core}}$ for a shower of $S(50) = 13\text{m}^2$ is approximately half of that of showers of $S(50) = 0.3\text{m}^2$.

(iii) $\Delta\psi_{\text{core}}$ is weakly correlated to the zenith angle of showers, with uncertainties increasing the more inclined the shower.

3.3.3 DATA COMPRESSION

After finding an accurate arrival direction for each shower, it is necessary to make these available for source searching. The limited space in which data can be stored so as to be immediately and readily accessible, however, has meant that it has been necessary to develop a method for compressing each event record to a minimum number of bytes. The total hard disk storage space on the Amdahl is 920 Mbytes. If data is

stored on these disks in the format of the Pascal records produced by the analysis, this would allow only ~2 weeks data to be accessed at any one time. Not only does this record contain information that is not required for source searching such as detector densities and trigger times, it also stores real variables such as the zenith and azimuthal angles to much greater precision than is required. For the purpose of source searching, a compressed format has been developed in which each event is stored as a record of 20 bytes. Table 3.9 shows the parameters contained in each compressed event record along with the accuracy to which they are stored.

The compressed version of each variable, x , is the numerical binary representation of the integer X given by:

$$X = \text{TRUNC}((x - m_x) * t_x) \quad \dots \text{Eqn 3.29}$$

where m_x is a default value set to at least t_x less than the minimum possible value that the variable x can possibly take, and t_x is the minimum precision to which we wish to know x . A default value is flagged by setting x equal to m_x so that $X = 0$ is the default representation.

The compressed format reduces an event record by a factor of ~50 while retaining the essential information required to perform source searches on the data described in subsequent sections. There is sufficient permanent storage space on the hard disks to enable all the data from the array turn on to the end of 1990 to be stored in this form and to be accessed immediately.

3.4 Conclusions

(i) The analysis procedures described in this chapter are the result of a compromise which must be made between the 'ideal analysis' and the practical limitations of computing resources available to data processing for this experiment. The increased efficiency of the core location algorithm- the most time consuming process in the analysis (~60% of CPU time)- enables the analysis to 'keep up' with the data production, though some sacrifice must, nevertheless, be made in the accuracy of the

Paramter	Number of Bytes	precision
MR	8	ms
θ (refined zenith angle)	2	$\pm 0.002^\circ$
ϕ (refined azimuthal angle)	2	$\pm 0.006^\circ$
S(50)	2	0.002 m^{-2}
x_c, y_c (shower core coordinates)	2	0.02m
Shower type	1	Exact (integer)
τ^2 , the direction goodness of fit parameter	1	0.1

Table 3.8 The information stored in each compressed record used for source searching is shown along with the number of bytes used to store each shower parameter.

core positions.

(ii) S^2 was found to be the optimum weighting for the 'first try' centre of gravity core.

(iii) The rms value of the total error in the routine analysis derived core locations varies between $\sim 9.2\text{m}$ and 12.4m in the best (era 4) and worst (era 2) cases respectively. These errors arise from 2 sources: The statistical uncertainties in the position of the χ^2 minimum and the poor location of the exact position of the minimum due to limited CPU allocation. These two contributions are, on average, approximately equal.

(iv) The analysis core locations are better for showers triggering detectors with 30m spacings than with 50m spacings. Large showers have their cores better located than small showers, and adding lead to the detectors also appears to reduce the uncertainty in the core positions. ($\Delta R_{\text{rms}} = 12.36\text{m}$ before the addition of lead and 9.94m after)

(v) The core location errors produce an rms error in the final shower arrival direction of between 0.63° for era 4 and 0.81° for era 1. The total space angle shift for a given core shift decreases with increasing radius of curvature of the shower front and is, therefore, less for larger showers compared to small showers. The shift in arrival directions was also reduced by the addition of lead to detectors. The long tail in the distribution of angular uncertainties due to core position errors (Figure 3.17) indicates that a few showers would benefit greatly from more time being spent determining an accurate core position ($\sim 8\%$ have space angle shifts $> 1^\circ$ due to core location errors alone).

(vi) The inaccuracies in core position caused by using the relatively poor first try arrival direction in fixing the initial shower plane are relatively small (errors are greater than 10m for only 2% of showers) compared to those caused by limited CPU allocation to the core finding algorithm.

CHAPTER FOUR

THE MEASUREMENT OF THE AGE PARAMETER

4.0 Introduction

The high level of background cosmic rays, consisting mainly of protons, compared to the low fluxes of γ -rays from point sources has led many researchers to look for ways of distinguishing between showers initiated by these two different primaries. If γ -ray showers could be unequivocally identified as such, the background events could be eliminated, and sources would surely stand out. As it turns out γ -ray and proton induced showers appear very similar when observed at sea level. They are, however expected to differ in two important aspects: (i) γ -ray showers are expected to have a deficit of muons (Section 1.4.3). Monte Carlo simulations by, for example Stanev *et al.* 1985, predict the muon content of γ showers to be only $\sim 10\%$ of that of proton showers. (ii) γ -ray showers are expected to appear slightly less well developed, having steeper lateral distribution functions (ldf) than proton showers of the same size. According to Fenyves (1985) and Cheung and Mackeown (1987), this difference should increase with altitude of observation. Neither of these predictions, however, have been supported by observations: in the initial detection of Cygnus X-3 (Samorski and Stamm 1983) at PeV energies, on source events had only slightly fewer muons than background showers and, in addition, the signal was seen in older rather than younger events. Subsequent observations, eg Tonwar *et al.* 1988 and Protheroe *et al.* 1984 have found signals in older showers. Also a number of underground muon detectors, eg Soudan-1, (Marshak *et al.* 1985a,b) and NUSEX (Battistoni *et al.* 1985a,b) have seen muons apparently from the direction of Cygnus X-3 with modulation at the 4.8 hr period. A very recent report by the Soudan-2 collaboration claims emission from Cygnus X-3 shortly after a radio flare in January 1991 (Thomson *et al.* 1991). All these observations are in contradiction to

many theoretical predictions of high energy interactions. It would seem that identifying γ -ray induced showers is highly problematical.

Attempts to answer the question of the muon content of γ -ray showers are being made at *Haverah Park* by Nottingham University. Their muon detector, however has an area of only 40m² and is, therefore, too small to be very powerful in distinguishing between γ -ray and proton induced showers. This chapter is concerned with the 'age' of showers, its measurement and its use in distinguishing between γ -ray and proton induced showers. The age parameter, s , appearing in the NKG function (equation 1.5), describes the state of lateral development of a shower. It also reflects the longitudinal development of a cascade, so that showers at their maximum development have an age of 1, while those past maximum have $s > 1$ and are described as 'old'. A shower with an age of 2 has decayed to just 1 particle. As the shower progresses through the atmosphere, its particles become increasingly scattered due mainly to Coulomb scattering of electrons (see Section 1.4.1). In hadron induced showers, the opening angles of pion production also contribute to increasing the lateral spread of particles. Thus as showers become older, their lateral distribution becomes flatter.

4.1 Measurement of the age parameter

The method used to determine s is that of χ^2 minimisation which has been described in Chapter 3. Details of the technique, therefore, will not be given in any great depth here. There are, however, a few important differences in its implementation. In particular the minimisation takes place in 4 dimensions, shower size, s and x and y , the core coordinates. A conjugate gradient method is used to minimise χ^2 . Unlike the algorithm used to find the core position, however, this algorithm is not CPU limited as it is not intended for use in routine analysis of GREX events. Many more steps of the algorithm are used (12 compared to the average of 2 in the routine analysis). Each step, i , in the minimisation consists as previously, of finding a conjugate direction, h_i (Section 3.3.1.4) and the subsequent minimisation of the projection of χ^2 along the

vector h_i . This line minimisation consists of repeated iterations in which a parabola is fitted to three points, P_1 , P_2 , and P_3 along h_i and the position of its minimum, P_4 , found by interpolation (Section 3.3.1.5). At the end of each iteration, the point with the largest χ^2 is rejected and the line minimum converged upon. About 20 steps are performed in this line minimisation.

Although the χ^2 minimum of all showers may be located to any desired degree of accuracy, it is doubtful that the small number of triggered detectors in showers close to the array threshold, which, due to the steepness of the cosmic ray spectrum, make up the bulk of recorded events, can provide sufficient information to allow the lateral distribution function of showers to be determined to any useful degree of accuracy. The usefulness of the age parameter determined in this way is investigated in the next section using simulated showers.

4.2 Usefulness of the determined age parameter

The most optimistic estimates for the accuracy of the measured age parameter and its correlation with the true shower age were obtained using simulated showers. No attempt was made to simulate shower development or the response of the detectors to individual particles passing through a detector. Rather, an NKG ldf of particles was assumed and the expected particle density at each detector calculated using its distance from the core in the shower plane and the assigned size and age of the shower. This density is converted to the expected numbers of particles passing through the detector by multiplying by the projected area of the detector in the shower plane. Finally, this particle number is fluctuated by the empirically determined density uncertainties (Equation 3.4) to give the 'observed' detector signal. Only densities greater than the detector threshold level (0.3m^{-2}) are recorded. Those greater than the ADC saturation level are set to arbitrarily high values to identify them as such. Showers that do not satisfy the triggering conditions of the array (≥ 5 detectors with densities ≥ 1 per detector) are rejected.

These simulated showers, then, have exactly the same lateral distribution function and density weights as those assumed by the minimisation algorithm in finding the shower parameters. The algorithm, therefore, has the best possible chance of determining accurate shower ages. A large number of sets of records containing detector densities were obtained in this way for showers of various sizes, zenith angles, ages and core positions.

4.3 Array response as a function of age

It may be expected that the array response is a function of shower age as well as shower size and zenith angle. If the mean ages of showers striking the array is to be determined, it is necessary that this dependence is measured and taken into account.

The probability of *the array* triggering for various types of showers was determined by measuring the proportion of simulated showers 'thrown' at the array that trigger it. The results for sets of vertical showers of different size and uniform distributions of ages between 0.5 and 2 are shown in Figures 4.1(i) (ii) for the 32 and 36 detector arrays respectively. The simulated showers all had cores uniformly distributed within the array boundary. The probability of array triggering is a strong function of shower size, and for showers of the same size and age, is larger for the 36 detector array than the 32 detector array due to the reduction in the mean detector spacing. It is also evident that for small showers, the array is more sensitive to young, steep showers. For showers with $S(50)$ less than the density required for a detector to be included in the trigger ($\sim 1.25\text{m}^{-2}$), it is likely that the triggering detectors will lie on a 30m rather than a 50m grid. Thus a steep shower, having larger densities at core distances $< 50\text{m}$ are more likely to trigger the array. For large showers, the reverse becomes true. The array is more sensitive to older showers. It is likely that for these showers, all detectors within 50m of the core will be triggered, so that large particle densities at $r > 50\text{m}$ will make the array more likely to trigger.

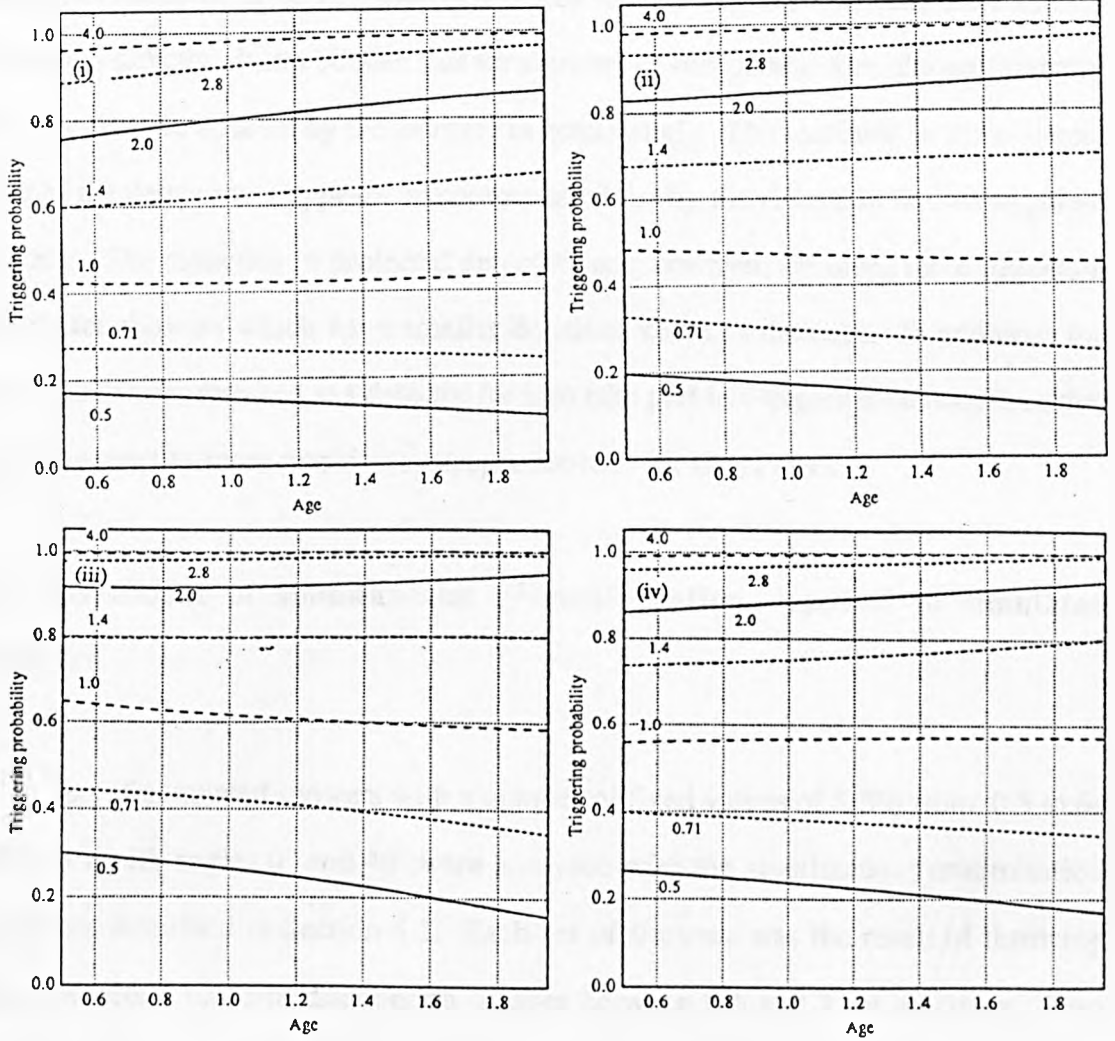


Figure 4.1 Triggering probabilities of the GREX array are shown as a function of age for showers of various sizes as determined by simulations. The figures on each plot show shower size in terms of the density at 50m (m^{-2}). (i) and (ii) show the probabilities for vertical showers triggering the 32 and 36 detector arrays respectively and (iii) and (iv) are for showers inclined at 40° to the vertical for the two arrays.

It is also useful to consider the effect of zenith angle on the sensitivity of the array. Figure 4.1 (iii) and (iv) show the triggering probability for showers inclined at 40° to the vertical plotted against s for 32 and 36 detector arrays respectively. The showers have the same range of sizes as those in Figures 4.1 (i) and (ii) and can, therefore, be compared directly. It can be seen that for showers of comparable size, the sensitivity of the array is little affected by the increase in zenith angle. The reduction in the projected area of the detectors, it appears, is compensated for by the reduction in their apparent spacing. The reduction in projected detector area, however, becomes more important for flatter showers which have smaller densities close to the core. In addition, the effective density required at a detector for it to take part in a trigger is increased, so that the array remains more sensitive to steeper showers for larger sizes.

4.4 Assessment of simultaneous χ^2 minimisation applied to simulated showers

Sets of simulated showers with a number of fixed values of $S(50)$ from 0.5 to 64 m^{-2} and zenith angles 0° and 40° were analysed with the simultaneous minimisation algorithm described in Section 4.1. Each set of showers was the result of throwing showers with a uniform distribution of ages between 0.5 and 2 at the array. Two groups of showers were obtained, one with cores uniformly distributed across the whole of the array, the second with cores within 30m of the array centre. The resulting age distribution of triggering showers for the first group is, therefore, as shown by the plots in Figure 4.1(i) to (iv) and is approximately uniform in all but the smallest showers ($S(50) \approx 0.5$) where there are more young showers. For the second group of showers, the probability of triggering was found to be ~ 1 for all sizes of showers, the detector spacing being closer here (30m) than it is in the rest of the array (50m). It was also hoped that the resolution of the array would be better for this set of showers with more detectors close to the core and involved in the trigger.

4.5 Correlation between simulated age and analysis-determined age

The scatter diagrams in Figures 4.2 (i) to (iv) show the age determined by the analysis s_a plotted against the simulated age, s_s , for vertical showers of different sizes. This set of showers are of the first group with cores uniformly distributed across the 36 detector array. In even the smallest showers, there are obvious *correlations* between these ages, which tend to indicate that the measured age may be of use in distinguishing between young and old showers. However, for showers with $S(50) \leq 4\text{m}^2$, the range of simulated ages is very large for a given measured age. The histogram in Figure 4.3 show the distribution of ages of showers for which the measured age is in the range 1.1 to 1.3, is very nearly uniform between 0.5 and 1.2 for showers of $S(50) = 2.8\text{m}^2$. It is also undoubtedly the case that for these small showers, the original distribution of ages of the simulated showers will greatly affect the distribution of the ages of showers assigned a given value of s_a . The measured age, therefore, tells us little about the true age of a small shower and is only of use in distinguishing between showers of the most extreme ages. It can however be used as a measure of s for showers with $S(50) \geq 4\text{m}^2$. Scatter plots of s_a against s_s also show good and useful correlation for showers inclined at 40° to the vertical and for $S(50) \geq 4\text{m}^2$ showing that the age resolution of the array is little affected by this increase in zenith angle.

Figure 4.4(i) and (ii) show examples of scatter plots obtained for showers of $S(50)$'s 1m^2 and 1.4m^2 respectively falling within 30m of the array centre. They show this correlation of measured age to simulated age to be better for showers close to the centre of the array, and this is found to be true for all sizes of showers. In particular, the measured age is useful for showers as small as $S(50) \sim 1.4\text{m}^2$.

In general, the measured age is an overestimation of the 'true' shower age, s . This is due to the fact that at large core distances where the expected density is less than threshold, only upwards fluctuations in the densities will be measured by the detectors. These measurements, then, tend to bias the determined age on the high side. In addition, in large showers, only downwards fluctuations will be measured in detectors

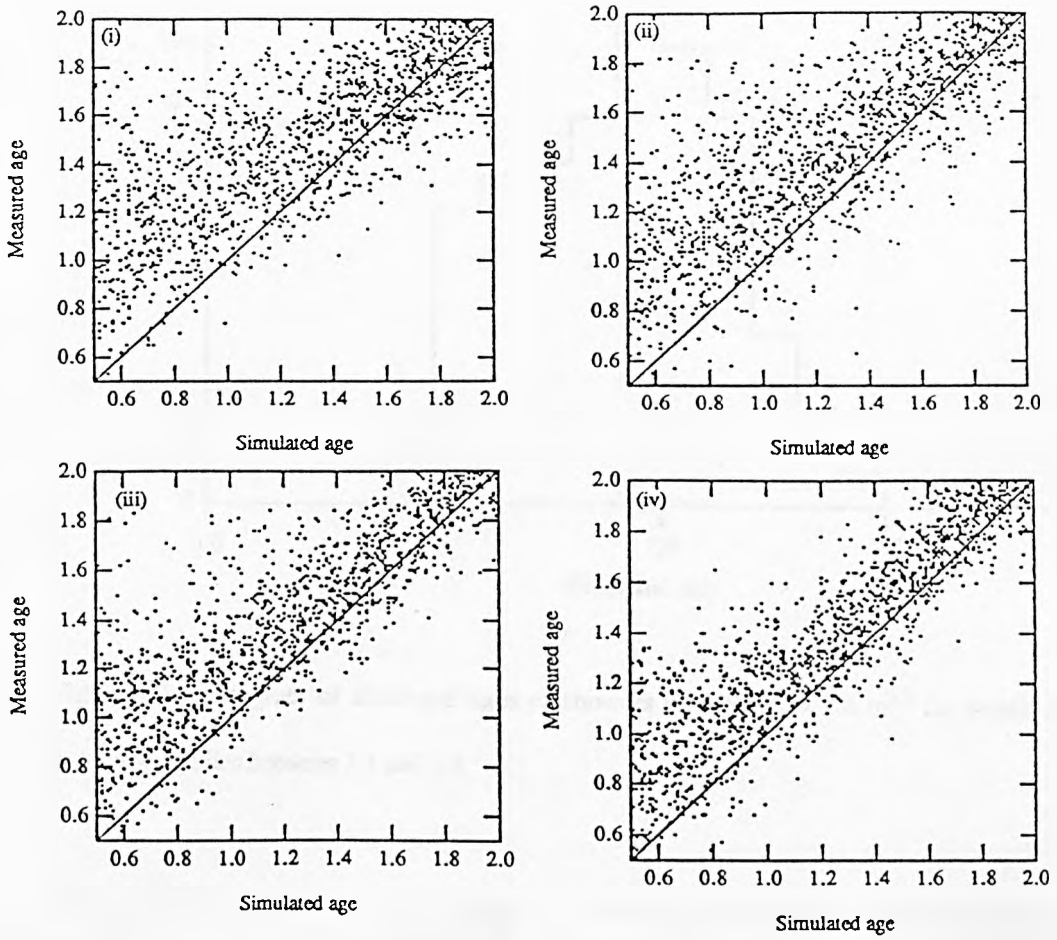


Figure 4.2 Scatter plots of measured age against simulated age for vertical showers with cores distributed uniformly across the 36 detector array and $S(50)$'s (i) 1.4 m^{-2} , (ii) 2.0 m^{-2} , (iii) 2.8 m^{-2} , (iv) 4.0 m^{-2} .

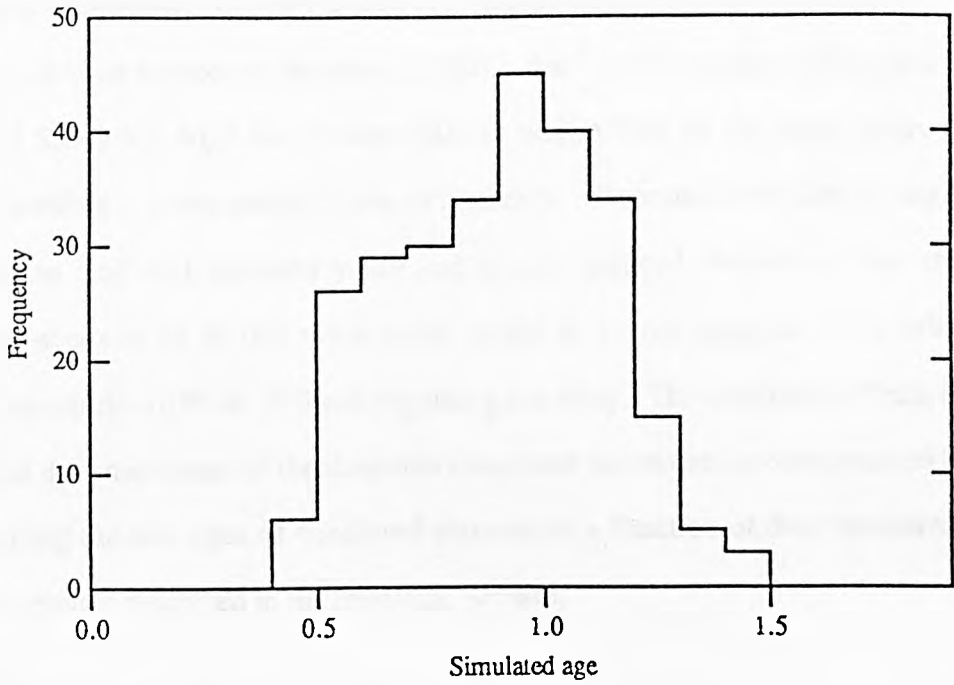


Figure 4.3 Histogram of simulated ages of showers with $S(50) = 2.8 \text{ m}^{-2}$ for which the measured age lies between 1.1 and 1.3

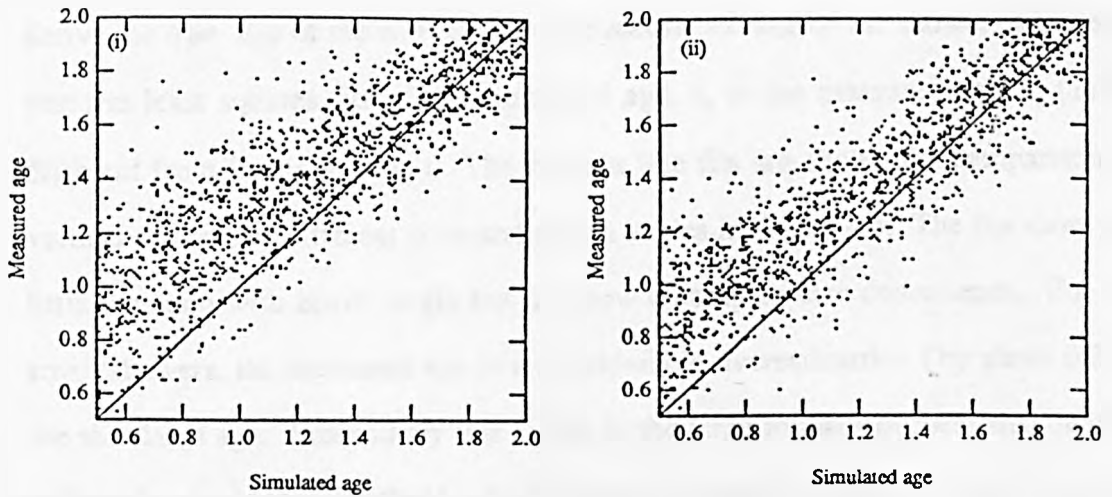


Figure 4.4 (i) and (ii) Scatter plots of measured age against simulated age for showers with cores lying within 30m of the array centre and with $S(50)$'s 1 m^{-2} and 1.4 m^{-2} respectively.

that are close to the core and at which a density greater than saturated is expected. These downwards fluctuations also tend to bias the measured age in the same direction.

For a limited number of showers, ($S(50) \geq 4\text{m}^{-2}$ for all showers falling inside the array, and $S(50) \geq 1.4\text{m}^{-2}$ for showers falling within 30m of the array centre) s is, then, measurable to some useful degree of accuracy. Theoretical calculations suggest a difference in s of ~ 0.1 between γ -ray and proton induced showers so that the age resolution needs to be of this order to be useful in source searches. This subset of showers constitute $\sim 10\%$ of all those triggering the array. The systematic effects due to the limited dynamic range of the detectors described above can be compensated for by parametrising the true ages of simulated showers as a function of their measured age. This correction is described in the following section.

4.6 Deriving a better estimate for the true age of showers

Scatter plots of s_a vs s_s for sets of showers with good age resolution are fitted well by straight lines for fixed values of shower size and zenith angle. Since we wish to derive the *true* age of the shower from the *measured* age of the shower, we need to perform least squares fits of the simulated age, s_s to the measured age, s_a (this is different from fitting s_a to s_s). The straight line fits are shown for comparison for vertical showers of different sizes and zenith angles in Figure 4.5. The fits show very little variation with zenith angle but do show a complex size dependence. For very small showers, the measured age is a considerable overestimation (by about 0.2) of the simulated age. Presumably this is due to the large number of measured densities expected to be below threshold. As the size increases, the measured age becomes a better estimate of the true age, until at very large sizes the number densities expected to be above saturated have a significant effect, and the measured age begins get worse again.

The straight lines are described by equation 4.1:

$$s_c = m (s_a - 1.5) + s_{1.5} \quad \dots\text{Eqn 4.1}$$

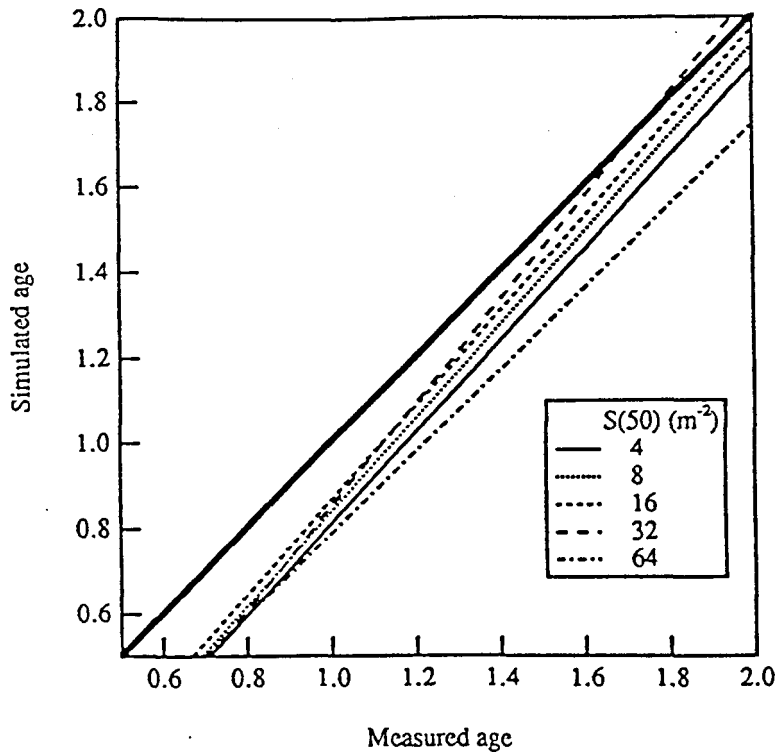


Figure 4.5 Straight line fits of simulated age to measured age for vertical showers of various sizes are shown for comparison. The inset gives the shower size in density at 50m for each fit

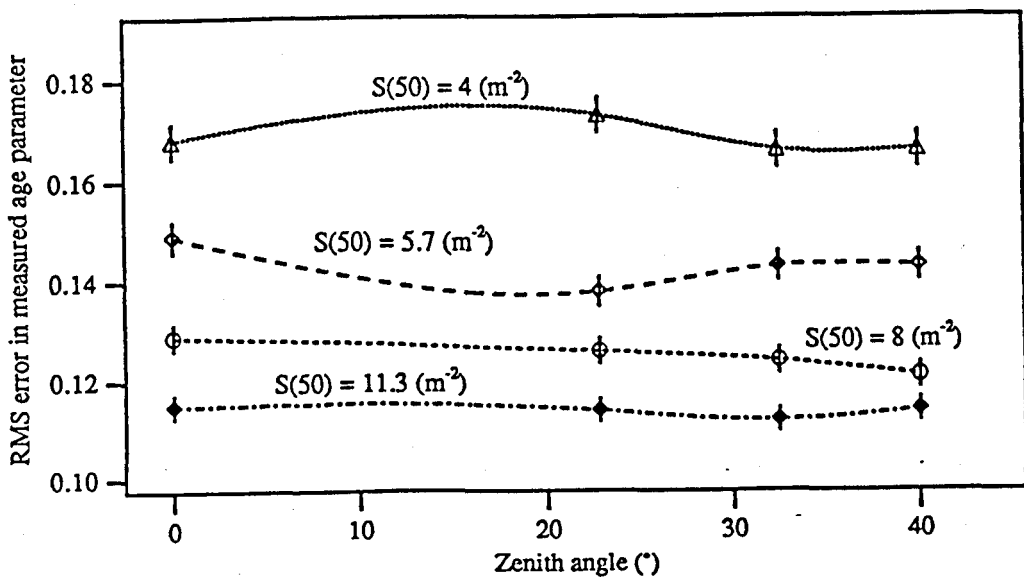


Figure 4.6 The RMS error in the 'corrected' age parameter, s_c , is shown plotted against zenith angle for showers of various sizes with cores distributed uniformly across the whole of the 36 detector array.

where m and $s_{1.5}$ are dependent on zenith angle and shower size. $s_{1.5}$ is the expected value of the simulated age for a measured age of 1.5. In measuring the ages of real showers, a better estimate of the true age of showers, s_c , is obtained from the age derived directly from χ^2 minimisation, s_a , using equation 4.1. The coefficients m and $s_{1.5}$ are those derived from fits of simulated age to measured age for simulated showers of the same size and zenith angle as the real shower. This age, henceforth referred to as the 'corrected' age is typically 0.15 less than s_a .

4.7 Random uncertainties in shower age

The uncertainty in shower age, s , derived using equation 4.1 is given by the RMS deviation of the simulated ages, s_s , from this fit, ie the RMS value of Δs given by:

$$\Delta s = s_s - s_c \quad \dots \text{Eqn 4.2}$$

These RMS values are shown plotted against zenith angle for showers of various sizes for the 36 detector array in Figure 4.6. There is little variation of uncertainty in age with zenith angle. The errors, however, do initially decrease with shower size, reaching a minimum and then increasing again for very large showers where a significant number of detectors become saturated. They are shown plotted against shower size and can be compared for vertical showers from the two core distribution groupings and the 32 and 36 detector arrays in Figure 4.7. It can be seen that the age resolution is better for showers whose core lie within 30m of the centre of the array than others. It is also improved by the extra 4 detectors in the 36 detector array. For the period when the saturated level of the detectors was only 20 particles, the uncertainty due to large numbers of saturated detectors becomes apparent at smaller sizes. Figure 4.8 shows a comparison of the errors plotted against shower size for the 32 detector array before and after the ADC change.

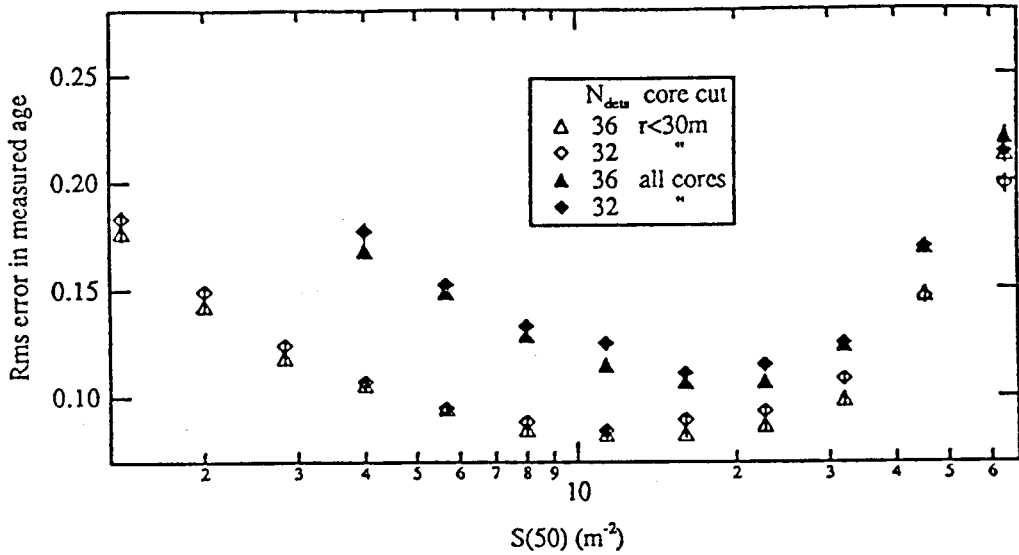


Figure 4.7 The RMS errors in the corrected age parameter of vertical showers are shown plotted against shower size and are compared for the 36 detector (triangle symbols) and 32 detector (diamonds) arrays and for cores lying within 30m of the centre (un-filled symbols) and those uniformly distributed across the whole of the array (filled symbols)

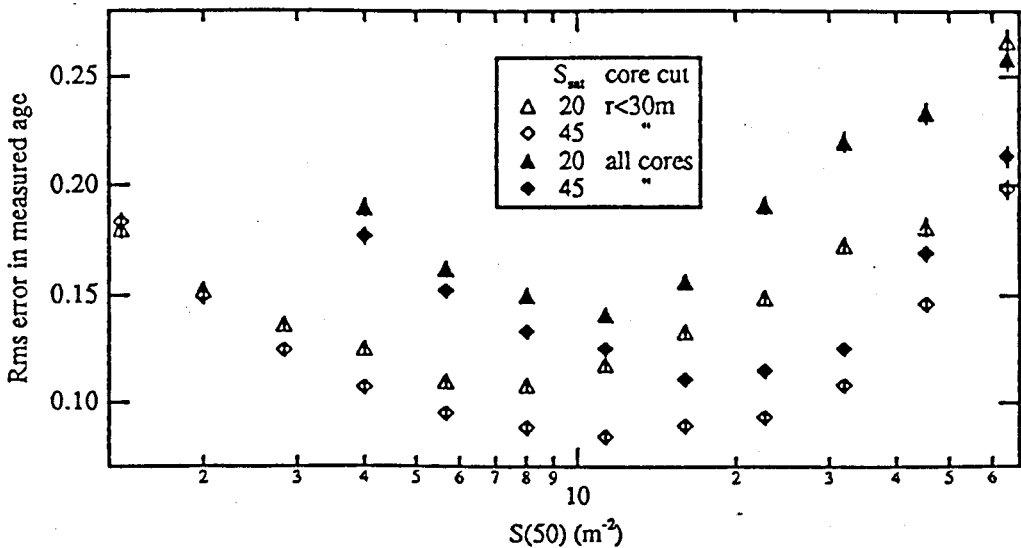


Figure 4.8 Comparison is made of the errors in the corrected age parameter of vertical showers for the array consisting of 32 detectors with saturation at 20 particles and 45 particles - triangular and diamond symbols respectively. Open and filled symbols represent showers with cores falling within 30m of the array centre and uniformly distributed across the whole array respectively.

4.8 Measurement of ages of real showers

It has been shown that the technique of χ^2 minimisation described above can be successfully applied to age determination for showers with $S(50) \geq 4\text{m}^{-2}$ or for showers with $S(50) \geq 1.4\text{m}^{-2}$ for showers with cores falling within 30m of the centre of the array. Although the lateral distribution of shower particles may not follow the NKG function exactly, and the non-linear response of detectors has to some extent been ignored, it has, nevertheless, been demonstrated that the measured age of showers allows us to distinguish between young and old showers. Useful comparison can also be made with results quoted by other groups that measure age in the same way.

The mean value of the corrected age parameter, s_c , for showers falling within 30m of the centre of the 32 detector, unleaded array, is shown plotted against shower size for various zenith angle ranges ($\theta < 22^\circ$, $22^\circ < \theta < 30^\circ$, $30^\circ < \theta < 35^\circ$, and $35^\circ < \theta < 40^\circ$) in Figure 4.9. To enable useful comparisons to be made both between showers at different zenith angles and results of different groups, the shower sizes have been normalised to the number of particles for an equivalent shower inclined at 20° to the zenith using an attenuation length of 160gcm^{-2} derived by Watson (1988).

The age of small showers at all zeniths is seen to rise rapidly with size reaching a maximum and decreasing more slowly for large showers with a gradient of ~ -0.25 per size decade. That these effects are not wholly due to changing characteristics of shower development, but are rather an artefact of triggering conditions, is evidenced by the fact that the size at which the maximum in age occurs increases on going to larger zenith angles. Showers of size $\sim 1.2 \times 10^5$ particle ($E_p \approx 1.6 \times 10^{15}$ eV) are the oldest of the vertical showers ($\theta < 22^\circ$) compared to the oldest steeply inclined showers ($35^\circ \leq \theta \leq 40^\circ$) which have sizes of $N \approx 9.5 \times 10^5$ particles ($E_p \approx 9.6 \times 10^{15}$ eV). Figure 4.10 shows the mean age of showers in the 4 zenith angle ranges plotted as a function of the directly observed shower size parameter, $S(50)$. The peak in ages is seen at the same $S(50)$ at all zenith angles. It would appear, therefore, that much of the complex size

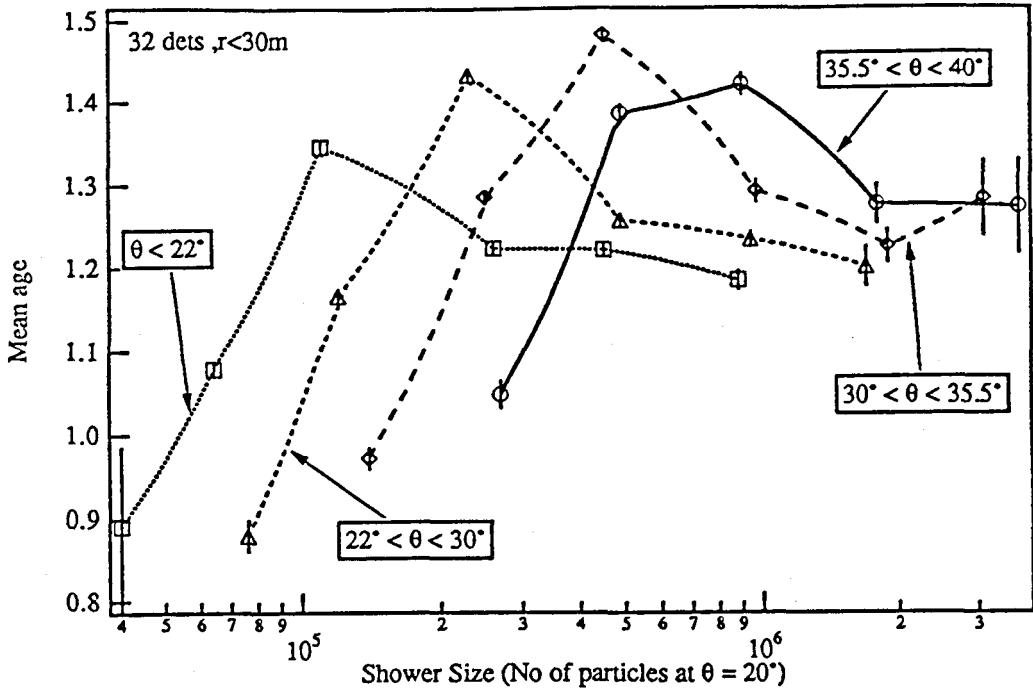


Figure 4.9 The mean (corrected) ages of showers falling within 30m of the array centre (32 detectors, un-leaded) are shown plotted against shower size for 4 zenith angle ranges (refer to labels). The shower size is in particles for the equivalent shower inclined at 20° to the horizontal, which corresponds to an atmospheric depth of 1083 gcm^{-2} .

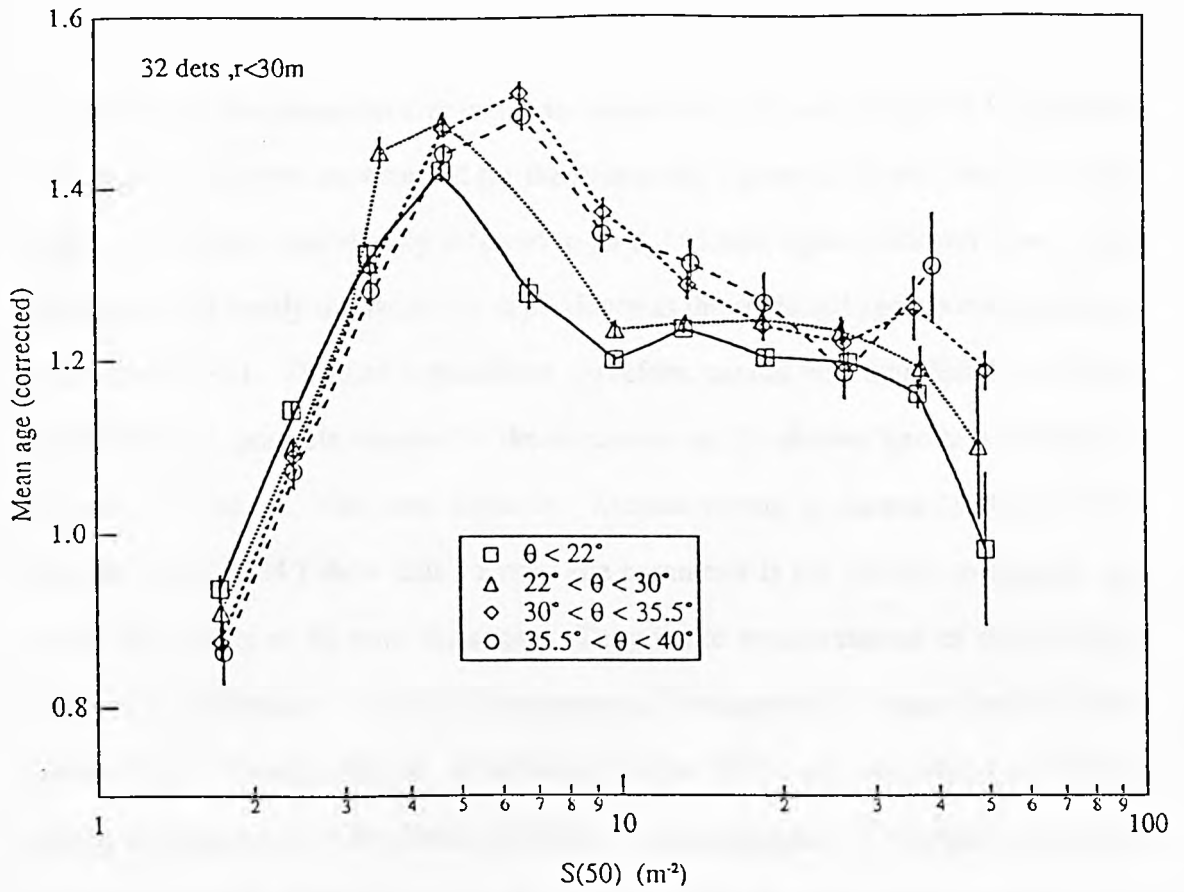


Figure 4.10 The mean (corrected) ages of showers falling within 30m of the array centre (32 detectors, un-leaded) are shown plotted against $S(50)$ for 4 zenith angle ranges (refer to labels).

dependence of the age parameter is due to measurement biases. Figure 4.11 shows the mean ages of showers uncorrected for the systematic biases due to the limited dynamic range of detectors (previously referred to as s_a) plotted against shower size. These ages show very nearly the same size dependence as the corrected ages, but with each age increased by ~ 0.1 . The size dependence, therefore, cannot be a manifestation of these corrections. A possible reason for the variations in the shower age is the change in steepness of the ldf with core distance. Measurements at Akeno (920gcm^{-2}) by Nagano *et al.* (1984) show that a single age parameter is insufficient to describe any particular shower at all core distances. They make measurements of the local age parameter (LAP) which describes the steepness of the lateral distribution function over a narrow range of core distances. It is found that the LAP decreases with core distance having a minimum at $\sim 30\text{m}$ beyond which it increases again. The mean distance of triggered detectors used to measure age increases with size so that this variation in the LAP with core distance will manifest itself as variation in age with shower size. This effect may, to some extent explain the increase in age with shower size for $S(50) \leq 7\text{m}^{-2}$. The spacing of detectors close to the centre of the array is 30m , so that for small showers, the mean distance of triggered detectors lies close to the minimum in the LAP. On increasing size, the mean distance of triggered detectors and so the measured age will increase. That the measurement of age is dependent on the configuration of detectors can be seen in Figure 4.12 which shows a comparison of ages obtained for showers falling within 30m of the centre of the array and those of showers falling more or less uniformly across the whole of the array. For the latter group of showers, poor age resolution precludes meaningful comparisons for showers with $S(50) < 4\text{m}^{-2}$. A clear difference is observed, however, in larger showers, with those falling within 30m of the centre appearing younger than those falling in other parts of the array. All showers of this size have 100% probability of triggering the array so that the difference in measurements must be due to the density sampling differences.

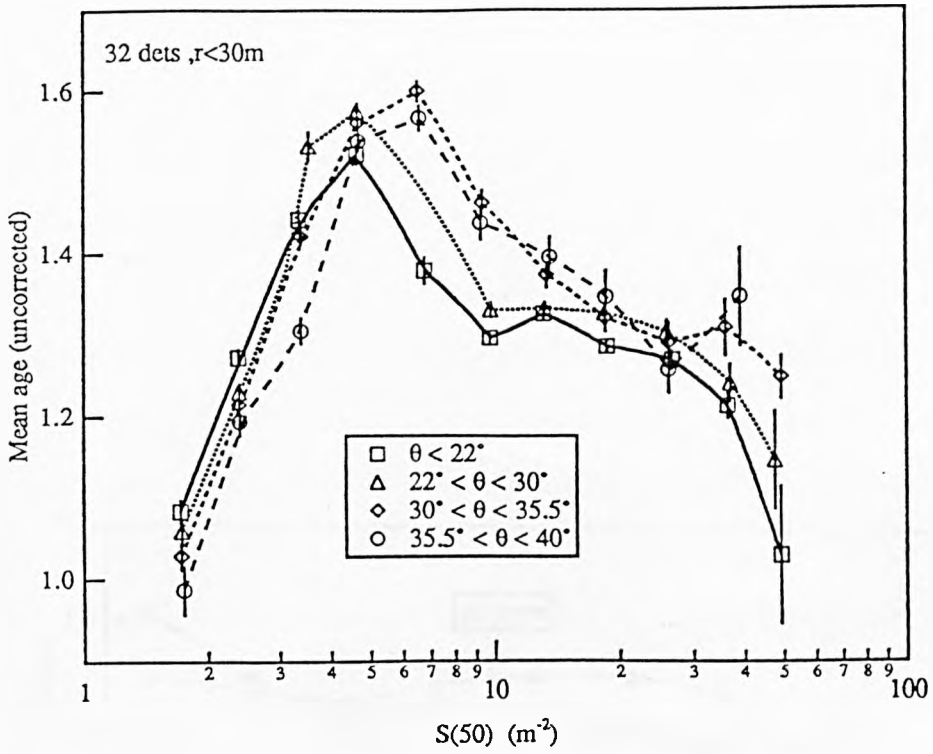


Figure 4.11 The mean measured age parameters un-corrected for the limited dynamic range of detectors are shown plotted against $S(50)$ for 4 zenith angle ranges (refer to labels). All showers have cores lying within 30m of the array centre, and the array consists of 32 un-leaded detectors.

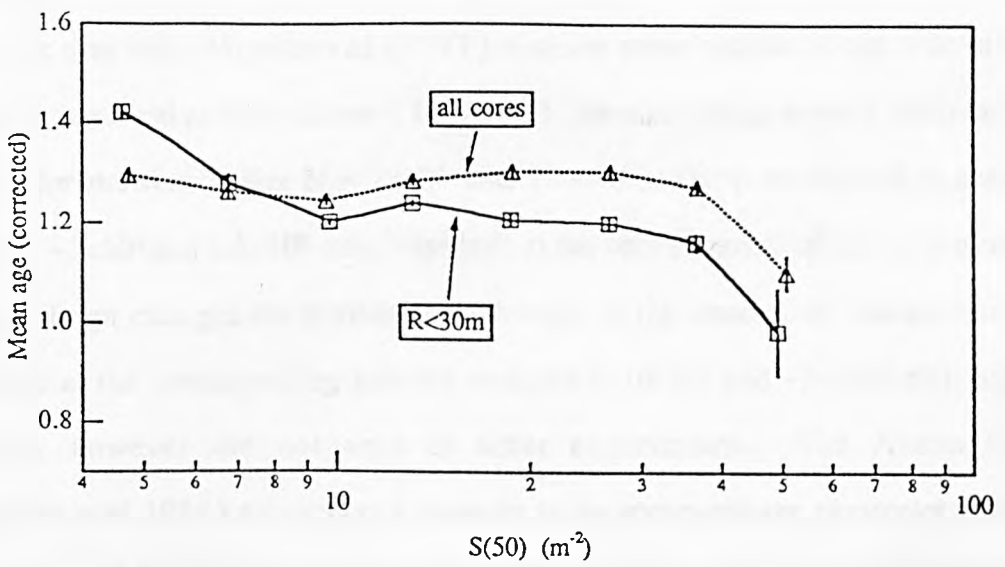


Figure 4.12 The mean age of showers is shown plotted against $S(50)$ for cores lying within 30m of the array centre (square symbols), and for those with cores spread over the whole of the array (triangular symbols)

Showers with $S(50) \geq 7m^{-2}$ show a complex dependence of age with size, though large showers appear somewhat steeper than small ones. A similar size dependence was observed by Gerhardy (1983) making measurements with the Buckland Park array which is situated at sea level ($1060gcm^{-2}$). Age is seen to increase rapidly with size to a maximum at $N \approx 6.8 \times 10^5$ (normalised to vertical) and then declines at a rate of ~ 0.25 per decade for large showers. This dependence is seen in showers of all zeniths. The increase in age for small showers is attributed to the fact that, for showers with energies close to the array threshold, the detection efficiency is higher for younger showers than old. Miyake *et al.* (1977) also see some decline in age with size for showers observed at high altitude ($735gcm^{-2}$). He also claims to see a sharp increase in age for showers of size $N \approx 2 \times 10^5$ and $N \approx 10^7$. These correspond to sea level sizes of $\sim 3 \times 10^4$ and 1.5×10^6 which are both at the very extremes of our measurements. These abrupt changes are attributed to changes in the interaction characteristics of hadrons at the corresponding primary energies ($\sim 10^4$ eV and $\sim 5 \times 10^{16}$ eV). Similar effects, however are not seen in other experiments. The Akeno Group (Nagano *et al.* 1984) also report a decrease in the measured age parameter with size and a bump at $N \approx 10^7$, but attribute these effects to variation in the LAP and transition effects within the thick scintillator used to make measurements of particle numbers. These transition effects were studied by comparing densities measured in 50mm and 4mm thick scintillators. It was found that greater signals are observed in 50mm scintillators. The proportional increase in signal is greatest at core distances of $\sim 1m$ but is negligible at distances greater than $\sim 10m$. They are, therefore, important for the closely spaced array at Akeno, but probably have little effect for GREX. This increased density near the core would result in a reduction in the measured age. It was also found that the transition effects were greatest in younger showers, so that much of the variation in measured age was attributed to these effects. In contradiction to this, in the same paper, it is stated that little variation in the transition effect is seen with changing shower size. The Kobe Group (Asakimori *et al.* 1986) have also shown the scintillator transition effects to change little with shower size.

A decrease in shower age with size might be expected from simple arguments concerning the development of the shower. Showers with larger size tend to reach their maximum lower in the atmosphere as the particles need to penetrate more atmosphere before reaching critical energy. This reasoning is supported by results of Monte Carlo simulations made by Fenyves (1985) which show that the mean age of showers initiated by primaries of energies 10^{15} eV and 10^{16} eV (resulting in showers at sea level of $\sim 10^5$ and 1.6×10^6) are 1.33 and 1.26 respectively. Simulations by Cheung and Mackeown (1987) also predict a decrease in age with shower size.

There are also reports of age increasing with shower size. Abdullah *et al.* 1981 making measurements with the sea level array at Durham quote ages of ~ 1.16 and 1.32 for vertical showers of sizes 2.5×10^5 to 5×10^6 and 5×10^6 to 5×10^7 respectively after allowing for the variation in collecting area of their array with shower age and size. It is suggested that this change may be due to change in primary composition at the knee in the primary spectrum. Simulations by Bray *et al.* (1964) show that the expected density at the core of an air shower is proportional to the energy per primary nucleon, whereas the total number of particles in the shower is proportional to the total energy of the primary. Thus a shower produced by a large nucleus would appear to have a flatter ldf. However, Abdullah *et al.* also acknowledge the fact that the observed effect could be due to the increase in the mean distance at which density measurements are made for large showers. Khristiansen *et al.* (1981) made detailed measurements of the ldf of electrons using Geiger Muller tubes, thus greatly reducing problems due to transition effects in scintillator measurements. These studies showed that the mean ldf varies little over a large range of shower sizes from $\sim 7 \times 10^4$ to $\sim 2 \times 10^7$ particle. The variation in the steepness of the showers with core distance, however was still observed.

The results of measurements of the variation of age with shower size are somewhat contradictory. Much of the disagreement between experiments may be attributed to different analysis techniques, and more importantly detector configuration and shower selection. The type of detector will also affect age measurements due to the

different transition effects within each.

4.9 Transition effects in lead shielding

Transition effects in lead shielding may be observed by comparing the ages of showers detected by the array before and after 8mm lead sheets were placed on top of each detector. Figure 4.13 shows the mean age of vertical showers from each of these periods plotted as a function of $S(50)$. Small showers with $S(50) \leq 5\text{m}^{-2}$ show a slight steepening in their l_{df} with the addition of lead, appearing slightly younger, while larger showers have measured ages slightly larger for the covered detectors compared to those that are uncovered. Studies of the transition effect in 1mm and 5mm thicknesses of iron have been carried out by the Kobe Group (Asakimori *et al.* 1986) using two detectors placed one above the other with the iron plate between. The ratio of densities measured in the lower detector to those measured in the upper detector for the 5mm thickness was approximately 1.5 at very small core distances of $\sim 1\text{m}$ and falls approximately linearly with the logarithm of core distance to approximately 1 at a distance of $\sim 50\text{m}$. This apparent steepening is expected for showers observed by detectors shielded with a high 'z' absorber. The critical energy of particles decreases rapidly with increasing nuclear charge of absorber. Thus an 'old' shower entering the shield will be 'rejuvenated': Photons will be more likely to pair produce than be Compton scattered and electrons more likely to emit bremsstrahlung radiation than ionise. Very low energy particles, however, a long way from the core will be more rapidly absorbed. Thus a shower would be expected to appear younger. Surprisingly this does not appear to be the case for large showers.

4.10 Zenith angle dependence of age

The complex and strong size dependence of the age parameter masks what might be expected to be a weaker zenith angle dependence for shower of the same size

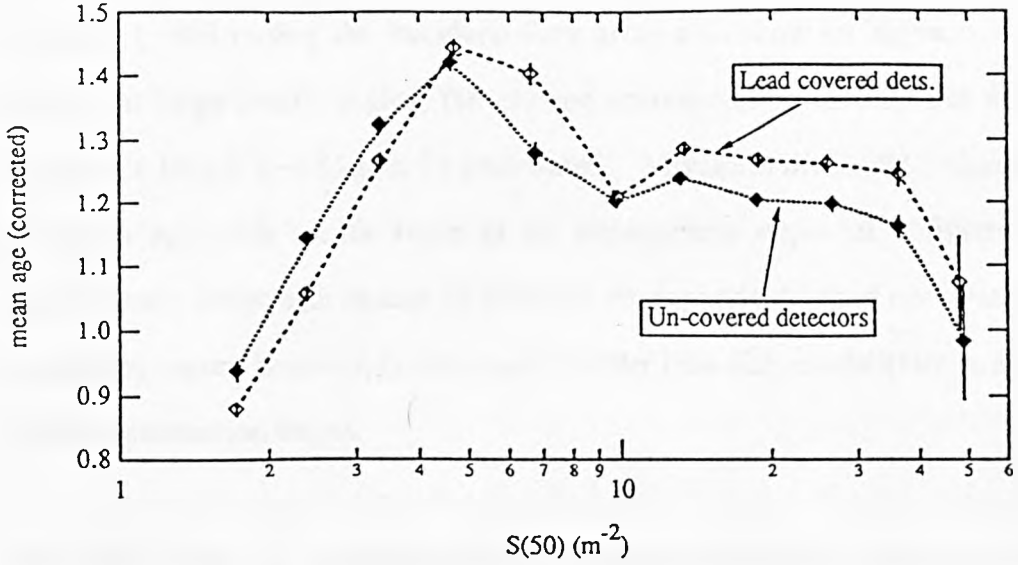


Figure 4.13 Comparison of the age parameter measured with lead covered and un-covered detectors. The mean ages of vertical showers with cores lying within 30m of the array centre are shown plotted against $S(50)$.

normalised to a fixed atmospheric depth. Referring again to Figure 4.9, there does indeed appear to be a weak zenith angle dependence for the largest shower sizes, with showers at large zenith angles appearing slightly older. This difference is difficult to quantify at fixed shower size. That showers at large zeniths appear older than vertical showers of the same size is to be expected as they have been further attenuated by the additional atmospheric absorber that they have penetrated. The measurements by Gerhardy (1983) using the Buckland Park array also show an increase in age for showers at large zenith angles, the change corresponding to 0.13 per additional attenuation length ($\sim 185\text{gcm}^{-2}$) penetrated. Miyake *et al.* (1981) also report a change in age with zenith angle at an atmospheric depth of 735gcm^{-2} being approximately linear with change in effective atmospheric depth of observation. The change they report, however, is very much smaller than that reported by Gerhardy at only ~ 0.06 per attenuation length.

4.11 Use of the age parameter to distinguish between nucleon and γ -ray initiated EAS

Certainly the single most important claim for emission of PeV γ -rays from a point source was the detection of Cygnus X-3 by the Kiel Group (Samorski and Stamm 1983). This observation acted as a catalyst to many people working in the field at the time to initiate point source searches in their data. The reported dc signal at a significance level of 4.4σ was observed in showers whose measured age was greater than the median (1.3). It was believed that γ -ray induced showers would appear older than hadron induced showers which are continuously rejuvenated by the subcascades generated by the primary as it penetrates deeper in the atmosphere, its original direction little altered. Confirmation of emission from Cygnus X-3 followed shortly from the Haverah Park group (Lloyd-Evans *et al.* 1983), but no age cut was made in this data set. Since these initial observations, a number of other groups have imposed a high age cut in their data in order to favour γ -rays and hence improve signal to noise ratios. In

particular, the Adelaide Group making observations of Vela X-1 with the Buckland Park array imposed an age cut to improve their signal (Protheroe *et al.* 1984). Events whose age was less than the median age (1.3) were rejected. The resultant data set showed no significant dc excess but had a strong narrow peak in the ~ 9 day orbital period at a phase of ~ 0.63 . The overall chance probability of this observation was estimated to be 10^{-4} . When showers of all ages from within 2° of the direction of Vela X-1 were examined, the phase bin centred on 0.63° contained no events with age < 1.3 . It would appear, therefore that if the excess in this bin of ~ 7 events is indeed due to γ -rays from the direction of Vela X-1, then these γ -rays produce EAS with significantly broader lateral distributions than background cosmic rays. On the other hand, if the 'signal' in old showers is simply a statistical fluctuation, the lack of events in the same phase bin with age less than 1.3 was hardly surprising, as only ~ 1 was expected. The age of showers measured at Buckland Park show a strong size dependence which has already been described (Section 4.8). The age of showers rises rapidly with size to a peak at $N \approx 7 \times 10^5$ ($s \approx 1.3$) and declines for larger showers. Selecting showers with $s > 1.3$, therefore, may actually represent a selection of median sized showers. This may enhance the signal in two ways:

- (i) low energy showers having poor angular resolution would be eliminated.
- (ii) If the Vela X-1 γ -ray spectrum at these energies is steeper than the background, or perhaps has a sudden cut off at large energies, then an excess would be more likely to be seen in the lower energy events. Thus, eliminating the highest energy showers would enhance the signal to noise ratio.

Cuts in age were also made by the Ooty Group in observations of Cygnus X-3 between June 1984 and Nov 1986 (Tonwar *et al.* 1988). A small, not particularly significant, dc excess at 1.8σ was seen in the complete data set for a bin centred on Cygnus X-3. Surprisingly, square bins were not used, but bins 4° wide in both declination and right ascension, these bins being somewhat narrower in space angle in RA than in declination. When an age cut is applied to the data, eliminating showers with $s < 1.4$, (rejecting $\sim 2/3$ of the data), the dc excess was increased to 3.4σ . Modulation

was also seen in the 4.8hr X-ray period. The use of such a high age cut (those by both the Kiel and Adelaide were at their median age) is justified by quoting the results of the simulations by Cheung and Mackeown (1987) which give the mean *longitudinal* age of showers initiated by primaries of energy $\sim 10^{15}$ eV at the mean atmospheric depth of observations of Cygnus X-3 to be 1.5. The fact that Monte Carlo simulations of nucleon induced air showers described in the same paper show, if anything that such showers have slightly flatter lateral distributions than their γ -ray counterparts is discounted on the basis that the mean age of the background showers measured at Ooty (≈ 1.1) is significantly smaller than the simulations would suggest. Another problem with the age cut at 1.4 is that the *longitudinal* age is, according to the same paper by Cheung and Mackeown, an overestimation of the *transverse* age (that appearing in the NKG function), the latter being ~ 0.22 smaller. Thus, the value of the NKG age of a γ -ray shower would be expected to be ~ 1.28 , so that rejection of showers with $s < 1.4$ would almost certainly remove a large number of γ -ray showers, if Cheung and Mackeown are to be believed.

The simulations by Cheung and Mackeown are in agreement with those by Fenyves (1985) and Hillas (1984) which show that there is little difference in the age of showers induced by protons and γ -rays which give rise to showers of the same sea level sizes. The latter are, if anything slightly steeper and become more so at higher altitudes, though the distributions greatly overlap at all altitudes. These simulations deny any possibility of using age cuts - particularly in selecting older showers - to enrich a data set with γ -ray induced showers. A number of possible explanations exist for this apparent contradiction between theoretical predictions and experimental evidence: (i) that hadrons or photons interact in an unexpected way at these energies. Perhaps γ -rays have a shorter radiation length and thus the showers attenuate faster than assumed in Monte-Carlo simulations. A corresponding increase in the mean free path of hadrons would be required to maintain the same attenuation length in proton induced showers. Another possibility is that the opening angle for pion production is less thus reducing the lateral spread of hadron showers. (ii) that the excesses observed from Vela X-1 and

Cygnus X-3 are due to particles other than γ -rays. Certain limits would be imposed on the nature of such particles: they must be neutral so as to remain undeflected by the galactic magnetic field, and be sufficiently stable to survive the journey from the source - this excludes neutrons at this energy which would have a mean lifetime at these energies (taking into account relativistic time dilation) of 1×10^9 s compared to the journey time from Cygnus X-3 and Vela X-1 of 5×10^{11} s and 2×10^{11} s respectively. Upper limits are also placed on the mass of the particles (Hillas 1984) by the fact that they retain timing information. Dispersion in arrival times would be expected for massive particles travelling at speeds less than that of light, if these particles are not mono-energetic. Consideration of the spread of velocities of particles of various masses leads to an upper limit of 0.2 MeV for the mass of the particles to retain the modulation in signal at the 12.6ms pulsar period observed at TeV energies from Cygnus X-3. If only the modulation at the 4.8 hr period is to be believed, then this upper limit is increased to 60 MeV. Neutrinos are also excluded as they would not interact in the upper atmosphere. There is little choice left, therefore, but γ -rays. (iii) that the observed 'signals' at PeV energies are simply statistical fluctuations in the background. There is certainly some support for this view (Chardin and Gerbier 1989), and the lack of confirmation of observations by other experiments coupled with poor statistics and confusing and often contradictory cuts made in data (age being one of them) serve only to increase skepticism. (iv) that age cuts actually represent cuts in other shower parameters such as shower size - this has already been discussed with reference to Adelaide's Vela X-1 result. Another, less likely possibility is that selecting older showers favours those observed at large zenith angles. This would affect the phase analysis of sources. In particular, if the source has a period which divides almost exactly into 1 sidereal day (eg Cygnus X-3, $P \approx 1/5$ day) or is almost an integer multiple of a sidereal day (eg Vela X-1, $P \approx 9$ days), then the period during which it was at large zenith angles, close to the limit of the arrays acceptance horizon, would occur at approximately the same time in its orbital period. Finally it is possible that the angular resolution of events is better for older showers. This being the case, eliminating

poor resolution events, with low age would, somewhat indirectly, improve signal to noise ratios.

4.12 Conclusions

The detailed analysis described in this chapter has shown the determination of the age parameter with the GREX array to be highly problematical for showers close to the array threshold, where the small numbers of triggered detectors and large density fluctuations make accurate measurement of the ldf impossible. It is, however, possible to measure the age of showers as small as $S(50) \approx 1.4\text{m}^{-2}$ falling within 30m of the array centre and for larger showers, $S(50) \geq 4\text{m}^{-2}$, distributed across the whole of the array. These showers constitute only ~10% of all events triggering the array and are not a sufficient sample to make the calculation of age worthwhile given the significant random and systematic errors that clearly exist. The ages of all events, therefore, are not calculated routinely for the purpose of source searching. The mean age of all events lying within 30m of the array centre with $S(50) \geq 1.4\text{m}^{-2}$ is 1.29. The measured age of events with $S(50) \leq 8\text{m}^{-2}$ increases with shower size to a maximum of ~1.5 for showers of $S(50) \approx 8\text{m}^{-2}$, above which it appears to decrease. The same trend is seen in showers at all zenith angles. Much, if not all, of this size dependence may be due to transition effects within the detectors, and the different core distances at which densities are sampled with change in shower size. In large showers, there is some evidence for increased age at large zenith angles, though the exact dependence is uncertain due to the large size dependence already mentioned.

CHAPTER FIVE

METHODS OF SEARCHING FOR SOURCES OF γ -RAYS

5.0 Introduction

The low fluxes expected from sources of Ultra High Energy γ -rays along with the high fluxes of background cosmic rays tend to lead to poor signal to noise (S/N) ratios in Extensive Air Shower experiments. The S/N ratio can be maximised by reducing the uncertainty in the mean background and by maximising the useful on-time of the array during which on-source and off-source showers will be accepted. Attempts have also been made in some observations to reduce the numbers of background events by making selection criteria *that might favour* γ -ray induced showers. These include selecting older, more developed showers (Chapter 4) and rejecting showers with large muon content.

Generally, in EAS experiments, the on-source events are accepted in a bin of some solid angle, ω_{on} , centred on a candidate source. The off-source events used to calculate the contribution of the background are collected from a different part of the sky, of solid angle, ω_{off} , over which the total number of events collected per unit solid angle would be expected to be the same as that of the on-source bin in the absence of a real signal.

The best estimate of the signal, or the number of counts attributed to the source is given by

$$s = N_{on} - \langle N_b \rangle \quad \dots \text{Eqn 5.1}$$

where N_{on} is the number of counts in the region ω_{on} and $\langle N_b \rangle$ is the estimate of the number of those counts that are due to background events. This estimate is given by:

$$\langle N_b \rangle = \alpha N_{off} \quad \dots \text{Eqn 5.2}$$

where N_{off} is the number of events collected in the region ω_{off} and α is a factor used to

account for the difference in solid angle of collection of off- and on-source events

$$\alpha = \omega_{\text{on}}/\omega_{\text{off}} \quad \dots\text{Eqn 5.3}$$

Generally, $\sqrt{\langle N_b \rangle}$ is taken to be the Poisson uncertainty in the number of background events in the on-source bin and results are quoted as 's / $\sqrt{\langle N_b \rangle}$ sigma results'. These quoted levels of significance, however, fail to take properly into account the uncertainties in the calculated expected background rate which are a consequence of Poisson fluctuations in the total number of off-source events, N_{off} . These uncertainties are important in the case where the off-source collecting solid angle, and hence N_{off} , is small.

An appropriate method of calculating the significance of a signal taking into account both the Poisson fluctuations of the background in the signal bin and the uncertainty in the mean background was found by Li and Ma (1983). They point out that if λ is the ratio of the likelihoods of the null hypothesis (the apparent signal being due entirely to background fluctuations) to the likelihood that all of the apparent excess is associated with a genuine source, then $-2\ln\lambda$ follows a χ^2 distribution with 1 degree of freedom. They go on to derive an expression for λ using Poissonian statistics and give the significance of a signal, S as:

$$S = \sqrt{2} \left\{ N_{\text{on}} \ln \left[\frac{1 + \alpha}{\alpha} \left(\frac{N_{\text{on}}}{N_{\text{on}} + N_{\text{off}}} \right) \right] + N_{\text{off}} \ln \left[(1 + \alpha) \left(\frac{N_{\text{off}}}{N_{\text{on}} + N_{\text{off}}} \right) \right] \right\}^{\frac{1}{2}} \quad \dots\text{Eqn 5.4}$$

where the result may be quoted as an 'S standard deviation' result. In the case of the null hypothesis being true, S has a Gaussian distribution with mean of 0 and a standard deviation of 1. Thus the chance probability of a given observation, in the case of an excess of events in the on-source bin is obtained by integrating over the Gaussian distribution function in the limits $S \rightarrow \infty$. Consequently, the ideal method of source searching will maximise the signal to noise ratio by increasing the useful observational time of the experiment and by maximising the solid angle over which off source events are collected. This Chapter describes two methods for assessing the background. Section 5.1 describes the 'dec strip' method where the background events are accepted in a narrow strip in declination centred on the source. This is the most widely used

method for evaluating the background in E.A.S. experiments. Section 5.2 describes the 'Azimuthal' method in which the background is calculated from events whose zenith angles are close to that of the source. The relative merits of the 'azimuthal' and 'dec strip' methods of calculating the background are discussed in Section 5.3.

5.1 The 'dec strip' method of source searching

On-source events are accepted in, for example, a square bin in declination (δ) and Right ascension (RA) of dimensions $\Delta\delta$ and ΔRA the centre of which is at the declination, δ_s , and right ascension, RA_s , of the candidate source. Square bins are obtained by taking the width in RA to be

$$\Delta RA = \Delta\delta / \cos\delta \quad \dots \text{Eqn 5.5}$$

The background events are accepted in n bins whose centres are at the same declination as the source but at an angular distance ΔRA , $2\Delta RA$ etc on either side of the source (Figure 5.1). Thus, the solid angle of each off source bin is equal to that of the on-source bin, and the ratio of on-source to off-source collecting solid angles is given by:

$$\alpha = 1/n \quad \dots \text{Eqn 5.6}$$

To minimise the uncertainty in the mean background contribution to the on source bin, we need to maximise the number of off-source bins.

5.1.1 SIGNAL TO NOISE RATIO DEPENDENCE ON BIN SIZE

For a constant source strength and background, it is possible to calculate an ideal bin size. The graph in Figure 5.2 shows the S/N ratio as a function of bin width in units of standard deviations of the point spread function (σ) for both circular and square bins. The noise is taken to be the Poisson fluctuations in the mean counts in the bin for a background count of 1 count per solid angle of σ^2 . The signal is calculated as follows:

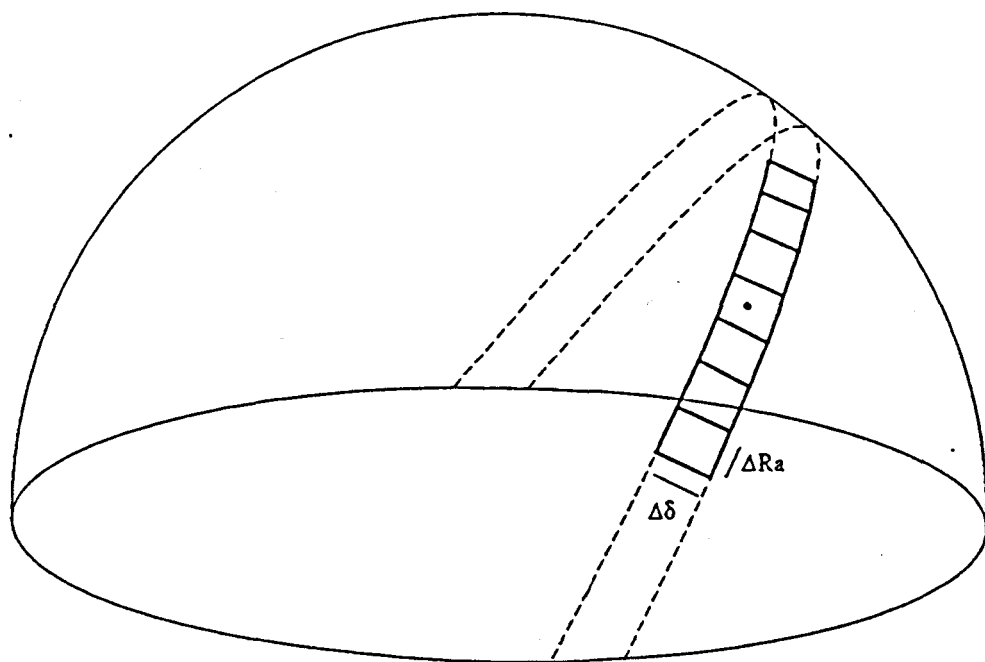


Figure 5.1 Binning events in the 'dec strip' method of source searching. Bins are of dimensions $\Delta\delta \times \Delta Ra$. On-source events are accumulated in the central bin while off-source events are accumulated in the remaining bins. All bins pass through the same range of zenith and azimuthal angle as they each transit in turn.

Let x and y be the angular distance from a given source position in two perpendicular directions. If x and y are Gaussian distributed variables, each with standard deviation, σ , then the probability that the event will lie in the square region $x \rightarrow x+dx$ and $y \rightarrow y+dy$ is given by:

$$P(x \rightarrow x+dx, y \rightarrow y+dy) = \left(\frac{1}{\sqrt{2\pi}\sigma} \exp\left(-\frac{x^2}{2\sigma^2}\right) dx \right) \left(\frac{1}{\sqrt{2\pi}\sigma} \exp\left(-\frac{y^2}{2\sigma^2}\right) dy \right) \dots \text{Eqn 5.7}$$

Thus, if there are a total of N_s source events, the expected number of events attributable to the source within a square bin of width a centred on the source is given by

$$s = \frac{N_s}{2\pi\sigma^2} \int_{-a/2}^{a/2} \exp\left(-\frac{x^2}{2\sigma^2}\right) dx \int_{-a/2}^{a/2} \exp\left(-\frac{y^2}{2\sigma^2}\right) dy \dots \text{Eqn 5.8}$$

These two integrals are calculated numerically.

For a circular bin, the integral is solved by a change to polar coordinates. The probability that an event from the source will be observed within an infinitesimally thin annulus of radius r and width dr is given by

$$P(r \rightarrow r+dr) = \frac{1}{2\pi\sigma^2} \times 2\pi r \exp\left(-\frac{r^2}{2\sigma^2}\right) dr \dots \text{Eqn 5.9}$$

so that the expected number of events within a circular bin of radius r' centred on a source of strength N_s is given by the integral of this expression between the limits 0 and r' . This integral is found analytically and is given by:

$$s = 1 - \exp\left(-\frac{r'^2}{2\sigma^2}\right) \dots \text{Eqn 5.10}$$

In both cases it is assumed that the source strength is $N_s = 1$ in obtaining the graph in Figure 5.2. The optimum bin sizes for which the S/N is maximum along with the percentage of N_s included in those bins are given for circular and square bins in Table 5.1. The S/N ratio falls off more slowly for bin sizes greater than optimum than for those less than optimum and it is therefore better to choose bins that are slightly larger than optimum in cases where the exact width of the p.s.f. is uncertain.

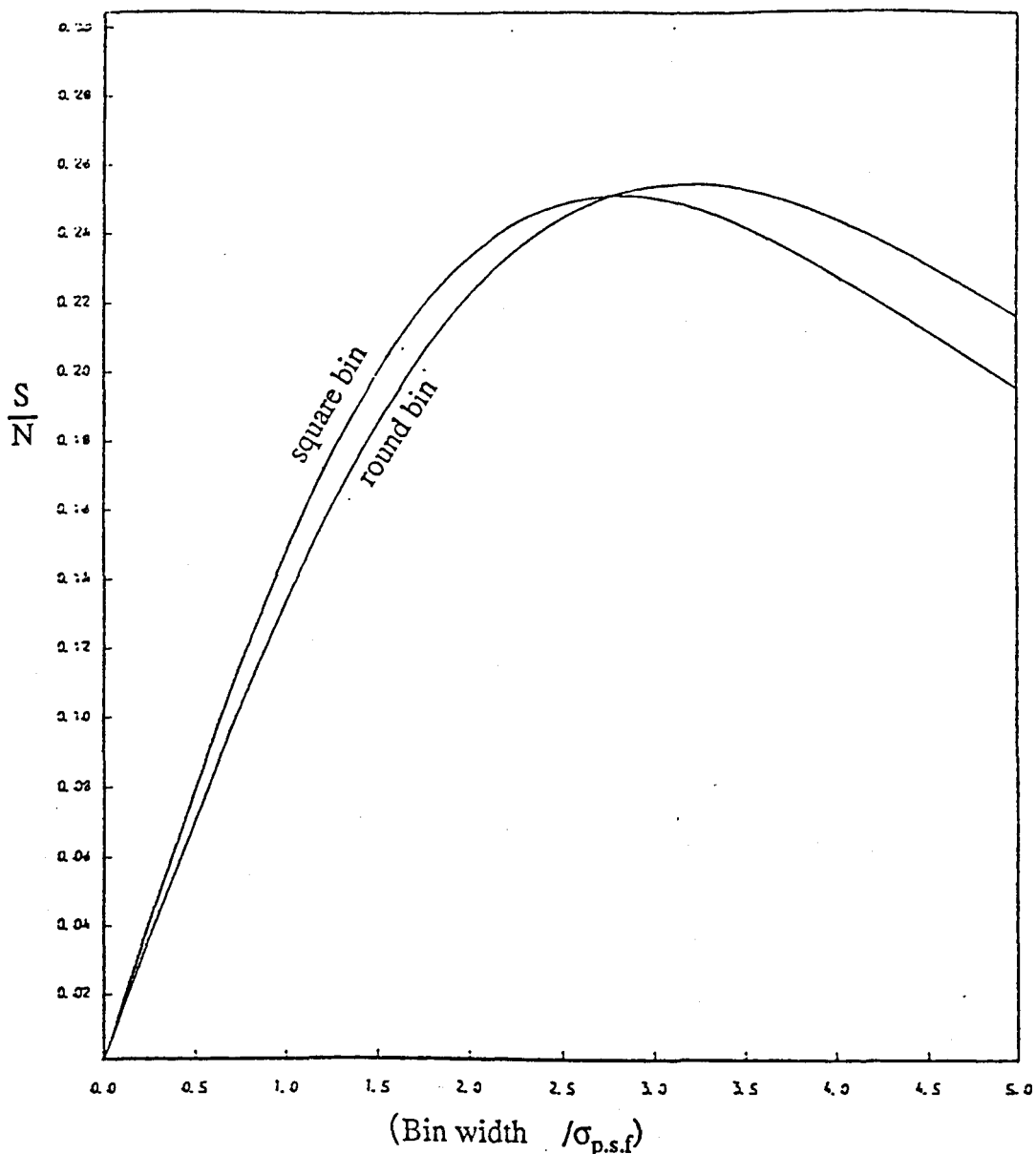


Figure 5.2 The signal to noise ratio (in arbitrary units) is shown plotted as a function of bin diameter for circular bins and width for square bins. Bin dimensions are in units of standard deviations of the assumed source point spread function.

	Optimum bin width/diameter ($\sigma_{p.s.f}$)	signal included in bin (%)
Square bin	2.80	70.3
Round bin	3.17	71.5

Table 5.1 The round and square bin widths that maximise signal to noise ratios in source searches in units of angular resolution.

5.1.2 CHOICE OF BIN SIZE FOR USE WITH HAVERAH PARK DATA

Since no sufficiently strong and reliable dc source of PeV γ -rays has yet been observed by this experiment, or for that matter any other, it has not been possible to make direct measurements of the point spread function of the array. It is assumed, therefore that the spread in assigned arrival directions for γ -rays from a point source is equal to the angular uncertainties of background showers. These arrival direction errors arise from timing uncertainties which are due to shower front thickness, finite pulse rise times, instrumental resolution and uncertainty in detector coordinates. The accuracy of a determined arrival direction varies greatly from shower to shower. Naturally, large showers, with greater numbers of triggered detectors, have their direction better located than small showers. In addition, a good geometrical arrangement of triggered detectors spread over a large area will give good directions compared to an arrangement in which timing detectors tend to be strung out in a line. The angular resolutions for showers categorised according to size, zenith angle and this spatial arrangement of detectors (pattern type) were determined by Bloomer (1990). The Appendix gives a summary of the angular resolutions currently adopted for the GREX array. Individual showers are grouped so that the array has approximately the same angular resolution for all events within each subset. In searching for a source of γ -rays, a bin size equal to the optimum binsize for the showers of worst angular resolution within each group is used for all the events within that group. Thus the numbers of on- and off-source regions are accumulated for each group separately. The square bins vary greatly in size. For instance, for the lead covered array, the smallest bin has $\Delta\delta = 1.37^\circ$ and the largest, $\Delta\delta = 4.66^\circ$. These are shown for comparison in Figure 5.3. Having accumulated the on- and off-source events for each group, N_i^{on} and N_i^{off} respectively, the total number of on- and off-source events are calculated:

$$N^{\text{on}} = \sum_{i=1}^n N_i^{\text{on}} \quad \dots\text{Eqn 5.11}$$

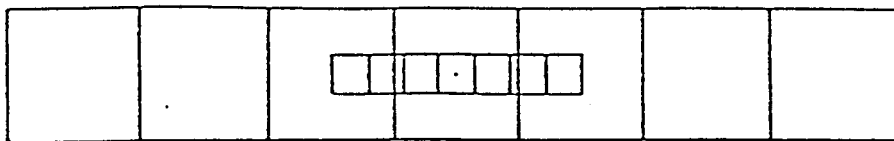


Figure 5.3 Comparison of the largest ($\Delta\delta = 4.66^\circ$) and smallest ($\Delta\delta = 1.37^\circ$) square bins used for source searches after Bloomer (1990). The width of the bins in RA is given by $\Delta\delta / \cos\delta$.

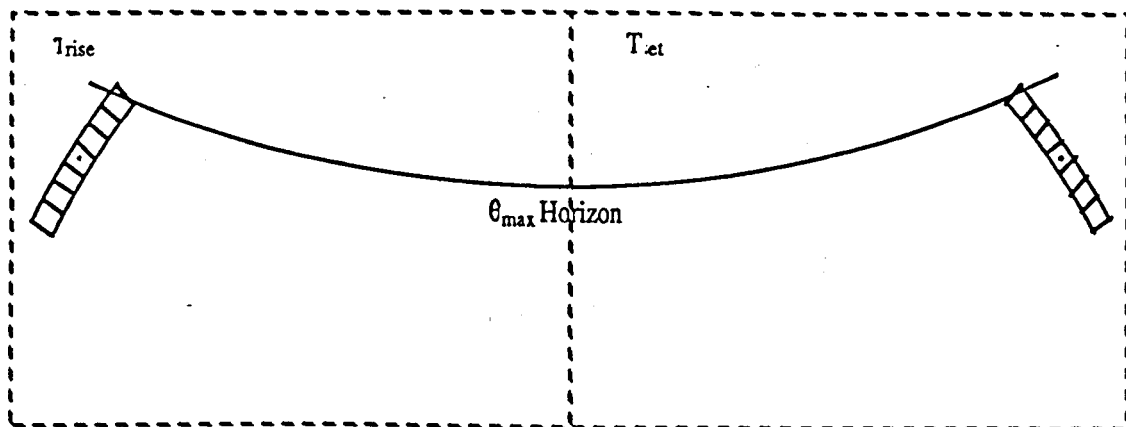


Figure 5.4 The 'shortened sidereal day'. Events are only expected with zenith angle less than θ_{\max} and hence in the time interval between the rise of the leading edge of the search strip rising above the θ_{\max} horizon (T_{rise}) and the trailing edge of the strip setting below this horizon (T_{set}).

$$\text{and } N^{\text{off}} = \sum_{i=1}^n N_i^{\text{off}} \quad \text{..Eqn 5.12}$$

where n is the total number of shower groups. In this way, the optimum signal to noise ratio is achieved for showers having a wide range of angular resolutions.

5.1.3 METHODS OF GUARANTEEING EQUAL EXPOSURE IN ON- AND OFF-SOURCE BINS

The demand for equal exposure in all bins means simply that the expected background rate integrated over the specific time interval of interest be the same for each. This is an obvious prerequisite for making meaningful comparisons of on- and off-source count rates. On a long term basis - over a year or so - accepting all events while the array is turned on would not be expected to produce a systematic difference in exposure between the bins. However on a day-to-day basis this is certainly not the case and may lead to under or over estimation of the background. Gamma-ray sources are notoriously transitory in their behaviour: there have been claims that Her X-1, for example, shows short term enhancement on time scales of between 3 and 100 minutes (see Chapter 6). It is therefore important to obtain equal exposure on all time scales. It is convenient to consider the transit of the source over a single sidereal day to illustrate this problem. A zenith angle cut in the data at θ_{max} will also be imposed. We now need to impose the condition that the expected counts in all the bins be equal in the shortened sidereal day between the leading edge of the search strip rising above the θ_{max} cone, T_{rise} , and the trailing edge setting below θ_{max} , T_{set} (Figure 5.4) for events from that sidereal day to be accepted. Two methods for achieving this will be compared.

5.1.4 EQUAL ON-TIME METHOD

For each bin, i , the time for which the array is on between rise time, T_i^{rise} , and set time, T_i^{set} , can be calculated, T_i^{on} . Demanding equal on-time then simply means that all T_i^{on} are equal within some fractional tolerance. This method, although guaranteeing that each bin collects data above the event horizon for the same length of time on any particular day, does not guarantee equal exposure. The count rate per unit solid angle observed by the GREX array is a strong function of zenith angle varying as $\cos^7\theta$. Hence if the array is turned off for a short time ΔT , a bin at θ_1 will effectively lose a number of events, N_1 given by:

$$N_1 \propto \Delta T \cos^7\theta_1 \quad \dots\text{Eqn 5.13}$$

similarly a bin at θ_2 will lose N_2 events given by:

$$N_2 \propto \Delta T \cos^7\theta_2 \quad \dots\text{Eqn 5.14}$$

if $\theta_1 > \theta_2$ then $N_1 < N_2$ and the total count rate in bin 1 will be less than in bin 2. This situation can easily arise without violating the equal on-time requirement. Consider the case illustrated in Figure 5.5. The array is turned on at some time T_1 before the rise of the leading edge of the search strip Figure 5.5(i). Some time after all the bins have risen above θ_{max} , T_2 , the array is turned off, Figure 5.5(ii). At time T_3 , before any bins have begun to set, the array is turned back on, Figure 5.5(iii). Finally the array is turned off at time T_4 when all the bins have set, Figure 5.5(iv). It can be seen, in this case, that all bins will have the same on-time. Bin 1, however, will have passed through zenith angles θ_1 to θ_2 and bin 7 through angles θ_3 to θ_4 while the array was turned off. The two bins will, therefore, have different exposures. The same is true for all the bins. The background estimated in this way will be a poor estimate of the background contribution to the on-source bin and systematically incorrect on a day to day basis. When averaged over many days, however, this method is unlikely to introduce a significant systematic error.

A further problem with this method is that the demand for equal on-time over

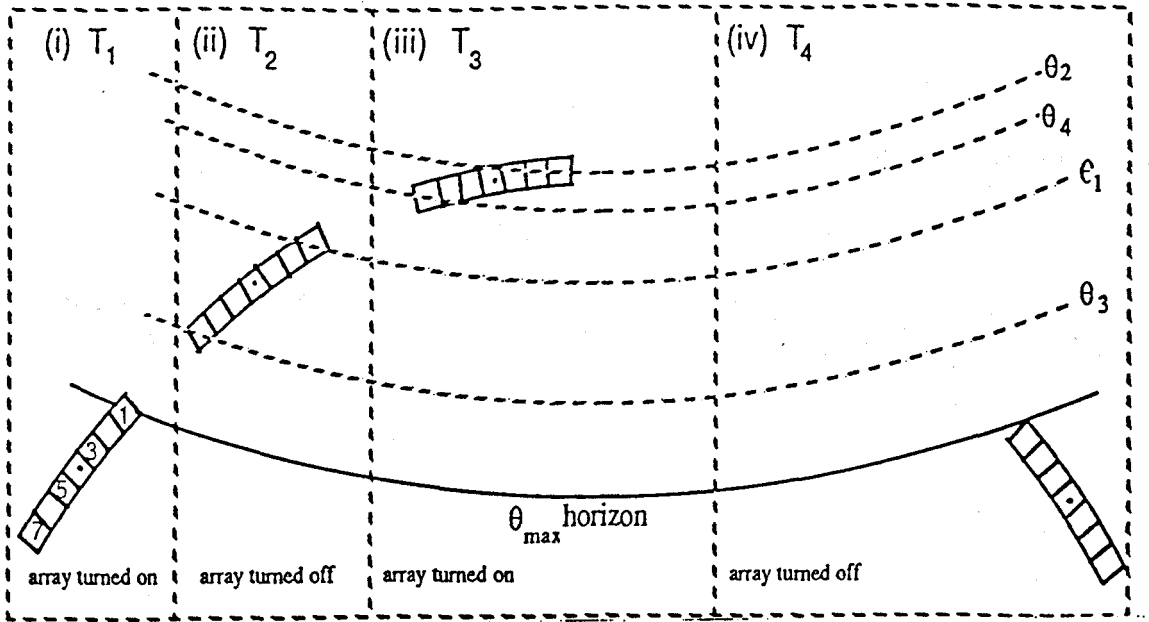


Figure 5.5 A typical day in which the demand for equal on-time in all bins does not lead to equal exposure across the whole strip. The array is on for the whole sidereal day except for a short period between T_2 (fig. (ii)) and T_3 (fig. (iii)) during which all bins are above the θ_{\max} horizon.

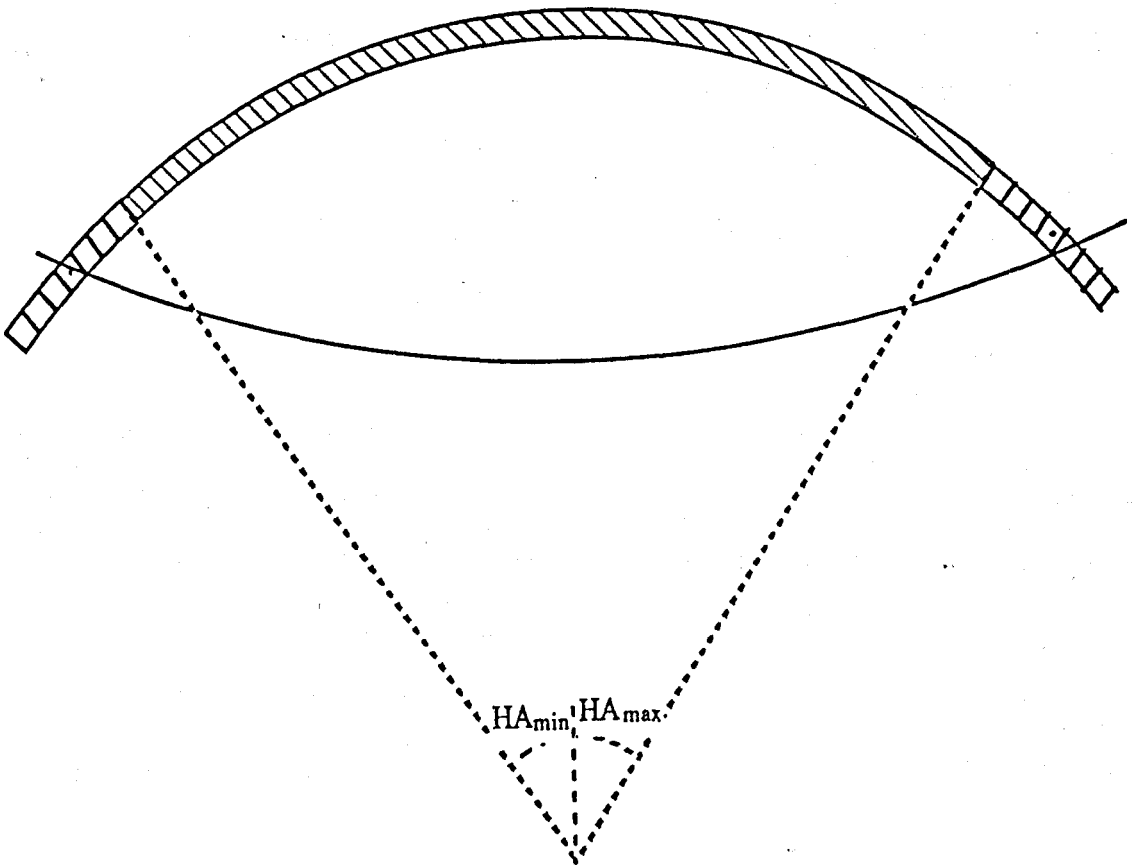


Figure 5.6 Equal exposure in all bins is guaranteed by only accepting events with hour angles in the range HA_{\min} to HA_{\max} , the hour angles of the leading edge of the search strip at array turn on and that of the trailing edge at turn off respectively.

a complete sidereal day in all search bins may lead to the rejection of nearly complete days and the loss of potentially useful data. This will occur when the array is turned on when only part of the search strip has risen or turned off when only part of the search strip has set.

Both these problems can be solved using the following method that guarantees equal exposure in all bins and maximises the useful observation time on a source.

5.1.5 EQUAL EXPOSURE METHOD

By only accepting showers whose hour angles lie between the hour angle of the leading edge of the search strip, HA_{\min} , at the time at which the array is turned on, T_{on} , and the hour angle of the trailing edge of the search strip, HA_{\max} , at the time at which the array is turned off, T_{off} , equal exposure for all bins is guaranteed. Figure 5.6 illustrates this method applied to a day similar to the one discussed in the previous section where the array was turned on when the search strip had only half risen and turned off when only a fraction of the strip had set. HA_{\min} and HA_{\max} are as described previously. It can be seen that all the bins pass through the shaded region of the sky. They therefore all pass through the same range of zenith and azimuthal angles and will have equal exposure. The useful on-time is then equal to the difference in the minimum and maximum hour angles.

It is useful to view this situation as the array turning on and off at different times for each bin. The turning on and off times for each bin are given by the times at which the bin passes through HA_{\min} and HA_{\max} respectively. The graphs in Figure 5.7 show the background rates in bins 1, 3, 5, and 7 as a function of absolute time for the case illustrated in Figure 5.6. The total number of counts expected in each bin is simply the integral of the count rate represented. It is obvious that the integral number of counts between T_{on} and T_{off} is different. If however the effective turning on and off times of each bin are T_i^{on} and T_i^{off} respectively as illustrated, then we would expect to have the

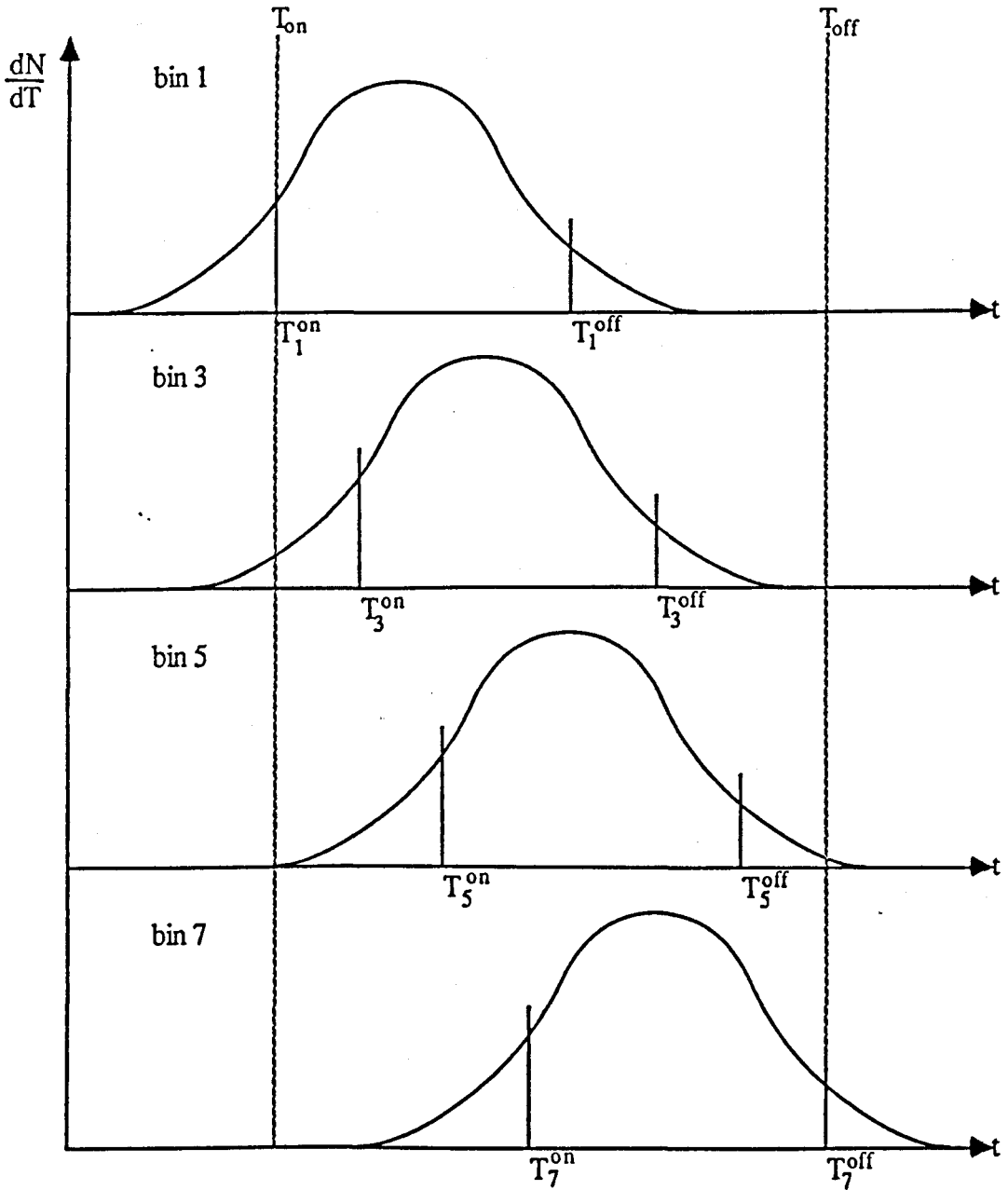


Figure 5.7 The count rate for a number of search bins is shown as a function of time. The bins are numbered leading edge first (refer to fig. 4.6). The array is turned on some time after bin 1 has risen (T_{on}) and off before bin 7 has set. Selecting minimum and maximum hour angle between which to accept events is equivalent to switching each bin, i , on and off at different times (T_{on}^i and T_{off}^i) to maintain the same exposure (area under graphs) in each.

same exposure in each bin. The differences in turning on times of consecutive bins is simply the width of the bins in RA.

5.2 Azimuthal Method

The new method for calculating the cosmic ray background which will henceforth be referred to as the azimuthal method was developed in an attempt to maximise the solid angle of collection for off-source events and hence reduce the uncertainty in the background. This is particularly important in searches for signal enhancements on the time scale of a day or so, when the background rate leads to a large relative uncertainty in the determined value of that background. Such searches are currently seen as very important search strategies due to the transitory nature of sources which has already been mentioned. On-source events are collected in a bin centred on the source: it is computationally easy, unlike in the dec-strip method, to use a circular bin which leads to a small improvement in the signal to noise ratio over using square bins of about 2%. Off source counts are accepted in a strip of width equal to the diameter of the on-source bin in zenith angle and 360° in azimuth. Each off-source event is normalised to the on-source bin by correcting for the difference in solid angle of the on-source bin and that of the annulus (less, of course the area of the on-source bin) for collecting off-source counts. Figure 5.8 illustrates the technique. Events from within the circular bin surrounding the source direction, (θ_s, ϕ_s) are accepted as on-source events. Those showers whose directions lie in the remaining solid angle between zenith angles θ_1 and θ_2 constitute the off-source events. For each off-source event, $\Delta\phi_i$, the difference in azimuth of the two points at which the line at constant zenith (equal to the zenith angle of the event) bisects the on-source bin is calculated. The expected contribution of the background to the on-source bin is given by:

$$N_b = \sum_i \left(\frac{\Delta\phi_i}{360 - \Delta\phi_i} \right) \quad \dots \text{Eqn 5.15}$$

This method has a number of advantages over the dec-strip method: (i) On-time is

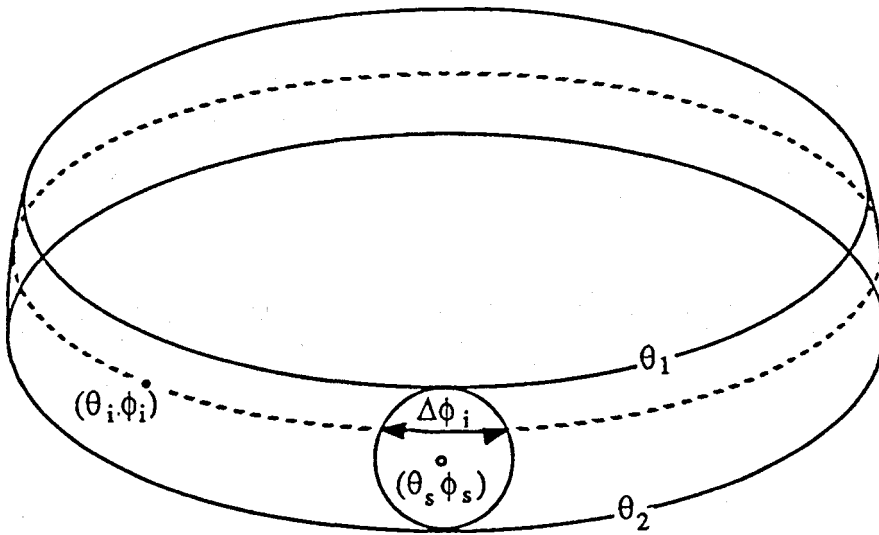


Figure 5.8 The azimuthal strip technique for calculating the background. On-source events are collected within the circular bin centred of the source at coordinates (θ_s, ϕ_s) while the background is calculated in the annulus between zenith angles θ_1 and θ_2 , and corrected for the difference in solid angle of the azimuthal strip and on-source bin (see text).

maximised as events may be accepted whenever the source bin is above the horizon, and the array turned on and (ii) events in off-source and on-source regions are collected simultaneously so that changes in atmospheric conditions such as temperature and pressure will affect the background rates equally in the two regions.

Although the off-source events are collected from precisely the same range of zenith angles as the on-source events, the same is not true for the azimuthal angles, and this may introduce a systematic effect in the background estimate. This is discussed in the next section.

5.2.1 THE AZIMUTHAL ASYMMETRY OF THE GREX ARRAY

Sources, particularly those transiting at large zenith angles may only be observed as they pass through a narrow range of azimuthal angles. Cygnus X-3, for example rises above a zenith angle of 40° at azimuth 84° and sets at azimuth 275° , though the majority of observed events are from a much narrower range than this due to the steepness of the zenith angle distribution. Any geometrical asymmetry in the array may lead to the array having greater effective collecting area for showers from particular directions than those from other directions. If, therefore, a candidate source transits in a preferred region of the sky, then a greater flux will be measured in the on-source bin than in the remainder of the zenith angle strip from which the background is calculated, even in the absence of emission from the source itself. If this effect were not allowed for, it would lead to the excess flux being incorrectly attributed to a signal from the source. Conversely, if the source transits in an area of sky to which the array is less sensitive, the presence of a source may be masked due to overestimates of the background in the on-source bin.

Biases such as those described above may be caused by the slope of the array. This slope is illustrated in Figures 5.9(i) and (ii) which show the height of each detector above a horizontal plane through the centre of the array plotted against their x and y

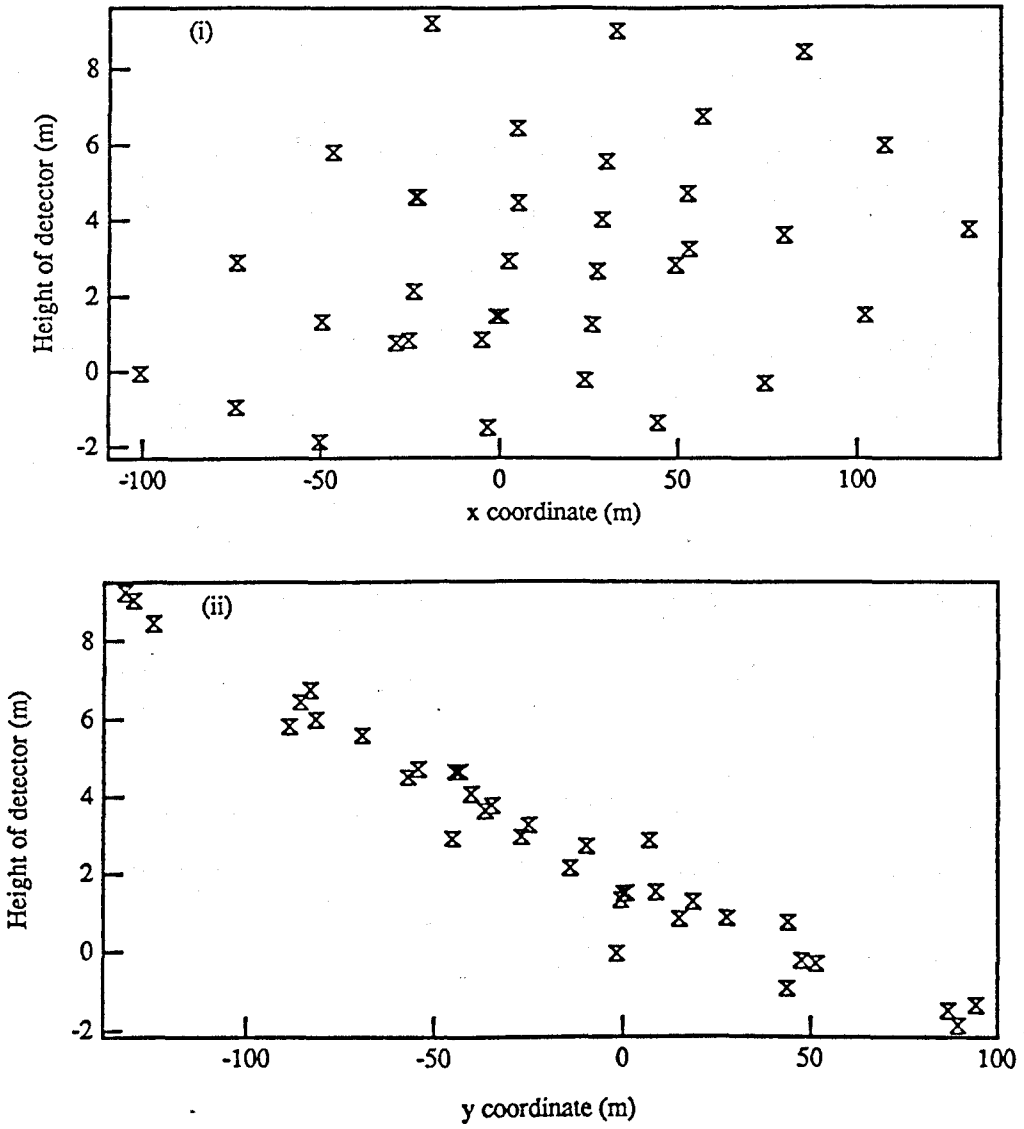


Figure 5.9 (i) and (ii) The height of detectors above a horizontal plane through 15 and 16 is shown plotted against the x and y coordinates of the detectors

coordinates respectively (the positive x and y directions point East and North respectively). The array is seen to be on a tilt, with the Southern most part of the array being some 10m above the Northern most part of the array. There is also a small gradient in the E-W direction. A plane fitted through the detector coordinates has a normal with azimuth, $\phi_n=342^\circ$ and zenith angle $\theta_n=2.9^\circ$

The sensitivity of the array to showers from different zeniths and azimuths has been found by measuring the distribution of directions of triggering showers lying inside the array. All these showers were collected between mid February 1986 and the end of September 1989 and are those satisfying the selection criteria applied to source searching which are given in Section 3.3.1.7. They represent 60% of all showers triggering the array during this period. Figure 5.10 shows the azimuthal distribution of all these events. Strong first and second harmonic modulations are seen in the data, both with peaks in approximately a northern direction. The precise amplitude and phase of these harmonics is calculated using Fourier transforms. This technique is well known and is described by Linsley (1975). The Fourier coefficients for the j'th harmonic are given by:

$$a_j = \frac{2}{N} \sum_{i=1}^N \cos(j\phi_i) \quad \dots\text{Eqn 5.16}$$

$$\text{and } b_j = \frac{2}{N} \sum_{i=1}^N \sin(j\phi_i) \quad \dots\text{Eqn 5.17}$$

where the summation is over N events, each event, i, having azimuth ϕ_i .

The fraction of events lying between f and $f+df$ is approximated by:

$$f(\phi) d\phi = \left(1 + \sum_{j=1}^n (a_j \cos(j\phi) + b_j \sin(j\phi)) \right) d\phi \quad \dots\text{Eqn 5.18}$$

where n is the number of harmonics evaluated. The amplitude of the j'th harmonic is given by:

$$r_j = \sqrt{(a_j^2 + b_j^2)} \pm \sqrt{\frac{2}{N}} \quad \dots\text{Eqn 5.19}$$

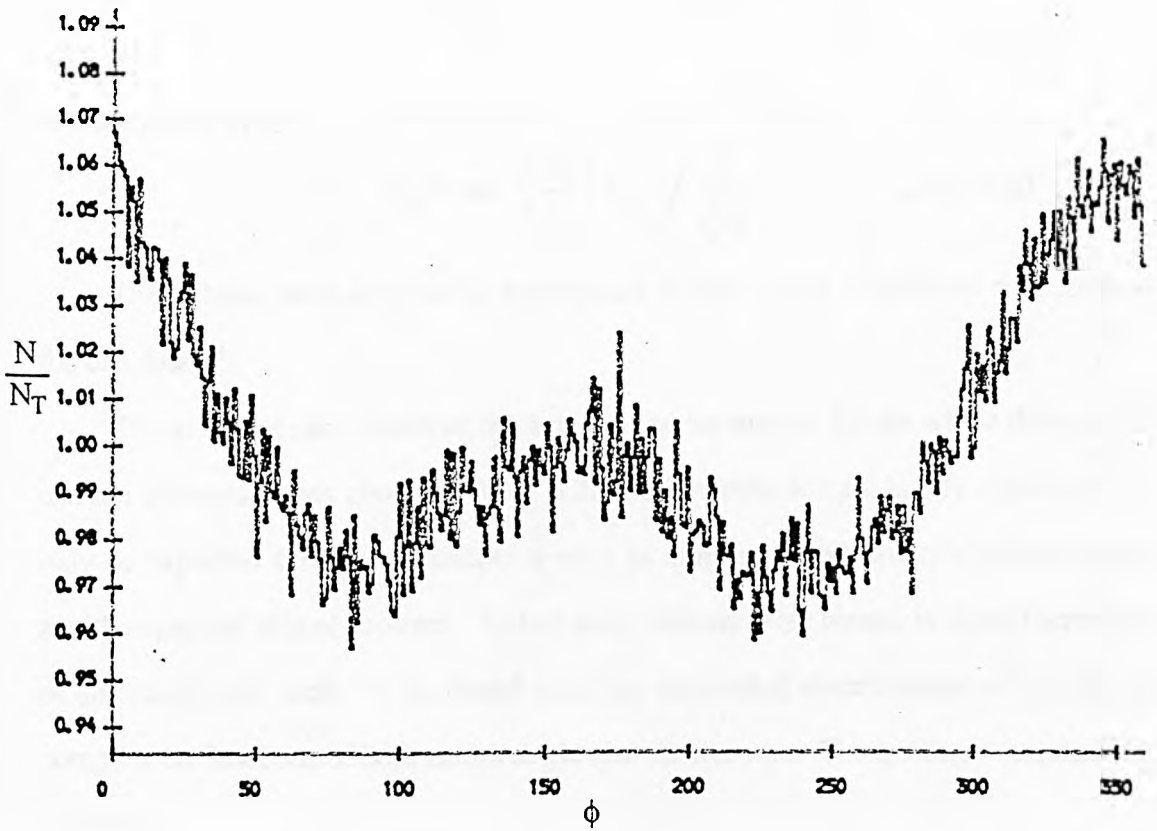


Figure 5.10 The azimuthal distribution of events selected for source searching.

Harmonic	Amplitude(%)	Phase (°)
1	2.56 ± 0.05	353.1 ± 1.2
2	2.58 ± 0.05	332.1 ± 1.1

Table 5.2 The amplitude and phases of the first and second harmonics in the azimuthal distribution of events selected for source searching.

and the phase ψ_j by

$$\psi_j = \tan^{-1}\left(\frac{b_j}{a_j}\right) \pm \sqrt{\frac{2}{r_j^2 N}} \quad \dots \text{Eqn 5.20}$$

The quoted errors only being appropriate in the case of $(r^2 N/4) \gg 1$ as is the case for this data set.

The amplitude and phase of the 1st and 2nd harmonics for the whole data set of 7 million showers are as given in Table 5.2. Both harmonics are highly significant. It may be expected that these harmonics vary in amplitude and possibly direction with zenith angle and size of showers. To test this, showers were binned in equal increments of $\ln[s(50)]$ and $\sec\theta$. It is found that the azimuthal distributions of events are complicated functions of both zenith angle and shower size. The results are summarised as follows.

A) Variation of the first harmonic with zenith angle and shower size.

It is found that for very small showers of all zeniths, the amplitude of the first harmonic r_1 , decreases from $\sim 4\%$ for showers of $S(50) = 0.5\text{m}^2$ to $\sim 0\%$ for showers of $S(50) = 1.6\text{m}^2$. The maximum sensitivity for showers of this size is to those from the South. For showers with $S(50) > 1.6\text{m}^2$, r_1 increases with size to a maximum of $\sim 10\%$ for showers of $S(50) > 5.8\text{m}^2$. For these showers, the peak is in approximately a northern direction. These changes, then, can be seen as a gradual reduction in the sensitivity to showers from the South compared to those from the North with increasing shower size. r_1 is shown as a function of shower size in Figure 5.11 (i). Harmonics with the peak in the South are assigned negative amplitudes. Figure 5.11 (ii) shows the phase of the peaks as a function of shower size.

As the mean size of showers varies with zenith angle, it is useful to describe the zenith angle dependence of the 1st harmonics for showers with narrow size ranges:

(i) large showers. For large showers with $S(50) \geq 5\text{m}^2$, the amplitude of the first harmonic is approximately constant at $\sim 11\%$ with zenith angle against which it is shown

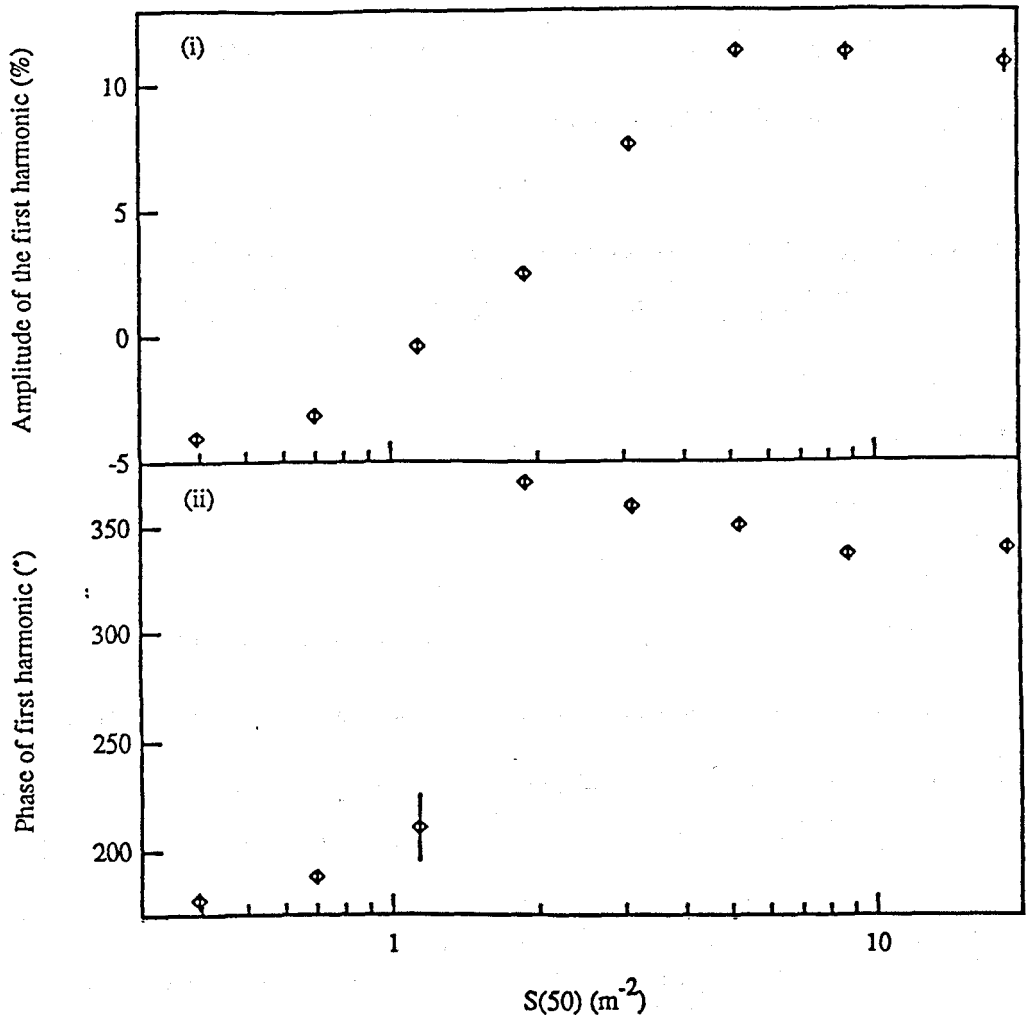


Figure 5.11(i) and (ii) The amplitudes and phases respectively of the first harmonics in the azimuthal distribution are shown as a function of shower size for events at all zenith angles. Harmonics with peaks in the north are represented by positive amplitudes, while those with peaks in the south have negative amplitudes.

plotted in Figure 5.12(i). The phases of the peaks for these showers are all in the North at $\sim 345^\circ$ and are shown plotted against zenith angle in Figure 5.12(ii). Again, these phases vary only slightly (with a range of 30°) but significantly with zenith angle. For large showers falling within the array boundary, which have a probability of 1 of triggering the array, one might expect the projected area effect to dominate and hence for the peak in the first harmonic to be at $\phi \sim 342^\circ$, the azimuth of the normal to the plane of the array. Indeed the phase of the first harmonic is seen to be close to, but not consistent with this azimuth, and it appears that another effect may be present. Simple geometrical arguments enable an upper limit to be calculated for the amplitude of the first harmonic caused by the projected area effect alone:

Figure 5.13 illustrates the difference in projected area for two showers, S_1 and S_2 , which are incident at the same zeniths but at azimuths separated but 180° . The projected area is maximum for S_1 whose azimuth coincides with that of the normal to the array, $\phi = \phi_n$, and minimum for S_2 with $\phi_2 = \phi_n + 180^\circ$. The projected areas are $A \cos(\theta - \theta_n)$ and $A \cos(\theta + \theta_n)$ for S_1 and S_2 respectively, and the fractional amplitude of the first harmonic due to this difference is given by:

$$r_1 = \frac{\cos(\theta - \theta_n) - \cos(\theta + \theta_n)}{\cos(\theta - \theta_n) + \cos(\theta + \theta_n)} \quad \dots \text{Eqn 5.21}$$

which simplifies to

$$r_1 = \tan \theta_n \tan \theta \quad \dots \text{Eqn 5.22}$$

It would be expected, therefore, that the amplitude would increase with increasing zenith angle, and, for the largest zenith angles considered ($\sim 40^\circ$), to have a maximum of $\sim 4\%$. Surprisingly, then, the amplitudes shown in figure 5.12(i) do not show these trends and tend to suggest another reason for this modulation.

(ii) Small showers. For small showers with $S(50) \leq 0.5\text{m}^{-2}$, it is seen that the acceptance is greater for showers from the South rather than from the North. The amplitudes of the peaks in the azimuthal distributions increase with zenith angle against which they are shown plotted in figure 5.14(i), but their phases vary only slightly with

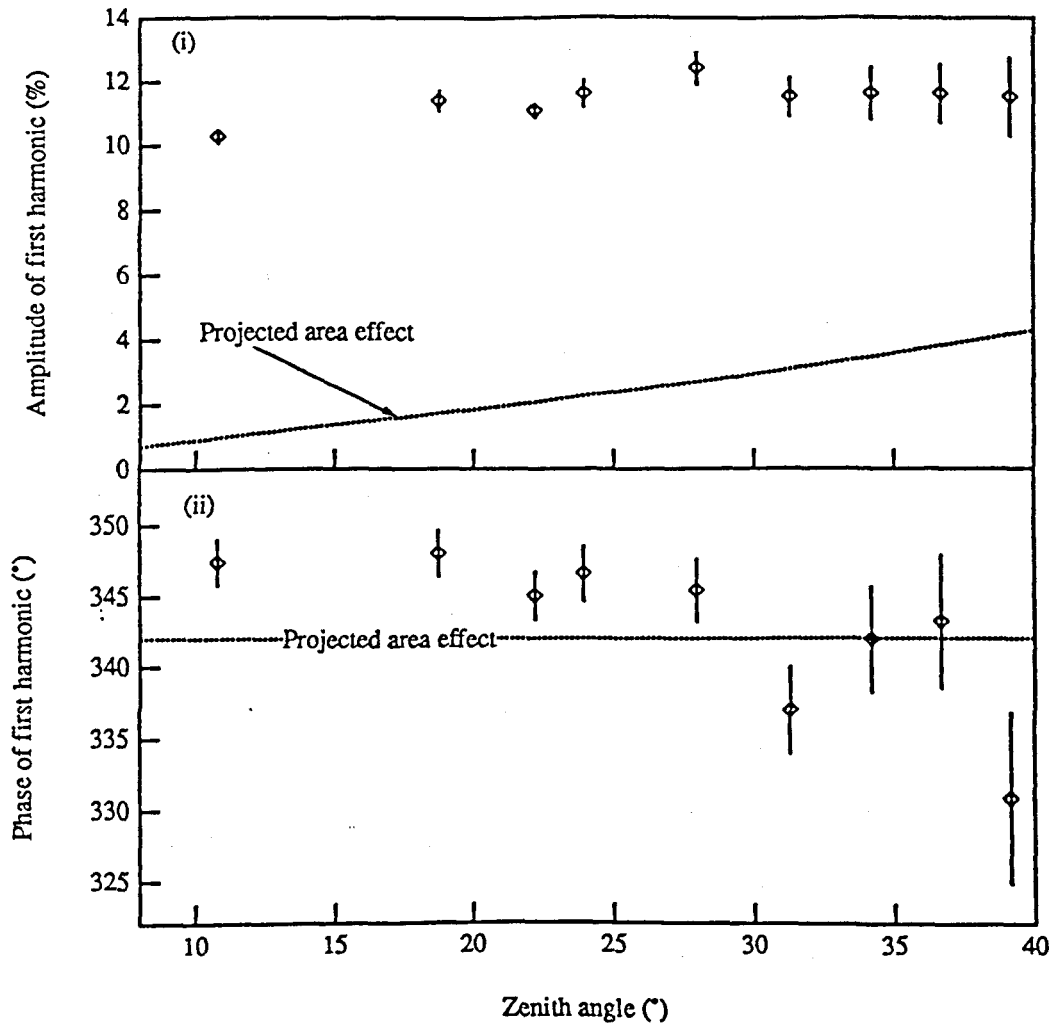


Figure 5.12 (i) and (ii) The amplitudes and phases respectively of the first harmonics in the azimuthal distribution are shown plotted as a function of zenith angle for showers with $S(50) \geq 5m^{-2}$.

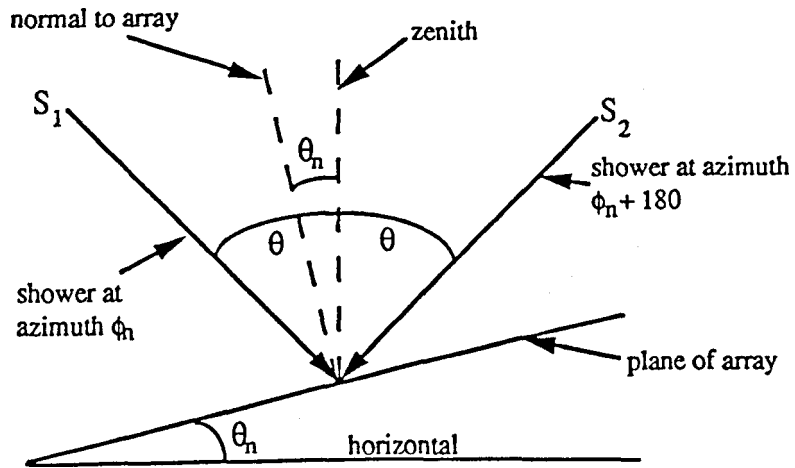


Figure 5.13 A schematic view looking along the plane of the array and illustrating the difference in projected area of the array for showers at the same zenith angles, but different azimuths. ϕ_n and θ_n are the azimuthal and zenith angles respectively of the vector normal to the plane of the array. The two showers have directions (θ, ϕ_n) and $(\theta, \phi_n + 180^\circ)$

zenith angle about a mean value of $(176.5 \pm 0.1)^\circ$ (figure 5.14(ii)). These events have energies close to the array threshold, so that it may be expected that for these showers, effects due to varying array sensitivity with zenith angle dominate over the projected area effect observed in large showers. For showers at large angles of incidence, the array appears foreshortened, and the detectors closer together than vertical showers. For showers at equal zenith angles, this foreshortening is greatest for showers at azimuth $(\phi_n + 180)^\circ$ and increases with zenith angle. The phase of the first harmonic is indeed close to, but inconsistent with $(\phi_n + 180)^\circ$ and does increase with zenith angle. To compensate for the foreshortening of the array, however, the projected area of each detector decreases with increasing angle of incidence. The effects giving rise to the first harmonics in small showers, then, are complex and more detailed calculations are required to explain their magnitudes and phases.

B) Variation of the second harmonic

The amplitudes, r_2 , and phases, ψ_2 , of the second harmonics are shown plotted against $S(50)$ in Figures 5.15 (i) and (ii) respectively and against zenith angles in Figures 5.16 (i) and (ii) respectively. It can be seen that both r_2 and ψ_2 are complex functions of shower size and inclination.

It is difficult to explain the occurrence of these second harmonics. The array is slightly longer in the North-South direction than in the E-W direction. The line of symmetry down this length of the array is at an angle of 35° to the N-S line. If the array were more sensitive to showers whose arrival directions were parallel to the length of the array, then this would give rise to a second harmonic. This effect should be negligible in very large showers which have a 100% chance of being detected. Indeed, the amplitude of the second harmonic is greatly reduced for very large showers, but is nevertheless still significant. Another problem is that the phase of the harmonic shows a strong $S(50)$ dependence and is, in all but the smallest of showers, inconsistent with the direction of the major axis of the array.

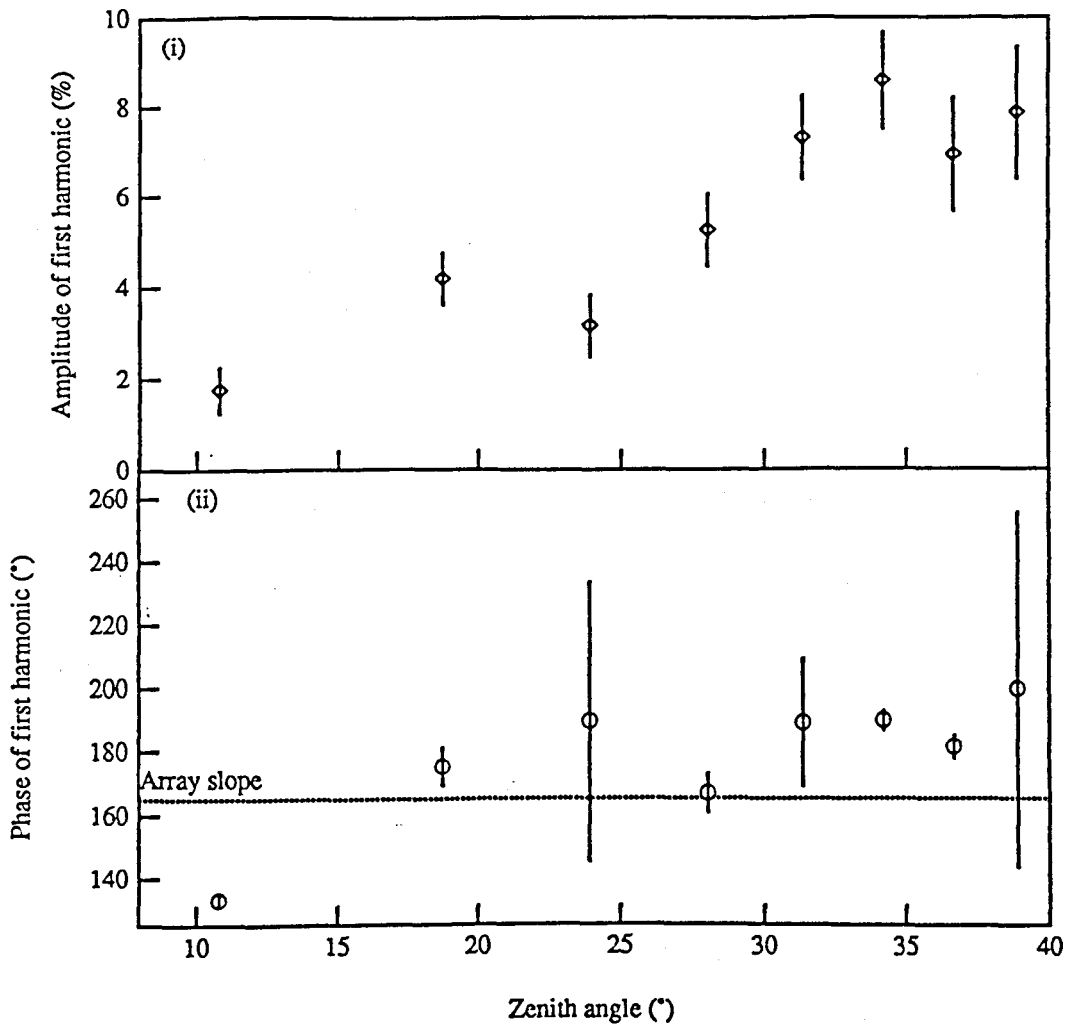


Figure 5.14 (i) and (ii) The amplitudes and phases respectively of the first harmonics in the azimuthal distribution are shown plotted as a function of zenith angle for showers with $S(50) \leq 0.5 \text{ m}^{-2}$.

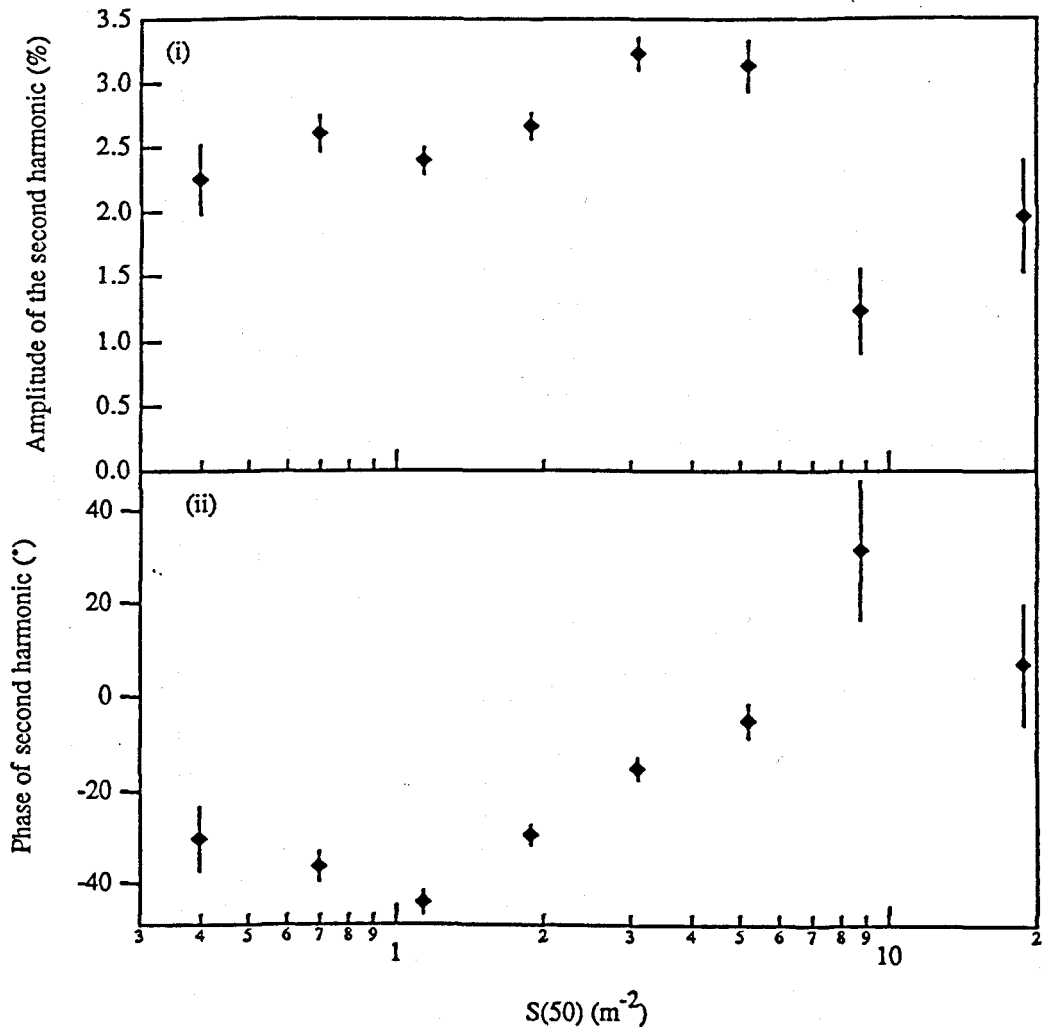


Figure 5.15 (i) and (ii) The amplitudes and phases respectively of the second harmonics in the azimuthal distribution are shown plotted as a function of $S(50)$ for showers at all zenith angles.

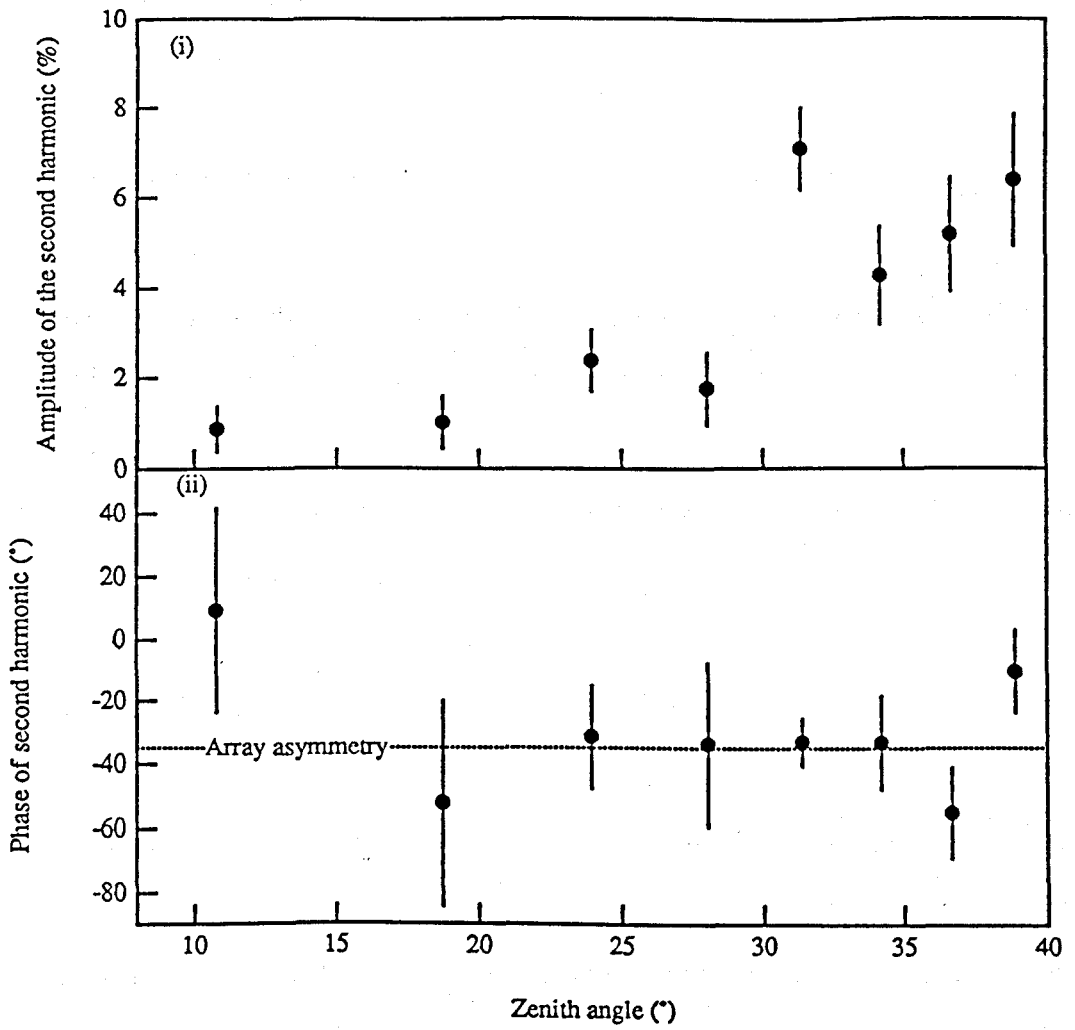


Figure 5.16 (i) and (ii) The amplitudes and phases respectively of the second harmonics in the azimuthal distribution are shown plotted as a function of zenith angle for showers at all zenith angles.

1st and 2nd harmonics in the azimuthal distributions are seen in all operational eras, with approximately equal magnitudes and zenith and size dependencies.

Evidently, complex calculations are required to understand the origins of both the first and second harmonics. Nevertheless, such understanding is not required to allow for these modulations when using the azimuthal technique for source searching: all that is needed is accurate knowledge of them. The necessary modifications to the method are described in the following section.

5.2.2 CORRECTING FOR THE AZIMUTHAL ASYMMETRY

The azimuthal dependence of background rates may cause a systematic error in the background estimate for the on-source bin in the case where the off-source events are collected from a different range of azimuths to that of the on-source. It is possible to correct the estimate of the background to the on-source bin if the azimuthal distribution of events is well known. The Fourier coefficients, a and b , of the 1st and 2nd harmonics defined in Equations 5.16 and 5.17 have been calculated for all events observed at Haverah Park. The events were binned in 8 equal increments of $\sec\theta$, 8 equal increments of $\ln[S(50)]$ and in the 4 operational eras of the array, making 256 bins in all. For bins in which the small number of events made the amplitude of the harmonic uncertain ($<3\sigma$), events were added from 3 neighbouring bins with similar sizes and zenith angles and the coefficients recalculated. The distribution function of events at a given zenith angle, size and operational era is then given by

$$f(\phi) = 1 + \sum_{j=1}^n (a_j \cos(j\phi) + b_j \sin(j\phi)) \quad \dots \text{Eqn 5.23}$$

For instance if N_1 counts are seen per unit solid angle at an azimuthal angle of ϕ_1 , then at the same zenith angle and era we would expect to see N_2 counts per unit solid angle at azimuthal angle ϕ_2 given by:

$$N_2 = \frac{N_1 f(\phi_2)}{f(\phi_1)} \quad \dots \text{Eqn 5.24}$$

Hence each off source event at ϕ must be corrected by the factor $f(\phi_{\text{source}})/f(\phi)$ where ϕ_{source} is the azimuthal angle of the source, so that now the estimate of the background contribution to the on source bin is :

$$N_b = \sum_i \left(\frac{\Delta\phi_i}{360 - \Delta\phi_i} \right) \left(\frac{f(\phi_{\text{source}})}{f(\phi_i)} \right) \quad \dots \text{Eqn 5.25}$$

5.2.3 TESTING THE ACCURACY OF THE AZIMUTHAL CORRECTIONS

Figure 5.17 shows the azimuthal distribution of the events after correcting for the first and second harmonic modulations described. This correction takes place as follows: Each event, i , at azimuth ϕ_i is binned in zenith angle, shower size and array era. The value of the expected azimuthal distribution function for this type of event at this azimuth, $f(\phi_i)$ is calculated as described in the previous section. Each event is then weighted with the reciprocal of this value. We would expect the distribution of these weighted events to be uniform. Indeed, the distribution is considerably flatter than that of unweighted events (Figure 5.8) and has residual first and second harmonics of amplitude no greater than 0.2%. In addition, when these events are grouped in the size, zenith angle and operational era bins, no significant harmonics ($>2\sigma$) remain with amplitudes greater than 3%.

5.2.4 SOURCES THAT TRANSIT CLOSE TO THE ZENITH

The azimuthal method is unsuitable for sources for which any part of the search bin passes over the zenith. For these sources, at zenith angles close to zero, only on-source counts will be collected, while the solid angle for collection of off-source counts is zero. This, then will lead to a systematic underestimate of the background while counts are accumulated in the on-source bin at the zenith. Therefore, for these

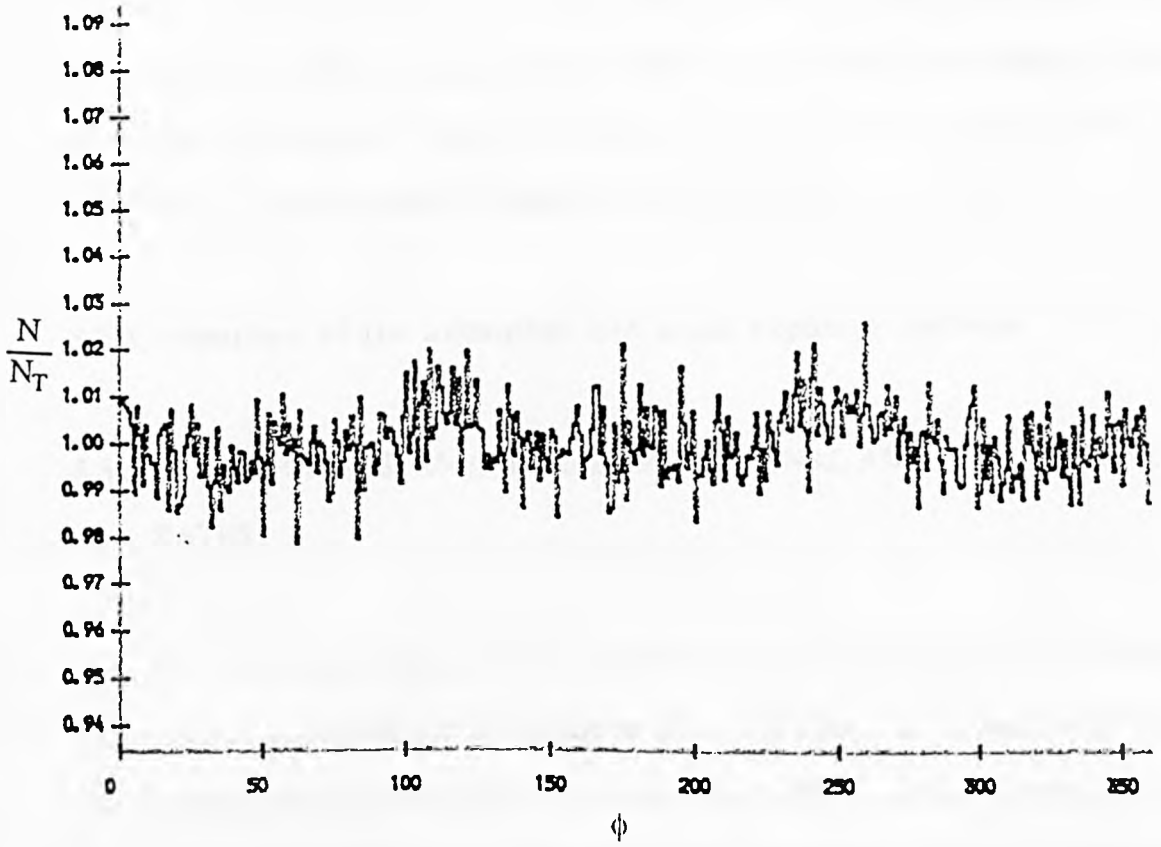


Figure 5.17 The azimuthal distribution after correction for the 1st and 2nd harmonics as described in the text.

sources, it is necessary to either cease accumulating events for the period that the search bin overlaps the zenith, or to use a different method for calculating the background such as the dec-strip method. Clearly, the latter choice is to be preferred as it would be undesirable to reject the period of observation with the highest count rate.

5.3 Comparison of the azimuthal and equal exposure methods

5.3.1 CHECK FOR SYSTEMATIC ERRORS IN SIGNAL AND BACKGROUND RATES

The background and on-source counts obtained by equal exposure and azimuthal techniques should obviously be consistent with each other. It is therefore useful to make a comparison between the two to ensure that all effects causing systematic errors in background rates have been eliminated. This is particularly important to ensure that the azimuthal asymmetry of detection by the array has been properly corrected. Searches were performed on the data set obtained over 43 months of observation between mid February 1986 and the end of September 1989 for a total of 12 dummy sources. 3 sources were chosen at each of 4 declinations, 30° , 37.5° , 45° and 65° . The lack of 'sources' between 45° and 65° being due to the problem of sources transiting close to the zenith. At each declination, the three 'sources' are at RAs of 0° , 120° and 240° . Only days for which the on-time of the array was 100% during the transit of both on- and off-source bins above the 40° event horizon were used so that the observation time for the two methods was identical.

The circular bins used in the azimuthal technique are $\sim 2\%$ smaller in solid angle than the square bins used for the equal exposure method. To make a direct comparison between the two methods, therefore, it is necessary to multiply the on- and off-source counts in the azimuthal method by 1.02. The fractional differences in the corrected on-source counts is shown plotted as a function of source declination in figure 5.18 (i)

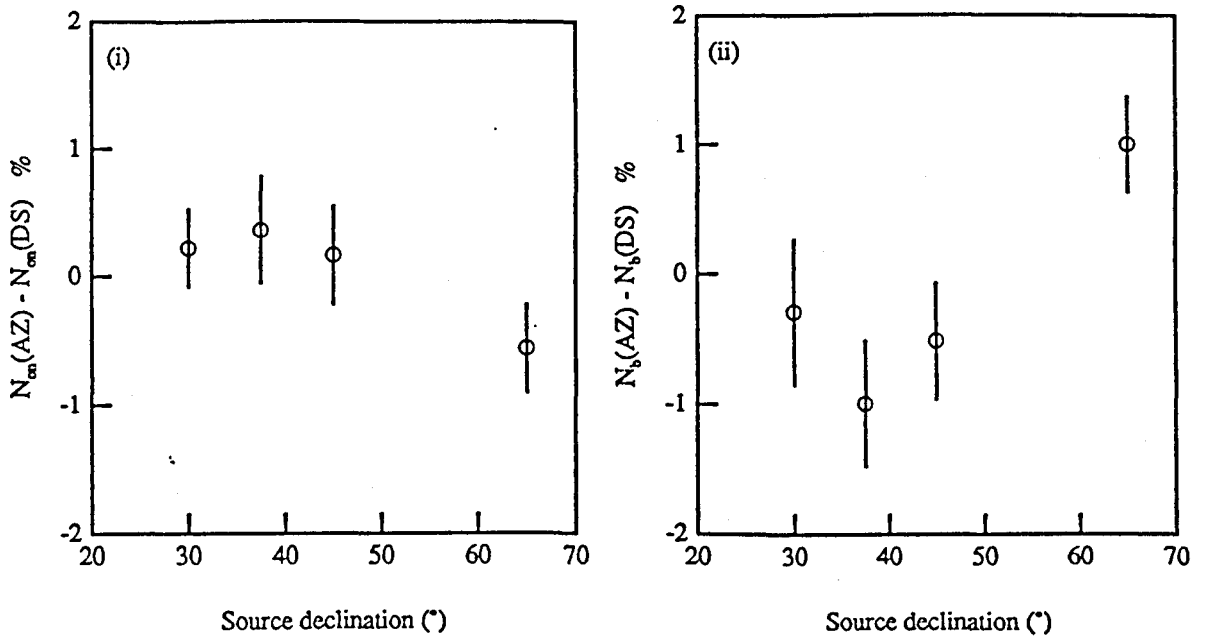


Figure 5.18 (i) and (ii) The percentage difference in on-source and off-source counts respectively obtained using the azimuthal and equal exposure methods for calculating backgrounds are shown plotted as a function of source declination. Results were obtained on 3 dummy sources at each declination and corrected for differences in collecting solid angles.

The error bars show the Poisson fluctuations in the expected number of counts in the non-overlapping regions of the square and circular bins (~18% of the area of a single bin). There is no evidence for any systematic difference in the number of on-source events obtained by each method. Figure 5.18 (ii) shows the fractional difference in the background estimate using the two methods. In this case the errors are due to Poisson uncertainties in the total number of off-source counts collected by the equal exposure method.

It is seen that the azimuthal method leads to systematic errors in the background estimates of no greater than ~1%, though this limit could be more accurately obtained given more observation time.

5.3.2 COMPARISON OF USEFUL ON-TIMES AND OFF-SOURCE SOLID ANGLE OBTAINED BY THE TWO METHODS

The percentage increase in useful on-time for the azimuthal method, T_{AZ} , over the 'equal exposure' method, T_{EE} , is plotted as a function of source declination for the 4.5 years of operation of the GREX array from March 1986 to September 1990 in Figure 5.19. In the case of a candidate source at the same declination of Cygnus X-3 (~40°), for example, the azimuthal technique gives ~17% more on-source observation time than the equal exposure method. This value increases to ~27% for a source at $\delta = 65^\circ$. The difference in on-times obtained by the two methods is due to array downtime. If the array is off for any time during the source transit, a large proportion of the complete sidereal day may be rejected by the method requiring equal exposure across the whole dec-strip. This rejection is more likely for sources that transit close to the zenith, as these sources spend more time above the θ_{max} horizon and the probability of array downtime during this period is increased.

To calculate the uncertainty in the background calculated using the azimuthal technique, it is necessary to calculate the effective number of off-source bins. This is

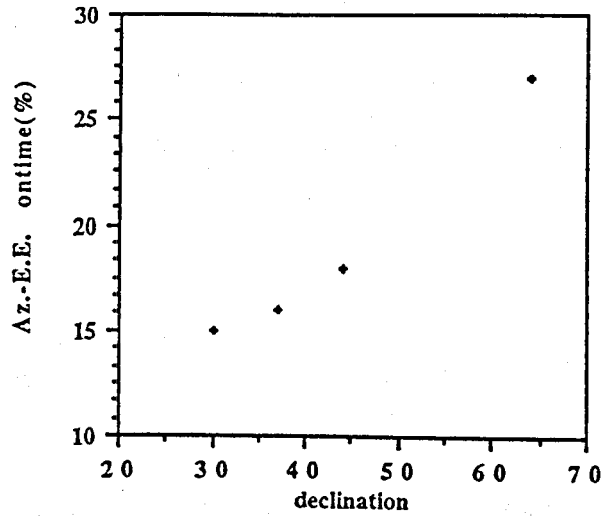


Figure 5.19 The percentage increase in useful on-time of the azimuthal technique over the equal exposure technique is shown plotted as a function of source declination.

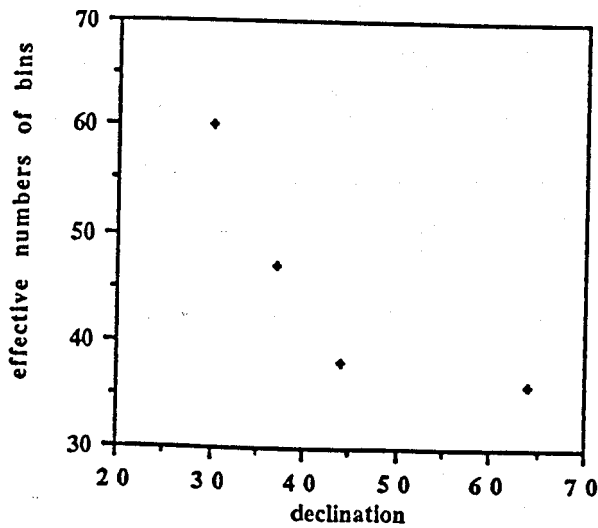


Figure 5.20 The effective number of off-source bins (the ratio of off-source to on-source solid angle) for the azimuthal technique is shown plotted against source declination.

given by:

$$n_{\text{eff}} = \frac{N_{\text{tot}}}{N_b} \quad \dots\text{Eqn 5.26}$$

where N_{tot} is the total number of events collected in the off-source region, and N_b is the calculated contribution of the background to the source bin. The uncertainty in this background is then given by:

$$\sigma_{N_b} = \sqrt{\frac{N_b}{n_{\text{eff}}}} \quad \dots\text{Eqn 5.27}$$

n_{eff} is plotted as a function of source declination in Figure 5.20. For the Equal Exposure method, the choice of number of off-source bins is limited mainly by the fact that the more bins that are used, the more days are likely to be rejected as the array is more likely to be off during the transit of one of the bins. In addition, having off-source bins separated by very large angles in RA increases the mean time difference of collection of off- and on-source and may lead to systematic errors in the calculation of the background in the on-source bin. On the other hand, reducing the number of bins reduces the accuracy of the background due to random fluctuations. The compromise adopted in the past for analysis of Haverah Park data has been 6 bins. The azimuthal technique, therefore, gives a great improvement over the equal exposure both in terms of the increase in useful on-time and in off-source collecting solid angle.

5.4 Conclusions

The Azimuthal technique potentially represents a great improvement over the old 'dec strip' method both in terms of maximising the observation time of a source and reducing the uncertainty in the estimation of the background contribution to the on-source bin. However as has been demonstrated, it is very difficult to eliminate all systematic biases such as the azimuthal asymmetry of the detecting array. These biases have been reduced in the GREX analysis so as to affect the background estimate by no more than 1%. If in the worst case, when the background is incorrectly estimated by

1%, such an error would become important in the search for a long term d.c. signal over the period of a number of years. For instance, if the level of the background is of the order of $N_b \sim 10000$, this error would cause the attributed significance of a signal to be incorrect by 1 standard deviation. For a source at the same declination as Cyg X-3 this would occur after 6 years, though for a source at higher declination, this period would be shorter.

The azimuthal method, however, is certainly superior to the dec-strip method for searches for short term emission on the time scale of the order of days. The larger solid angle from which off-source events are collected enables a typical factor of 1/3 reduction in the uncertainty in the background over the equal exposure method. In addition, as both on- and off-source events can be collected whenever the source is above the horizon, the azimuthal method gives an increase in useful on-time of $\sim 20\%$. Changes in atmospheric conditions such as temperature and pressure which lead to rate changes (Chapter 2) do not produce errors in the background for the azimuthal method as on- and off-source events are collected simultaneously. The same, however, can not be said of the equal exposure method. Attempts to improve background estimates by increasing the number of off-source bins will lead to a greater difference in the mean time between collection of on- and off-source events, and, in the presence of short-term event rate variations, this will lead to poor background estimates on short time scales. In addition, increasing the number of off-source bins is likely to lead to a reduction in useful on-time due to the demand for equal exposure in all bins.

CHAPTER SIX

A SEARCH FOR γ -RAY EMISSION FROM HERCULES X-1 AND 1E 2259 +586

6.0 Introduction

The aim of the work described in the previous chapters has been to develop methods to improve our ability to search for sources in the data base accumulated with the GREX telescope at Haverah Park. Although the sensitivity to shower age has not proved a practical discriminator, the methods developed to optimise the shower core location and the background estimations have proved useful. In this chapter, a search for γ -ray emission from two X-ray binary sources, Her X-1 and 1E2259 +586, in the data base which the author has helped to establish and optimise is described.

6.1 Search for γ -ray emission from Hercules X-1

Hercules X-1 is perhaps the most studied of all candidate sources at TeV energies. It is a low mass X-ray binary consisting of an accreting neutron star in orbit around its visible companion, HZ Herculis, an A type star. The system lies at a distance of ~ 6 kpc from our own solar system. At X-ray energies it exhibits 1.24s (pulsar spin), 1.7 day (orbital) and 35 day (precession of pulsar/accretion disc) periodicities. It has also been observed at infra-red, optical and ultra-violet wavelengths. Claims have also been made for pulsed emission at TeV and PeV energies

6.1.1 OBSERVATIONS AT X-RAY ENERGIES

Hercules X-1 was first discovered in the UHURU satellite survey

(Schreier *et al.* 1972, Tananbaum *et al.* 1972). Emission of the X-rays was seen to be modulated at 1.24s which was thought to be the pulsar period, the X-rays emanating from an off-spin axis magnetic pole onto which accreting matter fell. Every 1.7 days, the X-ray emission cut off for 0.24 days, during which it was proposed that the pulsar was eclipsed by its companion, 1.7d being the period of its orbit. In addition to this, the emission had low states every 35 days which were more difficult to explain. Subsequent observations (Jones and Forman 1976) showed two epochs of emission during the 35day period, the 2nd having 1/3 the amplitude of the first. Early models (e.g. Brecher 1972) suggested free precession of the neutron star spin axis to explain this modulation. More recent models (eg Roberts 1974 and Petterson 1975,1977) explain the 35day period in terms of wobble of the accretion disc caused by precession of HZ Herculis: the source of X-rays would be obscured when the plane of the accretion disc is along the line of sight of the observer on earth. The measurements of Jones and Forman (1976) also show a slight 'spin up' as might be expected for an accretion driven pulsar. Ogelman *et al.* (1985) report the results of EXOSAT observations of Her X-1 in which the 1.24s pulses observed in the X-ray low on-state were seen to be 180° out of phase with those in the high state. The most likely explanation for this phase shift was that the X-rays seen in the low state were from the opposite magnetic pole to those in the high state, this change being caused either by the change in perspective of the neutron star due to its precession, or a change in the position of the obscuring matter which allows each pole to be viewed in turn. The period observed in the EXOSAT data implied a spin up since 1972 of $\dot{P} \sim 2 \times 10^{-13} \text{ss}^{-1}$ and optical data obtained in 1987 show a period close to the extrapolated X-ray period. Jones *et al.* (1973) and Parmar *et al.* (1985) report the occurrence of extended low states in X-ray activity, presumably due to obscuration by thickening of the accretion disc.

6.1.2 HER X-1 AT OPTICAL AND INFRA-RED ENERGIES

1.7 day modulations are seen in optical observations of HZ Herculis (Liller 1972) presumably due to X-ray heating of the companion star by Her X-1. Davidson *et al.* (1972) report pulsations at the 1.24s pulsar period, presumably caused by the reprocessing of the X-rays of the pulsar on HZ Her. Similar pulsations are also seen at infra-red energies (Middleditch *et al.* 1983) with modulations at both the orbital period and the 35 day period.

6.1.3 TEV AND PEV OBSERVATIONS

On the 17th April 1983, the Durham group (Dowthwaite *et al.* 1984), using a Cerenkov telescope, observed a 3σ counting excess over a three minute interval while observing Her X-1. The arrival times of the on-source events collected during this interval were seen to be modulated at the 1.24s X-ray period: the time averaged flux was quoted as $F=(3\pm 1.5)\times 10^{-11}\text{ cm}^{-2}\text{s}^{-1}$ at $E>1\text{TeV}$. The emission came just after the turn-on of the main on-state and at an orbital phase of 0.76. On the 11th July of the same year, an apparent burst of γ -rays with energies in excess of 500 TeV of 40 minutes in duration was observed by the Fly's Eye group (Baltrusaitis *et al.* 1985). The burst occurred at an orbital phase of 0.66 during the low on-state in the 35d period. Surprisingly, the Durham group making simultaneous observations at the same site, but at TeV energies, did not detect any signal (Chadwick *et al.* 1985). A mechanism has been proposed whereby a beam of charged particles, accelerated to relativistic energies by the intense magnetic fields close to the neutron star, is steered toward the rim of the companion by its weaker magnetic fields. Interaction of this beam with matter either in the accretion disc or close to HZ Her could account for the emission of γ -rays via neutral pion decay. Such a mechanism could account for the lack of simultaneous emission at TeV energies: different energy particles within the beam would be deflected

by different amounts, so that a γ -ray emission would be expected to occur at different orbital phases for different energies (Gorham and Learned, 1986) Further support for the beam steering scenario came from observations by the Whipple group. Out of a total of 73 hours on-source observation time spread over 41 nights in 1984 and 1985, 7 interesting episodes of possible emission at energies above 250 GeV were identified lasting between 25 and 80 minutes (Gorham *et al.* 1986, 1987). The most significant of these was that occurring on the 16th June 1985, which lasted ~ 1 hour and had a chance probability of 7×10^{-6} before the number of statistical trials had been taken into account. The emission was unusual in that it occurred during X-ray eclipse implying that a beam of high energy particles must have, in some way been steered around the companion star.

Another interesting episode lasting 28 minutes was that occurring on the 4th April 1984 just after turn-on in the main on-state in the 35d period. Although statistically the weakest of the 7 intervals, it coincided with a detection by the Durham group (Chadwick *et al.* 1987) of modulation at the same pulsar period ($P=1.2377 \pm 0.0001$ s and 1.2376 ± 0.0004 s for the Whipple and Durham observations respectively). Neither of these detections by themselves were particularly significant: the chance probabilities were 1×10^{-3} and 3×10^{-3} before the number of epochs were taken into account. Nevertheless, their coincidence and the agreement between their spin periods is compelling. Just a few days earlier measurements had been made of the X-ray period using the EXOSAT satellite, these being in good agreement to the Whipple and Durham observations ($P_{X\text{-ray}} = 1.237792 \pm 0.0000002$).

In 1985, the Haleakala group observed three intervals, two on 14th June and one on the 16th June, each of duration 200s in which there were counting excesses $> 2.5\sigma$ (Resvanis *et al.* 1987). Sharp peaks were also seen in the distributions of arrival times when the events from each of the periods were folded at the X-ray pulsar period. During 1986 three claims for periodic emission were made which were remarkable for the fact that each detection was at the same period with a frequency $\sim 0.16\%$ greater than

the expected X-ray frequency. The first of these, reported by the Haleakala group (Resvanis *et al.* 1987, 1988), was made on the 13th May. They report a time averaged flux of $5 \times 10^{-11} \text{ cm}^{-2} \text{ s}^{-1}$ at $E > 250 \text{ GeV}$ and a chance probability of 0.7% for the signal modulation at a period $P = 1.23593 \pm 0.00018 \text{ s}$. The Whipple group (Lamb *et al.* 1988) observed an apparent signal modulation at a period of 1.2358s consistent with that of the Haleakala detection with a chance probability of 0.9% on 11th June at energies in excess of 600 GeV. The most significant of the three detections, however, was that made by the Los Alamos CYGNUS experiment at energies above 100 TeV (Dingus *et al.* 1988): in a burst attributed to γ -rays (on the 24th June), a significant peak was found in the periodogram when a range of periods was scanned using the Protheroe statistic, Ψ (Protheroe, 1985). This peak was at a period, $P = 1.2357 \pm 0.0003 \text{ s}$ which is very close to the other two detections of the same year. When the probabilities of the highest Protheroe value in the period range and the overall chance probability of the counting excess were combined, the overall chance probability of the detection was found to be $\sim 2 \times 10^{-5}$. The muon content of the on-source showers for this day, however, was found to be anomalously high compared to that expected for γ -ray induced showers. The consistency in the period in this series of observations and the high significance of the CYGNUS detection constitute the strongest evidence for emission of VHE and UHE γ -rays by Her X-1.

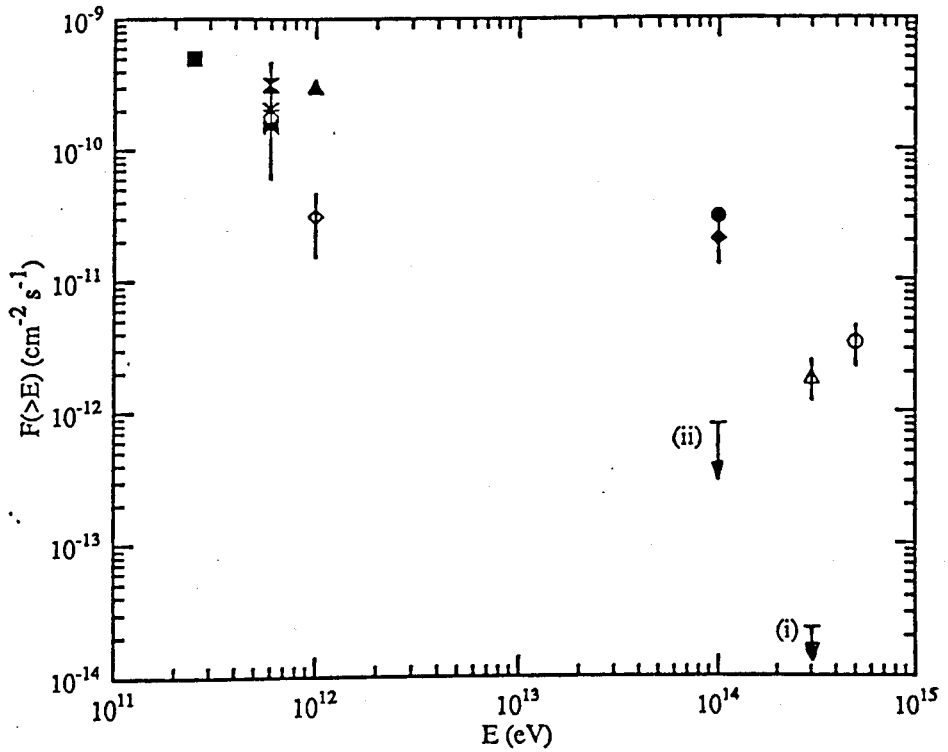
More recently, (Reynolds *et al.* 1990), the Whipple group have reexamined their data collected between 1984 and 1987. This group have recently had much success in applying imaging techniques to Cerenkov light detections of TeV γ -rays. Monte Carlo simulations showed that the expected Cerenkov image of γ -ray showers would be very different from that of proton induced showers. In observations on the Crab, this difference was exploited by making cuts based on Cerenkov images, in an attempt to eliminate background showers. The result was an increase in the significance of the signal from 5σ to 20σ despite a total reduction of 95% in the number of on-source events. When the same cut was applied to Hercules X-1 data, however, a signal

modulation for the whole period with a chance probability of 1% disappeared. A reexamination of the 11 June 1986 data, also showed the modulation at the previously reported blue shifted period to have disappeared.

Ko *et al.* (1990) report a flux upper limit of $8 \times 10^{-13} \text{ cm}^{-2} \text{ s}^{-1}$ for $E > 100 \text{ TeV}$ obtained from Fly's Eye2 data collected between Nov 1987 and June 1989. No significant modulations were seen at the 1.24s period during this era. In another recent paper, the Ooty group (Gupta *et al.* 1990) report a search for pulsed emission at energies greater than 0.1 PeV on a total of 685 days data collected between June 1984 to May 1987. Days on which the number of counts in a $4^\circ(\delta) \times 4^\circ(\text{RA})$ bin centred on the source exceeds 5 (they observe a background rate of ~ 2.48) were identified as being suitable for period analysis. Such days are not particularly unlikely, with a Poisson probability of $\sim 3\%$. Although a total of 24 days satisfied this condition, only 4 days, two of which were consecutive, were somewhat arbitrarily chosen due to their closeness to the Los Alamos burst which occurred on the 28th July 1986: namely 8th and 9th August, 1st July and 21st November 1986. All these days were analysed individually with the Protheroe test for periodicity, and while they all showed modulation at periods close to the Los Alamos period none were at particularly high levels of significance. When all episodes were amalgamated, a peak was seen at the Los Alamos period $P = 1.23577 \text{ s}$ with an estimated probability of 2.2×10^{-4} when the number of trial periods had been taken into account. There are severe doubts, however, as to the validity of the procedure of combining data for periodicity searches when they are so widely separated in time.

Yet another claim for a burst pulsed at a frequency 0.16% greater than the X-ray frequency was reported by the Haleakala group (Austin *et al.* 1990) who observed a transient emission lasting 15min on the 23rd May 1987.

The flux measurements and upper limits derived in observations at TeV and Pev energies are shown in Figure 6.1.



Reference	Epoch
△	Present work
◇	Dowthwaite et al. (1984)
○	Baltrusaitis et al. (1985)
×	Gorham et al. (1987)
⋈	as above
▲	Chadwick et al. (1987)
■	Resvanis et al. (1987)
*	Lamb et al. (1988)
◆	Dingus et al. (1988)
●	Gupta et al. (1990)
(i)	Present work DC
(ii)	Ko et al. (1990)

Figure 6.1 Claimed fluxes for transient emissions and upper-limits for long term observations of Hercules X-1. The legend gives references and epochs of observations for transient emissions

6.1.4 OBSERVATIONS OF HERCULES X-1 USING THE GREX ARRAY

Data collected between 5th March 1986 and 30th September 1990 have been examined for both long term and transient emissions from Hercules X-1. The total on-source observation time spanning the 4.5 years amounts to 9932 hours out of a possible 11,500 hours, the integrated time spent by the source above the 40° event horizon.

6.1.4.1 Search for DC emission from Her X-1

The complete 4.5 years of data have been analysed to look for steady emission from Her X-1. The background contribution to the on-source bins has been calculated using a strip in declination band with the source bin at the centre and 3 off-source bins on either side of the on-source bin. The demand for equal exposure across the whole of this strip (chapter 5) has reduced the total useful observation time to 8553 hours. No signal was seen over this observation time, during which the number of events in the on-source bin was 4714 and the expected background contribution to this bin was 4763.7. The flux upper limit for this observation span of $2.3 \times 10^{-14} \text{ cm}^{-2} \text{ s}^{-1}$ at $E > 3 \times 10^{14} \text{ eV}$ has been calculated using the method described by Protheroe (1984) and effective area calculations of Bloomer (1990). This limit can be compared to measurements of other experiments in Figure 6.1. The cumulative excess events in the on-source bin over the expected background are shown as a function of sidereal day since 1/1/86 in Figure 6.2.

6.1.4.2 Test for modulation at 1.7d and 35d periods of Her X-1

The arrival times of the on-source events corrected to the heliocentre have been examined for modulation at the 1.7d and 35d periods of Her X-1. The background events folded at these periods themselves show significant modulation ($\sim 3\sigma$) (Bloomer 1990) due to array downtimes and rate fluctuations caused by changes to

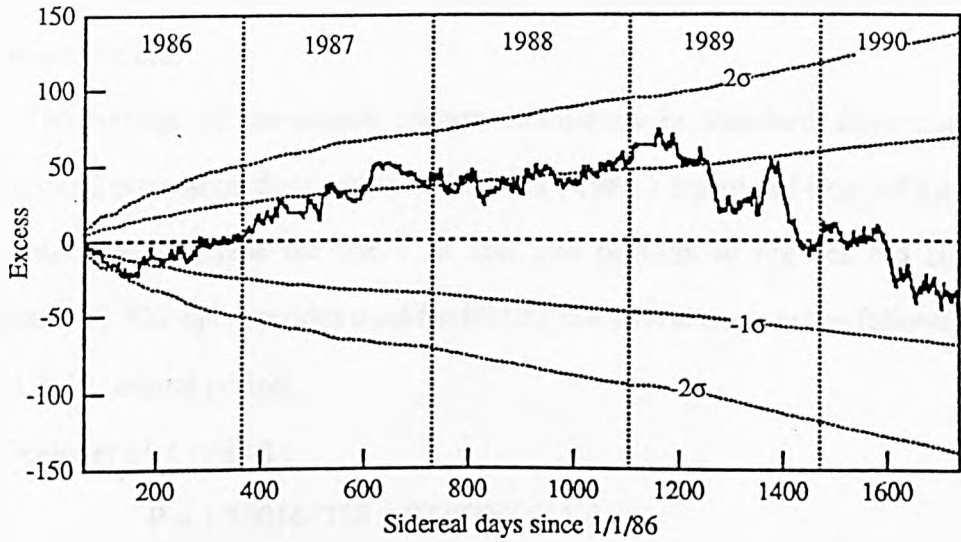


Figure 6.2 The cumulative excess of on-source counts over background counts for Hercules X-1 is shown as a function of the number of sidereal days since 1/1/86. Also shown are the 'excesses' that would correspond to signals/deficits with significances of 1σ , 2σ , 3σ , -1σ , -2σ , and -3σ .

the array. The mean expected number of events within each phase range in the two periods is therefore calculated by folding the background arrival times into the period of interest. As the off-source bins transit at different times from the on-source bin, it is necessary to correct for the phase shift this would produce in a period analysis by giving the arrival time of an event in an off-source bin a shift so that it appeared to come from the on-source bin.

The excess of on-source events calculated in standard deviations above background rates according to the Li and Ma (1983) equation (Eqn 5.4) are shown as a function of phase for the 1.7d and 35d periods in Figures 6.3 (i) and (ii) respectively. The ephemerides used for folding the arrival times are as follows:

(i) 1.7 day orbital period,

Deeter *et al.* (1981) :

$$P = 1.700167788 \pm 0.000000011 \text{ d}$$

$$\dot{P} = 0$$

$$\text{Epoch } (T_0) = 2442859.726688 \pm 0.000007 \text{ JD}$$

(ii) 35 day period,

Ögelman *et al.* (1985):

$$P = 34.928 \text{ d}$$

$$T_0 = 2445788.0 \pm 0.5 \text{ JD}$$

In both cases, then the period derivative is zero, and the phase of an event relative to T_0 is given by:

$$\phi = \frac{T - T_0}{P} \quad \dots \text{Eqn 6.1}$$

It can be seen that no significant modulation has been observed at either the 1.7d or the 35d periods. The reduced χ^2 's for each are 0.88 and 1.2 respectively.

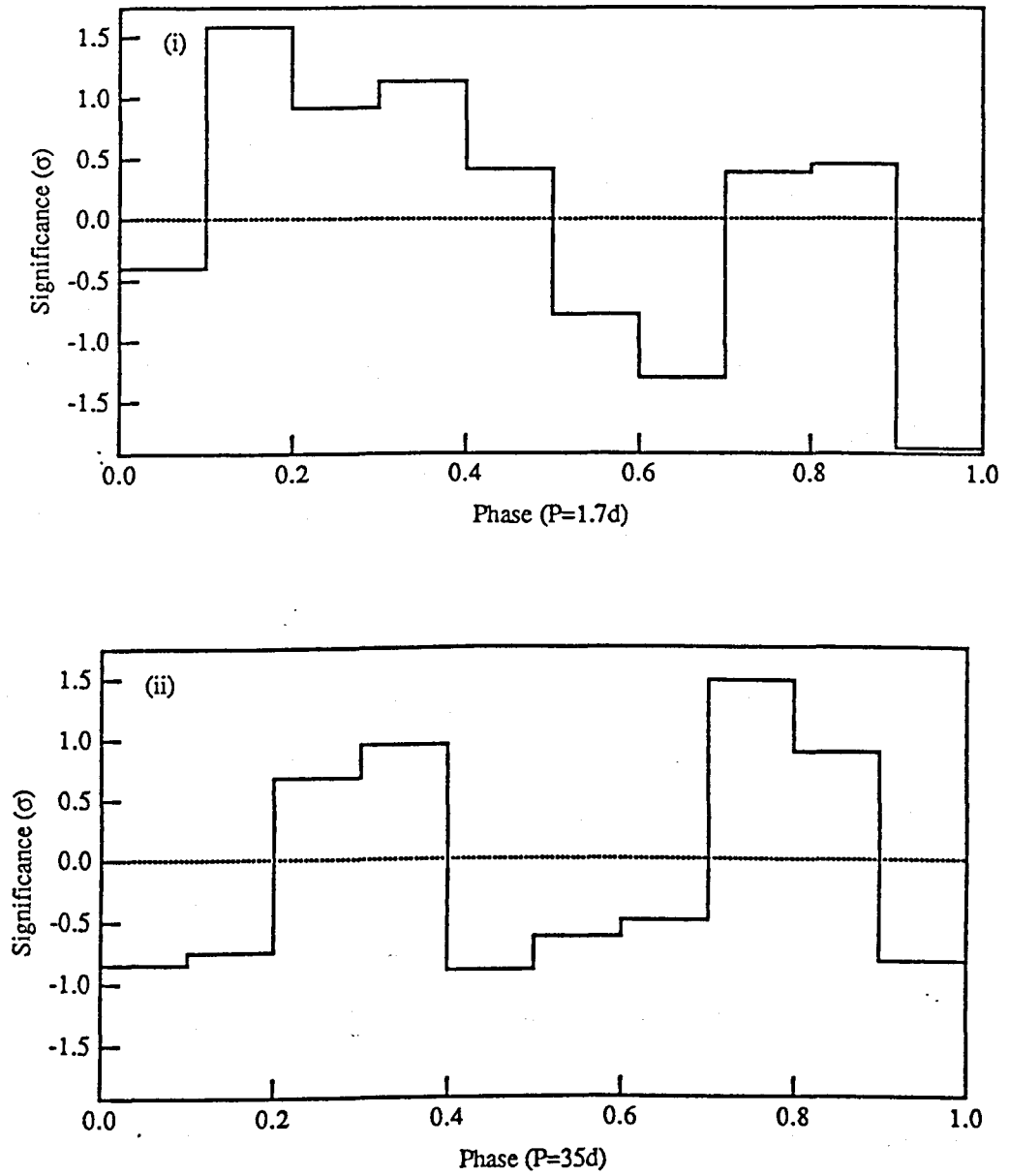


Figure 6.3 (i) and (ii) The excess of on-source events over background for Her X-1 is shown plotted in standard deviations against phase in the 1.7d and 35d periods respectively.

6.1.4.3 Search for sporadic emission from Her X-1

The 4.5 year data set has been examined on a day-to-day basis. The azimuthal strip technique was used to calculate the background for each sidereal day (chapter 5). Of the 1554 days examined during which on-source events were collected, 11 had excesses with Poisson probability less than 1%. These are listed in Table 6.1. One day is of particular interest. On the 20th May 1989, 11 events were observed on-source when only 2.46 were expected. This epoch is in an X-ray low state and, at source transit, the phase in the 1.7d period on this day was ~ 0.86 . The time averaged flux at $E > 3 \times 10^{14}$ eV was calculated to be $(1.8 \pm 0.6) \times 10^{-12}$ cm $^{-2}$ s $^{-1}$ by the method described by Bloomer (1990). Such an occurrence has a Poisson probability of only 5.3×10^{-5} .

However when one multiplies by the number of days over which the source was observed (1554), and by an additional factor of 10 to take account of the fact that Her X-1 was just 1 of 10 sources initially studied in this way (the Hercules high day being the most significant day observed for any source), it is seen that the excess on this particular day is not particularly significant in its own right. A period analysis was performed on the arrival times corrected both to the solar system barycentre and the barycentre of the Her X-1 binary system of this day to look for the 1.24s spin period (Lloyd-Evans, private communication). The Protheroe statistic (Protheroe, 1985), Ψ , was used which is sensitive to sharp spikes in the light curve and was used successfully by the Los Alamos group (Dingus *et al.* 1985). A range of periods between 1.235 and 1.24s was scanned corresponding to approximately $3 \times$ the 0.16% frequency shift observed in the Los Alamos, Haleakala and Whipple groups detections of 1986, and encompassing both this anomalous period and the X-ray period. A total of 2500 periods were tested corresponding to an oversampling of $20 \times$. The resulting periodogram is shown in Figure 6.4. A sharp spike with $\Psi = 5.9$ is seen at a period of 1.23595s, close to the Los Alamos period. The probability of such a high value of Ψ occurring at any period within the chosen range was assessed using Monte Carlo

Date of rise	N_{on}	B	P_{Poiss}	$\phi_{35\text{d}}$	$\phi_{1.7\text{d}}$
20/5/86	8	2.89	0.010	0.43	0.21
7/4/87	9	3.38	0.008	0.63	0.09
12/5/87	8	2.79	0.008	0.66	0.20
9/6/87	10	3.35	0.002	0.45	0.63
7/6/88	8	2.82	0.009	0.88	0.73
4/9/88	8	2.71	0.007	0.42	0.93
14/1/89	9	3.39	0.008	0.19	0.35
20/5/89	11	2.46	5.3×10^{-5}	0.81	0.86
16/10/89	11	4.19	0.004	0.07	0.25
22/6/90	12	4.77	0.004	0.204	0.90
28/8/90	11	4.4	0.006	0.117	0.193

Table 6.1 The Hercules X-1 days having less than 1% Poisson probability. N_{on} is the number of on-source events, B the background and ϕ_{35} and $\phi_{1.7}$ are the phase in the 35 day and 1.7 day periods respectively when the source is at transit.

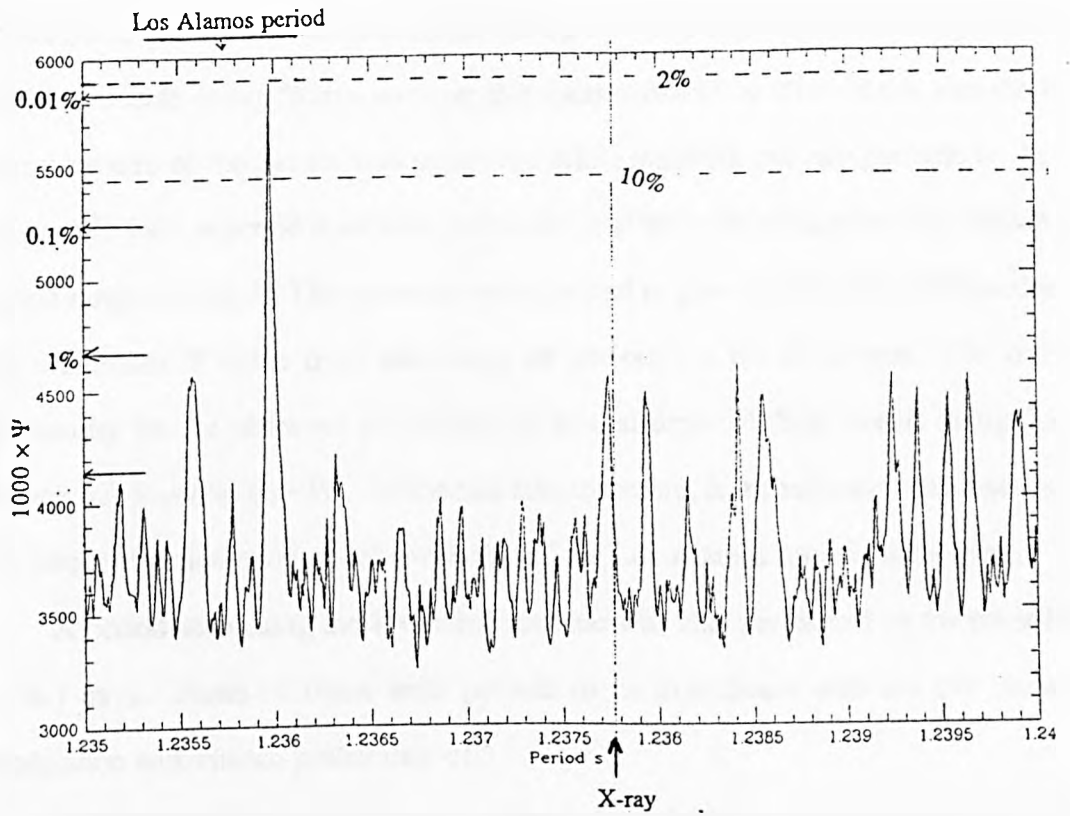


Figure 6.4 The value of the Protheroe statistic, $\Psi, (\times 1000)$ is shown plotted as a function of trial period for observations of Her X-1 on 20th May 1989. The expected X-ray period is shown along with the period measured by the Los Alamos group. Pre trial probabilities are marked on the left hand axis, while the upper and lower broken lines represent the 2% and 10% probability levels after accounting for the number of trials

simulations: each of the arrival times during this day were randomised by adding a random variable drawn from a uniform distribution from 0 to 10 s. In this way the long term structure of the events was preserved while washing out any periodicity in the range of interest, a period scan was performed, and the maximum value of Ψ within the period range recorded. This process was repeated to give a probability distribution of the maximum Ψ value over this range of periods and for 11 events. The overall probability for the observed periodicity of arrival times of these events being due to chance was found to be $\sim 2\%$. While this test, therefore, is inconclusive the closeness of the favoured period in our results with that of the Los Alamos result is interesting.

A period scan using the Protheroe statistic was also performed on the other high (1%) days. None of these tests proved to be significant with no day showing modulation with chance probability $< 10\%$

There is thus no evidence in the Haverah Park data for emission from Her X-1 on a time scale of individual days or over 4.5 years.

6.2 Search for emission from 1E 2259 +586

The compact X-ray source, 1E 2259 +586, herein after referred to as 1E for brevity, lies at a distance of ~ 4.7 kpc and is believed to be associated with the Supernova remnant G109.1-1.0. The source exhibits a ~ 7 s periodicity which has been observed at X-ray, infra-red and optical wavelengths thus identifying 1E as an X-ray pulsar. There have also been reports of emission of VHE γ -rays and of signals associated with underground muons. Claims have also been made for signal modulation at ~ 2300 s believed to be associated with orbital motion around a companion star. Further evidence for orbital modulation comes from infra-red observations, though the search for an optical counterpart has been somewhat inconclusive. If 1E is indeed a binary system then it is very unusual - only one other binary system with a direct link to a SNR, SS433, has previously been detected.

6.2.1 RADIO AND X-RAY OBSERVATIONS

The SNR G109.1-1.0 was first discovered in a radio survey (Wilson and Bolton, 1960). Further studies by RaghavaRoa *et al.* (1965) showed the radio emission from the shell structure of the SNR to have a non-thermal spectrum, while more recently, Hughes *et al.* (1981) made measurements of its distance ($\sim(4.7\pm 0.5)$ kpc), diameter (~ 33 pc) and radio luminosity ($\sim 2 \times 10^{34}$ ergs s⁻¹). They also give an upper limit to the age of the remnant (1.7×10^4 years).

Examination of Einstein satellite data (Fahlman and Gregory 1980a) revealed an X-ray hot-spot at the centre of curvature of G109.1 with coordinates (J1950.0):

$$\text{RA} = 22^{\text{h}}59^{\text{m}}2.63\text{s}, \quad \delta = 58^{\circ}36'37''.6$$

Further observations (Fahlman and Gregory, 1980b, 1981) showed the X-ray emission to be modulated at a period, presumably the pulsar spin period, of 3.4890 ± 0.0002 s. Detailed studies of emission within the vicinity of 1E also revealed a jet-like structure apparently emanating from the pulsar and impinging on the SNR shell. In 1983 it was discovered that the true pulsar period was $\sim 6.9786317 \pm 0.0000001$ s, double that previously stated, the light curve for arrival times folded at this period being double peaked and assymetrical (Fahlman and Gregory, 1983). Studies of phase shifts of the peak in the light curve in observations separated by 6 months enabled an upper limit to be calculated for the magnitude of the rate of change of pulsar period, $|\dot{p}| \leq 2 \times 10^{-11}$ s s⁻¹. A search was also made for modulation at an orbital period, by measuring the delay in the light curve peak relative to a fixed phase over a period of 3.6 hours. When these delays were folded at a period of 2300s, a sinusoidal modulation was observed, presumably at the orbital period, though this result is not highly significant. The length of the projected semi-major axis ($a_x \sin(i)$) was estimated, from the amplitude of the time delays, to be 0.17 ls. Evidence for the binary nature of the system containing 1E also comes from optical observations and infra-red observations (Section 6.2.3).

Exosat observations were made of 1E on 1st and 2nd December 1984. Hanson *et al.* (1988) and Morini *et al.* (1988) report pulsar periods of $p = (6.978720 \pm 0.000006)\text{s}$ and $(6.978725 \pm 0.000008)\text{s}$ respectively. These measurements, with periods greater than the Einstein periods imply a spin down. An intermediate measure of the period with the Tenma satellite (Koyama *et al.* 1987) and more recent Ginga satellite data (Makino, 1987) confirm this increase in period. The history of the X-ray periods is plotted in Figure 6.5.

6.2.2 INFRA-RED AND OPTICAL OBSERVATIONS

A survey of the region in the neighbourhood of 1E (Fahlman *et al.* 1982) using a charge coupled device (CCD) to intensify the image, revealed two stars with magnitudes 22.0 and 21.3 within the 8" error circle centred on the position of 1E. The fainter star at a separation of 4".9 from the nominal position of 1E was identified as the most likely candidate for the optical counterpart to the X-ray pulsar, as it also coincides with a source from which IR pulsations at a frequency close to that of 1E have been observed. These pulsations (Fahlman *et al.* 1982, Middleditch *et al.* 1983) were seen at frequency of 285.5mHz compared to the expected X-ray 2nd harmonic frequency of 286.6mHz. Such a frequency shift is consistent with the infra-red pulsations being due to the reprocessing of X-rays by a low mass companion orbiting the pulsar in the same sense (pro-grade) as the pulsar spin. The X-rays from the pulsar would impinge on the companion at a progressively later phase in the pulsar period, so that after one orbit, the IR pulsations would miss one cycle if the pulsations are at the fundamental frequency or two if, as in this case, they are in the second harmonic. The pulsar period derived by these arguments was consistent with the 2300s period derived from X-ray observations.

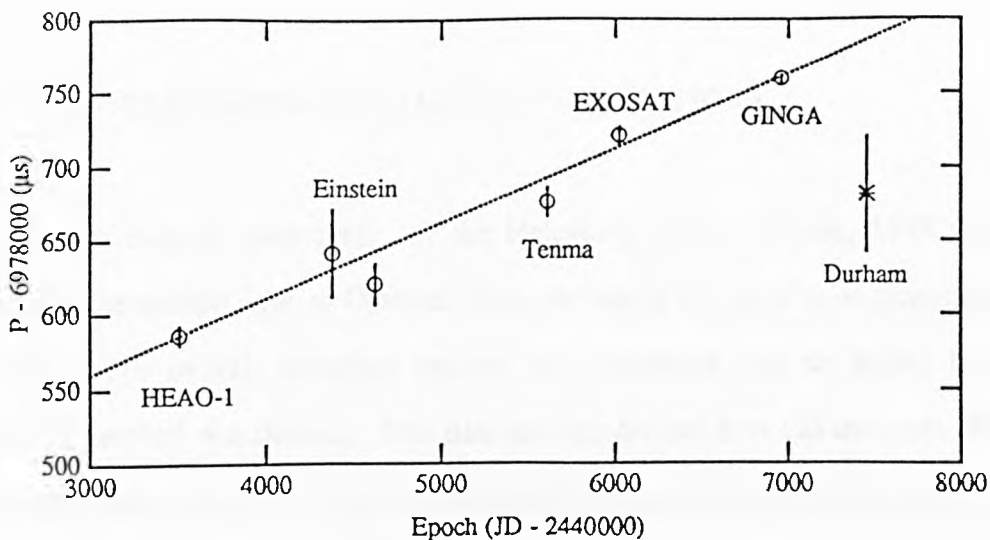


Figure 6.5 The 1E2259+586 pulsar periods measured by satellite observations are plotted as a function of epoch. The period measured by the Durham group is also shown for comparison. The straight line is a fit to the satellite measured periods only and has a gradient of $\dot{P} = (5.83 \pm 0.30) \times 10^{-13} \text{ss}^{-1}$.

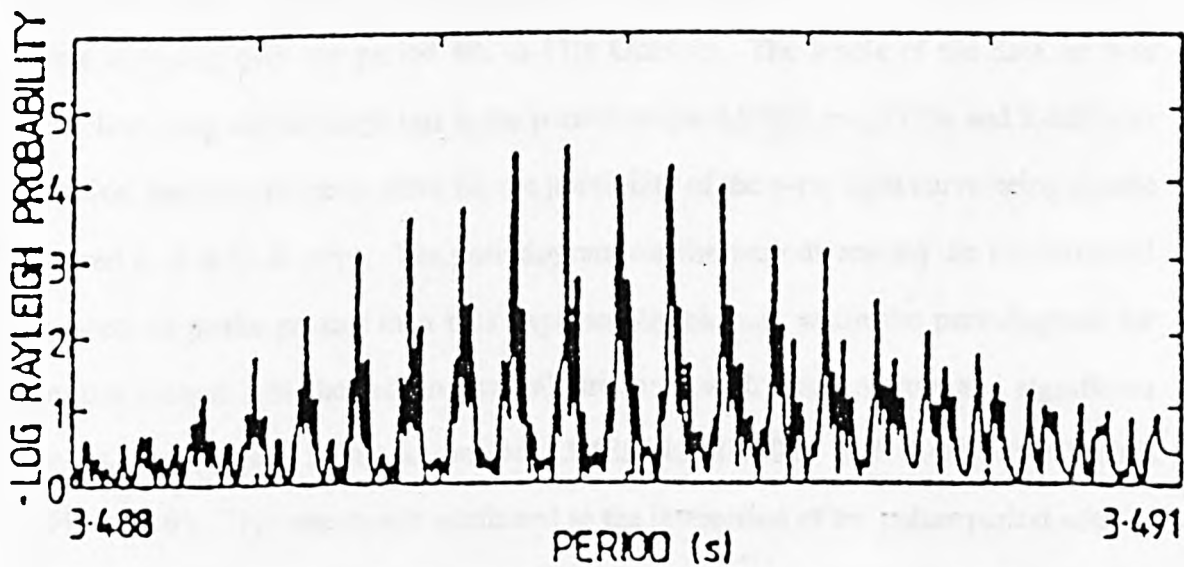


Figure 6.6 The Rayleigh scan performed on 1E data collected in observations made by the Durham group between the 4th and 11th October 1988.

6.2.3 VHE AND UNDERGROUND MUON OBSERVATIONS

1E was studied extensively by the Haleakala group (Weeks, 1988) at TeV energies in the months July to October 1986. A total of 51 hours on-source data were collected. No overall counting excess was observed and an upper limit of $1.32 \times 10^{-10} \text{ cm}^{-2} \text{ s}^{-1}$ was derived. This data set was divided into 125 intervals of 720s. 3 intervals were identified of interest due to apparent signal modulation at periods close to the pulsar period, though none of these were particularly significant. These days showed the strongest Rayleigh power in the first harmonic (the second harmonic was also tested). One of the days had peaks at the period consistent with the expected X-ray period (8/2/86) while the other two both had peaks at periods $\sim 1.3\%$ longer than the X-ray period (6/6/86 and 9/1/86).

In 1988, the Durham group made observations of 1E with their Mark IV gamma ray camera in La Palma (Brazier *et al.* 1990). A total of 13 hours on source data were collected over the period 4th to 11th October. The whole of the data set was searched using the Rayleigh test in the period ranges 6.9786s to 6.9793s and 3.4893s to 3.4896s, the latter range to allow for the possibility of the γ -ray light curve being double peaked as it is in X-rays. The periodogram for the periods around the fundamental showed no peaks greater than that expected by chance, while the periodogram for periods around 3.5s showed an unusual structure, with many narrow and significant peaks, the largest being at periods $3.48934 \pm 0.00002\text{s}$ and $3.48948 \pm 0.00002\text{s}$ (Figure 6.6). This structure is attributed to the interaction of the pulsar period with 24 hour periodicity caused by the 2 hour data collection intervals on consecutive nights being separated by 22 hours. The overall chance probability for the peaks was calculated to be 5.3×10^{-5} once the number of statistical trials had been taken into account. The time averaged flux for the period was $(2.0 \pm 0.8) \times 10^{-10} \text{ cm}^{-2} \text{ s}^{-1}$ at energies greater than 400 GeV, and the suggested fundamental pulsar period was either $(6.97868 \pm 0.00003)\text{s}$ or $(6.97896 \pm 0.00003)\text{s}$. Neither of these periods agree with

expected pulsar period of 6.97880s at the epoch of observation. Brazier *et al.* suggest two possible explanations for this disagreement: (i) 1E is a long period (>days) binary system and the period undergoes Doppler shifting or (ii) 1E is subject to short term spin-up and spin-down variations. Similar observations in June 1989 by the Durham group failed to detect pulsed emission (Turver 1990). Also in 1988, the Whipple observatory (Lamb *et al.* 1991) observed 1E for a total of 80 hours, 13 of which on the 5th to 9th October overlapped the Durham observation. No pulsed emission was seen in this data set with or without the azimuth cut (Section 6.1.3) which has been used with much success on observations of the CRAB. A flux limit of $1.4 \times 10^{-11} \text{ cm}^{-2} \text{ s}^{-1}$ at $E > 400 \text{ GeV}$ is quoted for the period of observation.

Finally, a tentative claim for emission associated with underground muons was made by the Soudan I experiment (Ruddick 1987). A Rayleigh scan was performed on data collected during 1986. A peak was obtained at a period of 6.978627s with an estimated chance probability of 2% taking into account the range of periods searched. They claim that this period is consistent with that reported by Fahlman and Gregory (1983) ($P = 6.978632\text{s}$). More recent satellite observations, however, which show a steady spin-down (Figure 6.5) predict a period of $P = 6.978720 \pm 0.000006\text{s}$ at the epoch of the Soudan observations.

6.2.4 OBSERVATIONS OF 1E2259 +586 WITH THE GREX ARRAY

Data collected between 5th March 1986 and 30th September 1990 has been examined for emission from 1E on both long and short term time scales. A total of 14500 hours of data have been collected during which the source was within 40° of the zenith.

6.2.4.1 Search for DC emission.

For the purpose of calculating the background over the entire observation time, off-source events were collected in a strip in declination, with three off-source bins on either side of the on-source bin. Only days on which all bins had equal exposure as described in chapter 5 were accepted in this analysis. The total useful observation time was thus reduced to ~12000 hours. During the period of 5/3/86 to 30/9/90, a total of 9306 on-source events were collected when 9082 were expected. This is a marginal excess of 2.3σ . The flux limit derived by the method of Protheroe (1984) from these results is $5.7 \times 10^{-14} \text{ cm}^{-2} \text{ s}^{-1}$ for $E > 3 \times 10^{14} \text{ eV}$.

6.2.4.2 Search for long term burst emission

Figure 6.7 shows the cumulative excess of on-source events over the background for the 4.5 years of observation. A steep rise in the signal is seen during the initial operational period of the array up to 16th May 1987. During these 144 sidereal days, a total of 1949 events were observed on-source while 1796.3 were expected. This excess, 10% of the background if attributed to 1E represents a flux of $(1.1 \pm 0.1) \times 10^{-13} \text{ cm}^{-2} \text{ s}^{-1}$ during this period. No attempt was made to assess the significance of this excess by itself as the selection of this time interval was highly arbitrary. Though the beginning of the period was at the turn on of the array, the end of the period was chosen to be that which gave the most significant excess (3.6σ). A large number of statistical trials were therefore incurred in choosing this period and the overall excess is probably not particularly significant. Nevertheless, the interval was identified as being one worthy of further investigation.

The space angle separations of the showers' arrival direction from the source direction, $\Delta\psi$, have been examined to look for a correlation between their distribution and the array point spread function which is expected to be approximately Gaussian.

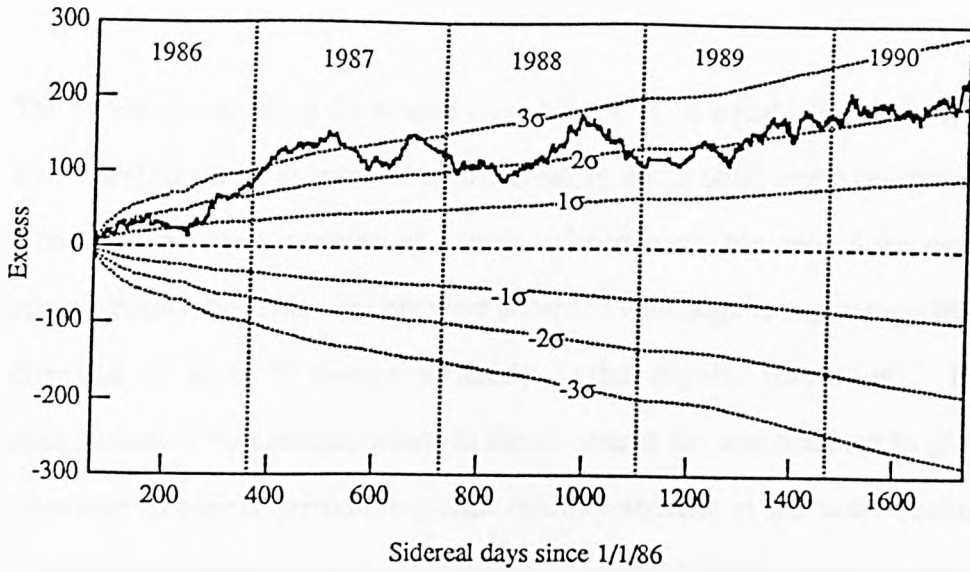


Figure 6.7 The cumulative excess of on-source counts over background counts for 1E2259+586 is shown as a function of the number of sidereal days since 1/1/86.

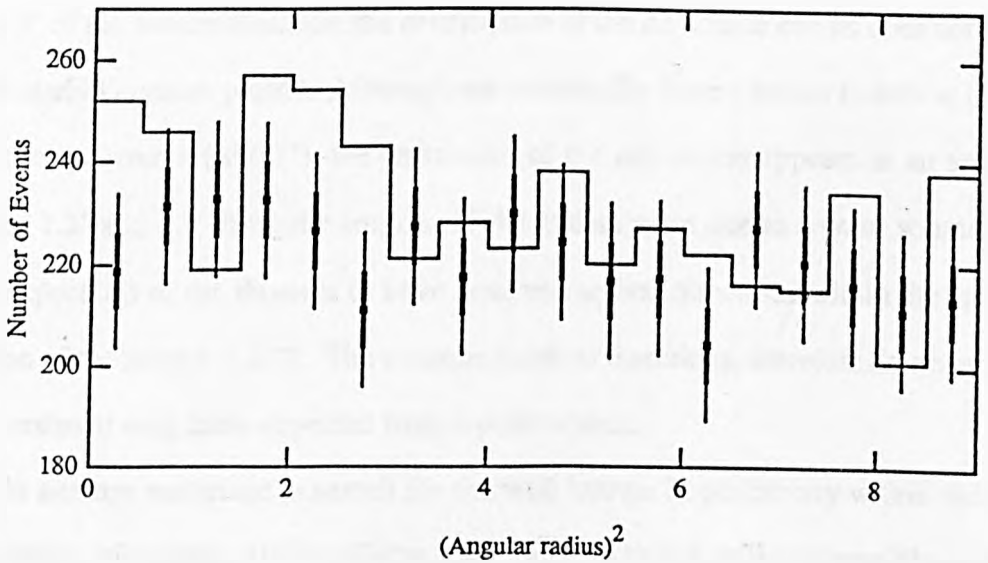


Figure 6.8 Histogram of the number of counts in annuli centred on 1E plotted against the square of the angular radius. Each bin has approximately the same solid angle. The points represent the expected background, B_i , in each bin. The thick and thin error bars show the uncertainty in the background and \sqrt{B} respectively.

The events surrounding the source were binned in 18 equal increments of $(\Delta\psi)^2$. Each bin, therefore, is an annulus of approximately equal solid angle centred on the source direction and the number of events within each bin would be expected to be approximately the same. Events were accepted with angular separations from the source direction of up to 3° (\sim approximately $3\times$ the angular resolution). The expected contribution of background events to the on-source bin was obtained by giving the same treatment to events surrounding four dummy sources at the same declination as the source, but separated from it by $-24^\circ, -12^\circ, 12^\circ$ and 24° in RA so that none of the regions overlap each other or the on-source region. Equal exposure of on-source and off-source regions was guaranteed by demanding 100% array on-time during the transit of all bins. The histogram in Figure 6.8 shows the distribution of $\Delta\psi$ in the on-source region. Also shown for comparison is the expected number of events within each bin obtained by averaging over the off-source regions. Although a net excess of events is observed within 2° of the source direction, the distribution of the on-source events does not show a particularly Gaussian profile. Although the statistically largest excess is seen in the bin closest to the source ($\Delta\psi < 7^\circ$), the remainder of the net excess appears in an annulus between 1.2° and 1.7° from the source. If the excess were due to a point source, one might expect $2/3$ of the showers to have assigned arrival directions within the angular resolution of the array ($\sim 1.25^\circ$). The measured arrival directions, therefore do not appear to be consistent with those expected from a point source.

No attempt was made to search for the well known 7s periodicity within the data for a number of reasons: (i) The X-ray light curve is broad so that a sensible circular statistic to use in searching for periodicity would be the Rayleigh statistic which was also used by the Durham Group (Brazier *et al.* 1990) and Haleakala (Weeks 1988). The Rayleigh probability of observing a modulation of fractional amplitude r in a set of N phases chosen at random is given by:

$$P(>r) = \exp(-k_0) \quad \dots \text{Eqn 6.2}$$

where $k_0 = r^2 N/4$. If the excess was 100% modulated at the expected periodicity, then

the fractional amplitude of the modulation of 1949 on-source events, of which the excess make up only 10%, would be ~ 0.05 . It can be seen that in this case $k_0 \sim 1$, and, even though the Equation 6.2 is only strictly valid for $k_0 \gg 1$, it is obvious that such a value of k_0 is quite likely by chance. The modulated signal would therefore be lost in the noise due to statistical fluctuations. (ii) If a signal is modulated at some period, P , then the phase of an event observed at time T is given by:

$$\phi = \frac{T - T_0}{P_0} - \frac{1}{2} \left(\frac{T - T_0}{P_0} \right)^2 \dot{P} \quad \dots \text{Eqn 6.3}$$

where P_0 is the period at time T_0 and \dot{P} is the period derivative. If we wished to look for a periodicity in data spanning a time interval ΔT over a range of possible periods, then we could arbitrarily set T_0 to the epoch of the first event. The phase of the last event would be given by:

$$\phi = \frac{\Delta T}{P_0} - \frac{1}{2} \left(\frac{\Delta T}{P_0} \right)^2 \dot{P} \quad \dots \text{Eqn 6.4}$$

In the case of 1E, the period derivative is not known precisely. A straight line fit to the graph of period vs observational epoch (Figure 6.5) gives $\dot{P} = (5.83 \pm 0.30) \times 10^{-13} \text{ ss}^{-1}$, though the quoted error is on the conservative side due to the uncertainty in the error of the most recent GINGA observation. If \dot{P} has an error of $\Delta \dot{P}$ then this would lead to a drift in the phase of the final event, $\Delta \phi$, which, to a first approximation, would be given by:

$$\Delta \phi = - \frac{1}{2} \left(\frac{\Delta T}{P_0} \right)^2 \Delta \dot{P} \quad \dots \text{Eqn 6.5}$$

To maintain periodicity, it is necessary to demand that this phase drift be less than 0.1, and this puts an upper limit on the length of the observation interval over which the period search takes place. In the case of 1E this limit is ~ 100 days. One would, therefore, not expect to be able to identify any periodicity in the 'burst period' whose duration is ~ 400 days. It would be possible to split the interval into 100 day sections, and period analyse each of these separately, but this approach would further reduce the expected value of k_0 mentioned in the previous section so that any periodicity would

remain undetectable. (iii) Although the satellite observations measure the pulsar period accurately, their duration is fairly short (~24 hours) and it is possible, therefore that the pulsar exhibits spin-ups and spin-downs over longer time scales, of say weeks, which have not been detected in satellite observations. Such effects would make detection of the pulsar period impossible in data collected over many months.

6.2.4.3 Search for emission on a day-to-day basis

The data were examined on a day to day basis for transient emission from 1E. The background contributions to the on-source bin for each day were calculated using the azimuthal strip technique described in chapter 5. The array was turned on for a total of 1557 sidereal days out of a possible 1673 while the source was above the 40° event horizon. Out of these days, 13 had an excess of on-source events with Poisson probabilities <0.01 and these are listed in Table 6.2. This result is not, in itself, statistically significant (16 days would be expected by chance) the 1% Poisson probability cut being used to identify days worthy of further study.

The 1E days showing large excesses ($P_{\text{pois}} < 0.01$) were analysed for modulation at the 7s pulsar period. In general, it is necessary to correct shower arrival times to their expected arrival times at the solar system barycentre (centre of mass) to allow for the relative motion of the point of observation on the earth to the source. In the case of a single day of observation of 1E, however, with observation times of events being separated by a maximum of 10 hours, correcting to the Heliocentre (Sun centre of mass) would cause an anomolous shift in the relative arrival times of the events of no more than 2ms, and a Doppler frequency shift of less than 1 part in 10^7 . In the case of the observed object being a binary system, one also needs to correct arrival times to its barycentre. The orbital characteristics of 1E, (if it is indeed part of a binary system) however, are insufficiently well known to be taken account of. The single direct measurement of phase shifts assumed due to orbital motion comes from ~3.6 hours of

Date	N_{on}	N_{b}	P_{pois}	T_1	P_1	Pr_1	P_2	Pr_2
21/8/86	17	8.61	0.007	64	6.98681	0.104	6.96667	7.3×10^{-3}
1/1/87	15	6.81	0.004	66	6.99726	1.9×10^{-3}	6.98767	0.035
7/3/87	11	3.96	0.003	43	6.97350	0.023	6.96285	0.020
12/3/88	13	5.43	0.004	84	6.97770	0.018	6.95878	7.5×10^{-3}
10/6/88	12	5.19	0.007	67	6.97280	4.6×10^{-3}	6.96458	2.1×10^{-3}
19/8/88	17	7.66	0.002	74	6.98207	0.016	6.96005	1.8×10^{-3}
28/8/89	18	9.33	0.008	70	6.96074	5.7×10^{-3}	6.97273	0.025
16/10/89	17	8.81	0.009	77	6.99420	1.3×10^{-3}	6.97717	6.2×10^{-4}
18/11/89	17	8.87	0.010	62	6.98413	7.4×10^{-3}	6.97890	0.016
31/12/89	19	8.76	0.009	68	6.97685	0.029	6.98586	7.9×10^{-4}
21/2/90	19	9.63	0.005	79	6.99190	8.9×10^{-3}	6.96233	0.012
30/3/90	18	7.79	0.001	83	6.96953	0.093	6.97581	3.2×10^{-3}
6/7/90	20	9.70	0.002	72	6.98194	0.011	6.96447	0.02

Table 6.2 The 1E2259+586 days having less than 1% Poisson probability. N_{on} and B are the on-source and background counts respectively and P_{Pois} is the Poisson probability of the counting excess. Also given are the results of the 7s period search. T_1 is the number of statistical trials for the search at the first harmonic, P_1 and P_2 are the periods of the maximum Rayleigh power for the first and second harmonics respectively, and Pr_1 and Pr_2 the probabilities of those powers.

Einstein satellite observations (Fahlmann and Gregory 1983) and show the projected semi-major axis ($a_x \sin(i)$) to be ~ 0.17 lt sec. More recent measurements by Hanson *et al.* (1988) with EXOSAT made over a continuous 23 hour period showed no evidence for orbital modulation and put a 3σ upper limit of 0.16 lt sec. on $a_x \sin(i)$. The indications are, therefore, that the effects on the arrival times due to any orbital motion are small compared to the pulsar period. As the X-ray light curve shows fairly broad peaks, the Rayleigh statistic which is sensitive to such features, was chosen to test a range of periods around the expected X-ray period. The Durham Group, if one accepts their conclusions used the Rayleigh test successfully in its detection. Their results showed the signal to be modulated in the second harmonic, as do X-ray observations, while the results of the Haleakala Group showed the signal to be modulated at the fundamental frequency, though this detection was not at a particularly high significance level. It was therefore decided to test for the first and second harmonics. It would also appear necessary to test a broad range of periods to allow for the possibility of the particle beam being reprocessed at some site remote from the neutron star but somewhere within the binary system such as in the accretion disc or in the vicinity of the companion star. This might be expected to produce a red shift in a prograde system as observed in infra-red pulsations from this object (Section 6.2.3), while blue shifts such as those apparently observed from Her X-1 at TeV energies (Section 6.1.3) are rather more difficult to explain but might, nevertheless, be present at these energies. For these reasons, a frequency range of $\pm 0.3\%$ of the expected X-ray period on each day was chosen over which to perform the Rayleigh test. The spacing of the independent Fourier frequencies is given by the reciprocal of the temporal separation of the first and last events within the interval of interest. This is typically $\delta f = 4 \times 10^{-5}$ Hz. The period spacing of the independent frequencies is then given by:

$$\delta P = P^2 \delta f \quad \dots \text{Eqn 6.6}$$

If the test is for modulation at the second harmonic, δP is $1/4$ of this as such a test is equivalent to testing for half the period. The number of independent Fourier frequencies

(IFF) within our chosen range is approximately ~ 20 (40 for second harmonic) though this varies depending on the range of arrival times of events within each day. The range of frequencies was oversampled by $20\times$ giving a total of ~ 400 trial periods. The number of statistical trials incurred in each period scan is given by the number of IFF $\times 3$ to account for oversampling (De Jager 1987). This is approximately 60 and 120 for the fundamental frequency and second harmonic respectively.

Due to the small number of events within each day, it is not possible to use equation 6.2 to determine the probability of observing a Rayleigh amplitude, r , at a given period. Instead these probabilities were assessed using Monte Carlo simulations. The 'pre-trial' probabilities so determined of the largest Rayleigh powers for each day and for both the first and second harmonics are given in Table 6.2 along with the estimated number of statistical trials for the scan for the fundamental frequency. It is clear that none of the days shows significant modulation at either the fundamental frequency or the second harmonic when the number of periods tested is taken into account. The most promising days are 18/11/89 and 21/2/90 on which the largest powers are seen in the second harmonics. The probability of observing these modulations by chance on any given day is 10%, and it is clear that the occurrence of such days is quite likely by chance in a random sample of thirteen. It can also be seen that the periods at which the Rayleigh power is maximum, $P=6.97717s$ and $P=6.98586s$ are different for the two days and also differ significantly from the X-ray period.

In conclusion then, no evidence has been found for emission from 1E either on a long term basis, or on a day to day basis.

6.4 Conclusions

Unfortunately, no emission of γ -rays from the two candidate sources Her X-1 and 1E2259 +586 have been established at an energy of about 1PeV. This result is consistent with those from the most sensitive experiments with the exception of the

remarkable Her X-1 episode recorded by the Cygnus group in 1986. Work with the GREX array will continue for about another year mainly with the aim of searching for transient emission.

APPENDIX**ANGULAR RESOLUTIONS OF THE GREX ARRAY**

Detailed measurements of the angular resolutions of the GREX array were made by sub-array comparisons (Bloomer 1990). No account was made of errors in the final arrival directions due to core position uncertainties. It was found that showers could be subdivided into groups ('resolution groups') according to the geometrical arrangement of their triggered detectors. All showers within the group that had the same size and zenith angle all had approximately the same angular resolution. Showers within each group were then further subdivided into 4 zenith angle and 4 S(50) ranges. The angular resolution of showers within each bin was then calculated for use in determining ideal bin sizes for use in source searching.

The uncertainties in core position also contribute to errors in the final arrival directions assigned to showers. These errors have been calculated by the Author by the method described in chapter 3.

This appendix gives details of the zenith angle, size and resolution groupings used, Tables A1, A2 and A3 respectively, and lists the angular resolutions determined by Bloomer for each of the bins and the additional directional uncertainties due to core location errors in Table A4.

$S(50)_b$	$\ln[S(50)]$	$S(50)$
1	-2.07 to -0.69	0.125 to 0.5
2	-0.69 to -0.69	0.5 to 2.0
3	-0.69 to 2.08	2.0 to 8.0
4	>2.08	>8.0

Table A1 $S(50)$ bins used for parametrising angular resolutions

θ_b	$\sec \theta$	θ
1	1.000 to 1.076	0.00° to 21.66°
2	1.076 to 1.153	21.66° to 29.85°
3	1.153 to 1.229	29.85° to 35.54°
4	1.229 to 1.305	35.54° to 40.00°

Table A2 Zenith angle bins used for parametrising angular resolutions

Pat. types	sub-array spacing(m)	N triggered detectors	Resolution Group
0	Un -patterned		
1	50	7	1
2	50	6	2
3	50	5	2
4	30	7	3
5	30	6	4
6	30	5	4
7	Any other 7 fold		2

Table A3 Pattern types and angular resolution groups

bins			-----Era 1-----		-----Era 2-----		-----Era 3-----		-----Era4-----	
R_b	θ	S_b	$\Delta\Psi_{\text{SDB}}$	$\Delta\Psi_{\text{core}}$	$\Delta\Psi_{\text{SDB}}$	$\Delta\Psi_{\text{core}}$	$\Delta\Psi_{\text{SDB}}$	$\Delta\Psi_{\text{core}}$	$\Delta\Psi_{\text{SDB}}$	$\Delta\Psi_{\text{core}}$
1	1	1	0.74	***	0.77	***	0.73	***	0.73	***
1	1	2	0.74	1.03	0.77	0.71	0.73	0.65	0.73	0.79
1	1	3	0.60	0.40	0.60	0.36	0.55	0.30	0.55	0.26
1	1	4	0.46	0.29	0.43	0.23	0.39	0.19	0.39	0.15
1	2	1	0.74	***	0.77	***	0.73	***	0.73	***
1	2	2	0.74	0.77	0.77	0.85	0.73	0.77	0.73	0.51
1	2	3	0.60	0.43	0.60	0.33	0.55	0.28	0.55	0.25
1	2	4	0.46	0.30	0.43	0.22	0.39	0.19	0.39	0.19
1	3	1	0.74	***	0.77	***	0.73	***	0.73	***
1	3	2	0.74	0.62	0.77	0.92	0.73	0.79	0.73	0.63
1	3	3	0.60	0.39	0.60	0.39	0.55	0.29	0.55	0.30
1	3	4	0.46	0.29	0.43	0.24	0.39	0.20	0.39	0.22
1	4	1	0.74	***	0.77	***	0.73	***	0.73	***
1	4	2	0.74	1.09	0.77	0.92	0.73	0.75	0.73	0.73
1	4	3	0.60	0.51	0.60	0.34	0.55	0.36	0.55	0.48
1	4	4	0.46	0.34	0.43	0.24	0.39	0.24	0.39	0.31
2	1	1	1.04	1.63	1.08	1.08	1.02	0.95	1.02	1.25
2	1	2	1.04	0.84	1.08	0.68	1.02	0.67	1.02	0.67
2	1	3	0.85	0.57	0.84	0.47	0.78	0.39	0.78	0.41
2	1	4	0.64	0.64	0.60	0.68	0.54	0.34	0.54	0.36
2	2	1	1.04	1.67	1.08	1.26	1.02	0.91	1.02	1.03
2	2	2	1.04	0.87	1.08	0.75	1.02	0.71	1.02	0.72
2	2	3	0.85	0.57	0.84	0.48	0.78	0.41	0.78	0.41
2	2	4	0.64	0.69	0.60	0.55	0.54	0.28	0.54	0.38
2	3	1	1.04	1.52	1.08	1.24	1.02	0.93	1.02	1.11
2	3	2	1.04	0.90	1.08	0.76	1.02	0.67	1.02	0.68
2	3	3	0.85	0.63	0.84	0.51	0.78	0.45	0.78	0.43
2	3	4	0.64	0.67	0.60	0.53	0.54	0.31	0.54	0.45
2	4	1	1.04	1.14	1.08	1.14	1.02	1.19	1.02	1.27
2	4	2	1.04	1.00	1.08	0.84	1.02	0.72	1.02	0.72
2	4	3	0.85	0.71	0.84	0.62	0.78	0.49	0.78	0.46
2	4	4	0.64	1.11	0.60	0.50	0.54	0.56	0.54	0.48

Table A4 Angular resolutions.. continued overleaf

----Bins----			-----Era 1-----		-----Era 2-----		-----Era 3-----		-----Era4-----	
R_b	θ	S_b	$\Delta\Psi_{\text{SDB}}$	$\Delta\Psi_{\text{core}}$	$\Delta\Psi_{\text{SDB}}$	$\Delta\Psi_{\text{core}}$	$\Delta\Psi_{\text{SDB}}$	$\Delta\Psi_{\text{core}}$	$\Delta\Psi_{\text{SDB}}$	$\Delta\Psi_{\text{core}}$
3	1	1	0.79	0.73	0.79	0.57	0.71	***	0.71	***
3	1	2	0.79	0.42	0.79	0.35	0.71	0.32	0.71	0.29
3	1	3	0.65	0.25	0.65	0.24	0.60	0.25	0.60	0.24
3	1	4	0.50	***	0.50	***	0.48	***	0.48	***
3	2	1	0.88	0.43	0.88	0.44	0.80	0.49	0.80	0.49
3	2	2	0.88	0.42	0.88	0.33	0.80	0.33	0.80	0.36
3	2	3	0.72	0.28	0.72	0.21	0.68	0.23	0.68	0.20
3	2	4	0.55	***	0.55	***	0.54	***	0.54	***
3	3	1	0.96	***	0.96	***	0.89	***	0.89	***
3	3	2	0.96	0.42	0.96	0.42	0.89	0.38	0.89	0.30
3	3	3	0.79	0.29	0.79	0.27	0.75	0.43	0.75	0.40
3	3	4	0.61	***	0.61	***	0.60	***	0.60	***
3	4	1	1.00	***	1.00	***	0.93	***	0.93	***
3	4	2	1.00	0.44	1.00	0.36	0.93	0.52	0.93	0.36
3	4	3	0.82	***	0.82	***	0.79	***	0.79	***
3	4	4	0.63	***	0.63	***	0.63	***	0.63	***
4	1	1	1.12	0.94	1.12	0.68	1.01	0.77	1.01	0.80
4	1	2	1.12	0.63	1.12	0.54	1.01	0.51	1.01	0.50
4	1	3	0.92	0.38	0.92	0.36	0.85	0.32	0.85	0.34
4	1	4	0.70	***	0.70	***	0.68	***	0.68	***
4	2	1	1.24	0.85	1.24	0.68	1.14	0.63	1.14	0.75
4	2	2	1.24	0.70	1.24	0.57	1.14	0.52	1.14	0.52
4	2	3	1.02	0.40	1.02	0.31	0.96	0.28	0.96	0.31
4	2	4	0.78	***	0.78	***	0.77	***	0.77	***
4	3	1	1.37	1.11	1.37	0.78	1.26	0.79	1.26	0.63
4	3	2	1.37	0.75	1.37	0.56	1.26	0.53	1.26	0.52
4	3	3	1.12	0.35	1.12	0.29	1.07	0.30	1.07	0.32
4	3	4	0.86	***	0.86	***	0.86	***	0.86	***
4	4	1	1.42	1.02	1.42	0.79	1.32	0.74	1.32	0.71
4	4	2	1.42	0.70	1.42	0.64	1.32	0.60	1.32	0.50
4	4	3	1.16	0.55	1.16	0.58	1.11	0.34	1.11	0.32
4	4	4	0.89	***	0.89	***	0.89	***	0.89	***

Table A4 The angular resolutions of the GREX array. $\Delta\Psi_{\text{SDB}}$ are the resolutions determined by Bloomer and $\Delta\Psi_{\text{core}}$ are the RMS errors in arrival direction due to uncertainties in core position. Bins marked '***' have insufficient events to calculate $\Delta\Psi_{\text{core}}$ (<0.1%) ($\Delta\Psi_{\text{SDB}}$ for these are calculated by extrapolation)

REFERENCES

- Abdullah *et al.* (1981) Proc. 17th ICRC (Paris), 6, 151
- Alvarez L.W. and Compton A.H. (1933) Phys. Rev., 43, 835
- Asakimori K. *et al.* (1986) II Nuovo Cimento, 91A, 62
- Auger *et al.* (1939) Rev. Mod. Phys., 11, 288
- Austin R. *et al.* (1990) Proc. 21st ICRC (Adelaide), 2, 110
- Baltrusaitis R.M. *et al.* (1985) Ap. J. Lett., 293, L69
- Battistoni G. *et al.* (1985a) Phys. Lett., 155b, 465
- Battistoni G. *et al.* (1985b) Proc. 19th ICRC (La Jolla), 1, 62
- Bloomer S.D. (1990) PhD Thesis, University of Leeds.
- Bloomer S.D. *et al.* (1988) J. Phys. G.: Nucl. phys., 14 645
- Bray A.P. *et al.* (1984) II Nuovo Cimento, 32, 827
- Brazier K. *et al.* (1990) Nucl. Phys. B (Proc. Suppl.), 14A, 196
- Brecher K. (1972) Nature, 239, 323
- Chadwick P.M. *et al.* (1985) Proc. 19th ICRC (La Jolla), 1, 251
- Chadwick P.M. *et al.* (1987) Proc. Workshop on techniques in Ultra High Energy
Gamma Ray Astronomy (Reidel), p121
- Chardin G. and Gerbier G. (1989) Astron. Astrophys., 210, 52
- Cheung and Mackeown (1987) Proc. 20th ICRC (Moscow), 5, 433
- Clay J. (1932), Proc. Roy. Acad. Amsterdam, 35, 1282
- Clay R.W *et al.* (1987) Proc. 20th ICRC (Moscow), 1, 250
- Davidson A. *et al.* (1972) Ap. J., 177, L97
- De Jager (1987) PhD thesis, Potchefstroom, South Africa.
- Deeter J.E. *et al.* (1981) Ap. J., 247, 1003
- Dingus B. *et al.* (1988) Phys Rev. Lett., 61, 1906
- Dowthwaite J.C. *et al.* (1984) Nature, 309, 691

- Dowthwaite J.C. *et al.* (1984) *Nature*, 309, 691
- Fahlman G.G. and Gregory P.C. (1980) *Nature*, 287, 805
- Fahlman G.G. and Gregory P.C. (1981) *Nature*, 293, 202
- Fahlman G.G. and Gregory P.C. (1983) IAU Symp. No. 101., Venice (Reidel), p445
- Fahlman G.G. *et al.* (1982) *Ap. J.*, 261, L1
- Fenyves E.J. (1985) Proc. Workshop on techniques in Ultra High Energy Gamma Ray Astronomy, eds. Protheroe and Stephens, Univ. of Adelaide, p124
- Gerhardy P. (1983) PhD. thesis, Univ. of Adelaide
- Gorham P.W. *et al.* (1986a) *Ap. J. Lett.*, 308, L11
- Gorham P.W. *et al.* (1986b) *Ap. J.*, 309, 114
- Greisen K. (1956) *Prog. in Cosmic Ray Physics* Vol 3, 1
- Gupta S.K. *et al.* (1990) *Ap. J. Lett.*, 354, L13
- Hanson C.G. *et al.* (1988) *Astron. Astrophys.*, 195, 114
- Hess V.F. (1913), *Phys. Zeits.*, 14, 610
- Hillas A.M. (1984) *Nature*, 312, 50
- Hillas A.M. (1985) Proc. 19th ICRC (La Jolla) 2 296
- Hillas A.M. (1985) Proc. 19th ICRC (La Jolla), 3, 445
- Hughes V.A. *et al.* (1981) *Ap. J. Lett.*, 246, L127
- Johnson T.H. (1933) *Phys. Rev.*, 43, 834
- Jones C. and Forman W. (1976) *Ap. J.*, 209, L131
- Jones C.W. *et al.* (1973) *Ap. J.*, 182, L109
- Khristiansen *et al.* (1981) Proc. 17th ICRC (Paris), 6, 39
- Ko S. *et al.* (1990) Proc. 21st ICRC (Adelaide), 2, 110
- Lamb R.C. *et al.* (1988) *Ap. J.*, 328, L13
- Lamb R.C. *et al.* (1991) 'Observations of TeV Photons at the Whipple Observatory'
(American Insitute of phys.)
- Lampton L. *et al.* (1976) *Ap. J.*, 208 177
- Li T. and Ma Y. (1983) *Ap. J.*, 272 317

- Liller W. *et al.* (1972) IAU Circ. No. 2415
- Linsley J. (1975) Phys. Rev. Lett., 34 1530
- Linsley J. (1986) Private communication to A.A.Watson
- Linsley J. (1987) Proc 20th ICRC (Moscow), 2 442
- Lloyd-Evans J. *et al.* (1983), Nature, 305, 784
- Makino F. (1987) IAU Circ. No. 4459
- Marshak M.L. *et al.* (1985a) Phys. Rev. Lett., 54, 2079
- Marshak M.L. *et al.* (1985b) Phys. Rev. Lett., 55, 1965
- Middleditch J. *et al.* (1983) Ap. J., 274, 313
- Millikan R.A. and Cameron G.H. (1926), Phys. Rev., 28, 851
- Miyake S. *et al.* (1977) Proc. 15th ICRC (Plovdiv), 12, 36
- Miyake S. *et al.* (1981) Proc. 17th ICRC (Paris), 6, 150
- Morini *et al.* (1988) Ap. J., 333, 777
- Muraki *et al.* (1991) Ap. J., 373, 657
- Nagano M. *et al.* (1984) J. Phys. Soc. Japan, 53, 1667
- Nishimura J. and Kamata K. (1952) Prog. Theor. Phys., 7 185
- Ögelmann H. *et al.* (1985) Sp. Sci. Rev., 40, 347
- Parmar A.N. *et al.* (1985) Nature, 313, 119
- Perret J.C. (1986), unpublished work (see also Bloomer S.D. (1990) PhD thesis,
Leeds University)
- Perret J.C. and Patel M. (1987) Haverah Park Internal Report: 'The GPIB Fast Transfer
System'
- Petterson J.A. (1975) Ap. J., 201, L61
- Petterson J.A. (1977) Ap. J., 281, 783
- Press W.H. *et al.* (1986) Numerical Recipes: the Art of Scientific Computing, p301,
Cambridge University Press
- Protheroe R.J. (1984) Astron. Express 1, 33
- Protheroe R.J. (1985) Proc. 19th ICRC (La Jolla), 3, 485

- Protheroe R.J. and Clay R.W. (1985) *Nature*, 315, 205
- Protheroe R.J. *et al.* (1984) *Ap. J.*, 208, L47
- Pugh-Winslow J. (1986) *Introduction to Statistical Analysis*, Addison-Wesley.
- RaghavaRoa R. *et al.* (1981) *Mon. Not. R., Ast. Soc.*, 129, 159
- Resvanis L.K. *et al.* (1987) *Proc. Workshop on techniques in Ultra High Energy Gamma Ray Astronomy* (Reidel), p131
- Resvanis *et al.* (1988) *Ap. J.*, 328, L9
- Reynolds D.T. *et al.* (1990) Preprint
- Roberts W.J. (1974) *Ap. J.*, 187, 575
- Ruddick K.E. (1987) K.E. Turver (ed.) *Proc. Workshop on techniques in Ultra High Energy Gamma Ray Astronomy*. (Reidel), p185
- Rutherford E. and Cooke H.L. (1903), *Phys. Rev.*, 16, 183
- Samorski M. and Stamm W. (1983) *Ap. J.*, 268, L17
- Schreier E. *et al.* (1972) *Ap. J.*, 172, L79
- Stanev T. *et al.* (1985) *Proc. 19th ICRC (La Jolla)*, 7, 219
- Suga *et al.* (1985) *Proc. Workshop on techniques in Ultra High Energy gamma ray astronomy (La Jolla)*, Publ. at Univ. of Adelaide, p48
- Tananbaum H. *et al.* (1972) *Ap. J.*, 174, L143
- Thomson K. *et al.* (1991) Oxford University preprint
- Tonwar S.C. *et al.* (1988) *Ap. J.*, 330 L107
- Turver K.E. (1990) Pre-print
- Van der Waalt E.J. *et al.* (1987) *Proc. 20th ICRC (Moscow)*, 1, 303
- Vladimirsky B.M. *et al.* (1973) *Proc. 13th ICRC (Denver)*, 1, 456
- Watson A.A. (1988) Haverah Park Internal Report: 'A note on the Attenuation Length of Air showers'
- Weeks D. (1988) PhD Thesis, University of Hawaii.
- Wilson R.W. and Bolton J.G. (1960), *Publ. Astro. Soc. Pacif.*, 72, 231

ACKNOWLEDGMENTS

This thesis would never have been written without the help of many people too numerous to mention - almost- but I'll give it a go... First and foremost, thanks must go to Professor Alan Watson, for reading (many times) manuscripts and many useful suggestions. Jeremy Lloyd-Evans must also be thanked for many helpful discussions/arguments and for his company and wit in my final few hours of purgatory. Over the past four years I have enjoyed the friendship of all of the members of the Haverah Park group (I hope!). I would also like to thank my mum (God bless 'er) for her encouragement and confidence in me. And finally.. anybody else that knows me!